

Kent Academic Repository

Full text document (pdf)

Citation for published version

Chin, Catherine Caroline (2018) Advancement in application of supercontinuum sources in biomedical imaging and OCT. Master of Philosophy (MPhil) thesis, University of Kent,.

DOI

Link to record in KAR

<https://kar.kent.ac.uk/70368/>

Document Version

Publisher pdf

Copyright & reuse

Content in the Kent Academic Repository is made available for research purposes. Unless otherwise stated all content is protected by copyright and in the absence of an open licence (eg Creative Commons), permissions for further reuse of content should be sought from the publisher, author or other copyright holder.

Versions of research

The version in the Kent Academic Repository may differ from the final published version.

Users are advised to check <http://kar.kent.ac.uk> for the status of the paper. **Users should always cite the published version of record.**

Enquiries

For any further enquiries regarding the licence status of this document, please contact:

researchsupport@kent.ac.uk

If you believe this document infringes copyright then please contact the KAR admin team with the take-down information provided at <http://kar.kent.ac.uk/contact.html>



Advancement in application of supercontinuum sources in biomedical imaging and OCT

University of
Kent

Catherine Caroline Chin

School of Physical Sciences

University of Kent

Thesis submitted for Master of Philosophy degree

November 2018



The work presented in this thesis was performed:

- Between August 2014 and January 2016, within the Applied Optics Group, at the University of Kent, School Physical Sciences, Canterbury, CT2 7NH, United Kingdom, and
- Between February 2016 and July 2017, at NKT Photonics A/S, Blokken 84, Birkerød, 3460, Denmark

This work was supported by the Marie Curie ITN European grant number 607627 (FP7-PEOPLE-2013-ITN) under project UBAPHODESA (www.ubaphodesa.com)

Preface

Acknowledgement

Since the work in this thesis transcends multiple disciplines of science and technology, I am grateful for the assistance I received from personnel in the School of Physical Sciences, Jennison School of Computing, Medway School of Pharmacy, NKT Photonics A/S, DTU Fotonik at the Technical University of Denmark, and The Maidstone and Tunbridge Wells NHS Trust Hospital.

First, I would like to express my greatest gratitude towards Prof Adrian Podoleanu, for supervising this work, and revising the technical writings on published works. This research work was partly performed at NKT Photonics, I extend my appreciation towards Dr Lasse Leick, Dr Thomas Feuchter, Dr Peter Moselund and Prof Ole Bang for making this thesis possible. I'm thankful for the technical advice and support I received from the NKT team.

Many thanks to Dr Adrian Bradu, Dr Sylvian Rivet and Dr Manuel Marques for the good training in using the master/slave OCT system, without which the collaboration with external clinicians would not been able to run smoothly. I also extend my gratitude to Prof John Schofield, and Miss Mona Khandwala for their patience in teaching me the medical terminologies when we authored the imaging paper on skin cancer.

I sincerely appreciate the time and effort by Dr Gulprit Lall, for the wonderful research experience we had, at Charles River laboratory in Ramsgate and in Medway, Kent.

I also enjoyed the many discussions, outreaches and social outing events we had between the ESRs for the last three years. Michael Maria, Felix Fleischhauer, Sophie Caujolle and Magalie Bondu – thank you! Many thanks, to Rasmus Engelsholm, Laurant Huot and Patrick Bowen for your technical support in the lab.

Finally, I am indebted to the many support from my parents, Vincent Chin and Irene Lim, and for their tremendous encouragement throughout these years.

Abstract

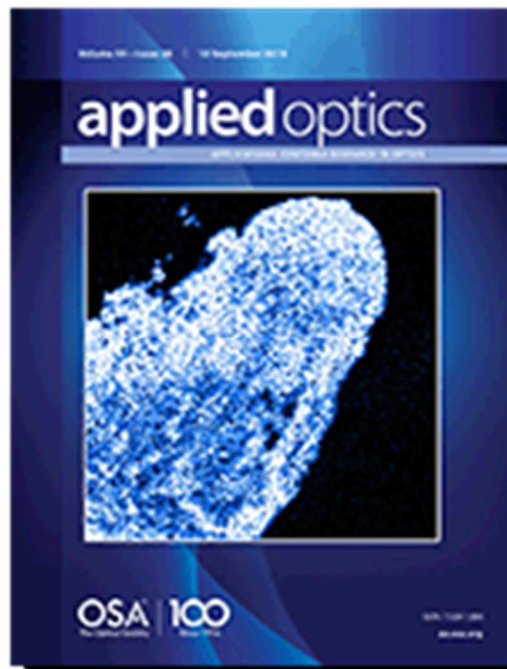
This thesis describes the applications of supercontinuum (SC) sources in biomedical imaging and optical coherence tomography (OCT). Three applications of ultra-broadband imaging were identified, and performed. The first application involves clinical study of eyelid basal cell carcinoma (BCC), a very common type of skin cancer among people with light skin tone in developed countries. The aim was to develop a fast and accurate detection of BCC without first needing surgical intervention. The second application relates to photo receptors in mammalian eye. Retina decoding involving photoreceptor response was performed, using a dual-wavelength light source, tuned at different intensity and exposure duration. The study was conducted to assist diagnosis in age-related macular degeneration (AMD) and to detect symptoms in early-stage vision loss. The third application aims to enhance document security and reduce counterfeit. A novel broadband polarisation-sensitive (PS-) OCT prototype was developed. Powered by SC sources, this revolutionary spectrometer based OCT system scans for birefringent imprints in composite materials, such as cotton-fibre, polymer substrate and dichroic ink pigments in banknotes. Polarisation properties were evaluated and analysed.

To enable high-quality OCT application, measurements of dispersion, noise and polarisation extinction ratio (PER) were carried out. Noise was characterised to assist the development of low-noise SC sources. Dispersion was compensated so that high axial resolution ($< 5\mu\text{m}$) imaging can be achieved. The PER was studied to allow efficient selection and control of polarisation from the light source as well as that in the OCT system.

Finally, the works concluded further improvement in PS-OCT system was needed, by incorporating the master/slave technique and an automatic switch for sequential detection.

Publications and conference papers

1. **C. Chin**, F.Toadere, T. Feuchter, L. Leick, P. Moselund, A. Bradu, and A. Podoleanu, "Acousto-optic tunable filter for dispersion characterization of time-domain optical coherence tomography systems," *Applied Optics* Vol. 55, Issue 21, 5707-5714 (2016).
2. **C. Chin**, A. Bradu, R. Lim, M. Khandwala, J. Schofield, L. Leick, and A. Podoleanu, "Master/slave optical coherence tomography imaging of eyelid basal cell carcinoma," *Applied Optics* Vol. 55, Issue 25, 7378-7386 (2016). [featured on front page of issue 25]



3. **C. Chin**, R. D. Engelsholm, P. M. Moselund, T. Feuchter, L. Leick, A. Podoleanu, O. Bang, "Polarization extinction ratio and polarization dependent intensity noise in long-pulse supercontinuum generation," *Proc. SPIE 10089, Real-time Measurements, Rogue Phenomena, and Single-Shot Applications II*, 100890L (April 2017).
4. [awaiting publication] **C. Chin**, R. D. Engelsholm, P. M. Moselund, T. Feuchter, L. Leick, A. Podoleanu, O. Bang, "Polarization extinction ratio and intensity noise in long-pulse supercontinuum generation," *Opt. Expr.* (2017).

List of figures

1.1	Resolution versus penetration depth for different imaging technologies.....	8
1.2	Therapeutic window with absorbance as function of wavelength for well-known tissue composites.....	9
1.3	Anatomy of a human eye	10
1.4	Photoreceptors in a human eye	11
1.5	Sensitivity and light response of typical human photoreceptors	12
1.6	Different layers of human skin	13
2.1	A simple Michelson interferometer in free space	18
2.2	A simple fibre based interferometer with a 2x2 directional coupler	22
2.3	A time-domain interferometer with output A-scan, sensitivity and axial range	24
2.4	Spectrometer based Fourier domain interferometer in free-space	26
2.5	A swept-source based interferometer in free space	28
2.6	Experimental construction of master/slave interferometer based on a SS-OCT in fibre ..	30
2.7	Composition of an SLD diode	34
2.8	Superlum BroadLighters series SLD at 1300 nm with 20 mW output	35
2.9	Optical spectrum and coherence function at full output power for Superlum BroadLighters series SLD model S1300-G-I-20	35
2.10	Optical spectrum of Axsun swept-source model SS1300-OCT at 1 μm	36
2.11	NKT Photonics SuperK Extreme supercontinuum source	39
2.12	NKT Photonics SuperK Compact supercontinuum source	39
2.13	Supercontinuum spectrum from SuperK Extreme and SuperK Compact	40
3.1.1	Illustration of a time-domain fibre-based interferometer for noise measurement	47
3.1.2	Distribution of electric fields at input and output ports of a directional coupler.....	49
3.1.3	In-house balance detector with two InGaAs photodiodes for noise and SNR measurements in an OCT system	51
3.1.4	Oscilloscope readout of noise power (AC fluctuation) sampled over 100 kHz electrical bandwidth and the linear DC component at balance detector	63
3.1.5	Theoretical SNR for optical sources with different bandwidth at 1300 nm	64
3.1.6	Measured noise power relative to input power	65
3.1.7	Measured SNR in TD-OCT system for optical sources of 35 nm and 150 nm.....	67
3.2.1	Experimental set-up for polarization extinction ratio measurements for a long pulse supercontinuum system	71
3.2.2	Experimental results for full length nonlinear fibre of 8.5 m	74
3.2.3	Experimental results for three fibre lengths of 8.5 m, 4.5 m and 1.5 m at full pump power (100%)	75
3.2.4	Experimental results for 4.5 m non-linear fibre length at high 100% and low 30% pump power	77
3.2.5	Spectra, (bottom) PER for 1.5 m NLF length at low power levels (30%) for three optimisations	78
3.2.6	spectra, (bottom) PER for all three optimisations with NLF length at 1.5 m at full pump power	79
3.2.7	Schematic diagram for birefringence measurement of nonlinear fibre	80

3.2.8	Birefringence measurement with reference spectrum, and spectra of two fibre lengths with interference fringes	82
3.2.9	Full wavelength birefringence measurement	83
3.2.10	Experimental setup for pulse-to-pulse RIN measurement using a high-speed GHz oscilloscope, photo detectors and combination of band pass filters (BPF)	84
3.2.11	Pulse-to-pulse RIN amplitude measured with an oscilloscope and band pass filters	84
3.2.12	RIN measured at two power levels (100% & 30%) for NLF length at 8.5 m.....	86
3.2.13	RIN measured at two power levels (100% & 30%) for NLF length at 4.5 m.....	87
3.2.14	RIN measured at two power levels (100% & 30%) for NLF length at 1.5 m.....	87
3.2.15	Near-Gaussian symmetric probability distribution for RIN measured at 1000 nm (BW 10 nm) on polarisation axis optimised to maximum total power (P_{\max}).....	89
3.2.16	Long-tailed probability distribution for RIN measured at 1500 nm (BW 12 nm) on polarisation axis optimised to maximum total power (P_{\max}).....	89
3.2.17	Long-tailed symmetric probability distribution for RIN measured at 1650 nm (BW 12 nm) on polarisation axis optimised to maximum total power (P_{\max}).....	90
3.2.18	Pulse height histograms at selected wavelengths optimised for two polarisation components (P_{\max} and P_{\min}) on full SC power (100%)	91
3.2.19	Skew and kurtosis calculated from intensity histogram for two polarisation directions at full SC power (100%)	92
4.1	Illustration of broadening of FWHM of a pulse travelling through a dispersive medium	103
4.2	Dispersion slope as function of dispersion versus wavelength	104
4.3	A Gaussian shaped pulse with FWHM indicated	105
4.4	Broadband supercontinuum source (NKT SuperK Extreme) with its output fed into two spectral filtering accessories (either into the AOTF or SuperK Split)	108
4.5	Graphical control user interface for output wavelength selection at the AOTF.....	108
4.6	Output spectrum from SuperK Split splitter module	109
4.7	System configuration for dispersion characterisation using a time-domain OCT system at 1300 nm	110
4.8	Illustration of iterative glass addition method for dispersion compensation in the 1300 nm system	111
4.9	Δ OPD versus wavelength λ_m for different DCG length	112
4.10	Interference strength versus wavelength λ_m selected by AOTF	114
4.11	Autocorrelation function for 1300 nm system	115
5.1	Illustration of linearly, circularly and elliptically polarised EM waves, and their Jones vector directions	124
5.2	Illustration of s- and p-polarisation states for incident, transmitted and reflected lights interacting between air and glass interface	125
5.3	Experimental set up of a broadband dual-spectrometer PS-OCT system powered by a supercontinuum source	131
5.4	Pixel number to wavelength calibration curve for Wasatch Cobra-S model spectrometer (650-950 nm)	133
5.5	Sensitivity roll-off for Wasatch Cobra-S spectrometer	134
5.6	The “reference sample spectrum” recorded at the output of (top) Channel 1, using spectrometer SP1 and (bottom) Channel 2, using spectrometer SP2	135

5.7	The sample with a crossed out section showing the scan area of 8 mm × 8 mm of specimen 1	136
5.8	The sample with a crossed out section showing the scan area of 8 mm × 8 mm of specimen 2	136
5.9	PS-OCT image output from (left) horizontal polarisation, and (right) vertical polarisation for Specimen 1	137
5.10	Post-processed PS-OCT images of Specimen 1 (left) intensity image showing reflectivity, (right) phase retardation	137
5.11	PS-OCT image output from (left) horizontal polarisation, and (right) vertical polarisation for Specimen 2	138
5.12	Post-processed PS-OCT images of Specimen 2 (left) intensity image showing reflectivity, (right) phase retardation	138
6.1	MS-OCT system configuration	147
6.2	Illustration of Master/Slave raster made from 3 categories of images. (a) 40 <i>en-face</i> OCT images separated axially by 5 μm (measured in air), (b) two cross-section OCT images acquired from two orthogonal orientations and (c) an average of the <i>en-face</i> images displayed for guidance. The horizontal size of all images and the vertical size of <i>en-face</i> OCT images: 3 mm × 3 mm. The vertical size of the two cross section images is 3 mm × 1.5 mm (measured in air). The <i>en-face</i> images have 200×200 pixels while the cross section images 200 × 300 pixel	150
6.3	Illustration of assembling cross-section scans from <i>en-face</i> images. <i>En-face</i> images are delivered by the MS-OCT technique	151
6.4	Histology images of nodular BCC corresponding to tissue sample of Case 1	152
6.5	Results of Case 1. Cross section OCT images of eyelid BCC taken from three consecutive transverse slices at the centre of the sample	152
6.6	Results of Case 1. <i>En-face</i> OCT images of eyelid BCC taken at different depths. The depth was measured from the top of the sample in air	153
6.7	Results for another region of Case 1. (left): histology image showing blocks of BCC tumours. (right): <i>En-face</i> OCT image of corresponding region taken at a depth of 780 μm from top of sample (measured in air)	153
6.8	Histology images of superficial BCC from tissue sample of Case 2. The image on the left shows a tumour exhibiting nested and budding patterns. The lateral size × depth size of the left image is 4 mm × 3 mm	154
6.9	Results of Case 2. Cross section OCT images of eyelid BCC taken from the centre of tumour. (1) sweat ducts. (2) blood capillary under the dermis layer. (3) suspected areas of BCC. The lateral size × depth size of image is 1.5 mm × 0.6 mm	155
6.10	Results of Case 2. <i>En-face</i> OCT images of eyelid BCC taken at different depths between 450 to 950 μm. The depth was measured from the top of sample in air. The arrows show the areas of BCC correlated with histology data in Fig. 6.8. The size of each image is 1.5 mm × 1.5 mm	155
6.11	Histology images of Case 3. Image in (b) shows an enlarged view of the white boxed region in image (a). Image (c) shows an enlarged view of the black box area of image (a). The image (d) shows an enlarged region of image (b) indicating presence of nodular pigmented type BCC tumour lobules beneath the epidermis. Magnification: (a) ×20, (b) ×50, (c) ×100, (d) ×200	156

6.12	Results of Case 3. Cross section OCT images of suspected BCC taken at three lateral positions from the centre of sample. The arrows show the areas with pigment correlated with histology images. The lateral size \times depth size of each image is $1.5 \text{ mm} \times 0.6 \text{ mm}$	157
6.13	Results of Case 3. En-face OCT images of eyelid BCC taken at different depths in the range $425\text{-}650 \mu\text{m}$. The depth was measured from the top of the sample in air. The arrows show the areas of BCC. The size of each image is $1.5 \text{ mm} \times 1.5 \text{ mm}$	157
6.14	Orthogonal views of a pig embryo with cross-section diameter between $80\text{-}100 \mu\text{m}$ in ImageJ (top left: en-face slice XY, top right: YZ, bottom left: XZ). The cross-section yellow line indicates the centre of the image	162
6.15	Illustration of Master/Slave raster scan for pig embryo made from 3 categories of images a) 40 <i>en-face</i> OCT images separated axially by $5 \mu\text{m}$ (measured in air), (b) two cross-section OCT images acquired from two orthogonal orientations and (c) an average of the <i>en-face</i> images displayed for guidance	163
6.16	Volumetric 3D views of a pig embryo with cross-section diameter of $100 \mu\text{m}$ in ImageJ	164
7.1	Spectral sensitivity profiles of the classic retinal photoreceptors	171
7.2	Stimulus protocols for a Xenon arc consisting of: (a) a single 480 nm light pulse for 60s , and through the SCWL and (b) a dual stimulus generated at 560 nm for 60 s and at 480nm signal for the last 45s	172
7.3	Stimulus protocols for supercontinuum consisting of a dual stimulus generated at 560 nm for full 60 s and at 480nm signal for the last 45s (from $t=15\text{s}$ onwards).....	173
7.4	Stimulus protocols for a supercontinuum consisting of: a single 480 nm light pulse for 60s	173
7.5	Pupil area was measured by drawing ellipses around the circumference of the pupil in dark adapted, dilated (left) and constricted (right) eyes	174
7.6	Schematic of a single Xe Arc light source used to provide a stimulus	175
7.7	Schematic of the dual stimulus SCWL light source	176
7.8	Spectral line output of SuperK VARIA (NKT Photonics A/S, Denmark)	177
7.9	The pupillary light reflex of dark-adapted mice using a 480 nm light generated by a Xe arc source	179
7.10	Irradiance responses using a 560 nm light (orange curve) and irradiance responses using a $560 \text{ nm}+480 \text{ nm}$ (light red curve) stimulus	179
7.11	Pupil images from dark adapted ($t=-3\text{s}$) through to 560 nm light ($t=10\text{s}$) and finally $480 \text{ nm}+560\text{nm}$ ($t=20\text{s}$)	180
7.12	The dark adapted pupillary response from a 480 nm Xe arc versus a dual $480 \text{ nm}+560 \text{ nm}$ pulse, with same irradiance response profile ($p>0.05$)	181
7.13	Experimental setup used in Charles River laboratory	183
7.14	Multi-wavelength output of the NKT SuperK Varia module	183

List of tables

2.1	Different phase condition for interference and output intensities	21
2.2	Optical components and their abbreviations for an MSI	29
3.1.1	Parameters of a basic PIN photo detector used for noise characterisation.....	52
3.1.2	Signal variation vs input power for the EPN regime	66
3.2.1	Measured total spectral power for three different pump power levels	73
3.2.2	Skew and kurtosis calculated for polarisation with highest power (Pmax).....	92
4.1	Sellmeier coefficient constants for N-BK7 glass	113
4.2	Comparison between Experimental and Calculated FWHM of Autocorrelation Function for Six Values of Dispersion for system at 1300 nm	116
5.1	Jones vectors for different polarisations	125
5.2	Input and output polarisations with QWP and HWP	126
6.1	Four major statistical risk factors of BCC patients	143
6.2	Four major BCC subtypes and their associated histomorphology features	144
7.1	Effective quantal flux density calculated at different wavelengths and illuminating power levels	178

Glossary of Abbreviations

°C	Celsius (unit)
3D	three-dimension
A	Amperes (unit)
AC	alternating current
ADC	analogue to digital converter
AF	audio frequency
Ag	silver
AM	amplitude modulation
AMD	age-related macular degeneration
AOG	Applied Optics Group
AOI	angle of incidence
AOR	angle of reflectance
AOTF	acousto-optic tuneable filter
AR	anti-reflection
ASE	amplified spontaneous emission
Au	gold
B	birefringence
BAL	balance
BCC	basal cell carcinoma
BK7	borosilicate <i>Krone</i> (crown glass)
BN	beat noise
BPD	balance photo detector
BPF	band pass filter
BS	beam splitter
BW	bandwidth
C	Coulombs (unit)
CCD	coupled charge device
CD	chromatic dispersion
CDF	cumulative distribution function
CF	collimation fibre
CG	coherence gate
CL	coherence length

CM	confocal microscope
CNS	central nervous systems
Cp	capacitor
CR	contrast ratio
CS	channelled spectrum
CSLM	confocal scanning laser microscopy
CT	computed tomography
CUDA	compute unified device architecture
CW	continuous wave
DAC	digital to analogue converter
DAQ	data acquisition
dB	decibel (unit)
dBm	decibel-milliwatts (unit)
DC	direct current
DCG	dispersion compensation glass
DF	dynamic focus
DG	diffraction grating
DIFF	differential
DR	dynamic range
DM	dichroic mirror
DNA	deoxyribonucleic acid
DOF	depth of focus
DSP	digital signal processing
DU	demodulation unit
ELEC	electrical
EM	electromagnetic
EPN	excess photon noise
ESA	electrical spectrum analyser
EU	European Union
F	farad (unit)
FC	fibre coupler
FC/PC	fibre-optic connector/ physical contact
FD	Fourier domain
FL	focal length
FFT	fast Fourier transform

FLIM	fluorescent lifetime imaging microscopy
FPGA	field programmable gate arrays
FTIR	Fourier transformed infrared spectroscopy
FWHM	full width at half maximum
FWM	four wave mixing
GDD	group delay dispersion
Ge	Germanium
GP	general practitioner
GPU	graphics processing unit
GS	galvanometer scanner
GVD	group velocity dispersion
HDR	high dynamic range
HeNe	helium neon
HFUS	high frequency ultrasound
HOD	higher order dispersion
HWP	half wave plate
Hz	hertz (unit)
I	inductor
IEEE	Institute of Electrical and Electronics Engineers
InGaAs	Indium gallium arsenide
IF	intermediate frequency
IM	intermodulation
IR	infrared
IRC	irradiance response curve
INTS	integrating sphere
J	Joules (unit)
JPEG	Joint Picture Experts Group
K	Kelvin (unit)
L	lens
LC	inductor-capacitor (circuitry)
LCI	low coherence interferometry
LCD	liquid crystal display
LD	light dark
LNA	low noise amplifier
LO	local oscillator

LP	linear polarisation
LPF	long pass filter
LT	light tube
LTI	linear time invariant
M	mirror
MI	modulation instability
MLS	motorised linear (translation) stage
MMF	multimode fibre
MO	microscope objective
MPM	multi-photon microscopy
MRI	magnetic resonance imaging
MS	master/slave
MSE	mean-squared error
MSF	mean-squared fluctuation
MSI	master/slave interferometry
NA	numerical aperture
ND	neutral density
NEC	noise equivalent current
NHS	National Health Service (UK)
NI	National Instruments
NIF	non-image forming
NIH	National Institute of Health (US)
NIR	near infrared
NLF	nonlinear fibre
OCT	optical coherence tomography
OEM	original equipment manufacturing
Op-amp	operational amplifier
OPD	optical path difference
OPL	optical path length
OPT	optical
OSA	optical spectrum analyser
OSC	oscilloscope
P	polariser
PAM	photo-acoustic microscopy
PBS	polarisation beam splitter

PC	polarisation controller
PCB	printed circuit board
PCF	photonic crystal fibre
PDF	probability density function (maths & stats) portable document format (file)
PD	photo diode
PER	polarisation extinction ratio
PHH	pulse height histogram
PLL	phase locked loop
PLR	pupillary light reflex
PM	polarisation maintaining
PMD	polarisation mode dispersion
PNG	portable network graphics
PR	photo receiver
PRF	pulse repetition frequency
PSD	power spectral density
PSF	point spread function
PS-OCT	polarisation sensitive optical coherence tomography
QWP	quarter wave plate
R	resistor
RCM	reflectance confocal microscopy
RCG	retinal ganglion cell
RIN	relative intensity noise
RF	radio frequency
S	sensitivity
SC	supercontinuum
SCWL	supercontinuum white light
SD	spectral domain
SEM	scanning electron microscope
SHG	second harmonic generation
Si	Silicon
SLD	super-luminescent diode
SLO	scanning laser ophthalmoscopy
SMF	single mode fibre
SN	shot noise

SNR	signal to noise ratio
Sp-OCT	spectrometer based optical coherence tomography
SPIE	Society of photo-optical instrumentation engineers
SPM	self-phase modulation
SRS	stimulated Raman scattering
SS	swept source
T	temperature
TD	time domain
TFT	thin film transistor
TH	threshold
TIA	trans-impedance amplifier
TIFF	tagged image file format
TIR	total internal refraction
TOD	third order dispersion
TN	thermal noise
TS	translation stage
TTL	transistor to transistor logic
UBB	ultra broadband
USAF	United States Air Force
UWB	ultra-wideband
USB	universal serial bus
UV	ultra violet
UVFS	UV fused silica
V	Volts (unit)
VIS	visible spectrum
W	Watts (unit)
WL	wavelength (λ)
Xe	Xenon
XPM	cross-phase modulation
ZDF	zero dispersion fibre
ZDW	zero dispersion wavelength
ZO	zeroth order

Table of contents

0 Preface	
0.1 Acknowledgement	i
0.2 Abstract	ii
0.3 Publications & conference papers	iii
0.4 List of figures	iv
0.5 List of tables	viii
0.6 Glossary	x
0.7 Table of contents	xv
1 Introduction	1
1.1 Background	2
1.2 Chapters summary	3
1.2.1 Technology limitation	6
1.3 OCT in biomedical applications	9
1.3.1 Optical properties in tissues	9
1.3.2 The eye	10
1.3.3 The skin	12
1.3.4 Investigative methods	14
2 OCT and sources	17
2.1 Low coherence interferometry	17
2.1.1 Free space coherence	17
2.1.2 Interference	19
2.1.2.1 Conditions for interference	21
2.1.3 Fibre-based system	22
2.2 Time-domain OCT	23
2.3 Spectral domain OCT	25
2.3.1 Spectrometer based OCT	27
2.3.2 Swept-source (SS) based OCT	27
2.4 Master/slave OCT	29

2.4.1	Principles of operation	29
2.5	Optical sources	33
2.5.1	Narrowband sources	33
2.5.2	Supercontinuum sources	37
3	Noise and polarisation effects in ultra broadband OCT imaging	45
3.1	Noise in balanced OCT system	47
3.1.1	Coupler theory	47
3.1.2	Photodiode detection	51
3.1.2.1	Balance detection	51
3.1.2.2	PIN diode	52
3.1.3	Noise theory	53
3.1.3.1	Shot noise	54
3.1.3.2	Excess photon noise	55
3.1.3.3	Excess noise at low frequencies	57
(A)	Frequency dependent limitation	57
(B)	Optical beam limitation	57
(C)	Semiconductor limitation	58
(D)	Signal processing, filtering & rectification constraints	58
3.1.3.4	Thermal noise	59
3.1.3.5	Beat noise	59
3.1.3.6	Total noise power	60
3.1.4	SNR and sensitivity	61
3.1.4.1	SNR	61
3.1.4.2	Sensitivity	61
3.1.5	Noise measurement technique	63
3.1.5.1	Theoretical modelling	63
3.1.5.2	Experimental measurement	65
3.1.6	Summary of statistical noise	69
3.2	Polarisation and noise in long pulse supercontinuum	70
3.2.1	Polarisation extinction ratio characterisation	71
3.2.1.1	Optimisation to total power	73
3.2.1.2	Optimisation to maximum pump wavelength (1064 nm)	76
3.2.1.3	Optimisation to maximum power at red edge (1950 nm)	77
3.2.2	Fibre birefringence	80

3.2.3	Polarisation relative intensity noise	84
3.2.3.1	RIN	86
3.2.3.2	Pulse height histogram	88
3.3	Polarisation noise in OCT application	94
4	Dispersion in ultra broadband OCT systems	101
4.1	Dispersion and coherence	102
4.1.1	Coherence	102
4.1.2	Dispersion	103
4.1.3	Autocorrelation of a pulse	105
4.2	Methods to evaluate and reduce dispersion	107
4.3	Dispersion experiments	109
4.3.1	Dispersion measurement with time-domain OCT at 1300 nm	109
4.4	Dispersion analysis	111
4.4.1	Dispersion measurement with AOTF at 1300 nm	111
4.4.2	Dispersion measurement with FWHM of autocorrelation at 1300 nm	115
4.5	Comparison between AOTF and FWHM autocorrelation	117
4.5.1	Superiority of AOTF method	117
4.5.2	Minimising dispersion	118
4.5.3	Application of AOTF in broadband OCT dispersion measurement	120
5	Ultra broadband polarisation sensitive and Master/slave OCT	122
5.1	Proof of concept	124
5.1.1	Polarisation of light	124
5.1.2	Slow and fast axes determination	126
5.1.3	Jones matrices	127
5.1.4	Bank notes	128
5.2	PS-OCT system set-up	129
5.2.1	Polarisation selection and switching	130
5.2.2	Polarisation detection	132
5.2.3	Dispersion compensation and spectrometer calibration.....	133
5.2.4	Technical challenges	134
5.3	Imaging results	135
5.3.1	Birefringence samples	135
5.3.2	Cross-section images	136

5.3.3	Future work	138
6	Application of OCT in biomedical imaging	141
6.1	Clinical significance of BCC	143
6.1.1	Clinical classifications of BCC	143
6.1.2	Histology tissue imaging	145
6.1.3	Histology correlation	146
6.2	<i>En-face</i> imaging	146
6.2.1	Master/slave OCT machine	146
6.2.2	BCC correlation techniques and results	151
6.2.3	Comments on technology	158
6.3	Imaging of mammalian embryos	161
7	Application of supercontinuum light sources in vision science	169
7.1	Pupillometry	171
7.1.1	Pupil light reflexes in mammals	171
7.1.2	Animals and ethics	172
7.1.3	Image capture and analysis	172
7.1.4	Dual laser and multi-wavelength setup	175
7.1.4.1	Xenon Arc	175
7.1.4.2	NKT supercontinuum white light source	175
7.2	Pupil stimulus and results	177
7.2.1	Light stimulus	177
7.2.2	Advantages and significance	181
7.2.3	Potential breakthrough in vision science	182
8	Conclusion	185
8.1	Future works	189
	Appendices	191

1

Introduction

High-resolution optical coherence tomography (OCT) is fast emerging as an increasingly common non-invasive imaging of three-dimensional (3D) microstructures and biological tissues. It is used extensively in dermatology and ophthalmology [1-2]. The OCT technology was first reported by the research group of Professor James Fujimoto, at the Massachusetts Institute of Technology (MIT) in 1991 [3-4]. It incorporates the basic principle of low coherence interferometry (LCI) by improving multiple direction lateral scanning capabilities to enhance penetration depth [5-6]. This technique enables simple one dimensional (1D) axial scanning, and was later extended to two and three dimensional (3D) tomography. According to its inventor, Fujimoto et al, that OCT has significant advantages over its nearest comparable imaging modalities, such as confocal microscopy (CF) and multiphoton microscopy (MPM) [7-8]. In comparison, OCT offers high sensitivity imaging, high axial resolution, and long working distances [9]. OCT generally has a much higher resolution but also lower penetration depth when comparing to ultrasound, photo-acoustic microscopy (PAM), computed tomography (CT) and magnetic resonance imaging (MRI) [10]. On the flip side, CF and MPM can provide comparable or better resolution to OCT, but with much lower sensitivity and therefore shallower penetration depth. In recent years, specialists in this field have discovered ways to extend axial imaging resolution of OCT with broadband optical sources. Many publications have suggested that the supercontinuum (SC) sources, such as those manufactured by NKT Photonics and Fianium, is the way forward. This idea of employing SC sources with OCT resonated with among researchers at Applied Optics Group (AOG), particularly group leader Prof. Adrian Podoleanu and Dr Adrian Bradu. Since 2013, a collaboration with NKT Photonics was sought, to explore ways to improve SC sources for use in OCT imaging. The outcome was the successful European Union (EU) grant for project UBAPHODESA (Ultra-Bandwidth Photonics Developed, Sources and Applications). UBAPHODESA's main objective was to develop ultra-broadband optical sources to improve OCT imaging systems for biomedical applications. This thesis summarises the three years research works carried out to achieve that goal.

1.1 Background

The UBAPHODESA project heavily emphasises on application related research and product integration, such as: (a) assembly of high resolution, low noise OCT imaging technology for the eye and OCT endoscopy; (b) assembly of systems to exploit the broad bandwidth of supercontinuum in spectroscopy and nonlinear optics applications, and; (c) evaluate the potential of photo acoustics in adding diagnostic contrast, and be a suitable light weight, compact and portable technology ready in the clinic. On the research part, the main motivation is to establish a link between the source performance and the clinical setting, in order to clarify how to improve diagnostic contrast and imaging quality up to the level of clinical acceptance.

Since NKT Photonics is mainly an optical source manufacturer, they have no prior experience in areas related to OCT. It is costly to acquire such knowledge in an industrial setting and time-consuming to train new personnel. On the other hand, the University of Kent already has expertise in OCT, but needs access to cutting-edge supercontinuum sources. Therefore, as the world's leader in supercontinuum source manufacturing, NKT Photonics was the ideal industrial partner. Their experience has indicated the need for specialised research in the area of noise. Characterisation of supercontinuum to understand noise in a variety of broadband optical set-ups has been very important for them. These are the knowledge NKT Photonics urgently need to design and produce low-noise sources for their customers. There are a wide range of applications with supercontinuum lasers: OCT imaging, material characterisation, metrology and remote sensing. The intent was that, through this European collaboration, the early stage researchers (ESRs) should characterise and optimise the supercontinuum sources at NKT, integrate them with high-resolution OCT systems designed in Kent, and commercialise the final imaging solutions to clinicians. However, as these systems are meant to be broadband, several technical challenges persist. Issues such as chromatic aberrations, dispersion and wave front distortion have to be resolved.

The UBAPHODESA project also has several other far-reaching objectives, such as to establish long lasting collaboration links between the partners involved, to secure Europe's lead in terms of photonics, optical broadband sources and applications, as well as by collaborating with the associated partners, to improve education of future specialists and empower them to react to avenues not identified as yet, for future and yet to be explored supercontinuum applications. That is why technical collaboration between NKT Photonics and academia can yield exciting results. With the expertise in laser system

design and manufacturing, engineers at NKT Photonics were able to allocate necessary resources to assist UBAPHODESA researchers during their work. The feedback from this collaboration was positive. Several ambitious projects and researches that transcend multiple scientific disciplines, such as the OCT clinical trials involving human subjects and laboratory animals, were realised.

To facilitate technical expertise transfers between academic and industrial partners, the works discussed in this thesis were performed at two sites: Applied Optics Group (AOG) at the University of Kent in Canterbury, UK and NKT Photonics A/S in Birkerød, Denmark. Equal amount of time were spent in both sites, amounting to 18 months each. While at the University of Kent, two research projects, one involving clinicians from the Maidstone Hospital, and another with the Medway School of Pharmacy, were conducted.

1.2 Chapters summary

This section provides a brief description on the contents of each chapter and their relevance to the topic of research as a whole. The works presented in this thesis are organised in the following order: one theoretical chapter (Chapter 2), one practical chapter (Chapter 3), two experimental chapters (Chapters 4 and 5), and two application chapters (Chapters 6 and 7).

Chapter two is a theoretical chapter reviewing past and current development of OCT techniques as well as broadband light sources. We begin by presenting the brief concept of coherence and interference, using a simple Michelson interferometer. We move on to show how a basic interferometric imaging system has evolved into the modern OCT technologies. We then continue into derivations of mathematical expressions for the OCT signals in both spatial and temporal domains, while we look into fundamental origin of lateral and axial scanning, before extending these concepts into producing a 3D tomography. We also look into the applications used today in various biomedical hot-topics such as dermatology and ophthalmology. This chapter also includes a description on the different types of OCT techniques: time domain, spectral domain (including spectrometer based and swept-source based operations) and finally our master/slave (MS) system. We go further into the capabilities and drawbacks of several OCT techniques explored, as are their various practical uses. Some of the practical details of implementation are also discussed, particularly those which are of relevance to the

methods employed in the following chapters. We conclude this chapter by looking into various optical sources for OCT systems, from narrowband to broadband.

Chapter three is the practical chapter assessing measurable parameters, such as noise, polarisation extinction ratio (PER) and balance detection to improve OCT imaging quality. We reviewed various types of noise sources, including ways of characterising them. Some of the noise discussed are from the optical source, while others are added by the interferometer. The classifications of noise with theoretical modelling form a large part of our study. We also find ways to optimise the SNR on OCT imaging, in an attempt to improve the axial resolution. Further in this chapter, we investigate the polarisation of supercontinuum generated in nominally non-birefringent silica photonic crystal fibres (PCF) over the entire spectrum of the source, from 450 nm to 2400 nm. We initially showed the degree of polarisation varies but in some parts of the spectrum there is a stable PER of over 10 dB. We later experimentally demonstrate how the spectrally resolved polarization develops with increasing power and along the length of the nonlinear fibre. The experimental results are compared to numerical simulations of coupled polarisation states, mimicking the experimental conditions. Subsequently, we illustrate the principle to correctly measure a single-shot pulse-to-pulse polarisation dependent relative intensity noise (PD-RIN) in two polarisation directions, and how the noise are analysed using long-tailed and rogue wave statistics. In this chapter, we used a range of narrow band pass filters (BPF) between 550 nm to 2000 nm, and fast photo detectors, to record pulses from the source. Peaks from these pulses are first extracted, and then the distribution of the pulse height histogram (PHH) is constructed. Analysis using higher-order moments about the mean (variance, skew and kurtosis) showed that: (1) around the pump wavelength of 1064 nm, the PD-RIN is lowest, PHH exhibits a Gaussian distribution, and higher order moments are zero, (2) further away from pump, PD-RIN increases in parabolic fashion, PHH follows a left-skewed long-tailed Gamma distribution, and higher-order moments increase. Spectrally, the difference of the PD-RIN in the two orthogonal axes increases with PER. We later show how birefringence increases with wavelength and how stimulated Raman scattering (SRS) has a role in spectral broadening.

Chapter four is the experimental chapter that shows the use of a broadband supercontinuum light source with an acousto-optic tuneable filter (AOTF) to characterise dispersion in OCT systems. The filter mentioned here is designed to sweep across two spectral ranges, from 800 to 900 nm and from 1200 to 1500 nm, respectively. In this chapter, we introduce a fibre-based time-domain OCT system, operating at 1300 nm. Dispersion compensation for 1300 nm was achieved using BK 7 glass rods in the reference

arm. The use of AOTF allows evaluation of dispersion in under and overcompensated systems. Further in the chapter, we evaluate the AOTF method using the wavelength dependence of the optical path difference (OPD) that corresponds to the maximum strength of the interference signals recorded using a mirror as object. In addition, a thorough comparison is made between the AOTF method and the more usual method based on measurement of the full width at half-maximum (FWHM) of the autocorrelation peak. This comparison shows that, based on our measured results, the AOTF method is more accurate in terms of evaluation of the dispersion left uncompensated after each adjustment. The AOTF method also provides information on the direction of dispersion compensation, which cannot be easily obtained with FWHM of autocorrelation method.

Chapter five is another experimental chapter. This chapter goes in length to explain the benefit of measuring polarisation properties in samples, and how a polarisation-sensitive broadband OCT system is useful in histology, bio-security and archaeology. A detailed theoretical discussion about PS-OCT begins from the very basic Jones formulation, to electric field rotation, and further into birefringence calculation. We also describe the construction of the PS-OCT setup, from initial polarisation selection, to how we controlled polarisation state at every stage of the interferometer system. Finally, we include a comprehensive discussion on polarisation receiver system that features a simple, switchable dual-spectrometer design. The detection mechanism allows us to extract both amplitude and phase information from two orthogonal polarisation directions.

Chapter six is the application chapter that incorporates functional OCT imaging and dispersion free master/slave interferometer technique on basal cell carcinoma (BCC), a common type of skin cancer. To illustrate the clinical application, we used a conventional swept source at 1300 nm, with sweeping speed of 50 kHz. The imaging part involves a three-step process. First, 384 channelled spectra using a mirror were stored for 384 optical path differences at the master stage. Subsequently, the stored channelled spectra (masks) were correlated with the channelled spectrum from the BCC tissue to produce 384 *en-face* OCT images (200×200 pixels) for the optical path difference values used to acquire the masks. Finally, these *en-face* slices were stacked to form a volume to cross-reference BCC tumour margins in the orthogonal plane. Per each eyelid sample, several *en face* images of 200×200 lateral pixels are produced in the time to scan laterally a complete raster of 1.6 s. Combination of the *en-face* views with the cross-sectioning views allow for better discrimination of BCCs comparable to using cross-sectional imaging alone, as previously reported using the conventional fast-Fourier-transform-based OCT techniques. As for the

optical source, we determined that it could be replaced with a broadband supercontinuum source while maintaining dispersion free imaging with master/slave technique.

Chapter seven is another application chapter focuses on the use of broadband supercontinuum light source to evaluate eye pupil response. In this chapter, we assessed the spectral sensitivity of the pupillary light reflex in mice using a high power super continuum white light (SCWL) source in a dual wavelength configuration. This novel approach was compared to data collected from a more traditional setup using a Xenon arc lamp fitted with monochromatic interference filters. Irradiance response curves were constructed using both systems, with the added benefit of a two-wavelength, equivocal power, and output using the SCWL. The variables applied to the light source were intensity, wavelength and stimulus duration through which the physiological output measured was the minimum pupil size attained under such conditions. We show that by implementing the SCWL as our novel stimulus we were able to dramatically increase the physiological usefulness of our pupillometry system.

Chapter eight sums up the work presented in this thesis, and the overall achievements during the three years of this research work. Also proposed in this chapter are area of interests that are worth further investigations.

1.2.1 Technology limitation

Similar to many imaging technologies, there are huge varieties of fundamentals and practical limitations in both OCT and supercontinuum. Among the frequently cited technical limitations, we have compiled a list of them here as the issues we will address in subsequent chapters of this thesis.

(a) Axial and lateral resolution

Many commercial OCT systems in the market lack the resolution to resolve sub-micron histology features, such as the retina layers in the eye or basal cell carcinoma on the skin. Out of the box improvement to lateral resolution of an existing OCT system can be relatively simple as this involves swapping the scanning (or telocentric) lens by another interface optics with higher numerical aperture (NA). The disadvantage, however, is that it reduces the depth of focus and hence the imaging depth range and sensitivity. Therefore, some form of dynamic focusing is then required, such as the methods described in [11-12] by Avanaki and Hughes. On

the other hand, improvements to axial resolution generally requires the replacement of optical sources and spectrometers to broadband version. In this thesis, we discussed extensively on the use of supercontinuum sources, and methods to overcome noise, dispersion and polarisation, in Chapters 3, 4 and 5 respectively.

(b) Signal to noise

The ability of an imaging system to discriminate useful features relies on its signal to noise ratio (SNR). Several parameters can degrade its SNR ratings, such as a noisy optical source, poor coupling efficiency between free-space to fibre interface, improper signal attenuation due to low power from the sample, and signal saturation at detector.

(c) Chromatic aberrations

The use of refractive optics such as lenses for ultra-high bandwidth imaging is particularly challenging. Since broadband spectrum can easily span across 300-500 nm wide, but very few use the full width, the ability to focus all wavelengths into one spot is not without issue. In general beam propagation, all lenses will have some chromatic aberrations. When focusing a beam, some parts of the will have its beam waist (or focal point) at a different distance due to the chromatic aberration of the lens. The focal length of each wavelength is different, resulting in different wavelengths focused on different positions, along the optical axis.

(d) Polarisation dependency

The challenge to spatially resolve *ex-vivo* and also *in-vivo* images due to polarisation changes in skeletal muscle, bone, skin and brain relies on the ability to control polarisation correctly. This area involves complex coherent detection technique to pick up the differential signal that contains two orthogonal polarization states of the signal formed by interference of light reflected from the biological sample and a mirror in the reference arm of a Michelson interferometer, polarization capabilities can also extend the penetration depth, indirectly by measuring the change in polarisation resolved depth structural changes in biological tissues, additional birefringence properties not otherwise detectable with conventional intensity only imaging technique, as example, any fibrous structure (organic or not) will influence the polarization of light, as shown in Chapter 5.

(e) Penetration depth

OCT relies on interference and therefore requires stable and deterministic phase relations between the interfering waves [9]. Due to scattering and absorption in the examined object, the number of photons in the backscattered wave conserving stable phase relations to the photons in the incident wave reduces with depth. The maximum penetration depth, Δz is therefore determined by the depth layer where the object wave exhibits sufficient strength to measurable interference, normally on a signal strength equal to that of the noise. Fig.1.1 shows achievable axial resolution against penetration depth for the different competing imaging technologies.

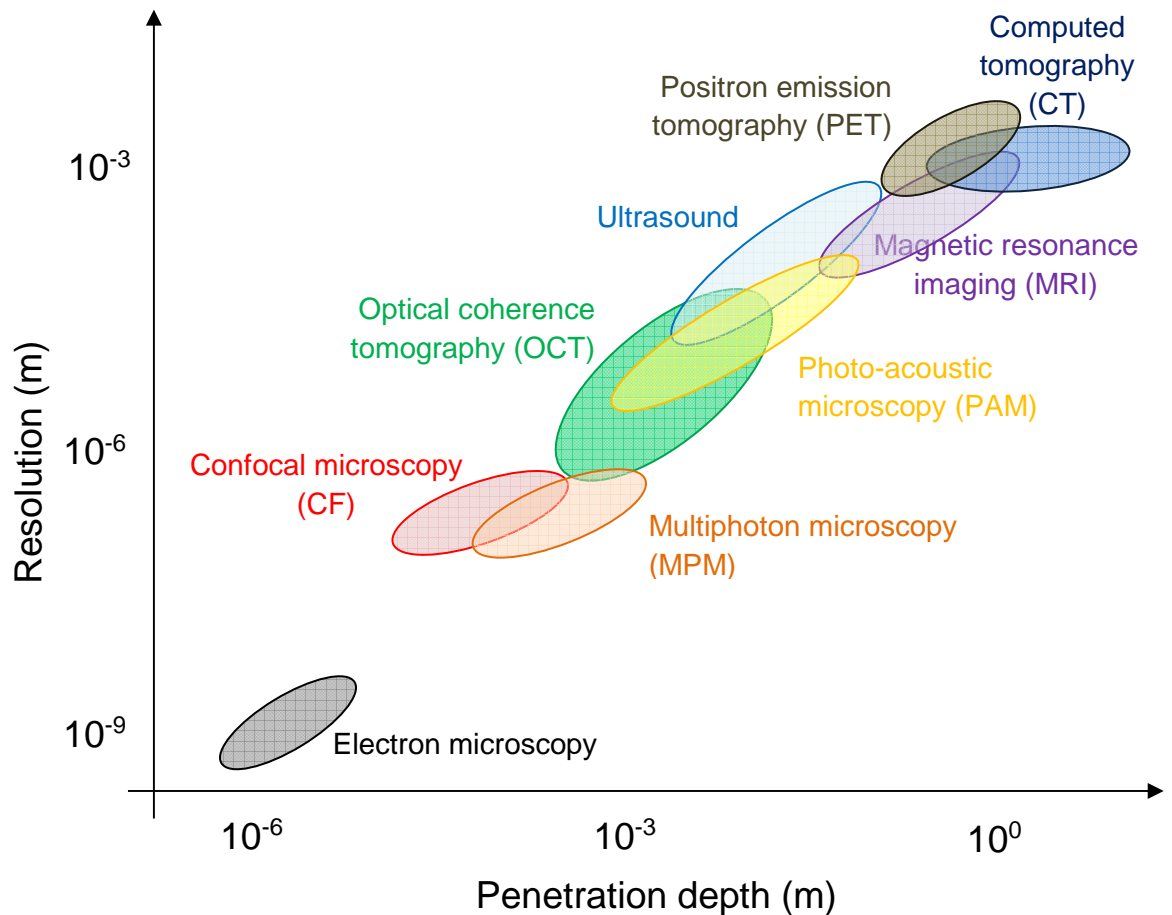


Fig.1.1 Resolution versus penetration depth for different imaging technologies

1.3 OCT in biomedical applications

OCT has become increasingly popular for skin and eye diagnosis. Since 2010, there are more than 100 peer reviewed papers published a year on the use of OCT in these areas. OCT is currently the preferred way to image the retina for glaucoma, as evidenced in [13]. Many recent OCT systems has also incorporate the scanning laser ophthalmoscope (SLO) technology in many hospitals and eye clinics in the UK, given the added benefits of better axial resolutions [14]. The main use of OCT on skin is to diagnose tumour development, such as the eyelid BCC. In this section, we introduce the basic anatomy of both eye and skin, and the optical properties of their tissue made up.

1.3.1 Optical properties in tissues

The therapeutic window generally represents the spectral window of the wavelength range from 600 nm to 1300 nm. Within the therapeutic window, the absorbance of the main constituents of the tissue is relatively small and the light penetrates sufficiently well in depth. In Fig.1.2, we show the absorption spectra for haemoglobin (HbO_2 and Hb), melanin and water [15].

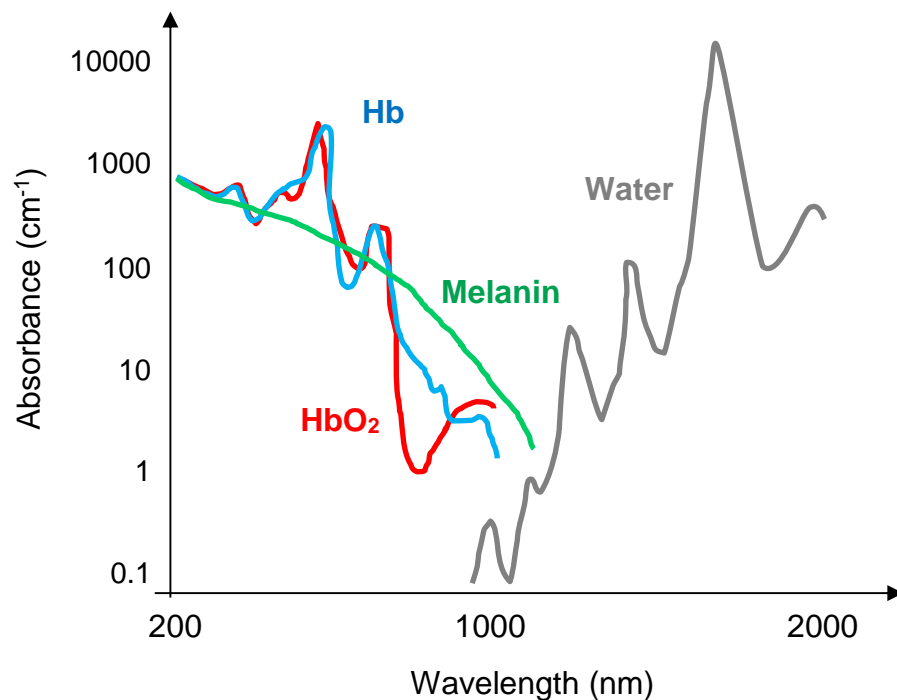


Fig.1.2 Therapeutic window with absorbance as function of wavelength for well-known tissue composites (Image reproduced from ref. [15])

1.3.2 The eye

The mammalian eye is a complex biological imaging system. In the simplest form, the anatomy of a human eye consists of an outer layer called cornea, an iris that controls the diameter and size of pupil and a lens, as shown in Fig.1.3. Light enters the pupil, focuses onto the retina and is detected by the photoreceptors [16].

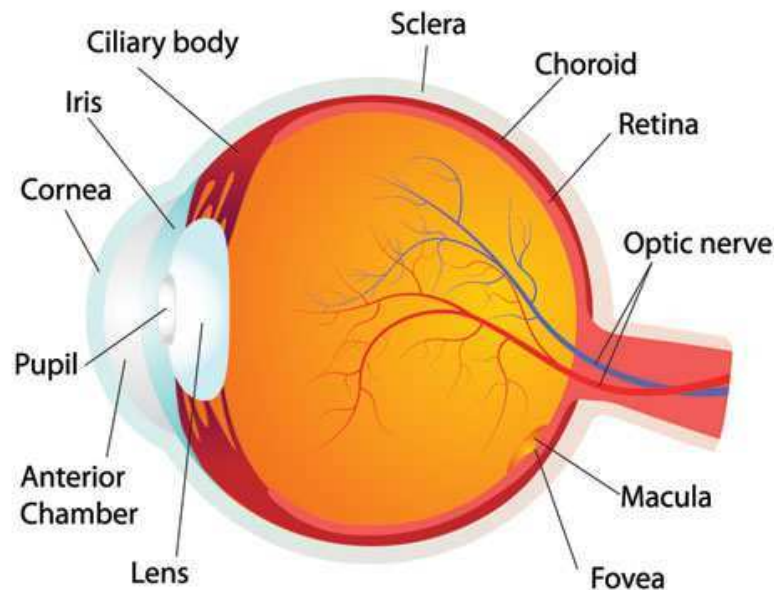


Fig.1.3 Anatomy of a human eye [Source: <http://www.rnib.org.uk/eye-anatomy>]

In the eye, there are two main types of photoreceptors, cone and rod, seen in Fig.1.3. Overall, there are estimated to be around 105 million photoreceptors in our eyes. Generally there are more rods than cones in our eyes, with their population spanning between 5 to 6 million cones, and between 80 and 90 million rods [17].

Cones are responsible for colour vision and detail image vision. Cones are typically 40–50 μm long, and have a diameter varies from 0.5 to 4.0 μm . There are three types of cones, marked S, M and L cones, which corresponding to their wavelengths response as shown in Fig.1.5. The S (short) cone has light sensitivity in blue (peak at 420–440 nm), M (medium) cone is highly sensitive in green (peak at 534–545 nm) and L (long) cones are sensitive to red portions of the visible spectrum (564–580 nm). Cone cells are most concentrated at the fovea, with a sparse distribution of cones towards the periphery of the retina [18].

Rods, on the other hand, are highly sensitive to light and can provide some grey scale vision in low-light environments. Rods have peak response between 490-500 nm ranges (Fig.1.5) [20]. Rods however cannot distinguish colour but provide only luminosity information. Rod cells are approximately 2 μm in diameter and distributed across most of the retina except the fovea and the optic disc, with a higher density in the peripheries of the retina than the central area. In the mammalian retina, there are two additional opsins, both involved in the formation of visual images: rhodopsin and photopsin in the rod and cone photoreceptor cells, respectively. In humans, melanopsin is found in intrinsically photosensitive retinal ganglion cells (ipRGCs) [19] as illustrated in Fig.1.4. Photoreceptors response to light stimulus, including melanopsin, form the basis of our study in Chapter 7.

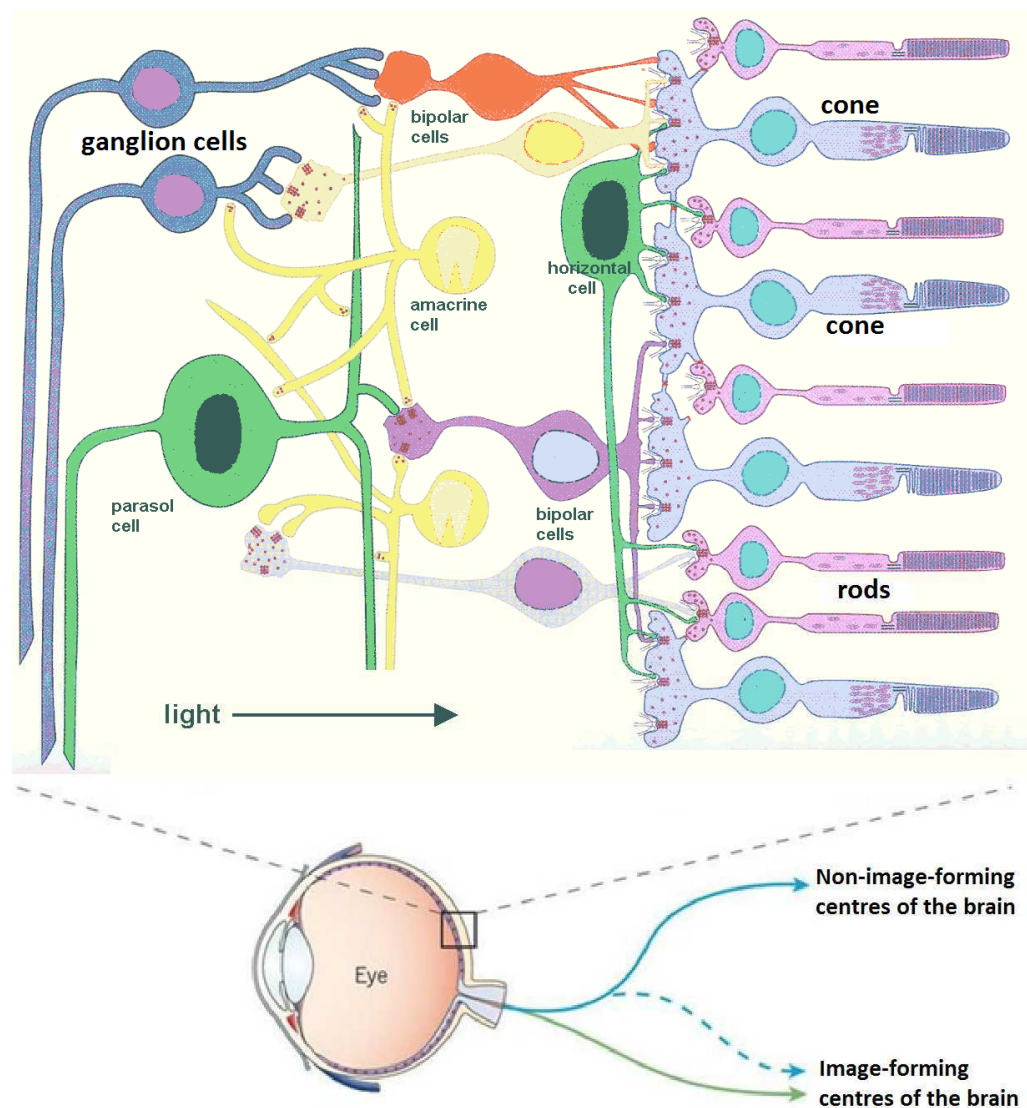


Fig.1.4 Photoreceptors in a human eye [Source: <http://www.bmb.leeds.ac.uk/illingworth/bioc3800/retina.gif>]

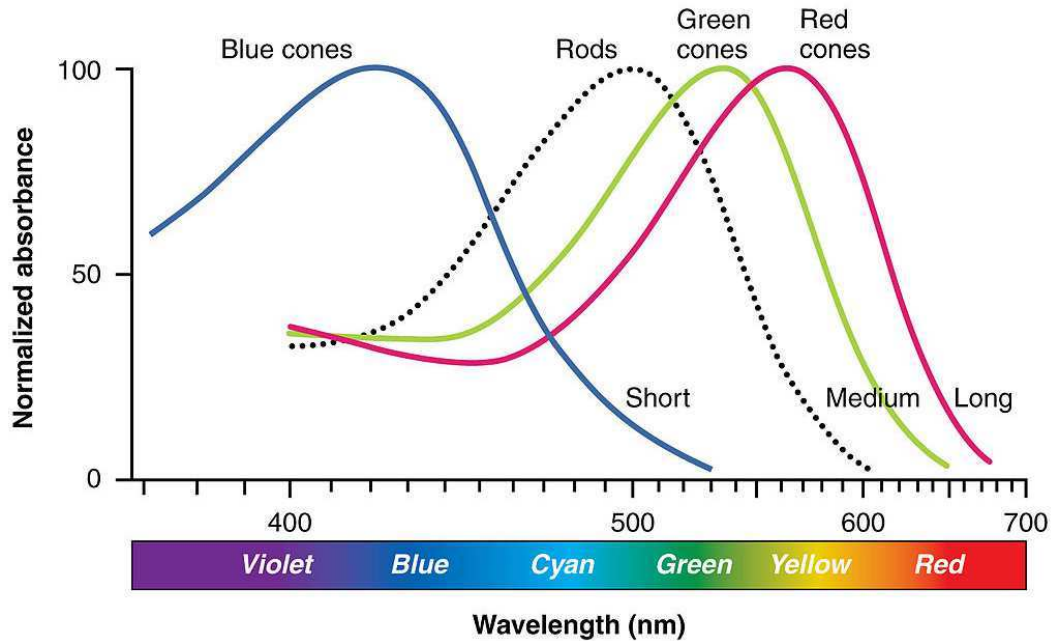


Fig.1.5 Sensitivity and light response of typical human photoreceptors (Source: http://www.wikiwand.com/en/Photoreceptor_cell, Ref [20])

1.3.3 The skin

The skin is undoubtedly the largest tissue organ in humans. Skin has three layers: epidermis, dermis, and hypodermis. In the simplest terms, the epidermis is outermost layer of skin, provides a waterproof barrier and creates our skin tone. The middle layer of the skin is the dermis, beneath the epidermis and contains tough connective tissue, hair follicles, and sweat glands. Finally, the deeper subcutaneous tissue is the hypodermis, typically consists of fat and connective tissue.

At the current stage of OCT development, main interests are focused on the epidermis. As mentioned previously, the epidermis is a thin but tough layer of skin that protects the body, while it gives skin its colour and makes and replaces new skin. The epidermis is made of several different types of cells, including squamous cells, basal cells melanocytes cells and among others.

Basal cells are round cells in the deepest part of the epidermis (commonly known as the basal cell layer). Their function is unclear. They continually divide, make new cells and push the older cells toward the surface of the skin where they are eventually shed [21]. The older cells eventually become mature keratinocytes and squamous cells.

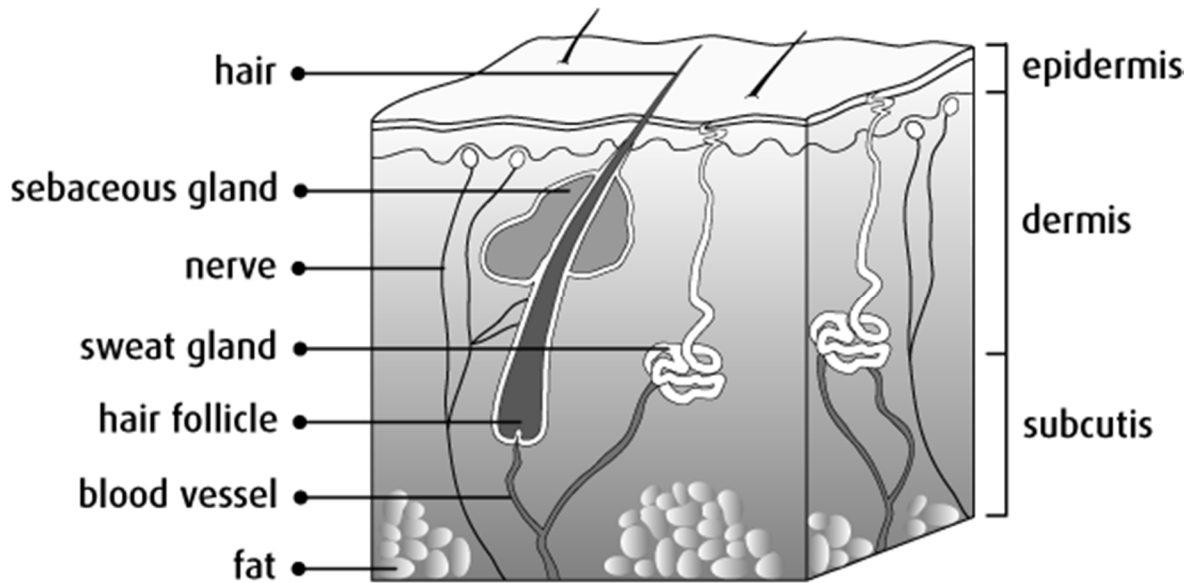


Fig.1.6 Different layers of human skin [source: <http://www.cancer.ca/en/cancer-information/cancer-type/skin-non-melanoma/non-melanoma-skin-cancer/the-skin/>]

Melanocytes are cells found in the deepest part of the epidermis along with basal cells. They are also found in hair follicles and the retina of the eye. The main function of melanocytes is to produce melanin – the very substance that gives skin its colour and helps to protect the body from harmful light radiation, such as those from the sun. Exposure to ultraviolet (UV) radiation from the sun propels melanocytes to increase melanin production. Therefore, longer sun exposure causes the skin to darken and become tanned. The extra melanin produced is transferred to other skin cells (keratinocytes) to protect the skin and the DNA in the cells from the damaging UV lights. DNA is composed of molecules inside the cell that program genetic information. DNA determines the structure, function and behaviour of a cell. The amount of melanin produced varies person to person, but it is largely due to an individual's genetic composition. People with fair-coloured skin can be assumed to have less melanin produced by their melanocytes, and are considered at higher risk of contracting skin cancer such as basal cell carcinoma (BCC) [22].

BCC is a type of non-melanoma skin cancer among Caucasian populations, and the most common malignant neoplasm of humans. The BCC can grow on any part of the skin, such as nose, cheek, finger and neck. However, the eyelid BCC is most common. BCC occurrences are also frequently diagnosed in people with fairer skin colour for reasons mentioned above. Chapter 6 dives into the symptoms of BCCs, along with their clinical significance and our approach to diagnosis using *en-face* master/slave OCT technique.

1.3.4 Investigative methods

Imaging human tissues have a challenge. One of them is to be able to improve penetration depth and maintain reasonable SNR. For the skin, OCT with proper wavelength of 1300 nm. A quantitative study [23] has found that biological tissues can allow an increase of the OCT imaging depth at 1600 nm compared to 1300 nm for samples with high scattering power and low water content. Our earlier studies with swept source [24] to compare 1300 nm to 850 nm also found the same conclusion on the use of longer wavelength on skin tissue imaging. Our results were confirmed by study by Tearney et al. in 1995 [25], which concluded that high numerical aperture OCT enhanced confocal microscopy have potential for non-invasive *in-vivo* diagnosis.

According to a study conducted by [26-27] light attenuation including both absorption and scattering in human skin reaches a minimum around 1300 nm wavelength due to the combination of diminishing scattering cross-section with wavelength and avoiding the resonant molecular absorption of common tissue constituents such as water, melanin and haemoglobin (see Fig. 1.2). By moving the operating wavelength of optical biopsy from 800 nm band, to 1200-1400 nm spectral range, not only can it increase the penetration depth in skin, but also reduce multiphoton absorption in cross sections, thus reduce the potential of photo damage and photo toxicity when imaging with higher optical power.

For the eye, wavelengths in the region of 1300 nm have little usefulness for practical ophthalmology applications, as they are absorbed by the water contents in the ocular chamber. Therefore, the use of 1300 nm is limited to the anterior eye segment, where it is used to image the sclera and iris (front section of the eye shown in Fig. 1.3) [28]. Other wavelengths range in 700-850 nm are more common for imaging the retina. Nevertheless, the complexity in wavelength selection to image the eye have prompted the industry to explore broadband sources to overcome this situation. Here, we will demonstrate a recent approach is to use the supercontinuum (SC) with multi-wavelength filtering and programmable stimulus duration. We illustrate the principle of operation with SC sources to evaluate retina photo receptors through pupil light reflex (PLR), all in Chapter 7.

En-face OCT on skin and SC with systematic retina decoding to detect and analyse response from the eye form the basis of our functional (or physiological) imaging application in this thesis.

References

1. J. Welzel, "Optical coherence tomography in dermatology: a review," *Skin Res Technol.* **7**(1), 1-9 (2001).
2. M. Adhim, J. S. Duker, "Optical coherence tomography – current and future applications," *Current opinion in ophthalmology*, **24**(3) 213-221 (2013).
3. D. Huang, E. A. Swanson, C. P. Lin, J. S. Schuman, W. G. Stinson, W. Chang, M. R. Hee, T. Flotte, K. Gregory, and C. A. Puliafito, "Optical coherence tomography " *Science* **254**, 1178-1181 (1991).
4. J. G. Fujimoto, C. Pitris, S. A. Boppart, M. E. Brezinski, "Optical Coherence Tomography: An Emerging Technology for Biomedical Imaging and Optical Biopsy," *Neoplasia*, **2**(1), 9-25 (2000).
5. R. C. Youngquist, S. Carr, and D. E. N. Davies, "Optical coherence-domain reflectometry: a new optical evaluation technique," *Opt. Lett.* **12**, 158-160 (1987).
6. O A. F. Fercher, C. K. Hitzenberger, G. Kamp, and S. Y. El-Zaiat, "Measurement of intraocular distances by backscattering spectral interferometry," *Opt. Comm.* **117**, 43-48 (1995).
7. N. Bouheraoua, L. Jouve, M. E. Sanharawi, O. Sandali, C. Temstet, P. Loriaut, E. Basli, V. Borderie, L. Laroche, "Optical coherence tomography and confocal microscopy following three different protocols of corneal collagen-crosslinking in keratoconus," *Invest. Ophthalmol. Vis. Sci.* **55**(11), 7601-7609 (2014).
8. B. Jeong, B. Lee, M. S. Jang, H. Nam, S. J. Yoon, T. Wang, J. Doh, B. G. Yang, M. Ho Jang, K. H. Kim, "Combined two-photon microscopy and optical coherence tomography using individually optimized sources," *Opt. Expr.* **19**, 13089-13096 (2011).
9. X. Zhang, H. F. Zhang, S. Jiao, "Optical coherence photoacoustic microscopy: accomplishing optical coherence tomography and photoacoustic microscopy with a single light source," *J. Biomedical Opt.* **17**(3), 030502 (2012).
10. J. P. Dunkers, D. P. Sanders, D. L. Hunston, M. J. Everett, W. H. Green, "Comparison of Optical Coherence Tomography, X-Ray Computed Tomography, and Confocal Microscopy Results from an Impact Damaged Epoxy/E-Glass Composite," *J. Adhesion* **78**, 129–154 (2002).
11. M. R. N. Avanaki, A. Aber, S. A. Hojjatoleslami, M. Sira, J. Schofield, C. Jones, A. Gh. Podoleanu, "Dynamic focus optical coherence tomography: feasibility for improved basal cell carcinoma investigation," *Proc. SPIE* **8225X**, 82252J (2012).
12. M. Hughes, A. Gh. Podoleanu, "Simplified dynamic focus method for time domain OCT," *Elec. Lett.* **45**(12), 623-624 (2009).
13. J. Kotowski, G. Wollstein, L. S. Folio, H. Ishikawa, J. S. Schuman, "Clinical Use of OCT in Assessing Glaucoma Progression," *Ophthalmic Sur. Lasers Imaging* **42**(0), S6-S14 (2011).
14. F. Felberer, M. Rechenmacher, R. Haindl, B. Baumann, C. K. Hitzenberger, M. Pircher, "Imaging of retinal vasculature using adaptive optics SLO/OCT," *Biomed. Opt. Expr.* **6**(4), 1407-1418 (2015).
15. B. L. Horecker, "The Absorption Spectra of Hemoglobin and its derivatives in the visible and near infra-red spectra," *J. Biol. Chem.* **148**, 173-183 (1943).
16. A. Roorda, D. R. Williams, "The arrangement of the three cone classes in the living human eye," *Nature* **397**(6719), 520-2 (1999).

17. L. T. Sharpe, A. Stockman, D. I. MacLeod, "Rod flicker perception: scotopic duality, phase lags and destructive interference," *Vision Res.* **29**(11), 1539-59 (1989).
18. D. Mustafi, A. H. Engel, K. Palczewski, "Structure of Cone Photoreceptors," *Prog. Reti. Eye Res.* **28**(4), 289-302 (2009).
19. M. Hatori, S. Panda, "The emerging roles of melanopsin in behavioral adaptation to light," *J. Mol. Med.* **16**(1), 435-446 (2010).
20. J. K. Bowmaker and H. J. A. Dartnall, "Visual pigments of rods and cones in a human retina," *J. Physiol.* **298**, 501-511 (1980).
21. National Health Institute (NIH) SEER Training Modules – Layers of the Skin, <https://training.seer.cancer.gov/melanoma/anatomy/layers.html> retrieved July 16, 2017.
22. Canadian Cancer Society – The Skin, "<http://www.cancer.ca/en/cancer-information/cancer-type/skin-non-melanoma/non-melanoma-skin-cancer/the-skin/?region=on>" retrieved July 16, 2017.
23. Kodach VM, Kalkman J, Faber DJ, van Leeuwen TG. Quantitative comparison of the OCT imaging depth at 1300 nm and 1600 nm. *Biomedical Optics Expr.* **1**(1), 176-185 (2010).
24. M. Khandwala, B. R. Penmetsa, S. Dey, J. B. Schofield, C. A. Jones, A. Podoleanu, "Imaging of periocular basal cell carcinoma using en face optical coherence tomography: a pilot study," *Brit. J. Ophthal.* **1136**, 1-5 (2010).
25. Guillermo J. Tearney ; Mark E. Brezinski ; Michael R. Hee ; Brett E. Bouma ; Joseph A. Izatt, et al. "Optical coherence tomography in multiply scattering tissue", *Proc. SPIE* **2389X**, 29 (1995).
26. R. R. Anderson and J. A. Parish, "The optics of human skin," *J. Invest. Dermatol.* **77**, 13-19 (1981).
27. P. C. Cheng, S. J. Pan, A. Shih, K.-S. Kim, W. S. Liou, and M. S. Park, "Highly efficient upconverters for multiphoton fluorescence microscopy," *Journal of Microscopy* **189**, 199-212 (1998).
28. S. Radhakrishnan, A. M. Rollins, J. E. Roth, S. Yazdanfar, V. Westphal, D. S. Bardenstein, J. A. Izatt, "Real-Time Optical Coherence Tomography of the Anterior Segment at 1310 nm," *Arch. Ophthalmol.* **119**(8), 1179-1185 (2001).

2

OCT and sources

The chapter provides an overview on the different optical coherence tomography (OCT) methods, and their basic principles of operation. A comprehensive analysis of their advantages and disadvantages is shown in relation to their widely used applications. The main OCT methods include classical time domain (TD), newer spectral domain (SD) and the master/slave (MS) implementations. Among the SD-OCT systems, we present two configurations: a spectrometer-based (Sp-) OCT and a swept-source based OCT [2]. This chapter begins by looking into white light interferometry, partial coherence and conditions to achieve interference, all in Sec.2.1. We then moved on to the different OCT methods, where we present TD-OCT in Sec.2.2, FD-OCT in Sec.2.3 and MS-OCT in Sec.2.4. Throughout these theory sections, we show and compare advantages of each method to the other, and how each method can be used to design and construct a working imaging system, all in a step-by-step way. Later in this chapter, we will present the appropriate pairing of a particular OCT method with the commonly used optical sources, which are to be discussed in later sections. In Sec.2.5, we will compare the different optical sources, such as the superluminescent diode (SLD), tuneable lasers or swept-source (SS), and the supercontinuum source (SC).

2.1 Low coherence interferometry

2.1.1 Free space coherence

Low-coherence interferometry (LCI) [1-2] uses low-coherence light beam to probe different layers of a sample. Light is first delivered onto the sample surface and through the material layer, and the reflected light is sent back to the interferometer. The reflected light at each different layer produces interference pattern that differs in signal strength. A single interface scan at a depth results in an interferogram containing the reflectivity profile. When an axial scan orthogonal to the surface is performed, a two-dimensional (2D) cross-

sectional image is generated. By combining multiple 2D scans, in the longitudinal direction, a three-dimensional (3D) volumetric image can be produced [3-4].

To aid our discussion, we will first consider a simple, Michelson interferometer in bulk, as shown in Fig.2.1. In this configuration, the light from an optical source enters a free-space beam splitter (BS), and it is split into reference and sample arms. The beam from reference arm reflects off a movable mirror, and recombines with the beam back propagated from the sample. The combined beam is sent to the photo detector. It is worth nothing that the optical beam travelling into and out of the two arms are on the same axis, therefore LCI observes the collinear condition [5]. We use this configuration to illustrate the principles of coherence and interference.

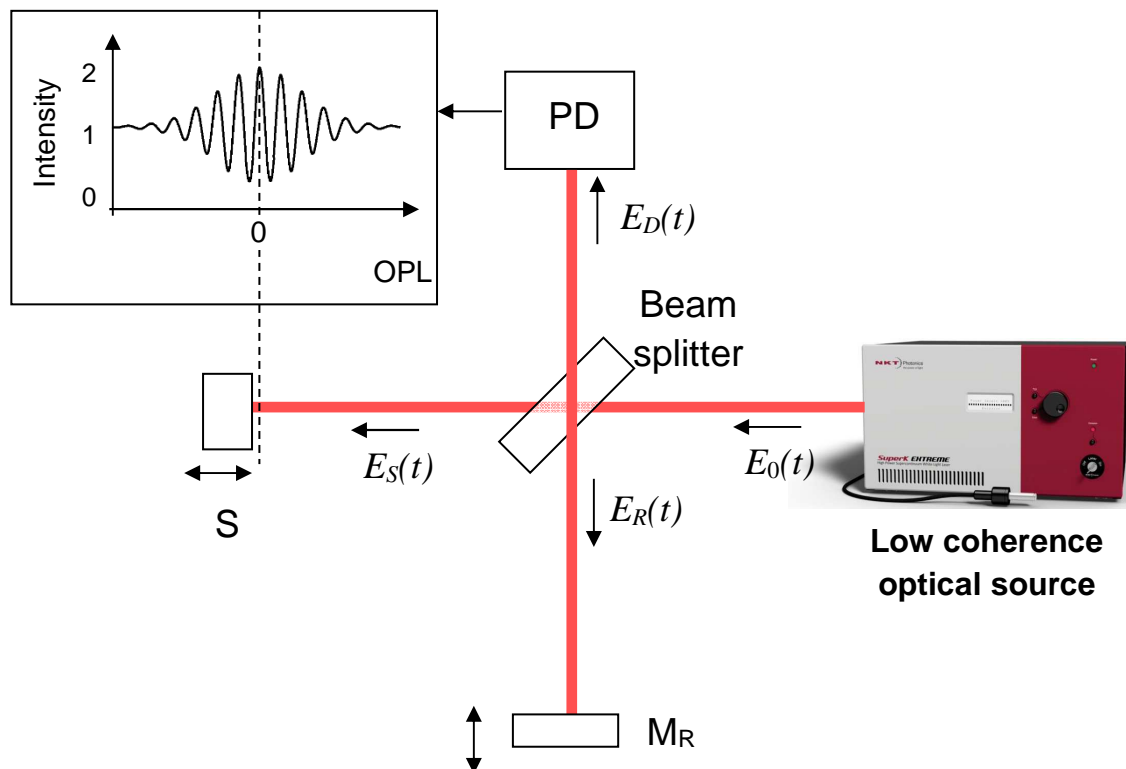


Fig. 2.1 A simple Michelson interferometer in free space (BS: beam-splitter, M_R : movable reference mirror, OPL: optical path length, PD: photo-detector, S: sample)

In low coherence interferometers (LCI), we consider two types of coherence of an electromagnetic (EM) waves: spatial and temporal. In spatial coherence, the optical sources should be single mode (SM) spatially, to allow efficient injection in SM fibre, maintain the uniform phase of the wave front, and retain the good transversal resolution. In

temporal coherence, the optical sources should be monochromatic, and exhibit high correlation between phases of a light at different points in space along the direction of propagation. The classical Michelson interferometer is based on amplitude division, and therefore is widely used to measure the temporal coherence of a source. Interference resulting from temporal coherence encodes the spectral content of the intensity distribution. Light waves with wavelength λ and $\lambda \pm \Delta\lambda$ with constructively interfere at some point in space until the propagation distance is equal to or longer than the coherence length of the optical source.

The coherence length, C_L , can be determined if the source central wavelength, and its optical bandwidth are known. The actual coherence length can be calculated as in Eqn. 2.1.

$$C_L \approx \frac{4 \ln(2)}{\pi} \frac{\lambda^2}{\Delta\lambda} \quad (2.1)$$

where λ is the central wavelength and $\Delta\lambda$ is the full-width at half maximum (FWHM) bandwidth of the optical source.

The coherence length can be theoretically derived from the FWHM of the autocorrelation function (AF) of the source's electric field [6-7], denoted by the symbol $\Gamma(x)$, as shown in Eqn. 2.2.

$$\Gamma(x) = \int_{-\infty}^{\infty} E(x)E(x+\tau)d\tau \quad (2.2)$$

where $E(x)$ is the electric field, and $E(x + \tau)$ is the autocorrelation function of electric field with time variable τ .

The autocorrelation function introduced here is related to the optical bandwidth of light source used, by the Wiener-Khinchin theorem, which states that the Fourier transform of the autocorrelation function was equal to the power spectral density $S(\nu)$.

$$S(\nu) = \int_{-\infty}^{\infty} \Gamma(\tau) \exp(jk\tau) d\tau \quad (2.3)$$

Our subsequent studies of noise in Chapter 3 and dispersion in Chapter 4 will involve the relationship between $\Gamma(x)$ and $\Delta\lambda$.

2.1.2 Interference

By referring to Fig.2.1, let us begin by writing the electric field of the light coming out from the broadband source in Eqn.2.4. We can also write the backscattered field from both reference and sample arms in Eqns.2.5 and 2.6, respectively.

$$E_0 = A_0 \cos(kz - \omega t) \quad (2.4)$$

$$E_R(z_R, t) = R_R A_0 \cos(kz_R - \omega t) \quad (2.5)$$

$$E_S(z_S, t) = R_S A_0 \cos(kz_S - \omega t) \quad (2.6)$$

where A_0 is the complex amplitude of the field, R_R and R_S are reflectivity of reference and sample arms, k is the wavenumber ($2\pi/\lambda$), z is the propagation direction, z_R and z_S are OPLs of reference and sample arms, ω is the angular frequency and t is time. The fields and intensities detected at photodiode become Eqn.2.6 and Eqn.2.7 [6-8].

$$E_{PD}(z_S, z_R, t) = E_R(z_R, t) + E_S(z_S, t) \quad (2.6)$$

$$I(OPD) = E_1^2 + E_2^2 + 2|E_1||E_2| \cos(k(z_R - z_S)) \quad (2.7)$$

After replacing $OPD = z_R - z_S$ in Eqn.2.7, integrating the output intensities over the detector bandwidth and performing an inverse FT, the photo-detected signal becomes Eqn.2.8. The complete derivations of electric fields to photo-detected intensities can be found in reference [4-8]. The noise and sensitivity discussions are found in Sec.3.1.3 and Sec.3.1.5 in Chapter 3.

$$I_{PD}(z_n) = E_1^2 + \sum_{n=1}^N E_{2,n}^2 + \sum_{n=1}^N 2|E_1||E_2| \gamma(z_n - z_0) \cos(2kz_n) \quad (2.8)$$

The first term in Eqn.2.8 is the DC component (E_1^2), which contains amplitude only but no depth information from the sample. The second term $\sum_{n=1}^N E_{2,n}^2$ is the cross correlation, which contains the information about the sample reflectivity profile. The third term $\sum_{n=1}^N 2|E_1||E_2| \gamma(z_n) \cos(2kz_n)$ is the autocorrelation function that contains both interference and phase information of backscattered signals reflected off different depth layers from the sample.

2.1.2.1 Conditions for interference

The conditions for interference [8] can be divided into four sections. We evaluate each in more details below by taking two electric fields E_R and E_S as shown in Fig.2.1.

(1) Polarisation condition

The dot product of two electric field is not null. Therefore, $\overline{E}_R \bullet \overline{E}_S \neq 0$

(2) Mono chromaticity condition

As velocity is the same for both waves, $\omega_R = \omega_S$, thus phase vectors become: $k_R = k_S$

(3) Time constant condition

The integration time of a photodetector τ can have an effect on phase constant of detected signal. This condition is dependent on the phase term in our equation as $\Delta\Phi = k(r_R - r_S)$ where $r_R - r_S$ is the OPD. In order for interference to occur, the phase term must be smaller than $1/\tau$. We can formula the different conditions where interference may or may not occur in Table 2.1 below, using the general photo detected signal $I(t)$.

Table 2.1: Different phase condition for interference and output intensities

Phase condition	Type of interference
$\cos(\Delta\Phi) = 1$	Fully constructive
$0 < \cos(\Delta\Phi) < 1$	Constructive if $I > I_S + I_R$
$\cos(\Delta\Phi) = 0$	No interference
$-1 < \cos(\Delta\Phi) < 0$	Destructive if $I < I_S + I_R$
$\cos(\Delta\Phi) = -1$	Fully destructive

(4) Coherence condition

Interference is produced as long as the $|\text{OPD}| < C_L$ of the optical source. The coherence condition limits the extent of the interference pattern in a vicinity around the spatial positions given by $\text{OPD} = 0$. The closer the OPD to the coherence length value, the less visible the interference pattern becomes. When the OPD exceeds the coherence length, no interference effects are visible.

2.1.3 Fibre based system

We have shown in previous section the flexibility of a free-space (or bulk) interferometer setup. However, the constant issue of beam misalignment and the need for periodic realignment, free-space configuration has fallen out of favour for use on a permanent prototype. On the other hand, a full fibre based system [9-10] allows the interferometer to be constructed in a more robust and reliable configuration, thus eliminating the need to worry about beam misalignment due to movement of optical components such as mirrors, lenses and beam splitters. To achieve a fibre based system, many of the optical sensitive parts are replaced. In a low coherence interferometer, the most crucial part of the system is the beam splitter. A replacement with 2×2 directional fibre coupler demonstrated by Podoleanu in [9] allows the interferometer to be made more compact, light-weight and easily transportable while the optical sources and detectors can be dismantled and re-assembled without having to worry about issues that might arise from free-space to fibre coupling when switching sources.

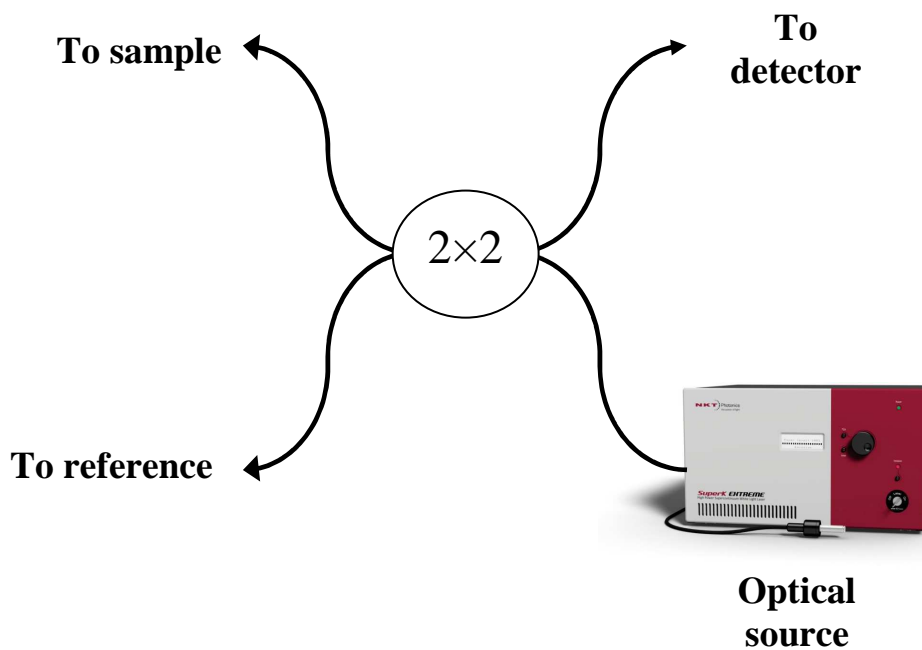


Fig. 2.2 A simple fibre based interferometer with a 2×2 directional coupler

2.2 Time domain OCT

One of the first developed technique in the field of OCT is the classical time domain (TD) system [3-5]. There are many distinct way to generate a three dimensional image with time-domain OCT technique. Time domain involves axial scanning by moving the reference mirror to access different depths in sample. This is achieved by varying the optical path difference (OPD) between reference and sample arms. Time delay between the two signals is equivalent to the distance these signals travelled in space. A typical TD-OCT setup in Fig. 2.3 consists of three main components: a broadband optical source, a Michelson interferometer (in bulk or fibre-based [9]) and a dual-channel balance detector, used to record and analyse the interference signal. We will discuss in Chapter 3 the structure of photo diodes, heterodyne detection and noise in TD-OCT systems.

The principle of operation is based on partial coherence interferometry, where the photodetector senses the variations in the interference, provided the OPD is less than the coherence length (C_L) of broadband optical source. To better describe the imaging process using TD-OCT, we can assume that the sample has a multi-layered structure. Each layer returns a replica of the incoming pulse train, delayed correspondingly by the distance between preceding and succeeding layers. By moving the reference mirror (M_R), the layer satisfying the coherence gate condition, $OPD < C_L$, can be selected. In Fig. 2.3, the selected layer corresponds to the position where the backscattered pulse train is matched temporally by the reference pulse train. Maxima of interference are obtained for each scattering sample in depth that satisfies the condition $OPD = 0$ (always). By scanning the OPD, a TD-OCT system outputs a reflectivity profile (A-scan) in depth. To enable two-dimensional (2D) imaging, a second transversal scanner has to be added into the sample arm, so that to the lateral scanning of the beam can be performed. Such implementation was first demonstrated by Huang et al. in 1991 [11], when the first OCT scan was made public. By collecting A-scans along the transversal direction, a cross-section image (or a B-scan) is generated. This method has been widely known in the OCT community as the full-field longitudinal (or axial) imaging method.

Another version of TD-OCT is *en-face* (or flying spot) OCT, based on one-dimensional (1D) reflectivity profiles or T-scans. The 1D T-scan are collected by flying the beam spot transversally, while maintaining the axial coordinate constant (putting the reference mirror, M_R at a fixed OPD). In this case, a B-scan image is constructed from many T-scans repeated for successive pixels in depth, by scanning fast laterally and slow axially, without moving the M_R . An *en-face* OCT system has the advantage in depth

sensitive imaging because it is capable of collecting a C-scan (constant depth) image, by repeating the T-scans for adjacent values of the orthogonal lateral coordinate, without needing to first construct a total volume from B-scan and then re-slice them orthogonally to the surface. In the flying spot method, the T-scans are oriented along the x -coordinate and repeated along the y -coordinate. Podoleanu and Rosen [12] has pioneered the implementation of flying spot OCT method back in 2008, and Podoleanu and Jackson had demonstrated the first 2D scanning with a galvanometer as early as 1998 [13]. This method is subsequently used as the basis for master/slave interferometry (MSI) technique to be discussed in Sec.2.4.

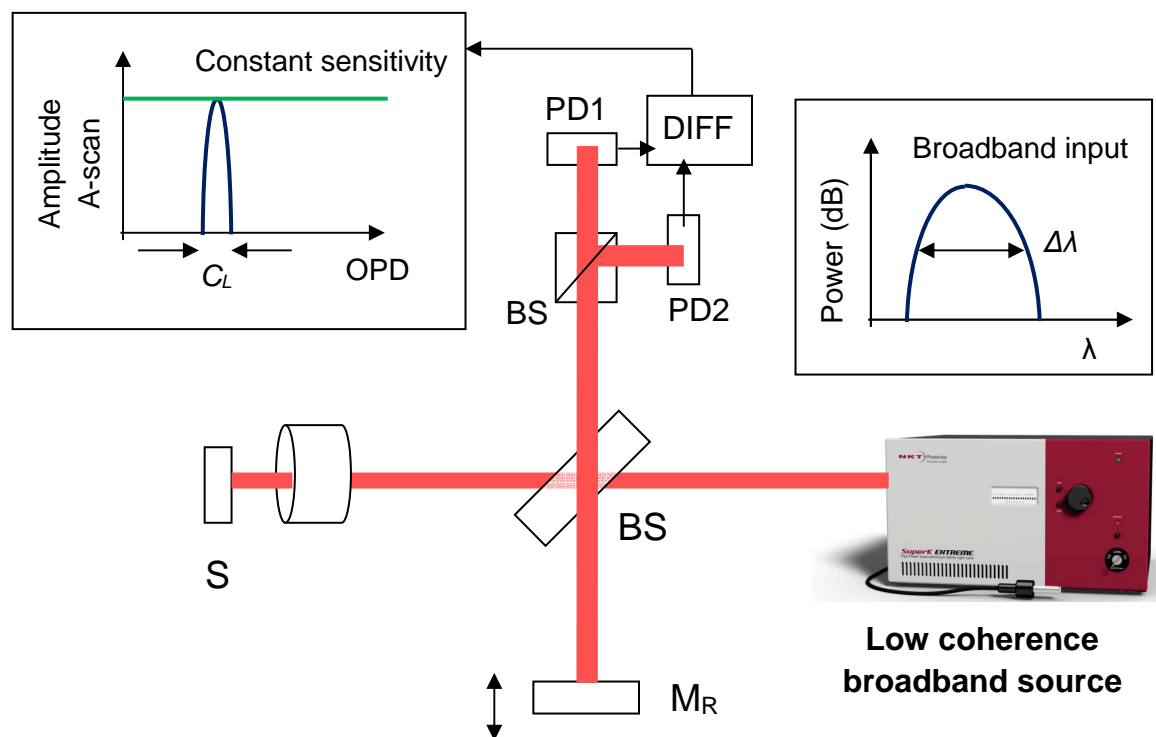


Fig. 2.3 A time-domain interferometer with output A-scan, sensitivity and axial range (M_R: reference mirror, BS: beamsplitter, S: sample, PD1&2: photo-diodes, DIFF: differential voltage output of photo-detector)

Despite the more recent adoption of SD- (or FD-) OCT, the TD-OCT remains popular as it is frequently used to study dispersion [14], dynamic focus [15] and optical distortion correction [16]. Since TD-OCT has an unlimited axial scan range, this technique now forms the basis for the more sophisticated master/slave interferometer (MSI). The principle of MSI (or MS-OCT) is discussed further in Section 2.4 of this chapter.

2.3 Spectral domain OCT

The spectral domain (SD-) OCT is also known as Fourier domain (FD-) OCT. In this section, we present the details of the two types of SD-OCT implementations: spectrometer based (Sp-) and swept-source (SS-) OCT. The spectral domain method has shown beyond doubt their capacity to produce reflectivity profiles (A-scans) from multiple depths with very high accuracy. Therefore, the promises of high resolution, high sensitivity [17-18] and faster measurement speed have resulted in SD-OCT becomes the *de-facto* method in the industry, and has since replaced TD-OCT in many commercial systems [18].

As TD-OCT only achieves interference with backscattered lights from both arms of the interferometer within the coherence gate of the source, SD-OCT is able to capture the signals directly from the entire depth range. The principle of operation between the two techniques is also different. SD-OCT detects spectrally resolved interference signals, which are generated by the optical path difference (OPD) between the reference mirror and the sample [17]. SD-OCT requires no depth scanning, and the acquisition speed is limited by the read-out rate of the line-scan camera or the sweeping-rate of the laser [19]. Real-time imaging is easily enabled because the data acquisition time in SD-OCT is much shorter compared to TD-OCT. In addition, several papers have reported that the sensitivity of SD-OCT to be at least 20 dB higher than that of TD-OCT [18].

The general difference between Sp-OCT and SS-OCT are (a) the light source used, and (b) the type of detector used. In Sp-OCT, typically a broadband light source such the supercontinuum (SC) is used to achieve better axial resolution. In the detection system Sp-OCT, the interrogation of spectrum at the interferometer output is carried out by a spectrometer, usually built using a prism or a diffraction grating employing a 2D linear array or a line camera. In the case of the SS-OCT, a tuneable laser source is used to sweep a narrowband output through a large optical bandwidth, allow the tuning the frequency of the laser source. The detection mechanism of SS-OCT consists of photo-detectors, similar to the one used in TD-OCT [17].

The similarities of Sp-OCT and SS-OCT are the techniques used to interrogate the modulation of the interference spectrum to gather information about the axial reflectivity profiles (A-scan). In both of these implementations, the A-scan is obtained by a fast Fourier transform (FFT) of the electrical signal proportional to the shape of the channelled spectrum at the interferometer output, hence called the SD- or FD-OCT.

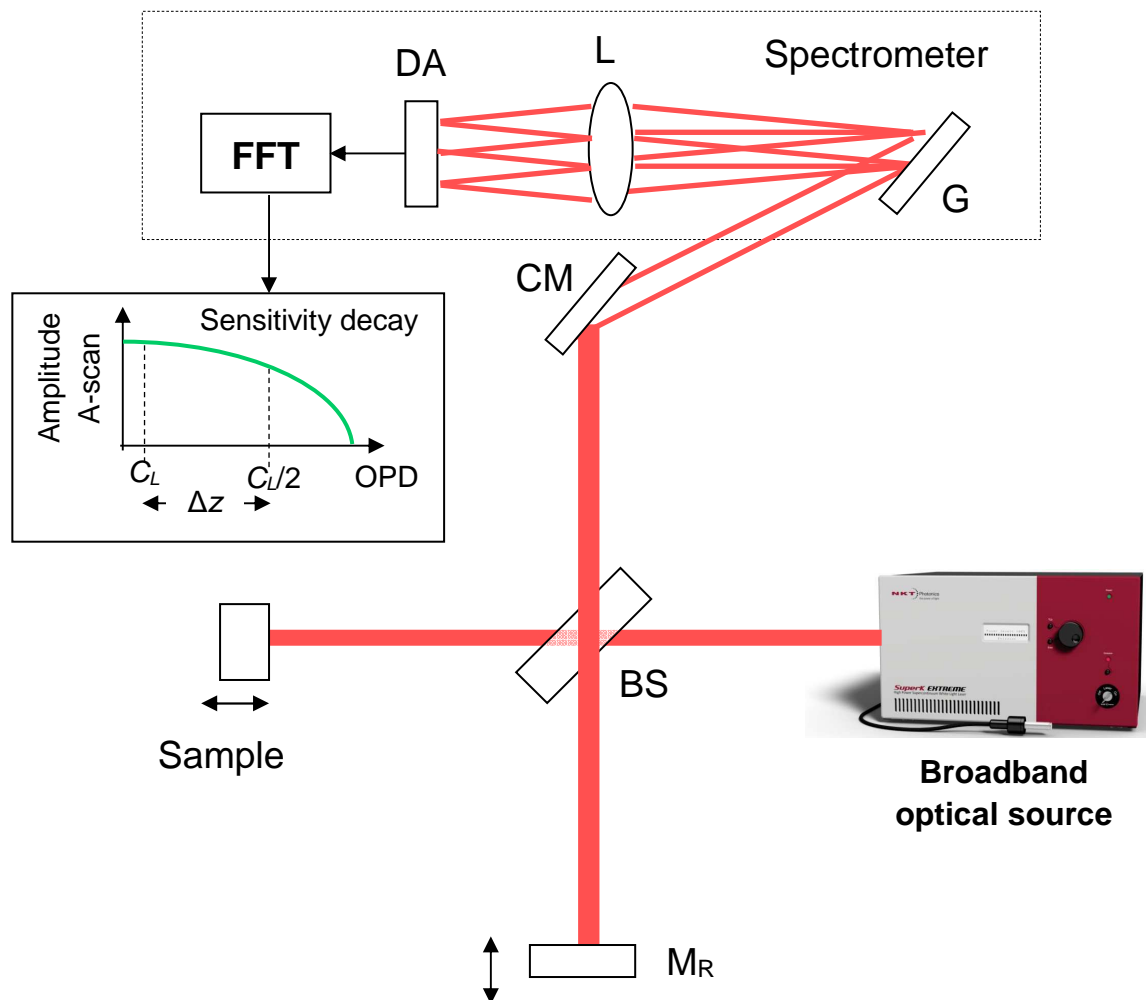


Fig. 2.4 Spectrometer based Fourier domain interferometer in free-space. (CM: curve/parabolic mirror, G: diffraction grating, M_R : reference mirror, S: sample, DA: data-acquisition module, L: lens, BS: beam splitter, OPD: optical path difference, C_L : coherence length, FFT: fast Fourier transform, Δz : displacement)

2.3.1 Spectrometer based OCT

The operation of the spectrometer based (Sp-) OCT basically demodulates the output optical spectrum. The spectrum exhibits peaks and troughs (channelled spectrum) and the period of such a modulation is proportional to the OPD in the interferometer. The larger the OPD, the larger the number of peaks is shown up in the spectrum. As we mentioned previously, the spectrometer uses a complementary metal oxide semiconductor (CMOS) or a charged coupled-device (CCD) camera.

The linear camera needs pixels of sufficient small size to be able to sample the succession of periodicity between peaks and troughs in the channelled spectrum. The linear camera in the spectrometer converts the received optical signal into electrical signals in time, so that each layer of the sample having a correspondent modulation periodicity dependent on depth. If a multi-layered sample is scanned, each layer has its own distinct spectrum modulation periodicity to another layer, depending on its depth. The spectral amplitude is subject to the level of signal being attenuated. A fast Fourier transform (FFT) is applied to the signal recorded by the linear camera and that translates the periodicity of the channelled spectrum into peaks of different frequency, versus the OPD. Such a profile is essentially the A-scan profile of the square root of reflectivity in depth.

The fast camera used in Sp-OCT has an advantage over the classical TD-OCT, when it comes to image scanning and acquisition speed. In comparison to galvo-scanners that operate at up to 16 kHz, the line camera is operating at tens of kHz or more. Most digital cameras nowadays have a line rate of 250 kHz or more, therefore significantly faster [20]. A detailed comparison between acquisition speed for *en-face* OCT, longitudinal OCT and Sp-OCT are shown in Table 2.2.

2.3.2 Swept-source (SS) based OCT

SS-OCT uses spectrally narrowband light sources with rapid wavelength swept speed. The output power, tuning range, sweeping rate and instantaneous coherence length of the light source determine the imaging speed, depth range and axial resolution of the SS-OCT system. In swept source, it is important to understand the distinction between the tuneable laser bandwidth $\Delta\lambda$ and its tuning linewidth ($\delta\lambda$).

Since we are using a photo-diode in SS-OCT, the $\delta\lambda$ needs to be much narrower than the spectral distance between the two peaks in a channelled spectrum. If the $\delta\lambda$ is very

small, it can be approximated with a Dirac delta function. Therefore, the photo-detected signal takes the exact shape of the channelled spectrum [19]. The photo-detector collects the time-varying interference signal. Similar to Sp-OCT, a fast Fourier transform (FFT) is performed onto this signal to translate the periodicity of the channelled spectrum into peaks of different frequency, related to the OPD. A depth reflectivity profile (A-scan) is then obtained. Fast tunability of laser sources minimises the time required to produce an A-scan. Recently, high-speed swept-source with several MHz tuning speed [21] has been developed. In 2010, a multi-MHz line rates system that used three different Fourier domain mode locked (FDML) laser has enabled depth scan rates up to 20.8 million lines per second [22]. Dispersion compensation was carried out to improve the coherence length and sensitivity roll-off of the MHz-FDML laser. The system was subsequently deployed for 3D retina imaging of the anterior chamber at 1300 nm [23].

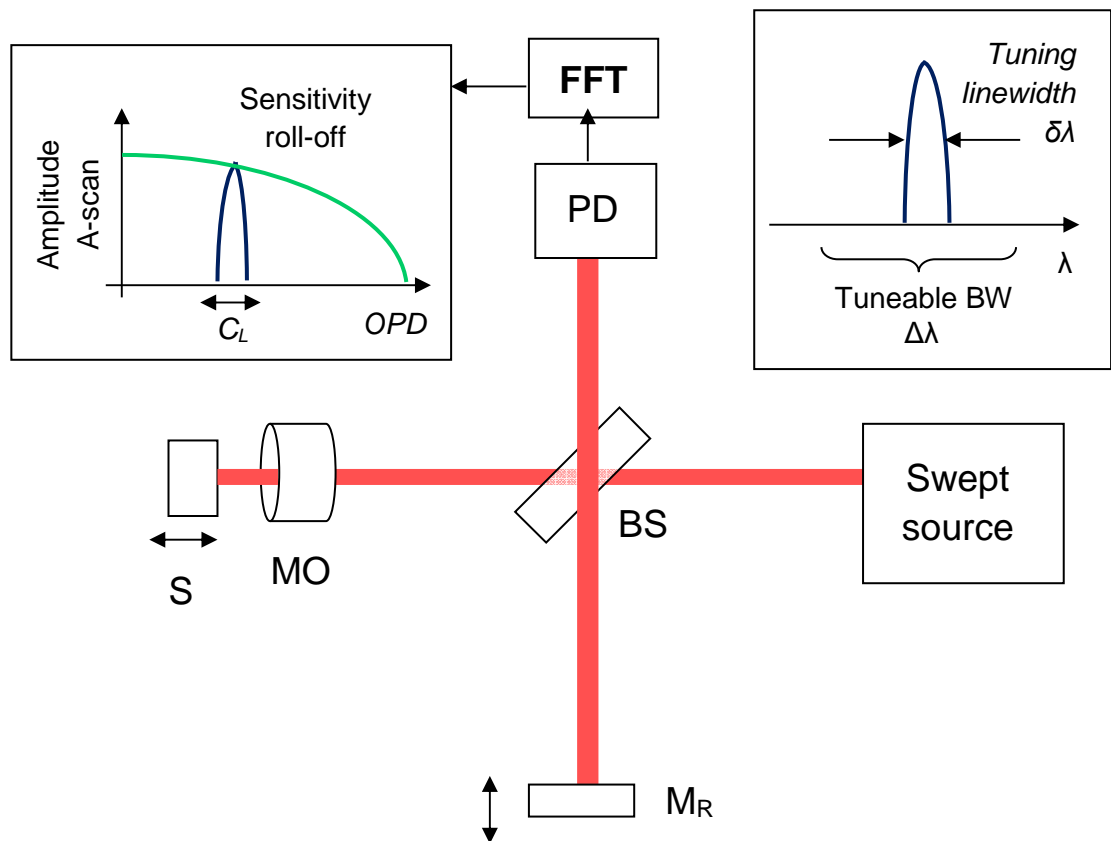


Fig. 2.5 A swept-source based interferometer in free space (M_R: reference mirror, BS: beam splitter, S: sample, PD: photo-detector, MO: microscope objective)

2.4 Master/slave OCT

2.4.1 Principles of operation

The master/slave (MS-) OCT is the most recent invention by Adrian Podoleanu and Adrian Bradu in the Applied Optics Group (AOG). This MS-OCT technique incorporates the advantages of time-domain, swept-source and spectrometer-based implementations, while removing the need of better signal sampling and data linearization before the Fourier transform (FT) processor. The MSI is based on comparing electrical signals proportional to channelled spectrum (CS) shapes at the interferometer output. It uses correlation as opposed to convolution in FFT. The higher the similarity of CS shapes, the larger the MSI signal. Since no FT is required, the MSI method does not need to organize the channelled spectrum data in equal frequency slots (or linearization). The dispersion was compensated for by matching the lengths of fibre and placing similar lenses with those used in the object arm, in the reference arm. With MSI, we can achieve the theoretical axial resolution without any re-sampling or linearization. Therefore, MSI is tolerant to nonlinearities when tuning the swept source [19, 25], and nonlinearities in the spectrometer grating [24].

The MS-OCT principle of operation involves the use of two interferometers, Master and Slave. A Slave Interferometer (SI) first “listens” to the operation of a Master Interferometer (MI). The SI and MI illustrated here are simple Michelson interferometers. It consists of two sets of beam splitters (BS), reference mirrors and object mirrors, for each interferometer. The terminology used in Fig.2.6 are described in Table 2.2.

Table 2.2 Optical components and their abbreviations for an MSI.

Optical parts	Slave interferometer (SI)	Master interferometer (MI)
Beam splitter (BS)	SBS	MBS
Reference mirror (RM)	SRM	MRM
Object mirror (OM)	-	MOM
Object	O	-

More specifically, signal is acquired by the Slave Interferometer on the right, for an OPD value determined by the Master Interferometer (MI). In the MI, the OPD_M is determined by the difference between the optical path lengths measured from the MBS to the two mirrors, MRM and MOM. In the Slave Interferometer, the OPD_S is determined by

the difference between the reference path length (measured from the SBS to the SRM) and the object path length (measured from SBS to different scattering points in the object, O).

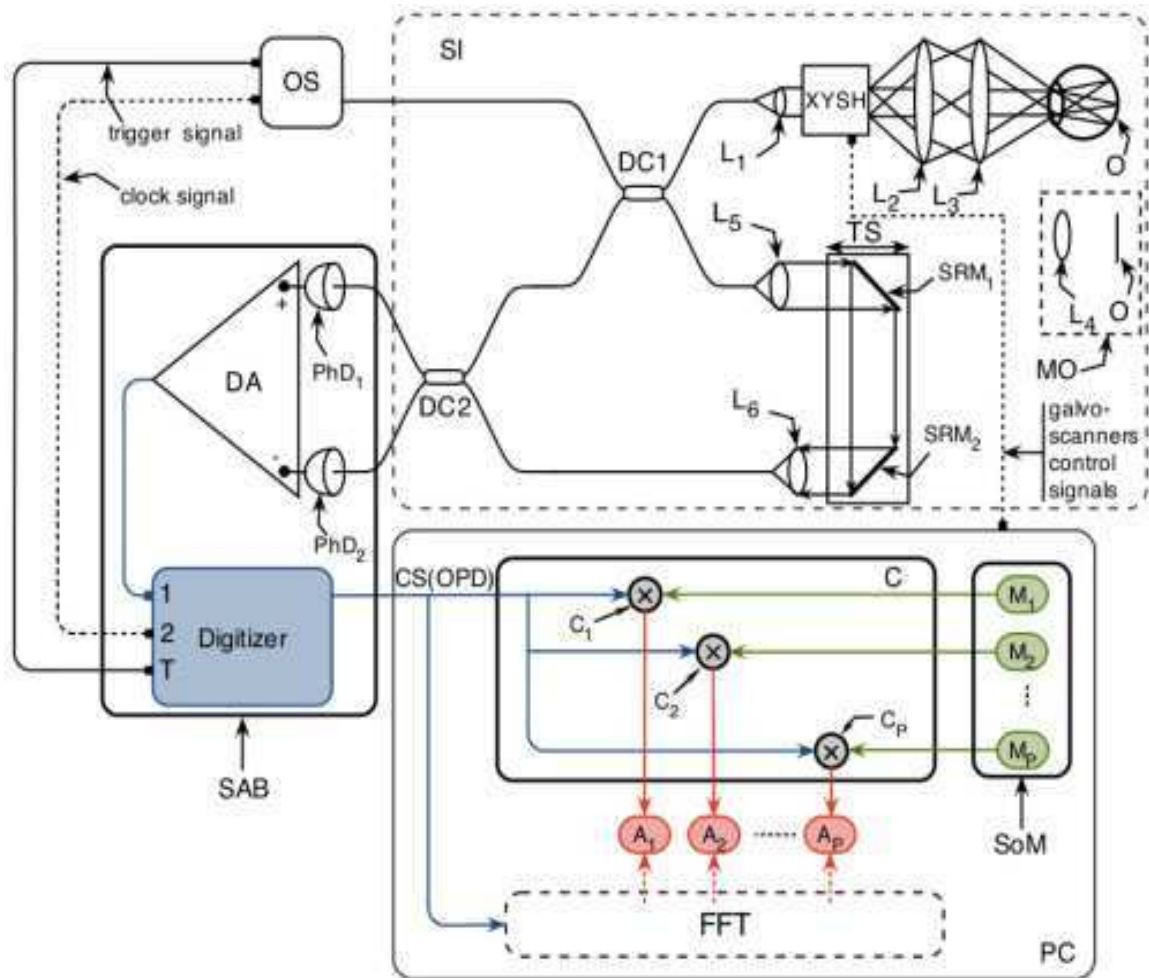


Fig. 2.6 A Experimental construction of master/slave interferometer based on a SS-OCT in fibre (OS: swept source; SI: slave interferometer; DC1, 20/80 single mode directional coupler; DC2: 50/50 single mode directional coupler; XYSH: two-dimensional lateral scanning head; L1 to L6: lenses; O: object; MO: model object; SAB: slave acquisition block; PhD1, PhD2: photo-detectors; DA: differential amplifier; CS(OPD): channelled spectrum delivered by the SAB; C: multiple channel comparison block equipped with P comparison blocks: C_1, C_2, \dots, C_P s; SoM: storage bank of P memories, M_1, M_2, \dots, M_P ; A_1, A_2, \dots, A_P : amplitudes of the interference signal from P scattering points inside the object O from respective depths z_1, z_2, \dots, z_P ; FFT: fast Fourier transformation block; PC: personal computer implementing the blocks C, SoM, FFT and display of images) [Source: <https://www.osapublishing.org/oe/fulltext.cfm?uri=oe-21-16-19324&id=260019>]

In contrast to conventional spectral (Fourier) domain interferometry, MSI delivers a signal from a single depth, z , within the object to be investigated. Initially, for the comparison operation required by the MSI method, correlation was used [24–28]. To improve on the calculation speed, a modified correlation operation was proposed [27,28], to deliver the value of an A-scan at depth z , the MSI signal. The amplitude of the signal originating from a certain depth in the object is obtained using the two equations below:

1. Correlation of the current channelled spectrum:

$$Corr(OPD) = CS(OPD) \otimes M(OPD_p)$$

where \otimes signifies the correlation operation, $CS(OPD)$ is the current channelled spectrum and $M(OPD_p)$ is stored channelled spectrum OPD at p position.

2. The amplitude of the correlation, $Corr$, over a window $W = 2S + 1$ points out of the $2M + 1$ around wavenumber $k = 0$

$$A(OPD_p) = \sum_{n=-S}^{+S} Corr(S_N)$$

where $Corr()$ is the correlation operation between the channelled spectrum I collected when the object is placed in the object arm (Slave stage), and the mask corresponding to the channelled spectrum CS_{exp} collected at the Master stage for an $OPD = 2z$, when the mirror is used as an object.

The master/slave technique is a revolutionary method in OCT. This can be said since the MS-OCT operates on a hybrid time-spectral domain methods. The TD side of MS-OCT allows selecting signal from a selected depth while scanning the laser beam across the sample. The SD side of MS-OCT improves sensitivity and speed advantage of the spectral in comparison with TD method. Thus, it allows collection of signals from any number of depths, as required by the user, i.e. of any number of *en-face* OCT images, from any depths, separated by any distance from the neighbouring *en-face* slices, all in a single-scan. When MS-OCT is implemented alongside conventional OCT configurations, the advantages are even more visible. These include:

- (a) In swept-source OCT, no k -clock is needed,
- (b) In spectrometer-based OCT, no resampling of data, no linearization and no calibration of spectrometer are needed.

The MS method is an alternative to the FT based method, as it eliminates several important drawbacks associated to the FFT technique (such as dispersion compensation) and allows real-time production of cross-sectional images. The practical illustration of MS-OCT is shown in Chapter 6, where we collaborated with the Maidstone NHS Trust Hospital to image three specimens of eyelid basal cell carcinoma (BCC). The practical aspects of system configuration, technical implementation as well as comparison between conventional imaging results in terms of speed and efficiency are discussed.

There are fundamental differences between TD and SD methods. One of such differences is the OPD. In TD-OCT, OPD data are collected sequentially, whereas in SD-OCT all OPDs are interrogated at once. Although SD methods are superior in terms of acquisition rate and better SNR, they present some shortcomings, as detailed in Table 2.2. Table 2.2 summarizes the parameters which determine the depth resolution and the axial range in each case, as well as other comparative features, with more details in [12].

Table 2.2 Comparison between different OCT technologies adapted from ref [12] (Podoleanu, “Optical Coherence Tomography,” Journal of Microscopy (2012)).

	<i>En-face</i> TD OCT	Longitudinal TD OCT	SD- and FD- OCT	SS-OCT
Axial resolution	Source optical bandwidth	Source optical bandwidth	Source optical bandwidth	Tuning bandwidth
Axial scan range	Unlimited	Unlimited	Limited by spectrometer	Limited by optical BW
Sensitivity vs OPD	Constant	Constant	Max in OPD=0	Max in OPD=0
Mirror terms	None	None	Exist for OPD≠0	Exist for OPD≠0
Max line rate	16 kHz	100 kHz	300 kHz	5 MHz
Time to create 3D volume of 500×500×500px	16 s	2.5 s	850 ms	50 ms

2.5 Optical sources

Broadband fibre optic sources are derived from the fibre optic amplifiers used in the telecommunications sectors. Due to the design specific for telecom use, many of these telecom fibre couplers are centred around 1300 nm (earlier designs) and 1550 nm (recent designs). In addition to that, many of the fibre couplers have bandwidth limitation issues, i.e. narrow band transmission up to several tens of nm (passband FWHM not greater than 100 nm). The same can be said for optical sources. In this section, we look into several optical sources most commonly used for OCT applications. They include the well-known super luminescent diode (SLD), short and long cavity swept-source (SS) and the broadband white light supercontinuum source (SC).

2.5.1 Narrowband sources

Superluminescent diodes (SLDs) are optoelectronic semiconductor optical amplifier (SOA) that emit low-coherence light of broad optical spectrum. It is designed based on the principles of superluminescence and light-emitting diode (LED). The SLDs have been around since the late 1980s. They are assembled similar to most laser diodes: an optical waveguide and a p - n junction diode, like the one in Fig.2.7. However, the main problem to obtain high power emission is to reach high optical gain within diode without using optical feedback. Earlier attempts to resolve this challenge include the use of a multi-mode Fabry Perot laser. Several mode suppression were used, and this include the deposition of antireflection coating on diode facets, and the introduction of un-pumped absorbing region in the waveguide. The aim was to achieve a single lobe, broadband superluminescent emission with high peak power and low spectral modulation, such the one shown in Fig.2.9. A more recent way to maximise output power is to use a pulsed SLD through direct current injection modulation as seeding source in a master oscillator power amplifier (MOPA) configuration [30].

In a conventional SLD there is no seed laser to supply input signal. It relies on weak spontaneous emission into the waveguide mode to build up, and is then amplified by strong stimulated emission. Most SLDs emit in one of the wavelength regions around 800 nm, 1300 nm, and 1550 nm, thus suitable for OCT applications in eye and skin. SLDs in the visible wavelengths are also available, however, but their availability is limited due to selection of readily available diodes and cost of manufacturing them. On the technical side, the emission wavelengths of SLDs are dependent on the band gap of the semiconductor

diode used. A semiconductor with a larger band gap such as AlGaAs emits a shorter wavelength, in the region of 800-900 nm. On the other hand, smaller band gap LEDs such as the GaInAsP emits a longer wavelength, usually between 1.3 μm to 1.6 μm . When a broader wavelength emission is necessary, the semiconductor composition can be varied to shift the central wavelength and optical bandwidth.

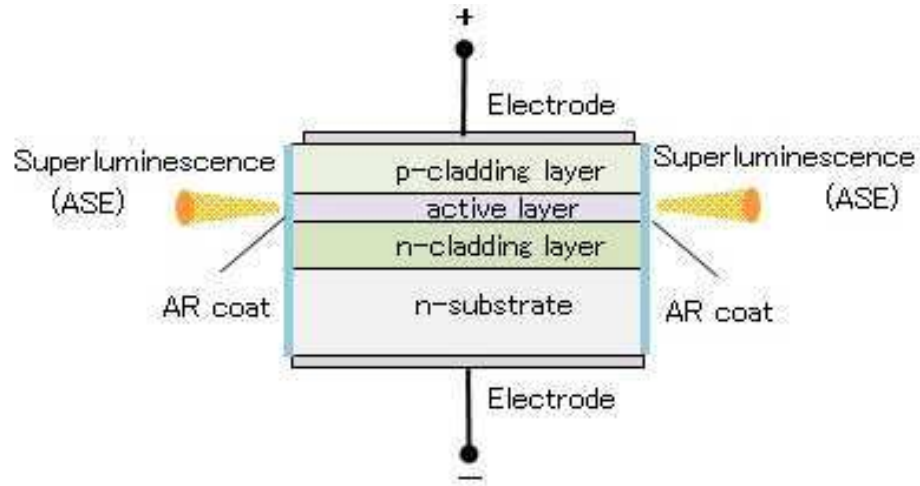


Fig. 2.7 Composition of an SLD diode (source: <https://www.fiberlabs-inc.com/about-sld/>)

Typical output powers are in the range from a few mW to about 40 mW. Their emission are spatially close to the diffraction-limit, therefore the spatial coherence and beam quality are very high. The optical bandwidth of an SLD is usually in the region of tens of nanometres, up to 150 nm for diodes emitting at 800 nm. This corresponds to a coherence length of 1-30 μm . The bandwidths of SLDs operating at wavelengths above 1 μm are even smaller, between 30-60 nm, such as the one in Fig.2.9. Apart from that, due to gain narrowing, there is a trade-off between higher output power and broader bandwidth. The SLDs are notoriously known for wavelength stability and durability. Because of the semiconductor gain medium, it is not susceptible to huge ambient temperature fluctuation and have short intrinsic noise. As such, we can expect very little wavelength drifts over long hours of continuous operation (< 100 pm/K). Furthermore, these diodes are pretty long-lasting, can they can have a lifetime that exceeds 20,000 hours, which are several times more than the operational cycles of a swept-source (4000-5000 hours) or a supercontinuum source (2000-3000 hours). The drawbacks of an SLD are bandwidth and power limitations.

The commonly used SLD sources in our laboratory is manufactured by Superlum, headquartered in Cork, Republic of Ireland. One of these model is the S1300-G-I-20 benchtop version from the Superlum S-BroadLighters series that delivers 20 mW output, dual-diode configuration with 30 nm bandwidth per diode. The product image, together with its manufacturer's measured optical spectrum and coherence function in full power mode, are shown in Fig. 2.8 and 2.9 respectively.



Fig. 2.8 Superlum BroadLighters series SLD at 1300 nm with 20 mW output (source: https://www.superlumdiodes.com/s_broadlighters.htm)

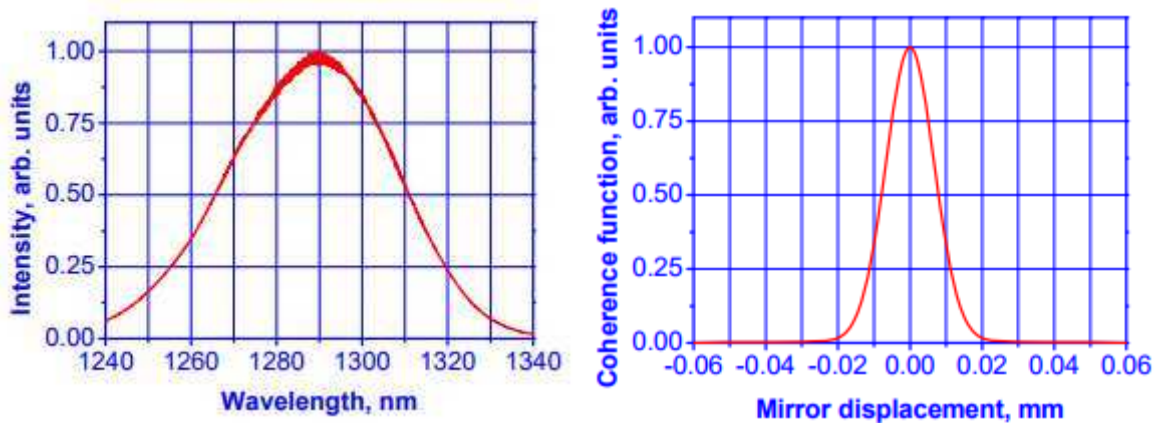


Fig. 2.9 (left) Optical spectrum and (right) coherence function at full output power for Superlum BroadLighters series SLD model S1300-G-I-20 (source: <https://www.superlumdiodes.com/pdf/s1300-g-i-20.pdf>)

Swept source (SS) is also called fast wavelength tuneable laser. Although the swept-source laser as a wavelength centred at approximately $1\ \mu\text{m}$, the laser sweeps across a narrow band of wavelengths with each scan. Most swept sources are narrowband with tuneable bandwidth between 80 nm to 150 nm. Despite operating on a smaller bandwidth than a supercontinuum source, SS generally have higher SNR than many broadband sources. The SS operates on the principles that all of the light is collapsed into a single wavelength, and that narrow wavelength is used to sweep across a wider range of wavelengths. This method substantially increases the SNR while also increase imaging speed and expand the source coherence length.

The use of SS in OCT has these advantages when compared to earlier version of SD-OCT: high sensitivity, slower sensitivity roll-off, high linearity sweeps, fast sweeping, deeper penetration, higher reliability and robustness, and lower cost [31]. Several implementation of SS in OCT include [32]. There are several commercial manufactures of swept source lasers, among them is Axsun Technologies, headquartered in Massachusetts, USA. One of the model we used to implement master/slave interferometer (MSI) in this thesis is SS1300-OCT benchtop version, with central wavelength at 1310 nm, bandwidth 100 nm, sweeping rate of 50 kHz, and capable of outputting 20 mW power. The output spectrum from manufacturer's datasheet is shown in Fig.2.10.

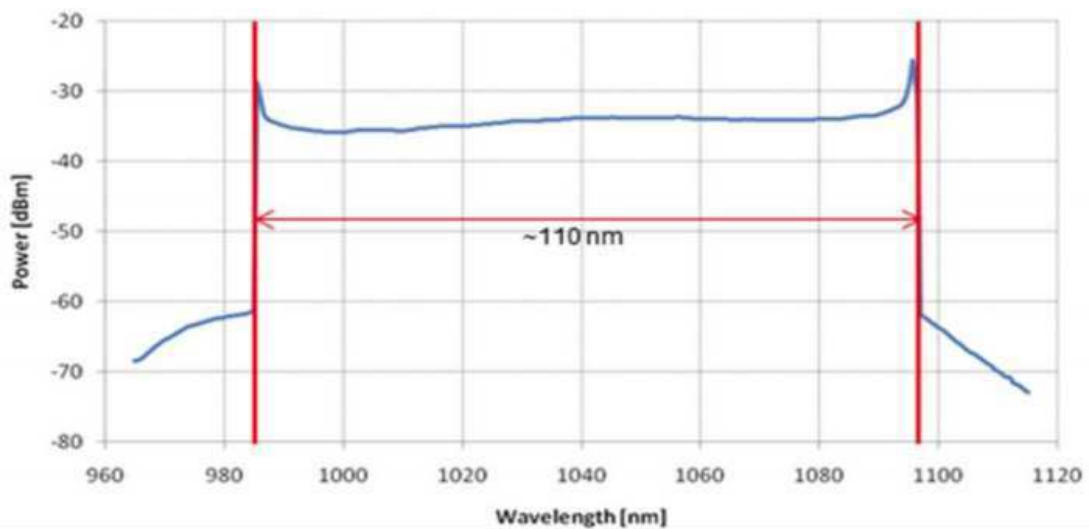


Fig. 2.10 Optical spectrum of Axsun swept-source model SS1300-OCT at $1\ \mu\text{m}$ (source: http://downloads.axsun.com/public/datasheets/Axsun_OCT_laser_datasheet.pdf)

2.5.2 Broadband sources

The supercontinuum generation (SCG) occurs when the narrow-band light from a pump laser undergoes an extreme nonlinear spectral broadening process to produce a broadband white light output. The output beam is usually spectrally continuous [33]. The two commonly used optical medium for SCG are: micro-structured fibre (MSF) or photonic crystal fibre (PCF). However, the SCG process was first reported in 1970 using a bulk BK7 glass [34]. Currently, SCG process can be carried out in terms of the injected pulse duration in two broad classes: short-pulse femtosecond regime [35] and long-pulse (picosecond, nanosecond and CW regimes) [33]. More recently, reports have confirmed the possibility of SCG to be performed in a variety of media and waveguides, such as water [37] and liquid [38].

Like all optical sources used for imaging, SC sources also exhibit spatial and temporal coherence [39-40]. At the output of SCG is light with very broad spectral bandwidth, thus low temporal coherence and very high spatial coherence. A high degree of spatial coherence allows tight focusing of the SC beam in free-space. High spatial coherence in this case is important since SC light is delivered from a single-mode (SM) fibre. A good beam injection is therefore essential. On the other hand, the high spectral bandwidth suggests a very low temporal coherence between pulses [39, 41]. Supercontinua generated from periodic pulse trains can have a high temporal coherence, since the electric fields corresponding to different pulses are highly correlated. Temporal coherence in SCG is essential for frequency combs generation in PCF. However, the process to generate frequency combs is influenced by several parameters of the seed laser, such as pulse duration, pulse energy, initial peak power, pump wavelength, fibre length and fibre dispersion [40,42].

The use of PCF has gained significant interest in the community due to their unusually low chromatic dispersion [43]. Low dispersion can allow a strong nonlinear interaction over a significant length of the fibre. Since spectral broadening happens as function of the fibre length, a longer fibre translates to broader spectral generation [44].

Pulse duration and peak power of the seed laser play an important role in SCG. Firstly, in the femtosecond pulse regime, the spectral broadening is largely caused by self-phase modulation (SPM) [36,45]. When a nominally birefringent fibre with anomalous dispersion is used, the combination of SPM and fibre dispersion can lead to complicated soliton dynamics, such as wave breaking effect and the splitting of higher-order solitons into multiple fundamental solitons in a process known as soliton fission [46-47]. Secondly,

when the SCG process involves pumping with pulses in the picosecond time regime, stimulated Raman scattering (SRS) and four-wave mixing (FWM) can cause pulse-to-pulse intensity fluctuation to increase [48-51], therefore producing higher relative intensity noise (RIN) at the output. Finally, SCG using seed laser with CW and longer fibres (greater than 100 m) has also been explored previously [52-54]. However, this CW regime is not the main area of research in NKT Photonics.

The noise properties of the generated continua are different in different parts of the spectrum [52]. When pumped with short pulses of 5 ps or less, SPM is the major nonlinear process. The phase coherence of the generated supercontinuum pulses can be very high, even after these pulses experienced massive spectral broadening [56-57]. The noise is time-invariant and deterministic, and can be modelled with NLSE (nonlinear Schrödinger equation). However, when higher-order soliton effects are involved, the SCG process can be very sensitive to even the smallest intensity fluctuations from the seed laser, resulting in huge differences in the properties of one pulse relative to another [58]. These fluctuations (or commonly known as relative intensity noise, RIN) can affect the stability of SCG process. It is therefore essential that we characterise the RIN and produce low-noise SC for better OCT imaging [59-62]. We have dedicated Sec.3.2 in Chapter 3 to study RIN, analyse the characteristics of pulses in generated supercontinua, and to find out the different factors that influenced them.

Nevertheless, the strongly nonlinear interaction of pulses within the SCG process makes it extremely complex to predict noise behaviours [51]. Thus, numerical simulation and pulse propagation modelling is required. In this project, despite a thorough experimental study on noise with SC sources were carried out [59], some of our results remained difficult to explain until future modelling is done.

Since NKT Photonics is our industry partner, we have access to their commercial SC sources, such as the SuperK Extreme and Fianium Whitelase. The SuperK Extreme models features the EXR series shown in Fig. 2.11). The EXR9 is the low-noise version and EXR20 is the high power version. In this thesis, we used the EXR9 for polarisation sensitive OCT in Chapter 5, and EXR20 for retinal decoding in Chapter 7. Apart from that, NKT Photonics also produces a compact version of SC source, the SuperK Compact (Fig.2.12). We used SuperK Compact in Chapter 3 to characterise the birefringence of nonlinear fibre (NLF) used in noise and polarisation measurements. The output spectra for SuperK EXR and SuperK Compact are shown in Fig.2.13.



Fig. 2.11 NKT Photonics SuperK Extreme supercontinuum source



Fig. 2.12 NKT Photonics SuperK Compact supercontinuum source

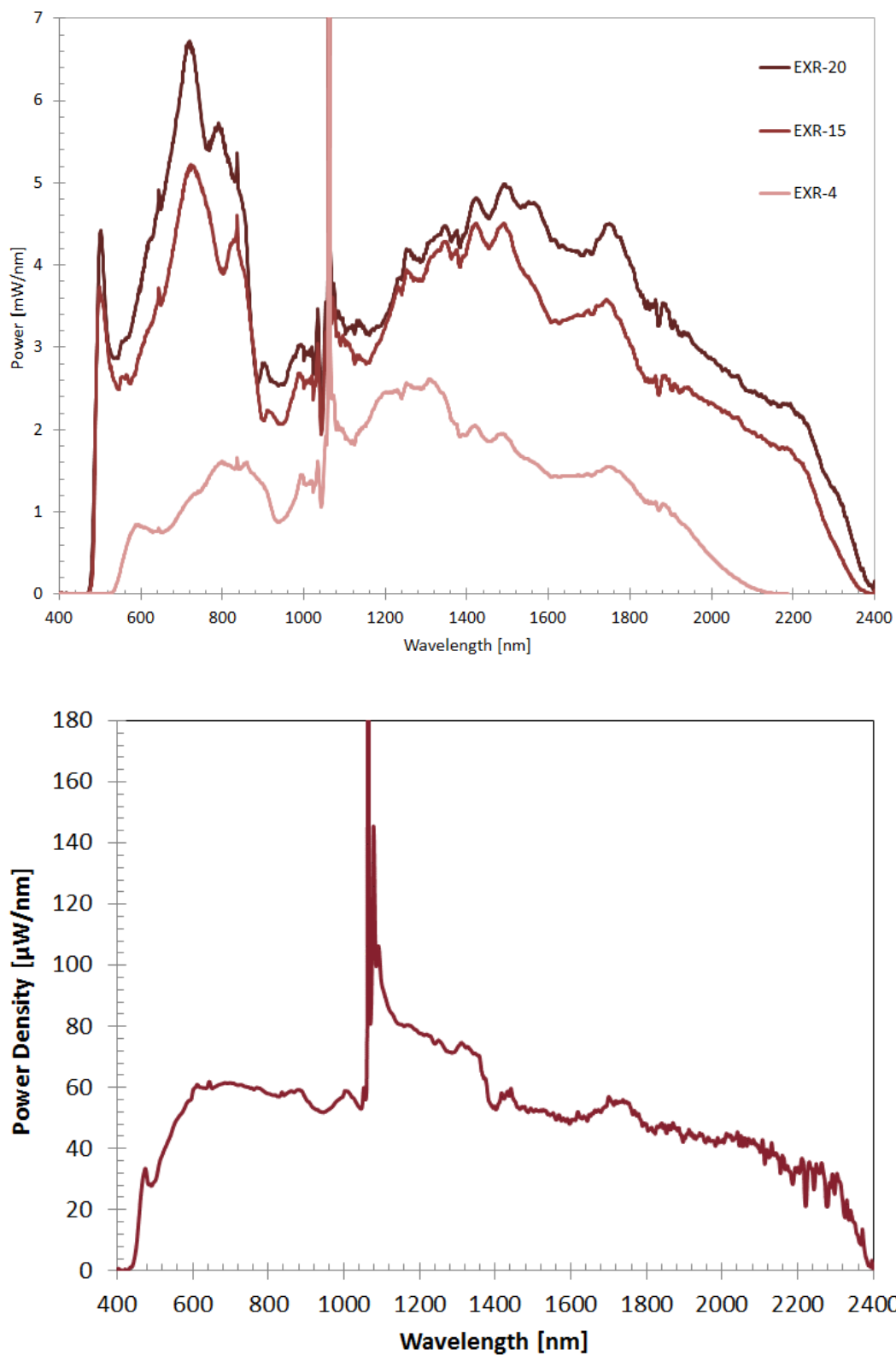


Fig. 2.13 Supercontinuum spectrum from (top) SuperK Extreme and (bottom) SuperK Compact

References

1. P. H. Tomlins, and R. K. Wang, "Theory, developments and applications of optical coherence tomography," *Journal of Physics D-Applied Physics* 38, 2519-2535 (2005).
2. L. V. Wang, and H. Wu, *Biomedical Optics: Principles and Imaging* (Wiley, New York).
3. M.R. Hee, B.E. Bouma, G.J. Tearney, *Handbook of Optical Coherence Tomography*, Chapter 2 (Marcel Dekker, New York, 2002).
4. M.E. Brezinski, *Optical Coherence Tomography Principles and Applications*, Chapter 3 (Academic Press, New York, 2006).
5. J.A. Izatt and M.A. Choma, *Theory of Optical Coherence Tomography*, *Optical Coherence Tomography Tech. and Appl.* Chapter 2, 47-72 (Springer, 2008).
6. O. Svelto, *Principles of Lasers* (Springer, 1998).
7. J. Goodman, *Fourier Optics*, 3rd Ed. (W. H. Freeman, 2004).
8. M. Born, *Principles of Optics: Electromagnetic Theory of Propagation, Interference and Diffraction of Light*, 7th Ed. (Cambridge Univ. Press, 1999).
9. A. Gh. Podoleanu, "Unbalanced versus balanced operation in an optical coherence tomography system," *Appl. Opt.* 39, 173-182 (2000).
10. A. M. Rollins and J. A. Izatt, "Optimal interferometer designs for optical coherence tomography," *Opt. Lett.* 24, 1484-1486 (1999).
11. D. Huang, E.A. Swanson, C.P. Lin, J.S. Schuman, W.G. Stinson, W. Chang, M.R. Hee, T. Flotte, K. Gregory, C.A. Puliafito and J.G. Fujimoto, "Optical Coherence Tomography," *Science* 254(5035), 1178-81 (1991).
12. R. B. Rosen, P. Garcia, A. Gh. Podoleanu, R. Cucu, G. Dobre, I. Trifanov, M. E. J. van Velthoven, M. D. de Smet, J. A. Rogers, M. Hathaway, J. Pedro, R. Weitz, "En-face Flying Spot OCT/Ophthalmoscope," *Optical Coherence Tomography*, Chapter 59, 1797-1832 (Springer 2015).
13. A. Gh. Podoleanu, G. M. Dobre, and D. A. Jackson, "En-face coherence imaging using galvanometer scanner modulation," *Opt. Lett.* 23, 147-149 (1998).
14. C. Chin, F. Toadere, T. Feuchter, L. Leick, P. Moselund, A. Bradu, and A. Podoleanu, "Acousto-optic tunable filter for dispersion characterization of time-domain optical coherence tomography systems," *Appl. Optics*, 55(21), 5707-5714 (2016).
15. M. R. N. Nasiri-Avanaki Ahmed Aber, S. A. Hojjatoleslami, Mano Sira, John Schofield, Carole Jones, A. Gh. Podoleanu, "Dynamic focus optical coherence tomography: feasibility for improved basal cell carcinoma investigation," *Proc. SPIE* 8225 X, 82252J (2012).
16. S. Ortiz, D. Siedlecki, I. Grulkowski, L. Remon, D. Pascual, M. Wojtkowski, and S. Marcos, "Optical distortion correction in Optical Coherence Tomography for quantitative ocular anterior segment by three-dimensional imaging," *Opt. Express* 18, 2782-2796 (2010).
17. A R. Leitgeb, C. Hitzenberger, and A. Fercher, "Performance of fourier domain vs. time domain optical coherence tomography," *Opt. Exp.* 11(8), 889-894 (2003).
18. J. F. de Boer, B. Cense, B. H. Park, M. C. Pierce, G. J. Tearney, and B. E. Bouma, "Improved signal-to-noise ratio in spectral-domain compared with time-domain optical coherence tomography," *Opt. Lett.* 28(21), 2067-2069 (2003).
19. M. Choma, M. Sarunic, C. Yang, and J. Izatt, "Sensitivity advantage of swept source and Fourier domain optical coherence tomography," *Opt. Exp.* 11(18), 2183-2189 (2003).

20. L. An, P. Li, T. Shen and R. Wang, "High speed spectral domain optical coherence tomography for retinal imaging at 500,000 A-lines per second," *Biomed. Opt. Expr.* 2(10), 2770–2783 (2011).
21. W. Wieser, B. R. Biedermann, T. Klein, C. M. Eigenwillig, and R. Huber, "Multi-Megahertz OCT: High quality 3D imaging at 20 million A-scans and 4.5 GVoxels per second," *Opt. Express* 18, 14685-14704 (2010).
22. W. Wieser, T. Klein, D. C. Adler, F. Trépanier, C. M. Eigenwillig, S. Karpf, J. M. Schmitt and R. Huber, "Extended coherence length megahertz FDML and its application for anterior segment imaging," *Biomed. Opt. Expr.* 3(10), 2647–2657 (2012).
23. B. Potsaid, B. Baumann, D. Huang, S. Barry, A. E. Cable, J. S. Schuman, J. S. Duker, J. G. Fujimoto, "Ultrahigh speed 1050nm swept source/Fourier domain OCT retinal and anterior segment imaging at 100,000 to 400,000 axial scans per second," *Opt. Express* 18(19), 20029–20048 (2010).
24. Adrian Gh. Podoleanu and Adrian Bradu, "Master–slave interferometry for parallel spectral domain interferometry sensing and versatile 3D optical coherence tomography," *Opt. Express* 21, 19324-19338 (2013).
25. Adrian Bradu and Adrian Gh. Podoleanu, "Calibration-free B-scan images produced by master/slave optical coherence tomography," *Opt. Lett.* 39, 450-453 (2014).
26. Adrian Bradu, Michael Maria, and Adrian Gh. Podoleanu, "Demonstration of tolerance to dispersion of master/slave interferometry," *Opt. Express* 23, 14148-14161 (2015).
27. Adrian Bradu, Sylvain Rivet, and Adrian Podoleanu, "Master/slave interferometry – ideal tool for coherence revival swept source optical coherence tomography," *Biomed. Opt. Express* 7, 2453-2468 (2016).
28. Adrian Bradu and Adrian Gh. Podoleanu, "Imaging the eye fundus with real-time en-face spectral domain optical coherence tomography," *Biomed. Opt. Express* 5, 1233-1249 (2014)
29. C. Chin, A. Bradu, R. Lim, M. Khandwala, J. Schofield, L. Leick, and A. Podoleanu, "Master/slave optical coherence tomography imaging of eyelid basal cell carcinoma," *Appl. Opt.* 55, 7378-7386 (2016)
30. M. Melo, J. M. Sousa, J. R. Salcedo, "Superluminescent diode versus Fabry-Perot laser diode seeding in pulsed MOPA fiber laser systems for SBS suppression," *Proc. SPIE* 9344XII, 93440I (2015).
31. S. Kishi, "Impact of swept source optical coherence tomography on ophthalmology," *Taiwan J. Ophthalmology*, 6(2), 58-68 (2016).
32. M. Choma, K. Hsu, J. A. Izatt, "Swept source optical coherence tomography using an all-fiber 1300-nm ring laser source," *J. Biomedical Opt.* 10(4), 044009 (2005).
33. J. M. Dudley, G. Genty, S. Coen, "Supercontinuum generation in photonic crystal fiber," *Rev. Modern Phy.* 78, 1135-117 (2006).
34. R. R. Alfano and S. L. Shapiro, "Emission in the Region 4000 to 7000 Å Via Four-Photon Coupling in Glass," *Phys. Rev. Lett.* 24, 584 (1970).
35. F. Poletti and P. Horak, "Dynamics of femtosecond supercontinuum generation in multimode fibers," *Opt. Express* 17, 6134-6147 (2009).
36. S. Coen, A. H. L. Chau, R. Leonhardt, J. D. Harvey, J. C. Knight, W. J. Wadsworth, and P. St. J. Russell, "White-light supercontinuum generation with 60-ps pump pulses in a photonic crystal fiber," *Opt. Lett.* 26, 1356-1358 (2001).

37. J. A. Dharmadhikari, G. Steinmeyer, G. Gopakumar, D. Mathur, and A. K. Dharmadhikari, "Femtosecond supercontinuum generation in water in the vicinity of absorption bands," *Opt. Lett.* 41, 3475-3478 (2016)
38. L. Wang, Y.X. Fan, Z.D. Yan, H.T. Wang, and Z.L. Wang, "Flat-plateau supercontinuum generation in liquid absorptive medium by femtosecond filamentation," *Opt. Lett.* 35, 2925-2927 (2010).
39. I. Zeylikovich and R.R. Alfano, "Coherence properties of the supercontinuum source," *Appl. Phys. B*, 77(2-3), 265-268 (2003).
40. V. A. Semenova, A. V. Tsyarkin, S. E. Putilin and V. G. Bespalov, "A method for the coherence measurement of the supercontinuum source using Michelson interferometer," *J. Phys. Conf. S.* 536, 012027 (2014).
41. I. Zeylikovich, V. Kartazhev and R. R. Alfano, "Spectral, temporal, and coherence properties of supercontinuum generation in microstructure fiber," *J. Opt. Soc. Am. B* 22, 1453-1460 (2005).
42. E. Baubeau, F. Salin, C. Le Blanc, "Spatio-temporal coherence properties of supercontinuum single filament in bulk media," Springer S. in Chem. Phys. Vol.63, Ultrafast Phenomena XI, 81-83 (1998).
43. K. Saitoh, M. Koshiba, T. Hasegawa, and E. Sasaoka, "Chromatic dispersion control in photonic crystal fibers: application to ultra-flattened dispersion," *Opt. Express* 11, 843-852 (2003)
44. A. Díez et al., "Control of the chromatic dispersion of photonic crystal fibers for supercontinuum and photon pairs generation," 11th Intl. Conf. LFNM, 1-2 (2011).
45. M. Suzuki, M. Baba, S. Yoneya and H. Kuroda, "Efficient spectral broadening of supercontinuum in photonic crystal fiber with self-phase modulation induced by femtosecond laser pulse," *Appl. Phys. Lett.* 101(19), 1110 (2012).
46. S. W. Harun, R. Akbari, H. Arof, H. Ahmad, "Supercontinuum generation in photonic crystal fiber using femtosecond pulses," *Laser Physics*, 21(7), 1215-1218 (2011).
47. G. Genty, M. Lehtonen, and H. Ludvigsen, "Spectral broadening of femtosecond pulses into continuum radiation in microstructured fibers," *Opt. Expr.* 10 (20), 1083-1098 (2002).
48. M. Liao, W. Gao, T. Cheng, Z. Duan, X. Xue, T. Suzuki and Y. Ohishi, "Flat and broadband supercontinuum generation by four-wave mixing in a highly nonlinear tapered microstructured fiber," *Opt. Expr.* 20(26), B574-580 (2012).
49. W. Yu, R. R. Alfano, C. L. Sam and R. J. Seymour, "Spectral broadening of picosecond 1.06 μm pulse in KBr," *Opt. Commun.* 14, 344-347 (1975).
50. S. Coen, A. Hing Lun Chau, R. Leonhardt, J. D. Harvey, J. C. Knight, W. J. Wadsworth and P. St. J. Russell, "Supercontinuum generation by stimulated Raman scattering and parametric four-wave mixing in photonic crystal fibers," *J. Opt. Soc. Am. B* 19, 753-764 (2002).
51. S. Pitois, G. Millot and P. Tchofo Dinda, "Influence of parametric four-wave mixing effects on stimulated Raman scattering in bimodal optical fibers," *Opt. Lett.* 23, 1456-1458 (1998).
52. Y. Yu, S. Ruan, J. Zhao and C. Du, "Continuous-wave supercontinuum generation in a 100-m high nonlinear photonic crystal fiber," *Proc. of SPIE Vol.* 6279, 62791B-1 (2007).
53. M. Prabhu, N. S. Kim and K. Ueda, "Ultra-Broadband CW Supercontinuum Generation Centered at 1483.4 nm from Brillouin/Raman Fiber Laser," *Japanese J. Appl. Physics*, 39(2), 4A (2000).

54. W. Gao, M. Liao, X. Yan, T. Suzuki, Y. Ohishi, "Quasi-CW supercontinuum generation in a HNLF pumped by sub-microsecond pulse," IEEE Xplore 17th Opto-Electron. Comm. Conf. 200-201 (2012).
55. B. Wetzel, A. Stefani, L. Larger, P. A. Lacourt, J. M. Merolla, T. Sylvestre, A. Kudlinski, A. Mussot, G. Genty, F. Dias, J. M. Dudley, "Real-time full bandwidth measurement of spectral noise in supercontinuum generation," Sci. Rep. 2(882), 1-7 (2012).
56. A. Zaytsev, C.H. Lin, Y.J. You, C.C. Chung, C.L. Wang and C.L. Pan, "Supercontinuum generation by noise-like pulses transmitted through normally dispersive standard single-mode fibers," Opt. Expr. 21(13), 16056-16062 (2013).
57. B. E. Olsson, P. Ohlen and D. I. Blumenthal, "Noise in sliced self-phase modulation broadened spectrum," CLEO Technical Digest. 39, 207-208 (2000).
58. T. Schreiber, J. Limpert, H. Zellmer and A. Tunnermann, "Radio frequency noise of femto- and picosecond pulse generated supercontinuum spectra," CLEO Conference vol.2, 2 (2004).
59. W. J. Brown, S. Kim and A. Wax, "Noise Characterization of Supercontinuum Sources for Low Coherence Interferometry Applications," J. Opt. Society Amer. A, 31(12), 2703-2710 (2014).
60. N. R. Newbury, B. R. Washburn, and K. L. Corwin, "Noise amplification during supercontinuum generation in microstructure fiber," Opt. Lett. 28(11), 944-946 (2003).
61. N. I. Nikolov, T. Sørensen, O. Bang, A. Bjarklev and J. J. Rasmussen, "Modelling of supercontinuum generation in highly nonlinear photonic crystal fibres," J. Optical Fiber Comm. Rep. 5(1-6), 1-21 (2008).
62. C. Chin, R. D. Engelsholm, P. M. Moselund, T. Feuchter, L. Leick, A. Podoleanu, O. Bang, "Polarization extinction ratio and polarization dependent intensity noise in long-pulse supercontinuum generation," SPIE Proceedings Vol. 10089, 100890L (2017).

3

Noise and polarisation in ultra-broadband OCT imaging

Noise measurement is an integral part of performance analysis in optical coherence tomography (OCT) system. The ability to improve signal-to-noise (SNR) for imaging relies on quantitative analysis of noise factors, both from the laser source, and those in the system. Noise in these systems is mainly caused by non-optimised optical configurations and sensitivity of the detection system. The detection mechanism used, such as homodyne or heterodyne can largely influence the noise. The difference in noise level is contributed by the difference in detector noise floor, photo-electrons dynamics of diodes, and the noise current. In our analysis of noise in Section 3.1, we consider a low-coherence Michelson interferometer applicable for different modalities of OCT techniques. This includes the classical time-domain (TD) system, to more recent Fourier domain (FD); swept source based spectral domain (SD) and the master-slave (MS) interferometer systems.

The signal-to-noise provides a relative measure of noise performance of the source. This is largely caused by the waveguide reflectivity and optical components used to construct the OCT system. At the source, optical power levels predominantly influence how much noise power is generated. At this stage of the characterisation process, noise can be classified into three broad categories: thermal noise (TN), shot noise (SN) and excess photon noise (EPN). In the vast majority of publication, the emphasis is placed on thermal and shot noises, while neglecting EPN.

The typical optical sources used are mainly the super luminescent diodes (SLD) and tuneable lasers such as swept source (SS). These optical sources have limited spectral bandwidth, usually between 70 nm to about 100 nm. However, with the advent of mode-locked lasers that offer femtosecond pulses and very high peak power, to supercontinuum (SC) sources with very broad optical bandwidth, additional noise power terms become significant.

In terms of optical bandwidth, we look into various factors that can affect the SNR of a fibre-coupled OCT system with balance detection. These factors typically include fibre-end reflectivity, cross-coupling efficiency, optical power at the source, and the beatings between various frequency components of a spectrum, in the case when a broadband optical source is used. A detailed comparison between SLD and SC sources reveals the influence of the optical source bandwidth on EPN power.

Various concepts of improving SNR using experiment of noise measurement in time domain OCT system have been suggested since the last decade. Sorin & Barney (1992) [1] proposed that by attenuating reference arm power deliberately while maintaining power in object arm could suppress relative intensity noise (RIN) from the source. This method can be achieved by using a fibre coupler with unequal splitting ratios. We will present in subsection 3.1.1 on how to allocate 20% incident power into the reference arm and 80% into the sample arm. In another experiment published by Takada et al. (1998) [2], the team illustrated that by employing a balance detection technique based on coherent heterodyne principle, it is sufficient to overcome thermal and electrical noise caused by the instability of receiver electronics circuitry. This method eliminates the need to manipulate reference arm parameters. Subsequently, in a year later, Rollins et al. (1999) [3] showed that besides relative intensity noise (RIN) and thermal noise, the power required in the OCT system to achieve shot noise threshold can be lowered using a dual-balance interferometer design. As a result, they managed to improve the overall SNR of a time domain OCT system by a factor of 6, using only up to 1 mW of source power.

As recent as in 2006, Haskell and Yoshino et al. [4] reported that despite various efforts in previous researches to eliminate different noise terms to improve SNR in OCT systems, none of them have taken into account an extra noise term called beat noise, despite being discovered by Mandel back in 1962 [5]. Beat noise (BN) is optical line width dependent. However, Haskell et al. suggested that balance detection can suppress beat noise, but only for source powers up to a few milliwatts. In addition, the effect of broadening the spectra bandwidth of the source allows an improvement in axial resolution and depth penetration of OCT system. When combined with low-noise high sensitivity detection mechanism, the use of broadband sources could make sub-micron resolution *in-vivo* imaging practical with the classical time domain OCT configuration.

In the second part of this chapter (Section 3.2), we'll look into the effect of polarisation extinction ratio (PER) and polarisation dependent RIN in SC sources.

3.1 Noise in balanced OCT system

3.1.1 Coupler theory

In this discussion we evaluated the noise from the optical source, using a time domain optical coherent tomography (OCT) system. A basic Michelson interferometer in fibre, as shown in Fig. 3.1.1, is constructed. In this interferometer, only straight through reference arm is used for evaluating noise from the optical source. The object arm is neglected for this purpose. On the other hand, for a full SNR experiment, a combination of both object and reference arms are used. In this section, we are interested in evaluating two electrical quantities: DC voltage and alternating current (I_{AC} , V_{DC}). To achieve that, we added a detection unit in Fig.3.1.

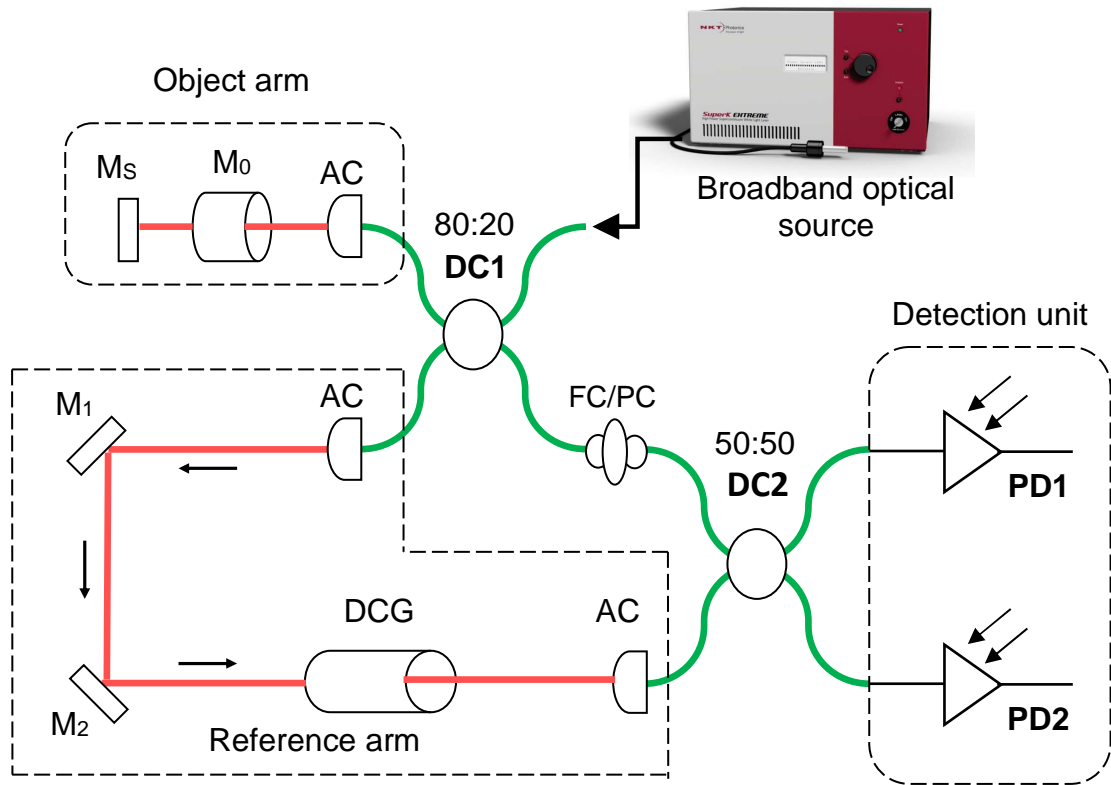


Fig.3.1.1: Illustration of a time-domain fibre based interferometer for noise measurements.

(AC: achromatic lens; DCG: dispersion compensation glass; DC1 & DC2: directional coupler; M_1 & M_2 : mirrors; M_0 : microscope objective, M_s : mirror as object; PD1 & PD2: photodiodes; red lines: free-space beam path; green lines: single-mode fibres.)

In a time domain OCT system, we employ two directional couplers, denoted as DC1 and DC2 in Fig. 3.1.1. These couplers form a fibre based configuration, and it is more robust than a standard bulk beam splitter normally used in a free space set-up. Light from a broadband source, for example a supercontinuum, first enters the first coupler DC1. The DC1 has a disproportional splitting ratio in two outputs. We aligned the output with 80% splitting ratio for our OCT object arm, and a 20% splitting ratio to our reference arms. In mathematical terms, we denote the coupling ratio as $\gamma_{11} = 0.8$ and $(1 - \gamma_{11}) = 0.2$, respectively.

In the reference arm, light is decoupled from fibre into free space with an FPR2 connector and an achromatic lens. While collimated, the light reflects off two silver mirrors, M_1 and M_2 . The beam path also contains a dispersion compensating glass (DCG) for dispersion adjustments. Systematic dispersion compensation in OCT systems is discussed in further details in Chapter 4. The free-space optical beam is then coupled back into a single-mode (SM) fibre of second directional coupler DC2. Another output of DC1 delivers light into object arm. In the object arm, instruments such as galvanometric scanners are usually in place to enable scanning of samples such as biological tissue or the retina. The object arm usually possess more challenges in noise control as many samples can attenuate or distort signal powers. For this reason, we allocate 80% of source power into the object. The light from the object is back propagated into the SM fibre of DC1, the same point where initial light into object arm was delivered. It is at this point where we introduce the notion of coupling efficiency: bar and cross coupling.

Similar to notation used earlier, γ_{11} and $(1 - \gamma_{11})$, a cross-coupling provides 80% of the backscattered light from the object arm to be sent into the second directional coupler DC2. Another 20% is delivered into the path that connects the source. To avoid damaging the source, a slight misalignment to the DC1 output can be done. However, as the signal from the sample is usually very weak, the risk of sending light straight back to the source is usually very low. The combination of two light beams input into DC2 causes mixing and beating of signals from object and reference arms. In time-domain, interference occurs only when two conditions are fulfilled:

- (1) the optical path length between the two arms are matched, and
- (2) optical path difference (OPD) is shorter than the light coherence length [6].

We evaluate outputs of DC2 as part of balance detection analysis in coupler theory, to be discussed further in Sec. 3.1.2. An illustration of directional coupler with varying splitting ratio can be represented by its electric field distribution at input and output ports, as shown in Fig.3.1.2. In a basic ideal 1:2 coupler, optical intensity delivered into one of two equal outputs has a factor of $1/\sqrt{2}$. To simplify our analysis of electric field in fibre, we need to first establish the relationship of spectral power at input and output ports. To illustrate this concept, we use an ideal directional coupler with equal splitting ratio (50:50). For this couple, we define coupling efficiency, $\gamma_{BAL} = 0.5$ for cross coupling and $(1 - \gamma_{BAL}) = 0.5$ for bar coupling. A simple representation of time varying electric field can be expressed in vector form, as in Eqn.3.1:

$$\vec{E}(t) = E \exp(-j(2\pi\nu_0 t + \varphi_0)) \quad [\text{V/m}] \quad (3.1)$$

where $2\pi\nu_0$ is the angular frequency (in m/s), t represents time (in s), φ_0 is the phase constant, E_0 is the amplitude of the wave. The vector $E(t)$ denotes the complex electric field composed of both real and imaginary parts, represented as $|E(t) \times E^*(t)|$ and carries a physical unit of Newton per Coulomb (N/C) or more conveniently volt per meter (V/m). Both parts of this vector field can be related by a Hilbert transformation \mathbf{H} , where $\text{Im}[E(t)] = j\mathbf{H}\{\text{Re}[E(t)]\}$. [7][8][9]

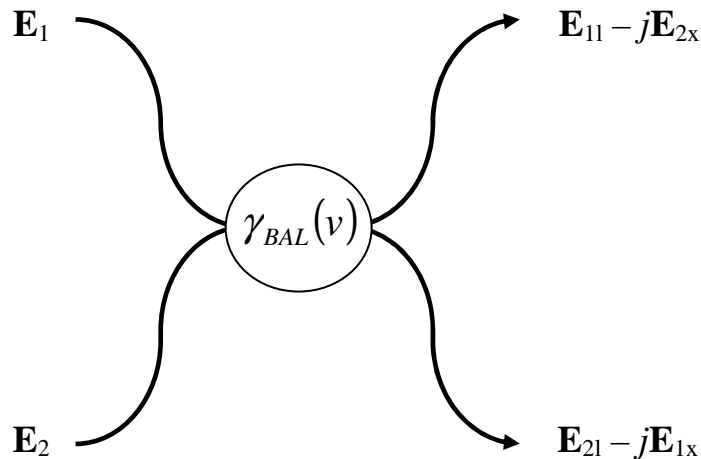


Fig. 3.1.2: Distribution of electric fields at input and output ports of a directional coupler. (Subscript '1': bar configuration, subscript 'x': cross configuration, γ_{BAL} : cross-coupling coefficient, $\mathbf{E}(t)$: complex electric field)

By considering the case where coupling efficiency is frequency dependent, where $\gamma_{BAL}(v)$ is dependent on input optical signal v , as in most practical application, or when cross and bar coefficient are dissimilar, we could write the outputs as in Eqn.3.2 and 3.3.

$$E_+ = \frac{1}{\sqrt{2}}(E_{1L} - jE_{2X}), \quad (3.2)$$

$$E_- = \frac{1}{\sqrt{2}}(E_{2L} - jE_{1X}). \quad (3.3)$$

To simplify our noise analysis, we prefer to use notion of photocurrent as opposed to electric field. From theory demonstration using Wiener-Khintchine theorem to evaluate autocorrelation of electric field $E(t)$, we could thus relate optical irradiance, I_{OPT} to the integral of power spectral density, or measured optical power, P_{OPT} obtained from a power meter. As such link is established, we could simply confirmed that modulus of electric field is also proportional to spectral distribution, as in Eqn.3.4

$$|E(t)| \propto \sqrt{I(t)} \quad (3.4)$$

Thus, the time-averaged photocurrent $i(t)$ is basically P_{OPT} divide by photoelectric conversion efficiency α of the diode. For that reason, we could now write the cumulative photocurrent at our detector as in Eqn.3.5 to Eqn. 3.7.

$$i(t) = i_+(t) - i_-(t) \quad (3.5)$$

$$\begin{aligned} i_+(t) &= \alpha[E_{1L}(t) - jE_{2X}(t)][E_{1L}^*(t) + jE_{2X}^*(t)] \\ &= \alpha\{|E_{1L}(t)|^2 + |E_{2X}(t)|^2 - jE_{1L}^*(t)E_{2X}(t) + c.c.\}, \end{aligned} \quad (3.6)$$

$$\begin{aligned} i_-(t) &= \alpha[E_{2L}(t) - jE_{1X}(t)][E_{2L}^*(t) + jE_{1X}^*(t)] \\ &= \alpha\{|E_{2L}(t)|^2 + |E_{1X}(t)|^2 - jE_{2L}^*(t)E_{1X}(t) + c.c.\}, \end{aligned} \quad (3.7)$$

where α is the coefficient of polarisation, subscripts X and L denote detected quantities after cross and bar configurations, subscripts $+$ and $-$ denote detected photocurrent at PD1 and PD2, respectively, and c.c. represents the complex conjugate terms of the sum of electric fields.

3.1.2 Photodiode detection

3.1.2.1 Balance detection

The output signals from the second directional coupler DC2 of our TD-OCT system shown in Fig.3.1.3 is delivered by two separate fibres into the in balance detection system. The detector is an in-house manufactured, high-responsivity balance receiver composed of two identical broadband PIN diodes. Each of these diodes has a responsivity curve averaging 0.8 A/W around the OCT wavelengths, from 1200 nm to 1400 nm. A trans-impedance amplifier (TIA) is used to convert low level photocurrent detected from the two photodiodes (PD1, PD2) into DC voltage. Two operational amplifiers (op-amps), each with a feedback resistor R_F and gain tuneable rheostat were used to construct a sum and a difference amplifier, with their potential outputs named SUM and DIFF respectively in Fig.3.1.3. A feedback capacitor C_F is placed at leg of PIN diode to suppress DC component and it acts as a rectified bridge for one period of instantaneous signal. An unamplified monitor output denoted DC bypasses the voltage feedback amplifier is used as the voltage reference, V_{REF} .

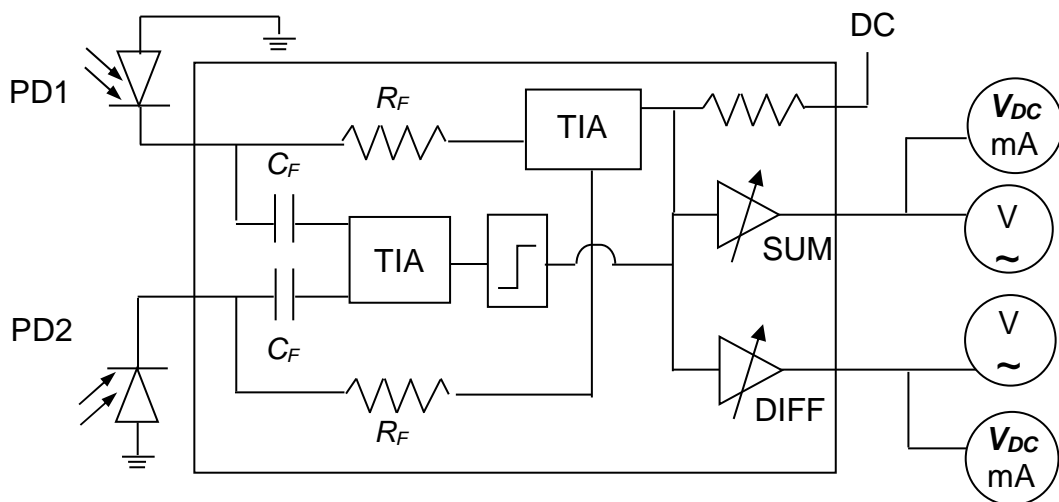


Fig. 3.1.3: In-house manufactured balance detector with two InGaAs photodiodes for noise and SNR measurements in an OCT system (TIA: operational amplifier, 300 MHz, AD, Σ : summing op-amp, Δ : differential op-amp; PIN: photodiode G10899-01K-FC-PC; R_F : feedback resistor, 2200 k Ω ; C_F : capacitor; HPF: high pass filter; V~: LEVELL broadband AC voltmeter 10 Hz to 3 MHz; V_{DC} : multimeter/oscilloscope 100 MHz)

3.1.2.2 PIN diode

A PIN diode is a typical *pn*-junction photodiode but has a large, wide, undoped intrinsic semiconductor region between *p*-type and *n*-type material. Common materials include AlGaAs and InGaAs. Upon illumination with optical power P , PIN diode records continuous photocurrent $i_e(t)$. The relationship of quantum conversion between electrons count, photocurrent and responsivity are as shown in Eqn.3.8 to 3.10 and Table 3.1.1. The noise equivalent current (*NEC*) is detector independent and is linked to its responsivity S , which is wavelength dependent [10].

$$\eta_e = \frac{\eta P \tau}{h\nu_0} \quad (3.8)$$

$$i_e = \frac{\eta P q_e}{h\nu_0} \quad (3.9)$$

$$S = \frac{\eta q_e}{h\nu_0} \quad (3.10)$$

Table 3.1.1: Parameters of a basic PIN photo detector used for noise characterisation

symbol	description
η_e	number of photoelectrons
η	detector quantum efficiency (Si 0.85 A/W for λ_0 at 1300nm)
h	Planck's constant (6.626×10^{-34} J.s)
ν_0	centre frequency of light source spectrum (Hz)
q_e	electron charge constant (1.6×10^{-19} C)
S	detector responsivity (A/W)
τ	observation time of photodiode illuminated with light (s)
<i>NEC</i>	noise equivalent current A/ $\sqrt{\text{Hz}}$

Balance detection works when all elements of spectral linewidth are equally split into two identical outputs, therefore a 50:50 ratio is necessary. For an SLD of bandwidth 60 nm, we generally have no problem of large deviation from 50:50 ratio using commercial fibre couplers with FWHM bandwidth of +/-40nm at 1300nm central wavelength. However, any mismatch due to splitting efficiency is of huge concern in operation of broadband super continuum sources such as the NKT SuperK Extreme and Koheras Versa.

These sources have very large optical bandwidth. When used with an OCT system at 800 nm, typical bandwidth of 300 nm can be expected. Therefore, to make detection compatible with all these broadband implementations, we need to take into account of different noise power as some of them can negatively degrade our system SNR. The most common occurrence is the huge photocurrent fluctuation in many narrowband detectors. The choices of broadband detectors are limited, and even if they are available, can be costly. One option is heterodyne detection. Heterodyne signal detection in time-domain OCT system can suppress flicker noise (generally known as $1/f$ noise) for signal bandwidth above audible frequency (AF) range, generally 20 kHz or higher. A heterodyne balanced detection system can additionally suppress low frequencies excess noise (Sec.3.1.3.3) that present in a non-balanced or homodyne configuration. Heterodyne detection can be achieved by allowing short exposure time ($< 10 \mu\text{s}$) to PIN diode at measurement. Further implementation is discussed in the noise measurement section.

3.1.3 Noise theory

Noise is defined as the mean square fluctuation (MSF, $\langle \Delta n^2 \rangle$) of random number of electrons on a photodiode over illuminated area A , over observation duration $\Delta\tau$ [11]. The evaluation of noise takes into account of fluctuations of the envelope power of AC current on the detector that resulted in a cross coupling efficiency (γ_{BAL}) of 0.5. As such, the interference signal $i_{AC}(t)$ can then be written as in Eqn.3.11 based on derivation of electric field in Eqns.3.6 and 3.7. Similarly, the DC current terms can be expressed as in Eqn.3.12.

$$\begin{aligned} i_{ac}(t) &= \langle i_+(t) - i_-(t) \rangle_{ac} \\ &= +\alpha[-jE_{2X}(t)E_{1L}^*(t) + c.c. + jE_{1X}(t)E_{2L}^*(t) + c.c.] \end{aligned} \quad (3.11)$$

$$\begin{aligned} i_{dc}(t) &= i_+(t) - i_-(t) \\ &= \alpha\{\langle P_{1L}(t) \rangle + \langle P_{2X}(t) \rangle - \langle P_{1X}(t) \rangle + \langle P_{2L}(t) \rangle\} \\ &= \alpha\{\langle P_1(t) \rangle + \langle P_2(t) \rangle\} \end{aligned} \quad (3.12)$$

where α is the coefficient of polarisation, c.c. indicates complex conjugates, subscripts X and L denote detected quantities after cross and bar configurations, subscripts $+$ and $-$ denote detected photocurrent at PD1 and PD2, respectively.

Photocurrent response for OCT system at detector output can be expressed by taking into account the cross-coupling terms of first directional coupler (DC1) and power from both arms of interferometer (P_{REF} and P_{OBJ}). Instantaneous photocurrents can be written as sum of optical power multiplied by photodiode responsivity for an equal split output from second directional coupler DC2, with 50% cross efficiency cancellation. Therefore, we could express $\langle i^2(t) \rangle$ the photo detected signal as in Eqn.3.13 [1].

$$\langle i(t) \rangle^2 = 2\alpha \sqrt{\langle P_{REF} \rangle \langle P_{OBJ} \rangle} \cos(2\pi\nu_0 t - \varphi_0) \quad (3.13)$$

where α is the coefficient of polarisation, $2\pi\nu_0$ is the angular frequency of light source (in Hz), φ_0 is the phase constant of the interfering light.

To take a look into the different noise terms, let us now consider a light beam from a single-mode non-polarised source. The root mean square (RMS) value of photocurrent fluctuation measured across a resistor at photodiode output can be described in Eqn.3.14. The equation combines two noise terms: shot noise (SN) and excess photon noise (EPN).

$$\begin{aligned} \langle \Delta I_{rms}^2 \rangle &= \langle \Delta I_{shot}^2 \rangle + \langle \Delta I_{EPN}^2 \rangle \\ &= 2q \langle I_{dc} \rangle B_{elec} + 2 \langle I_{dc}^2 \rangle \frac{B_{ELEC}}{\Delta\nu_{eff}} \\ &= 2q \left[\langle I_{1,DC} \rangle + \langle I_{2,DC} \rangle \right] B_{ELEC} + 2 \langle I_{1,DC} \rangle \langle I_{2,DC} \rangle \frac{B_{ELEC}}{\Delta\nu_{eff}} \end{aligned} \quad (3.14)$$

where B_{ELEC} is the electrical bandwidth (Hz), $\Delta\nu_{eff}$ is the effective frequency of light source (in Hz) and q_e is the electron charge constant (1.6×10^{-19} C).

3.1.3.1 Shot noise

Shot noise is produced in OCT system by beating between signals from fibre-end end reflection and reference arm, and is proportional to elementary electric charge q_e . The mean photocurrent $2\langle I_{DC} \rangle$ for shot noise can be further evaluated on contribution from cumulated currents of $\langle I_1 \rangle + \langle I_2 \rangle$ due to fibre-end reflection I_{FER} , and that due to reference arm signal I_{REF} . As such, shot noise power can be written as in Eqn.3.15.

$$\langle \Delta i_{SN}^2 \rangle = 2\alpha q_e B_{ELEC} (\langle P_1 \rangle + \langle P_2 \rangle) \quad (3.15)$$

where α is the coefficient of polarisation, B_{ELEC} is the electrical bandwidth (Hz) and q_e is the electron charge constant (1.6×10^{-19} C).

In a classical light analysis theory, shot noise is generated by a constant intensity signal, from photon fluctuation in the same spin state falling onto the detector area, within a coherence time of observation (τ). The distribution of these photon follow a probability distribution in Eqn.3.15, and it obeys the Poisson's statistical formulae with a mean square fluctuation (MSF) of $\langle \Delta n^2 \rangle = \langle n \rangle$. By taking into account of PIN photodiode quantum efficiency, α , we could write Eqn.3.16.

$$P(n) = \frac{\langle n \rangle^n e^{-\langle n \rangle}}{n!} \quad (3.16)$$

$$\langle \Delta n^2 \rangle = \langle \alpha n \rangle \quad (3.17)$$

3.1.3.2 Excess photon noise

Excess photon noise (EPN) is produced by the beating of Fourier components within the broadband optical spectrum, and its resulting noise power is inversely proportional to optical bandwidth Δv_{eff} of the source, as defined in Eqn.3.18. EPN is also technically called wave interaction noise or photon-bunching effect for that matter. We can therefore analyse EPN in the form of photon fluctuation in the particle nature of light.

$$\Delta v_{eff} = \left[\int P(v) dv \right]^2 / \int P^2(v) dv \quad (3.18)$$

By referring to Eqn.3.17, we could model this noise as $\langle n \rangle^2$, effectively adding a second noise term to make it becomes Eqn.3.19, subject to condition that coherence time of an optical source τ_C is smaller than coherence time of our detector τ_E . By considering the inverse proportionality between time and bandwidth, the linewidth of our source ought to be much larger than our detector bandwidth.

$$\langle \Delta n^2 \rangle = \langle \alpha n \rangle + \langle \alpha n \rangle^2 \quad \text{with condition } (\tau_C \ll \tau_E) \quad (3.19)$$

By relating Eqn.3.19 to Eqn.3.15, we could re-write it such that it follows the Bose-Einstein photon counting distribution. The resulting expression in Eqn.3.20 is the general expression for MSF of random photon, which is both strict sense stationary and ergodic.

$$P(n) = \frac{\langle n \rangle^n}{(1 + \langle n \rangle)^{n+1}} \quad (3.20)$$

The mean square current fluctuation in Eqn.3.14 can therefore be obtained by multiplying both sides of Eqn.3.19 with $(qE/\tau)^2$ and grouping the term $\langle n \rangle qE/\tau = I_{DC}$ as the time-varying photocurrent at detector output. Therefore, the final form of EPN as becomes

$$\langle \Delta I_{EPN}^2 \rangle = 2\alpha(I_{DC})^2 \frac{B_{ELEC}}{B_{OPT}} \quad (3.21)$$

$$\text{with } I_{DC}^2 = \langle P_1 \rangle \langle P_2 \rangle + \langle P_1 \rangle^2 + \langle P_2 \rangle^2 \quad (3.22)$$

To demonstrate the existence of excess noise current in bandwidth dependent broadband sources, as opposed to laser, we look into a comparison made by Morkel et al. (Southampton, 1989) between a HeNe laser and a 2 nm SLD source. In their noise characteristic measurement, a detection system employing a 500 kHz low-noise trans impedance amplifier (TIA) was used to monitor signal fluctuation within a 100 kHz electrical bandwidth to achieve signal-to-noise sensitivity over 600:1 and eliminate $1/f$ noise from SLD source. They recorded a 10 dB/decade of signal for SLD vs 5 dB/decade for HeNe. For this reason, they have shown in their experiment that, using noise curve from SLD output, due to an additional EPN term, total detected power increased by the power of two with respect to input signal I_{DC} . The measurement was done against a linear trend observed for HeNe laser. The HeNe laser is shot-noise-limited. Our interest to broadband OCT imaging will likely involve optical sources with bandwidth greater than 300 nm. The use of a supercontinuum (SC) source, such as SuperK Extreme from NKT Photonics A/S is a preferred choice. However, the issue of shot noise in a SC source will have to be evaluated thoroughly. For this reason, a dedicated experimental section in this chapter, Section 3.2.3 will discuss SN and EPN in SC in more details. The ratio, $R_{EPN/SN}$ of excess photon noise to shot noise for both coherent and incoherent sources can be verified as in Eqn.3.23, subjecting to bandwidth of both optical source (B_{OPT}) and detector (B_{ELEC}), for incoherent light fluctuations the inequality in Eqn.3.24 holds.

$$R_{EPN/SN} = \frac{I_{DC}}{2q_e B_{ELEC}} < 10^{-6} \quad (3.23)$$

$$2q_e B_{ELEC} I_{DC} \gg I_{DC}^2 \frac{B_{ELEC}}{B_{OPT}} \quad (3.24)$$

where B_{ELEC} is the electrical bandwidth (Hz), B_{OPT} is the optical bandwidth (Hz) and q_e is the electron charge constant (1.6×10^{-19} C).

3.1.3.3 *Excess noise at low frequencies*

A. Frequency dependent limitation

As measurement of noise power spans across several decades of frequencies, the use of a band pass filter to restrict measurement range is important. We can typically evaluate noise suppression performance up to generally 100 kHz without considering contribution of $1/f$ noise terms. However, in this case, effect of quantum noise suppression in audio frequency (AF) band is difficult to quantify without resorting to expensive equipment such as lock-in amplifier and high speed oscilloscope. In addition to EPN dependent on linewidth of optical sources mentioned above, several articles had also identified causes of excess noise at low frequency, in the audible range, up to 10 kHz, especially in the detection mechanism, to be discussed further in detailed in the following sub-section.

In low frequency detection, such as the most commonly used balance detection technique, the use passive electronic components like resistors, capacitors, inductors and op-amps in detection circuitry cannot be avoided. Many of these semiconductor parts have parasitic effect that is dependent on frequency. Detector sensitivity therefore has a frequency roll off effect. Detector units operating at frequency at a few 100 kHz will remain susceptible to a different IV response than analysis at audio frequencies.

B. Optical beam limitation

Another source of noise at low frequencies is beam jitter. Beam jitter occurs due to backscattering from mainly biological tissue sample, or object with imperfect surface and refractive indices. The primary concern in dealing with beam jitter is the distortion of beam quality, mode of transmission in fibre. It has to be noted that not all Gaussian shaped beam spot is re-injected back into single mode (SM) fibre core, and that can lead to fibre-end reflectivity – another undesirable effect in a free space to fibre OCT system. On the spectral side, independent to dispersion in the interferometer, this beam jittering issue often resulted in non-overlapping of Fourier components in a bandwidth in the interferometer, making spectral density of output beam non time invariant to the source beam. For example, a full 300 nm broadband light is measured in free space section of the interferometer, while at the detector, the measured optical bandwidth becomes narrowband.

Parasite interference is predominantly caused by optical alignment imperfection and non-optimisation of beam splitting ratios in a bulk beam splitter or within a directional coupler. Without an ideal $\gamma_{BAL} = 0.5$ splitting efficiency, this often leads to unequal photocurrents subtraction due to spectral shape distortion between light beams at two photodiodes. In addition to parasitic effect at detector, stray reflections due to scattering of light from original path beam in either sample arm due to surface imperfection or reference arm due to dust also able to alter non-coherence beam at interference.

C. Semiconductor limitation

Photosensitive diodes with built-in $p-n$ junction also contribute to dark current production resulted from random generation of electrons and holes within the depletion region of these devices. As a result, even at very low dark current magnitude of a few $\text{pA}/\sqrt{\text{Hz}}$, evaluating non-linearity of noise terms differentiating shot and excess noise at this current level is difficult.

D. Signal processing, filtering & rectification constraints

This phenomenon is due to signal amplification process. Ideally difference in photocurrents between two outputs (LO–local oscillator and IF–intermediate frequency) will result in subtraction to product differential value. However, non-subtracted photocurrent with frequency component above AF range will continue to degrade amplifier performance with increase in intensity noise ratio to amplified signal. In most practical case, despite use of low-noise amplifiers (LNAs) in the detector system, quantum noise remain to dominate noise power up to 10 kHz. Major disadvantage of using a non-balanced configuration is to provide flexibility to cancel photocurrents that are differ from LO value.

As we select our electrical noise bandwidth for frequency analysis, we employ a linear, time-invariant (LTI) filter for this process. When we pass a time varying, non-white spectral response photocurrents into this electronic filter, we expect to have output signal that is at least wide-sense stationary, where its 1st moment and auto covariance is invariant with respect to time. Nevertheless, the frequency response of the filter and integrated circuit does vary in time, resulting in non-white noise, signal whose power spectral density is not constant but random, and its joint probability density function (JPDF), mean and covariance changes with time.

3.1.3.4 Thermal noise

This form of noise is caused by the load resistor in a balance detector shown in Fig.3.2 is time incoherent and independent to noise produced by optical sources. The variance of thermal noise power due to circuit resistance and limitation of electrical bandwidth on analogue-to-digital conversion (ADC) process can be written as in Eqn.3.25.

$$\langle \Delta i_{thermal}^2 \rangle = (NEP)B_{elec} = \frac{4k_B T}{R_{load}} B_{elec} \quad (3.25)$$

where B_{elec} is the electrical bandwidth of the detector, k_B is the Boltzmann constant, T is the ambient room temperature (300 K), R_{load} is the resistance value (in Ω), NEP is the noise equivalent power ($A.Hz^{-1/2}$) as defined in Table 3.1. Thermal noise usually has very little effect to overall noise power, and therefore is negligible for most noise analysis.

3.1.3.5 Beat noise

Haskell et al. [4] disputed many findings by OCT researchers in area related to noise performance analysis. They have further noted that many previous publications had omitted an additional noise term – beat noise – in their Michelson interferometer system. The concept of beat noise, or loosely defined as fourth order interference in signal processing, can be obtained by correlating signals from two photodetectors that are separated in both space and time. It was first discovered by Alford and Gold back in 1958, when they showed a time delay produce by an interferometer with optical path difference (OPD) that is much greater than the light source coherence length (L_C). This effect has a correlated intensity fluctuation, in the form of a spectral modulation that was observed as a result of parametric down-conversion of correlated photon pairs in a superposition state.

According to Haskell et al. [4] and Mandel [5], the beat noise term is equal in magnitude but distinct from the cross term in the usual Bose-Einstein photon-bunching effect. The main cause of beat noise is not due to beatings between various frequency components in a spectral bandwidth, but rather due to two partially coherent and incoherent beams (P_{COH} and P_{INCOH}) reflected off a multi-layered material with varying refractive index. Independent of material dispersion, refractive index differences as a function of depth and thickness in an object can cause the backscattered beam to attenuate in signal strength, propagate at different speed, and lose spatial coherence at detector.

By referring to our Eqn.3.2, according to claims by Haskell et al. [4], this beat noise current term can be written as in Eqn.3.26:

$$\langle \Delta I_{Beat}^2 \rangle = \alpha^2 \frac{B_{elec}}{B_{opt}} [2\langle P_1 \rangle \langle P_2 \rangle] \quad (3.26)$$

where α is the coefficient of polarisation, B_{elec} is the electrical bandwidth, B_{opt} is the optical bandwidth, P_1 and P_2 are received power at photodiodes 1 and 2.

A detailed analysis carried out by Yoshino et al. [12] and affirmed by Haskell has demonstrated that beat noise, as similar to EPN term, is due to the changes in total optical power spectrum incident upon the PIN photodiodes causing interference in two partially coherent beams. The main reasoning could be laid upon wavelength dependent coupling efficiency shown in section 3.1.1 of this thesis.

3.1.3.6 Total noise power

Total noise power at output of balance detector can be written as sum of thermal noise, shot noise, excess photon noise and beat noise. As we assume an equal splitting ratio of 50:50 for the second directional couple DC2 under balance condition, the spectra response between its input and output is invariant, the contribution of frequency component shift is null. We could theoretically rewrite the total noise power to become Eqn.3.27, by combining Eqns. 3.14-3.15, 3.21, 3.25-3.26.

$$\langle \Delta i^2 \rangle = 2B_{elec} \left\{ \frac{2k_B T}{R_L} + \alpha q_e \{ \langle P_1 \rangle + \langle P_2 \rangle \} + \alpha^2 \frac{\langle P_1 \rangle^2 \langle P_2 \rangle^2}{\Delta \nu_0} \left(1 + \frac{2}{\langle P_1 \rangle \langle P_2 \rangle} \right) \right\} \quad (3.27)$$

where α is the coefficient of polarisation, B_{elec} is the electrical bandwidth, B_{opt} is the optical bandwidth, P_1 and P_2 are received power at photodiodes PD1 and PD2, k_B is the Boltzmann constant, T is the ambient room temperature (300 K), R_L is the load resistance (in Ω), ν_0 is the central frequency of light source (in Hz), q_e is the electron charge constant (1.6×10^{-19} C).

3.1.4 SNR and sensitivity

3.1.4.1 SNR

Signal-to-noise ratio (SNR) is a relative measure of superiority of detectable signal with respect to degradation in signal quality resulting from various events of photoelectron fluctuation in both input and output of photodetector system at unity bandwidth. By considering an optical source of different frequencies and random phases in a sinusoidal wave field, with a Gaussian component of noise due to spontaneous emission, electrical, thermal and mechanical instability in Eqn.3.1, we could derive a probability density function of noise $p(v)$ in the Gaussian form as a function of SNR in Eqns.3.28 and 3.29.

$$v(t) = V_0 \cos(\omega_0 t + \varphi_0) + V_{noise} \quad (3.28)$$

$$SNR = \frac{V}{\sqrt{\langle V_{noise}^2 \rangle}} \quad (3.29)$$

where ω_0 is the angular frequency (in m/s), t represents time (in s), φ_0 is the phase constant, V_0 is the amplitude of the signal and V_{noise} is the noise voltage.

3.1.4.2 Sensitivity

Sensitivity (Σ) of TD-OCT system in Eqn.3.30 can be achieved with minimal sample arm reflectivity $\min(R_S)$ and fibre-end reflectivity, $\min(R_{REF})$ [10]. The Advantage of using TD-OCT is that the illuminated power is proportional to photodiode current, for each A-scan. Therefore, DC current at detector is proportional to NEC . The NEC is much lower in FD-OCT since Fourier transformation takes into account of receiver quantum noise.

$$\Sigma_{TD-OCT} = \frac{1}{B_{ELEC}} \frac{2\gamma_{bal}(1-\gamma_{BAL})P_{OBJ}^2 R_{REF}}{P_{OBJ}\gamma_{BAL}R_{REF} \left(2q_e + P_{OBJ}\gamma_{BAL} \frac{R_{REF}}{\Delta v_{eff}} \right) + (NEC)^2} \quad (3.30)$$

where γ_{BAL} is the coupling efficiency of DC2, P_{OBJ} is the power from object, R_{REF} is the reflectivity of object, q_e is the electron charge constant, B_{ELEC} is the electrical bandwidth of the detector, NEC is the noise equivalent current and Δv_{eff} is the effective frequency of light source.

As excess-noise in FD-OCT is significantly larger (scaled by pixel value to factor power of \sqrt{N}), balance detection can't effectively suppress coherent noise and thus has no better sensitivity enhancement otherwise achievable in TD-OCT system. In an optimised TD interferometer, the splitting efficiency of first directional coupler (DC1) was deemed necessary to be indifferent to 50:50. As demonstrated by Rosa and Podoleanu [7], an optimum efficiency of 80:20 was found. In this case, reference arm power P_R is four times as huge as P_S , and therefore, the reflectivity in reference arm is much larger, at least $10\times$ the reflectivity in sample arm ($R_{OBJ} \ll R_{REF}$). The SNR notation in Eqn.3.29 becomes

$$SNR \propto \frac{P_{OBJ} R_{OBJ} P_{REF} R_{REF}}{P_{REF} R_{REF} + \gamma_{bal} P_{REF}^2 R_{REF}^2} \quad (3.31)$$

where γ_{BAL} is the coupling efficiency of DC2, P_{REF} is the power from reference arm and P_{OBJ} is the power from object arm.

In shot noise limited OCT system, we could work out SNR, where $NEB \approx 2\Delta f$ as in Eqn.3.32.[13] Signal-to-noise ratio as function of detector current for this system using incoherent sources of varying optical linewidth centred at 1300 nm is plotted in Fig.3.1.5.

$$SNR = \frac{1}{2} \frac{\alpha P_S R_S}{h\nu_0 NEB} = \frac{I_{DC}}{2q_e B_{elec} + I_{DC} \frac{B_{elec}}{B_{opt}}} \quad (3.32)$$

where α is the coefficient of polarisation, B_{elec} is the electrical bandwidth, B_{opt} is the optical bandwidth, P_S is power from the sample, R_S is the sample arm reflectivity, I_{DC} is the noise power from detector, ν_0 is the central frequency of light source (in Hz), q_e is the electron charge constant (1.6×10^{-19} C) and h is Planck's constant (6.626×10^{-34} J.s).

By Nyquist sampling theorem, our optimum bandwidth for BPF ought to be equal to or larger than $2\Delta f$. It is noted that wider detection filter bandwidth decreases sensitivity, and smaller bandwidth will decrease resolution. Incoherent light has no contribution to increase interference fringes, i.e. due to phase mismatch of frequency components in spectra bandwidth, and the auto covariance of them vary in time. Thus, no improvement over sensitivity or dynamic range is attained for very large band source ($\Delta\lambda > 100$ nm) in a narrowband directional coupler (BW ± 40 nm).

3.1.5 Noise measurement technique

3.1.5.1 Theoretical modelling

Noise characterisation of an optical source uses both arms of the interferometer shown in Fig.3.1.1. We take reference arm power as proportional to input power into our OCT system, and the object arm power as dependent on the surface reflectivity of the sample. The power of these two beams at the detector can be written as a function of the coupling ratio, as Eqn. 3.33 for reference arm, and Eqn. 3.34 for object arm.

$$P_{REF} = \gamma_{11} \gamma_{BAL} P_{OPT} \quad (3.33)$$

$$P_{OBJ} = (1 - \gamma_{11}) \gamma_{BAL} P_{OPT} \quad (3.34)$$

where γ_{BAL} is the coupling efficiency of coupler DC2, γ_{11} is the coupling efficiency of DC1, and P_{OPT} is the input optical power delivered to Port 1 of DC1 (Fig.3.1.1).

To evaluate P_{OBJ} correctly, we need the Fresnel reflectivity from the object, $O(v)$. A comprehensive noise measurement for all optical sources (SLD and SC) was done by recoding the voltages at the detector, V_{AC} and V_{DC} , using similar set of reference powers at with the same optical bandwidth. V_{AC} is the variance of output RMS signal. Noise signals were evaluated for electrical bandwidth B_{ELEC} of up to 100 kHz (or 10 μ s) using a voltmeter and an oscilloscope. Graph of noise power vs output DC voltage is shown in Fig.3.1.4. Modelling of SNR using Eqn.3.32 with a 50:50 DC1 is shown in Fig.3.1.5.

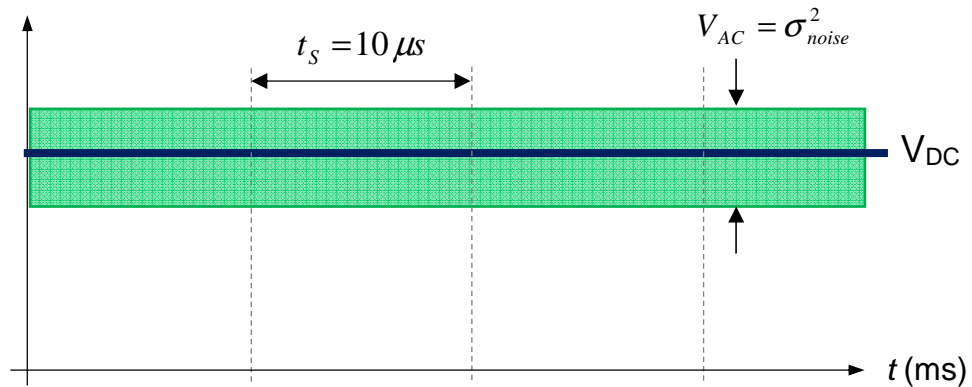


Fig.3.1.4: Oscilloscope readout of noise power (AC fluctuation) sampled over 100 kHz electrical bandwidth and the linear DC component at balance detector

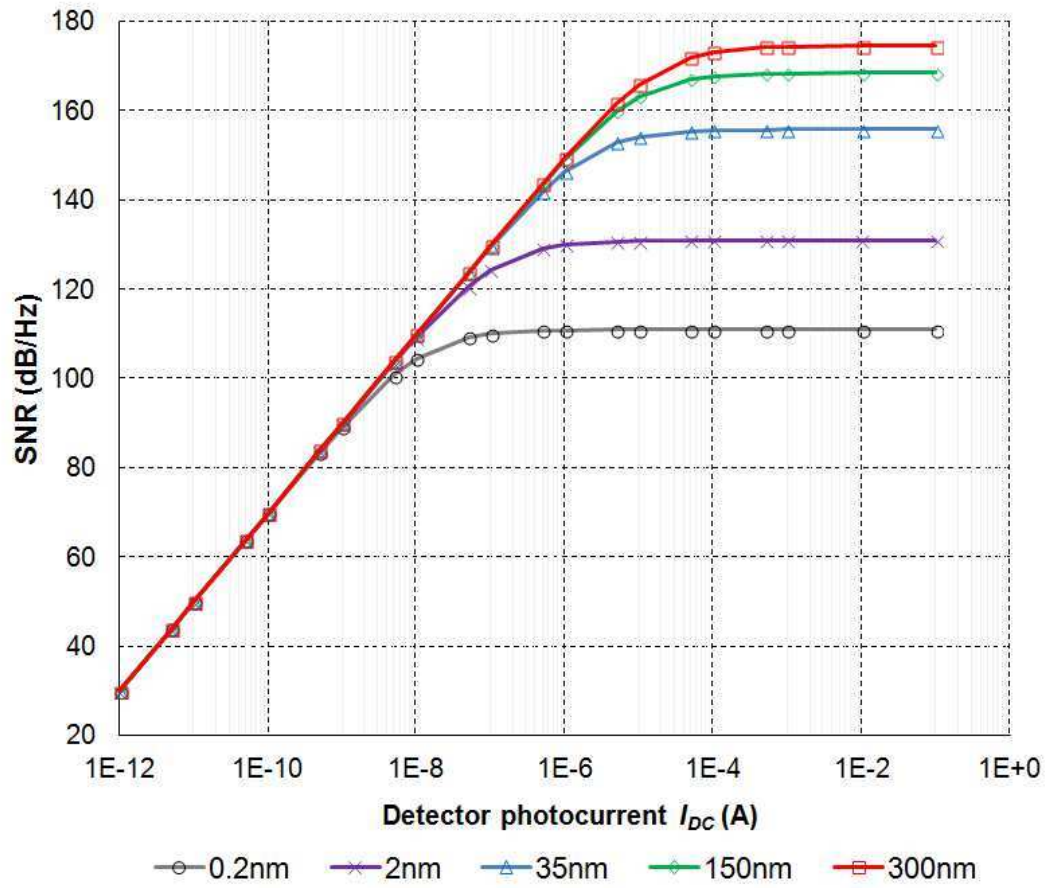


Fig.3.1.5: Theoretical SNR for optical sources with different bandwidth centred at 1300 nm

$$q_e = \frac{\Delta(U^2)}{\Delta I_{DC}} \quad (3.35)$$

From the simulation plot in Fig.3.1.5, I_{DC} is proportional to source power. We were able to relate DC current to electron charge using the slope up to $I_{th} = 1.8mA$ as equal to 1.818 Coulombs, using Eqn.3.35. Therefore, the equivalent noise power threshold necessary to access the EPN regime using optical sources of bandwidth $\Delta\lambda=150nm$ and central wavelength $\lambda_c = 1300nm$ can be calculated using Eqn.3.36. I_{DC} was measured across two parallel feedback resistors, $R=2.2 k\Omega$ before the TIA in Fig.3.1.3.

$$RI^2 = \frac{V_{AC}^2}{R_L} \quad (3.36)$$

3.1.5.2 Experimental measurements

It is essential to experimentally verify the detector current necessary to access the EPN regime. We run the noise power test on an SLD with dual-diode configuration (BW 35 nm and 60 nm), as well as three supercontinuum sources from NKT Photonics (SuperK EXR9, SuperK EXR20 and Koheras Versa, each with a BW of 150 nm).

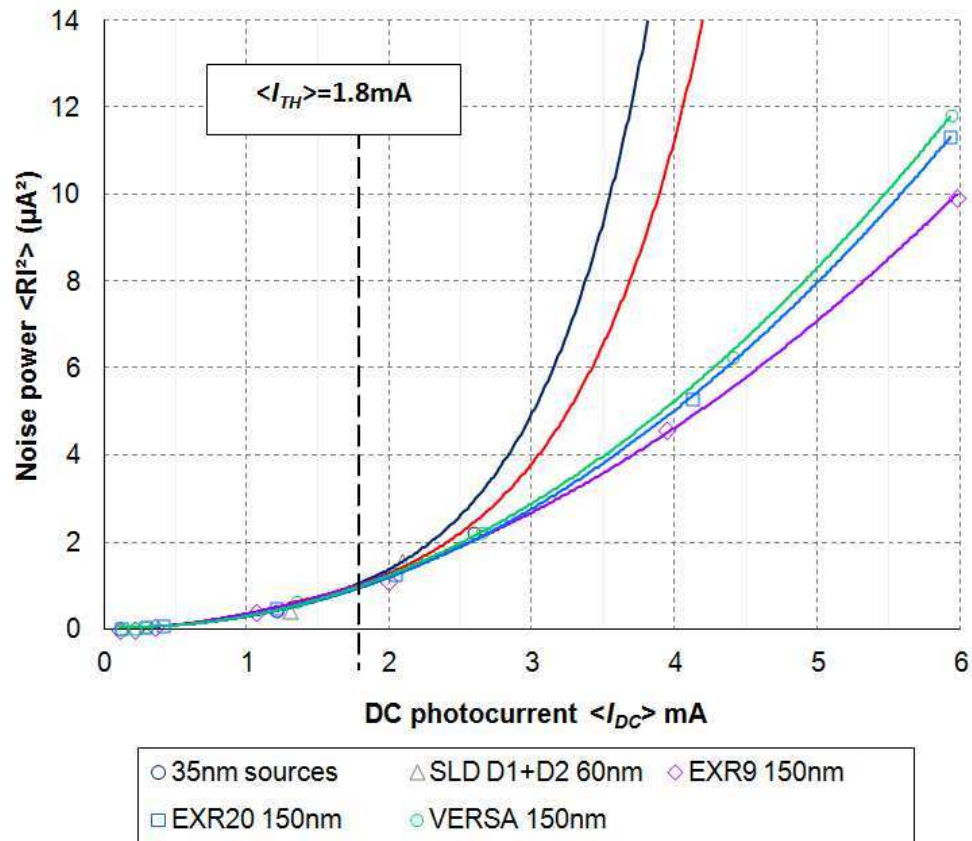


Fig.3.1.6: Measured noise power relative to input power

In the EPN regime, we observed a linear increase in noise power by a factor of $B_{elec}/\Delta v_{eff}$ relative to input current I_{DC} . We could then relate EPN to the time derivative electronic charge by RI^2/t^2 . For each optical source we evaluated noise for B_{ELEC} up to 100 kHz. For OCT application, we first evaluate the noise performance of a narrowband source, with central wavelength of 1.3 μm and bandwidth 35nm (or 6.31 THz). We calculated that coefficient $B_{elec}/\Delta v_{eff}$ equals to 0.016×10^{-6} , which is roughly corresponding to our measurement data of slope value in the region of 0.013×10^{-6} , for 35 nm SLD and for 150 nm supercontinuum sources (Versa, EXR9, EXR20).

Table 3.1.2: Signal variation vs input power for the EPN regime

Source	$\langle \Delta R I^2 \rangle / \langle \Delta I_{DC} \rangle$ $\times 10^{-6}$ [a]	$B_{ELEC} / \Delta v_{eff}$ $\times 10^{-6}$ [b]	P_{th} at $\langle I_{DC} \rangle = 1.8\text{mA}$ [μW] [c]
35nm (SC ^[c] , SLD)	0.0130	0.0158	Shot-noise limited
60nm (SLD D1+D2)	0.0081	0.0089	2.00
150nm EXR9	0.0033	0.0037	1.75
150nm EXR20	0.0032	0.0037	2.15
150nm VERSA	0.0031	0.0037	2.25

Notes:

[a] Slope calculated for values measured in Fig.1 using $(V_{AC})^2/V_{DC}$.

[b] Data calculated using B_{ELEC} at 100 kHz and respective B_{OPT} measured at FWHM.

[c] Minimum noise equivalent power needed to access the EPN regime.

[d] Supercontinuum sources: Versa, EXR9 and EXR20, all with 35 nm filtered spectrum.

Rectified signal from differential amplifiers (Fig.3.3) was used to measure SNR for four sources. SNR was measured by taking ratio of interference signal ($V_{REF} + V_{OBJ}$) over reference arm signal (V_{REF}) for B_{ELEC} up to 100 kHz. The SNR data was compared against signal into object arm with a reflectivity coefficient of 0.2 (80:20 DC1).

Our measurement shows variation in SNR with respect to input power, P_{IN} , where $P_{IN} \approx P_{REF}$. By using 1.25 mW reference arm power ($\Delta\lambda_{eff} = 35$ nm and $\lambda_C = 1.3$ μm , $P_{IN} = 3.3$ mW), we noticed +5 dB difference in SNR between SuperK EXR20 and Koheras Versa. On the other hand, EXR9 has better signal to noise than a typical SLD evaluated at similar reference arm power and optical bandwidth: +3 dB (against SLD at 35 nm), +12 dB (against EXR20) and +17 dB (against Versa).

It worth mentioning that beyond P_{LIM} ($P_{REF} = 1.25$ mW, $P_{IN} = 3.3$ mW) for 35nm optical bandwidth, SNR levels off and becomes independent of input power. This observation varies upon system configuration, noticeably due to limiting factors such as bandwidth and reflectivity in object arm. Therefore, SNR dependent noise from optical sources can only be evaluated for power threshold below P_{LIM} . On the other hand, larger bandwidth SLD has better SNR than two supercontinuum sources (SuperK EXR20 and Versa). The only explanation when SLD is superior to SC sources is that for lower input power, higher EPN threshold for lower input power. The low-noise version of SuperK Extreme (320 MHz, 20 ps) has an overall better SNR performance than SLD, EXR9 and Versa, with improvement of +11 dB (input 10 μW) to +27 dB (input 1.25 mW) over conventional SLD sources in our optical BW limited analysis (35 nm).

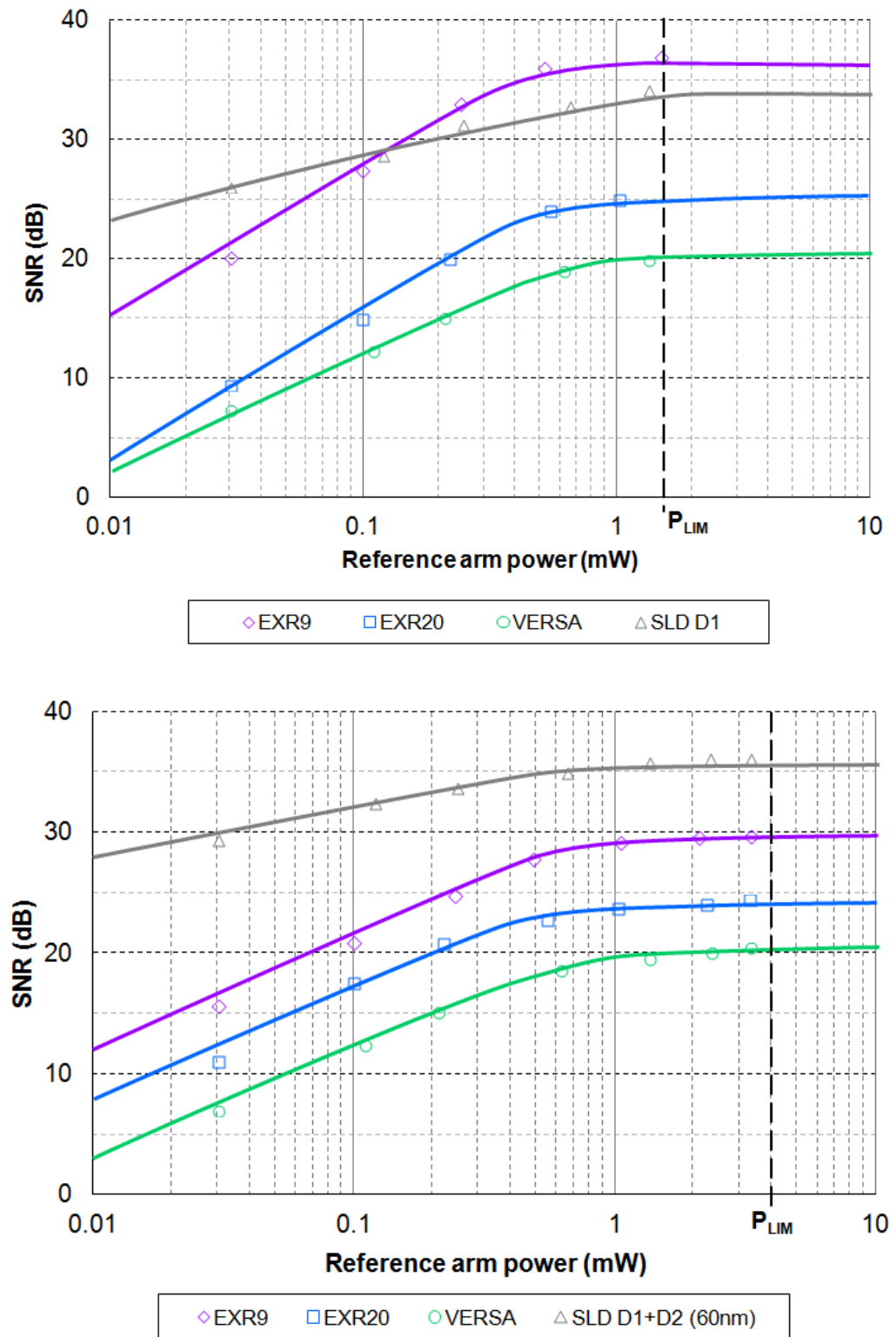


Fig.3.1.7 (top) Measured SNR in time-domain OCT system in variation to reference arm power with four different optical sources of 35 nm, and (bottom) 150 nm for NKT SC and 60 nm for SLD diodes.

In comparison to noise data, our minimum power to operate the SuperK EXR9 beyond shot noise regime was $1.75 \mu\text{W}$. However, we are not able to draw a conclusion if increasing the optical bandwidth from SuperK EXR9 can make the imaging less noisy than SLD of similar BW. Nevertheless, in terms of SNR ratings, comparison between two supercontinuum sources has again proven that with a 150 nm bandwidth, SuperK EXR9 is between +7 dB to +9 dB better than Versa. It has to be noted that our measured values of $B_{elec}/\Delta\nu_{eff}$ for 150 nm case varied despite every effort to have exactly 150 nm filtered optical spectrum going into and coming out from our OCT system by making ensuring we have $\Delta\lambda_{eff} = \Delta\lambda_{REF} = \Delta\lambda_{P1} = \Delta\lambda_{P2}$. Spectrum at each of these positions were measured with an OSA. Initial findings indicate that these small variations are due to dispersion of wavelengths in SM fibre and transmission band of two directional couplers used. We therefore able to conclude that:

- (a) In total noise power measurement, we observe a linear trend in shot noise regime for detector power up to 1.8 mA evaluated over an electrical bandwidth of 100 kHz. Noise power is a measure of photocurrent fluctuation in photo detector due to noise from the source.
- (b) Shot noise power is independent of laser linewidth ($\Delta\nu_{eff}$), thus a narrowband source (e.g. SLD) at 35nm and a broadband supercontinuum source (e.g. SuperK Extreme) at 200 nm makes no difference to current fluctuation at PIN diodes. Shot noise increases as we increased our amplifier bandwidth.
- (c) Excess photon noise is inversely proportional to optical bandwidth. With a 150 nm broadband source such as the EXR9, we can expect four times lower in total noise power compare to a 35nm SLD. Our results proved this was the case.
- (d) SNR measurement gives an in-sight into noise in OCT system. With a time domain interferometer, we observed that at similar reference arm power ($P_{REF} > 150\mu\text{W}$), the low-noise supercontinuum SuperK EXR9 gives slightly better SNR than SLD and two other supercontinuum sources, SuperK EXR9 and VERSA, when imaged with a sample of surface reflectivity $R > 0.3$.
- (e) Independent of optical bandwidth used, we showed that SuperK EXR9 gives better SNR in OCT imaging than two other supercontinuum sources (Versa and EXR20). We therefore verified the low-noise claims from NKT Photonics.

3.1.6 Summary of statistical noise

In the analysis of noise power, we provide an in-sight into basic physical quantities that affect optimisation of an OCT system using both coherent and incoherent optical sources and detection techniques. We began by analysing the photocurrent flow in directional coupler, deriving the equations from electric field to optical power, to show how noise power can be evaluated from the AC current fluctuation with optical couplers with different coupling efficiency. We have discussed thermal noise, shot noise and excess photon noise. We demonstrated that thermal noise is generated by instability in electrical circuitry of the photo detector and the resistor. Shot noise, on the other hand is due to quantum fluctuation of electrons at detector input that follows the Poisson statistical distribution of mean-square fluctuation (MSF) $\langle \Delta n \rangle = \langle n \rangle$. The third noise term, excess photon noise (EPN), is caused by beatings of various Fourier components in an optical spectrum. EPN follows the Bose-Einstein probability distribution of MSF $\langle \Delta n \rangle = \langle n^2 \rangle$. An additional term called beat noise was introduced to include partially coherent light signal and its reflectivity coefficient into the total noise calculation. A comparison of various techniques employed to improve SNR were discussed. These techniques include deliberately attenuating reference arm power with an iris to reduce saturation, and to unbalance photo detector system.

We have also analytically shown that despite an increase in the bandwidth of optical sources $\Delta\lambda$ (or $\Delta\nu$ in optical frequency), the upper limit of the SNR could not be extended further due to some of these main factors: (a) fibre-end stray reflections, (b) incoherent spectral bandwidth of signals, and (c) non-overlapping in time of spectral powers deviation from both arms of the interferometer that resulted in reduced interference fringes. It is also evident that by employing ultra-broadband optical sources such as the white light supercontinuum (SC) source from NKT Photonics can only marginally improve the SNR. However, this approach requires the SC source to be operating at its full power (100%). Nevertheless, we also discovered that by using a fibre-based OCT system, our ability to manipulate the source optical bandwidth for a gain in SNR is dependent on the transmission band of fibre couplers in use. A narrow band coupler is not suitable for systems running on SC sources, not only from the bandwidth perspective, but also due to various noise it generates. A complete redesign of the broadband coupler is therefore necessary, and should be a priority for the next project.

3.2 Polarisation and noise in long pulse supercontinuum

Long pulse supercontinuum (SC) light sources have traditionally been ignored when considered for optical coherence tomography (OCT) [16] owing to their poor noise performance. In the last decade, SC sources have made inroads into other fields of study, such as optical metrology [17], chemical sensing [18], fibre sensor technology [19] and white light trapping [20]. During these periods, super luminescent diodes (SLD) and tuneable lasers such as swept sources have been widely adopted by OCT developers [21]. However, many of these light sources struggled to provide sufficient optical bandwidth needed to response to the increasing demand for high axial resolution imaging, especially in the non-conventional wavelength range [22-23]. As recently, the use of SC sources have made a comeback again on tomography imaging and high-resolution OCT with SC has again been researched [24]. This time around, the main argument for SC wasn't on RIN, but the promising imaging results SC sources can deliver, based upon its wider optical bandwidth and higher power [25] than any other light sources.

We believe that the future of OCT relies heavily on the successful development of a low-noise version of the SC source, and ability to exploit the polarization effects delivered by these high performance sources. Recently, a simulation model has shown polarization dependent output power at longer wavelengths [26]. However, this was not experimentally verified in their later tests and is yet to be observed [27]. Nevertheless, an earlier study using direct time-domain measurements of the amplitude statistics has concluded that pulse to pulse stability depends on the pump power and input polarization [28]. We also note that, as early as 1995, polarization effects resulting in spectral broadening in weakly birefringent micro-structured fibre (MSF) had been investigated [29], with these tests later repeated for its highly birefringent counterpart [30]. For these reasons, we have initiated a comprehensive study on SC in three areas of interest: polarization extinction ratio (PER), polarization changes [31] in a nominally non-birefringent photonic crystal fibre (PCF), and polarization dependent relative intensity noise (RIN). Birefringence is an important area to investigate in SC generation as it provides important information on wave propagation in fibre that could transform polarization states and polarization-mode coupling [32]. We evaluated the birefringent profile of the output SC beam by using different nonlinear fibre lengths (3m and 10m, model SC-5.0-1040, NKT Photonics).

3.2.1 Polarisation extinction ratio characterisation

The schematic diagram of the first measurement set-up is shown in Fig. 3.2.1. A commercial long pulse broadband supercontinuum (SC) white light source (SuperK Extreme, NKT Photonics, Denmark) with a pulse repetition frequency (PRF) of 80 MHz and pulse duration of 5 ps is used for this experiment. The source consists of a pump laser unit and a non-linear fibre (NLF) of initial length 8.5 m. A test bench is set-up for the measurement in the following order: The output beam from the NLF is fed into a collimating lens (CL) and through a broadband double Glan-Taylor Calcite polarizer (350-2300 nm, Thorlabs) mounted on a manual rotation mount. The polarizer is used to select the two orthogonal polarization components of light from the SC source. The selected light is sent into an integrating sphere (INTS) and detected by an optical spectrum analyser (OSA). The integrating sphere is an essential part of the system set-up. Light from free space is collected at the input port of INTS and collected by a multimode fibre. The multiple reflections in the INTS scramble the polarization and spatial distribution of the light while ensuring a spectrally flat collection of the light. Therefore, the variation of polarization as function of wavelength is negligible. Two different models of OSA were used, one for short wavelengths (model AQ6315A, 350-1750 nm, ANDO, Japan) and another for long wavelengths (model AQ6375B, 1200-2400 nm, Yokogawa, Japan). For long wavelength measurements, a long pass filter (LPF) of cut-off wavelength 1250 nm was placed after the polarizer to filter out the spectrum folding effect that arises from the limited free spectral range of the AQ6375B.

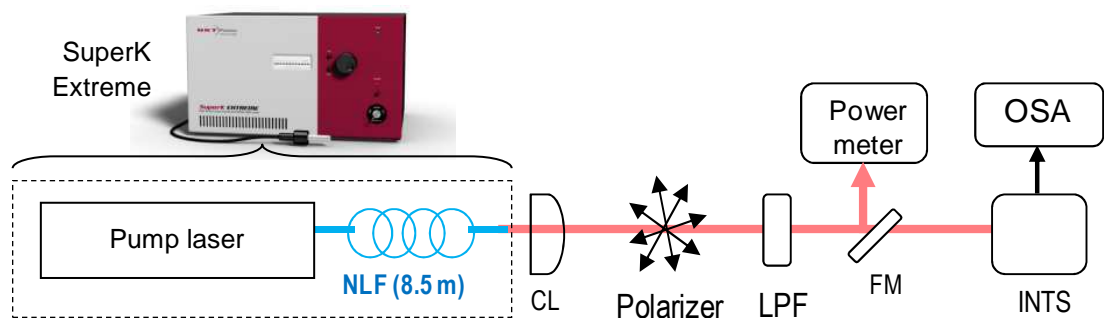


Fig.3.2.1 Experimental set-up for polarization extinction ratio measurements for a long-pulse supercontinuum system (NLF: nonlinear fibre of initial length 8.5 m, CL: lens collimator, LPF: long pass filter used with the longer wavelength OSA only, FM: flip mirror, INTS: integrating sphere, OSA: optical spectrum analyser)

Full wavelengths spectral data (450-2400 nm) for all measurements was collected in two stages, and then concatenated. First, a visible OSA was used to collect spectrum from 350-1750 nm. Subsequently, an IR wavelength OSA was used for range 1200-2400 nm. The data from IR OSA is scaled to spectral power obtained with visible OSA at five points: 1250 nm, 1350 nm, 1450 nm, 1550 nm and 1650 nm, to bring the IR OSA spectrum to overlap the visible OSA spectrum to an error of less than 0.05 dB. For power measurements, a flip mirror (FM) was placed along the beam path to send the light into a DC coupled thermal sensor power detector (10A-P, Ophir Optronics). Power reference measurements are performed for each spectrum taken with the OSA, and serves as the baseline to our spectrum calibration, i.e. stitching of two sets of spectral data. Power references are also important for different cases of wavelength dependent optimizations to be discussed in Sec. 3.2.1.1 to 3.2.1.3.

To verify our measurement reproducibility, we rotated our NLF to rotate the polarizations measured, and repeated our PER measurement to rule out PER artifacts from the set-up. We also induced stress to the NLF by first un-curving it, then bending it to small radius (<1 cm) and re-measured the PER for each case. This did not affect our result and thus verified that the PER of the output was not caused by coil-induced birefringence. We finally indirectly raised the fibre core temperature by changing the pulse duty cycle, using a pulse picker to operate our source from 2 to 80 MHz, with constant peak power to test the condition when higher average power was heating up the NLF, and repeated the PER measurements. This also did not change our results and thus verified that the PER was not caused by thermally related effects [33]. Appendix A1 shows the results of SC stability test to rule out measurement inaccuracies. Finally, it should be noted that although this paper only describes the study of a single SC sourced based on a particular fibre, very similar effects were measured on other SC sources made with the same NLF design but with another section of fibre as well as on SC sources using a different NLF design. The findings are therefore expected to be general for picosecond generated SC sources.

When one discusses PER of a light source one necessarily has to define a reference axis for the polarization. Since the fibre was nominally non-birefringent and the orientation between the fibre and the polarized pump system was unknown there was no obvious way to define this. Three definitions of the first axis of PER in our SC source have been identified: total spectral power (Sec.3.2.1.1), maximum power at pump wavelength (Sec.3.2.1.2) and maximum power at 1950 nm – the presumed long/red edge of the SC spectrum (Sec.3.2.1.3). Four different NLF lengths were also used: initial 8.5 m, 7.5 m, 4.5 m and 1 m. The other axis of PER is always set at 90° orthogonal to the first axis.

3.2.1.1 Optimisation to total power

We initially fixed our first axis of PER characterization to the polarizer angle that allowed the maximum total spectral power, as this is the method normally used for a narrow band laser. Polarizer angles for the maximum (P_{\max}) and minimum (P_{\min}) powers were determined by measuring the total power, and are here-in referred to as maximum and minimum polarizations, respectively. We began our measurement of PER using a NLF of length 8.5 m. To clearly illustrate the PER variation with pump power, we recorded our SC spectrum at three power levels (30%, 60% and 100%) for both maximum and minimum polarizations, and plotted $PER = P_{\max} [\text{dB}] - P_{\min} [\text{dB}]$, in Fig.3.2.2. The measured optical power after the polarizer for two polarisations is shown in Table 3.2.1.

Table 3.2.1 Measured total spectral power for three different pump power levels.

Polarization	Pump power levels		
	30%	60%	100%
Max	480 mW	1150 mW	1.5 W
Min	285 mW	650 mW	850 mW

Several deductions can be made from this data. First, we observed that for each power level, there is no PER in the visible part of the SC spectrum. Second, at the pump wavelength (1060 nm), PER decreases with increasing power of the pump laser. Specifically, when the pump power was increased from 30% to 60% then 100%, we obtained PER at the pump corresponding to 4.95 dB, 1.63 dB and 0.96 dB, respectively. When focusing only on the long wavelength range, we see a clear PER for all power levels and recorded maximum $PER > 10$ dB at the long edge of each SC spectra, for each power setting. One noticeable feature is that when pump power is increased, it pushes the PER further out into the red edge. The changing PER with increasing peak power clearly indicates that the PER is one of the effect of the nonlinear processes involved in the SC generation and not solely due to passive effect of the fibre or setup. One effect that could cause PER is the soliton self-frequency shift (SSFS), a consequence of Raman self-pumping that continuously red-shifts a soliton pulse, as reported in [34-37]. As Raman Gain is polarization dependent. SSFS could result in higher PER in the wavelength vicinity where it is present.

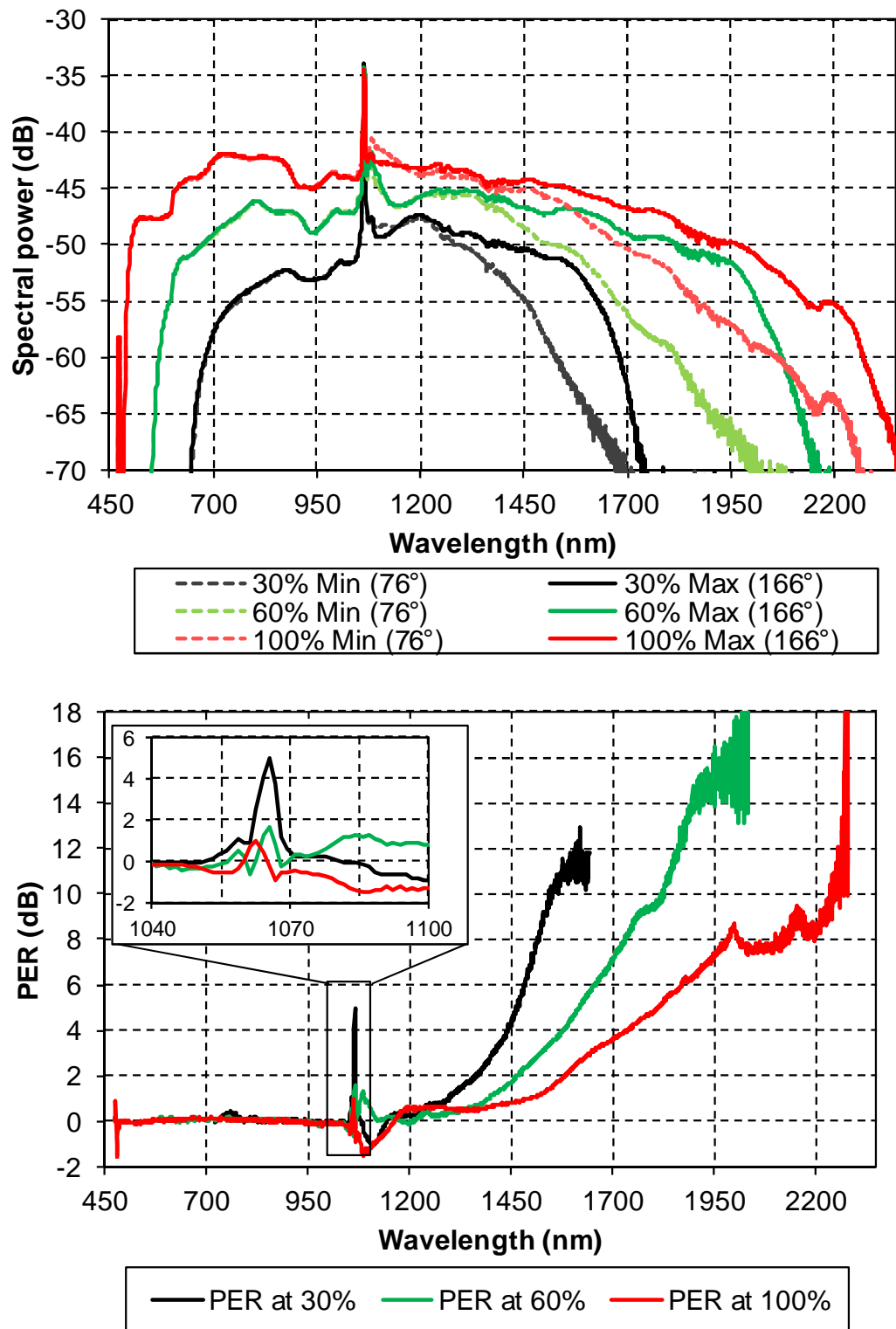


Fig.3.2.2 Experimental results for full length nonlinear fibre of 8.5 m. (Top) Two polarizations for each measured power level (30%, 60%, and 100%). (Bottom) PER for three pump power levels.

We extended our experiment to demonstrate the evolution of PER as a function of length, cutting back the NL fiber to 8.5 m, 4.5 m, and 1.5 m, successively, and repeating the previous measurements. In the PER measurements shown in Fig.3.2.3, solid lines show the maximum polarisation (P_{\max}), while dotted lines at minimum polarisation (P_{\min}). The minimum power is the lasing threshold where SC generation begins.

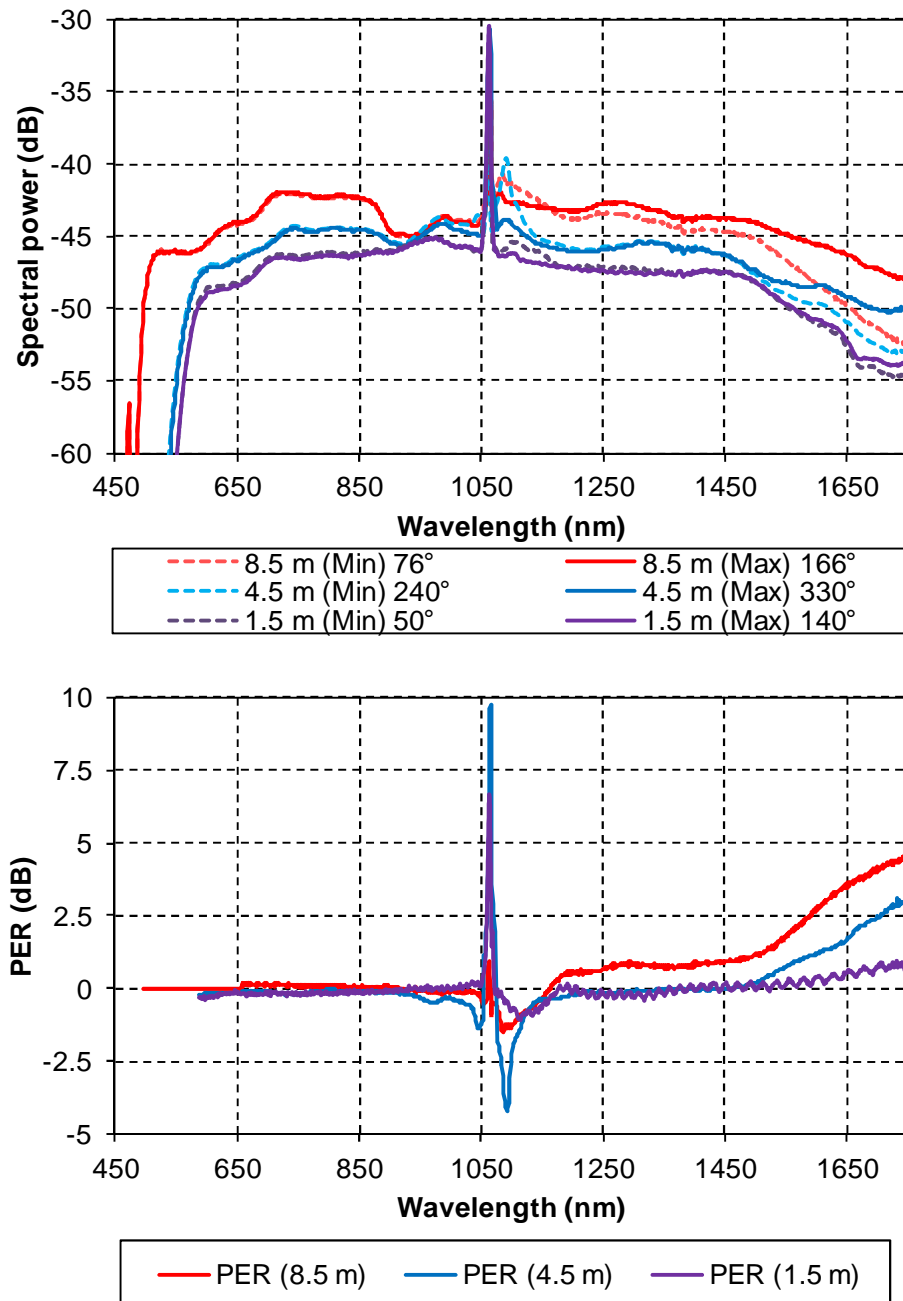
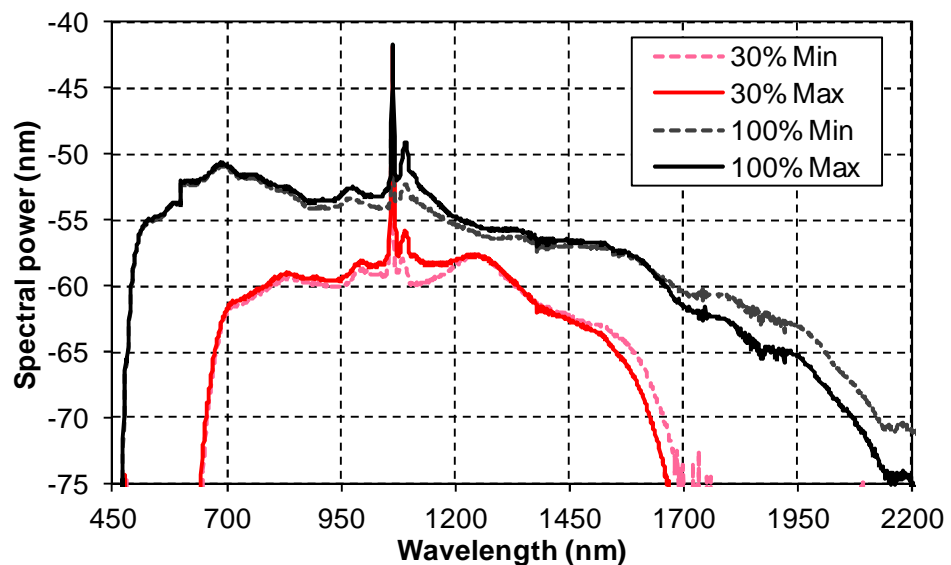


Fig.3.2.3 Experimental results for three fibre lengths of 8.5 m, 4.5 m and 1.5 m at full pump power (100%). Top figure shows spectrum of two polarizations (max, min). Bottom figure shows measured PER for spectrum to the yop figures.

At full pump power, we recorded a reduction in long wavelength PER with decreasing nonlinear fibre length. At the full length of 8.5 m, we recorded PER of 4.86 dB, followed by 2.8 dB (4.5 m) and 0.7 dB (1.5 m). Similar to the power measurement in Fig.3.2.2, we observed no PER in the visible part of the spectrum. However, on the long wavelength edge, we observed that the PER decreases as NLF length is cut back. It is worth noting that this correlation is highly dependent on the absolute signal power available on the long edge.

3.2.1.2 Optimisation to maximum pump wavelength (1064 nm)

As mentioned, the NLF was nominally non-birefringent. This is critical, as if it was truly non-birefringent the only introduction of PER should come from the PER of the pump, meaning the natural reference axis for PER would be the polarization angle which contained the maximum of amount of transmitted pump light. This was however not the angle that contained the maximum amount of total spectral power in our measurement. Therefore, a second analysis was made where the first axis was defined by the maximum pump power, with respect to the polarization rotation angle. A secondary spectrum (for minimum power) is recorded by turning the polarizer at 90° orthogonal to the reference position. Fig.3.2.4 illustrates measurements for PER with reference to pump power. These measurements were only carried out for fibre lengths of 4.5 m and shorter. We can compare the difference in PER measured using total spectral power and power referenced to the pump. Note that the negative PER in Fig.3.2.4 occurs after 1300 nm, and PER at the pump is 4.5 dB higher for the low pump power (30%).



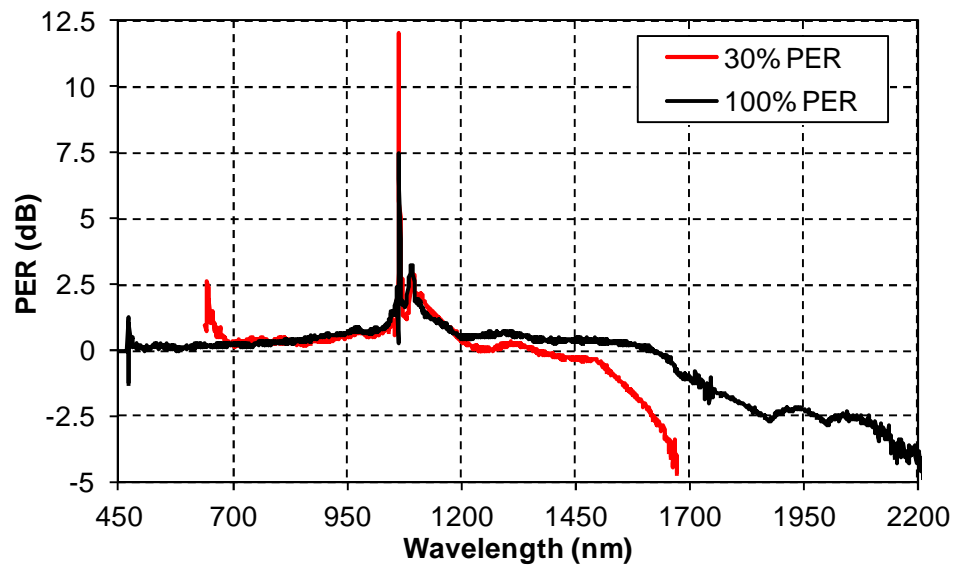


Fig.3.2.4 Experimental results for 4.5 m non-linear fibre length at high 100% and low 30% pump power. All power measurements are referenced to pump wavelength at 1064 nm.

Top figure shows spectrum of two polarizations (max, min). Bottom figure shows measured PER for spectrum to the top figures.

3.2.1.3 Optimisation to maximum power at red edge (1950 nm)

The last method of evaluation is based on the assumption that the nominally non-birefringent fibre actually has birefringence which affects the SC generation process and thus affects spectral broadening in one axis. It is then assumed that this effect from the fibre would become clearer the further one was from the pump wavelength. For this reason, the third method defines the first axis as the polarizer angle that transmits most light at the longest wavelengths: We shifted our measurement point to the spectrum red edge at 1.5 m fibre length, where detectable spectral power remains at 10 dB above noise floor. We found 1950 nm to be a good candidate on two basis:

- (a) SC spectrum at 100% pump power covers this wavelength, and
- (b) PERs at 100% obtained using two former optimizations are sufficiently larger at 1950 nm than at all shorter wavelengths other than the pump.

Measurement results at 1950 nm for 1.5 m fibre are plotted in Fig.3.2.5 and 3.2.6, with PER optimizations described in Sec. 3.2.1.1 and 3.2.1.2.

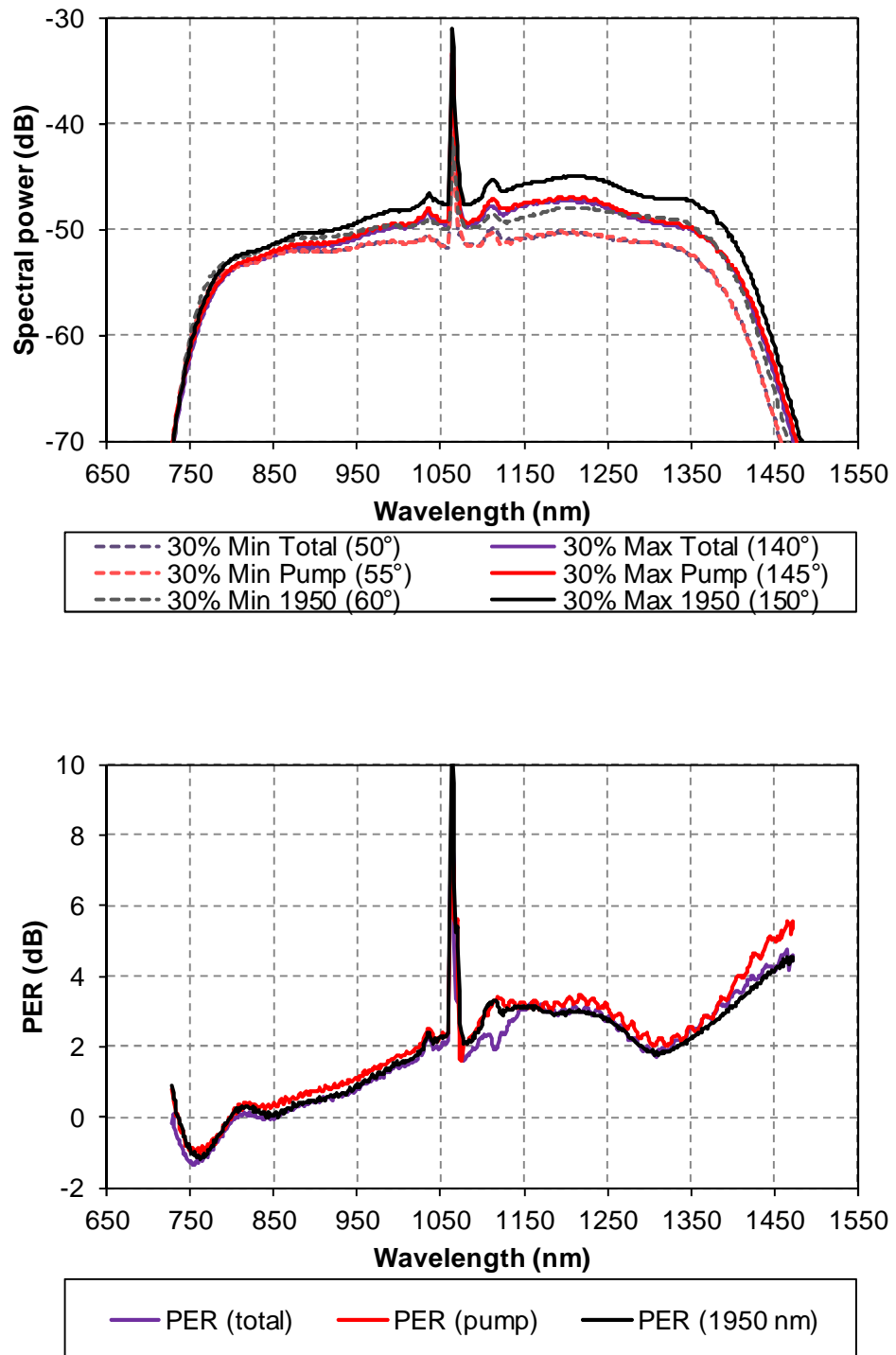


Fig.3.2.5 (top) spectra, (bottom) PER for 1.5 m NLF length at low power levels (30%) for three optimisations.

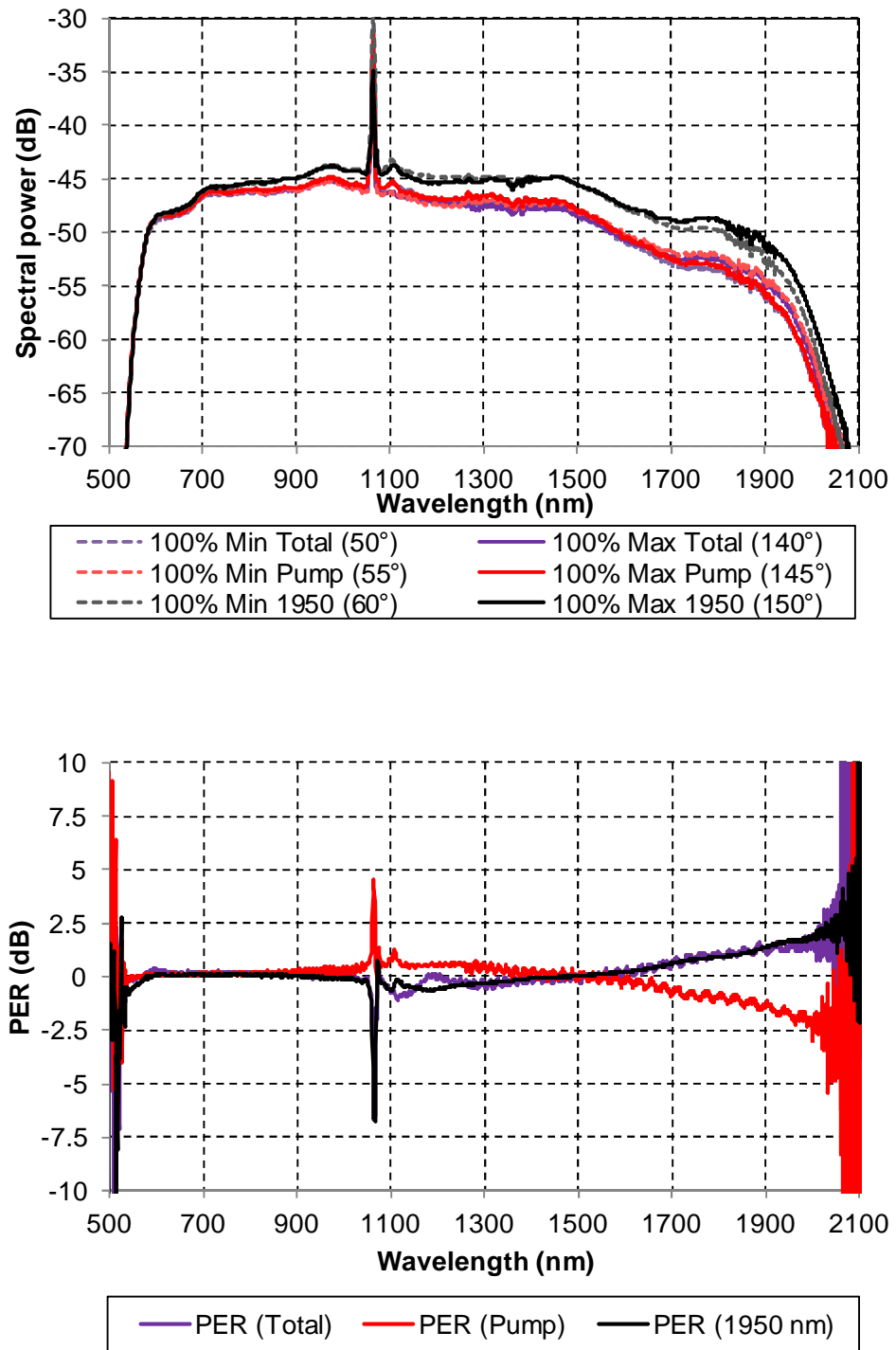


Fig.3.2.6 (top) spectra, (bottom) PER for all three optimisations with NLF length at 1.5 m at full pump power.

3.2.2 Fibre birefringence

Birefringence (or double refraction) is an important area to investigate in SC generation as it provides important information on wave propagation in fibre that could transform polarization states and polarization-mode coupling [38-40]. We evaluated the birefringent profile of the output SC beam by using different nonlinear fibre lengths (3 m and 10 m, model SC-5.0-1040, NKT Photonics). The NLF used was as mentioned nominally non-birefringent and no asymmetries in its structure were visible when it was inspected under a microscope however, as a PER was apparent in the output it was decided to measure the birefringence of the fibre. A separate test bench in Fig.3.2.7 was set-up for this purpose. We used a nanosecond SC source (SuperK Compact, NKT Photonics) that has a tuneable PRF, and a wider SC spectrum at much lower average power (40 mW, 22 kHz, 500-2200 nm) than the SC source used in the SC polarisation measurements, to eliminate the mal-effect in the coupling. The output of this SC source was released into free space while collimated, passed through Polarizer 1 where a linear vertical polarization was selected, and then recoupled into nonlinear fibre with an achromatic lens. Polarizer 2 was rotated at 45° orthogonal to Polarizer 1 along the beam optical axis, to obtain interference fringes at the output OSA. Interference patterns were recorded, and analysed.

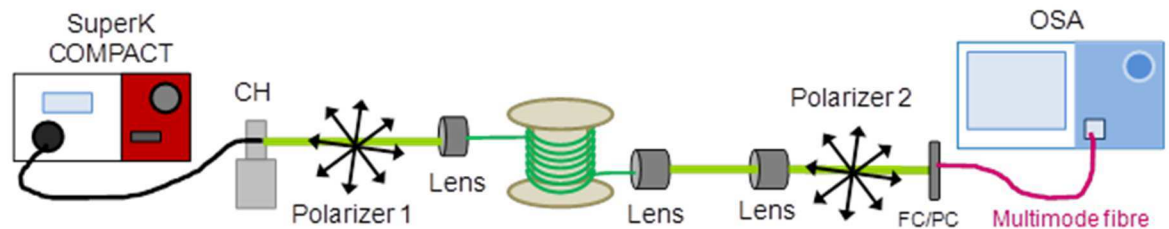


Fig.3.2.7 Schematic diagram for birefringence measurement of nonlinear fibre (CH: fibre to free-space collimator holder, thick horizontal line: free-space beam path, fibre spool: nonlinear fibre of lengths 3 m, 10 m, and 30 m, FC/PC: fibre connector, OSA: optical spectrum analyser)

A reference spectrum in Fig.3.2.8 was obtained without Polarizer 2 in place (see Fig.3.2.7), where the transmission spectrum of only linearly polarized light was recorded. Polarizer 2 was then inserted and rotated to produce maximum contrast interference fringes. Spectra for 3 m and 10 m fibres were recorded. The corresponding beat length B was calculated using Eqn. 4 [38-39],

$$B = \frac{2(\Delta\lambda)^2}{\lambda_{m+1} - \lambda_m} \quad (4)$$

where λ_m and λ_{m+1} are the wavelengths at proceeding and succeeding minima, and $\Delta\lambda$ is the midpoint between two minima. The relationship between beat length and birefringence is shown in Appendix A2.

The final n values for each case were obtained by dividing B to the fibre length (in meters) [41]. Measurement of broadband birefringence was particularly challenging due to the wide bandwidth of interest. To reduce chromatic aberrations in the coupling lenses, we performed two separate measurements covering two spectral bands: one for 750-1150 nm and another for 1150-1550 nm. Two spectra were then concatenated to produce Fig.3.2.8. The spectra (all three curves) in Fig.3.2.8 (top) showed a reduction in signal strength after 1450 nm. This observation was to be expected as it is in agreement to our earlier statement regarding chromatic aberrations. To obtain a full spectrum up to 2400 nm, one could theoretically extend the birefringence measurement above 1450 nm with a long wavelength OSA, and repeat the same measurement below 750 nm, and then subsequently concatenate the resulting spectra. However, our main aim here was to test for change in birefringence with different length of NLF, not solely on wavelength per se. From our measurement results, we see that the interference fringes recorded for $L=10$ m is roughly three times denser than $L=3$ m, and this observation is in good agreement with the fibre pitch-to-hole ratio found in the manufacturer's specifications. From the n plotted in Fig. 3.2.8 (bottom), we observed that the birefringence increases with wavelength, while remains low ($<10^{-5}$) for the entire SC spectrum range. It is therefore confirmed that the NLF we used for polarisation study is nominally birefringent.

Nevertheless, a full spectrum for 600-2200 nm was later recorded with two different OSAs: a short wavelength OSA for 350-1750 nm and longer wavelength OSA with a 1250 nm long pass filter for 1250-2200 nm. The longer range output were then concatenated together with the two shorter spectra, using the same procedure as in Sec.3.2.1, to produce Fig.3.2.9 for NLF length of 10 m.

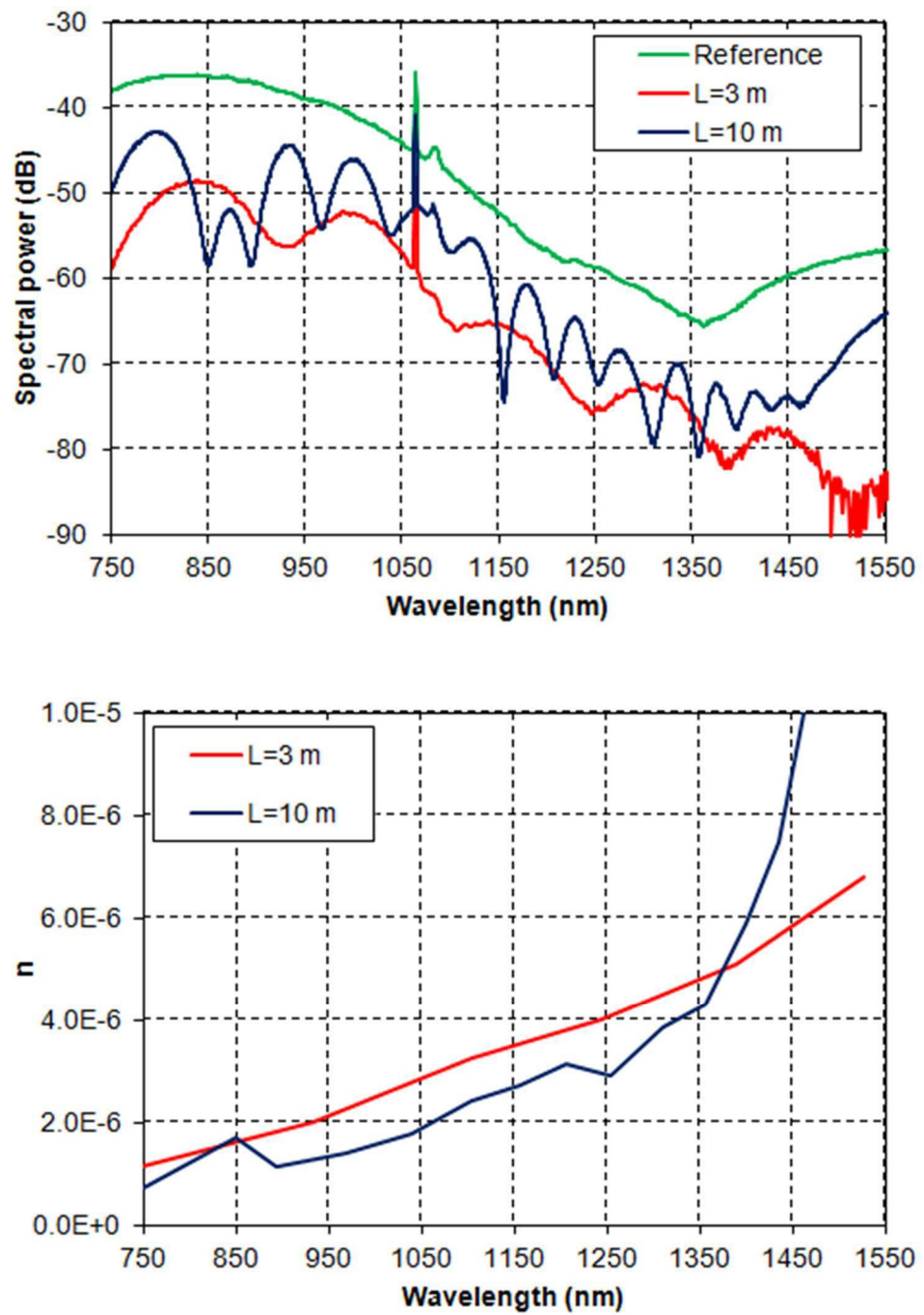


Fig.3.2.8 Birefringence measurement. (Top) Reference spectrum, and spectra of two fibre lengths with interference fringes. (Bottom) n values calculated using signal spectra in top figure.

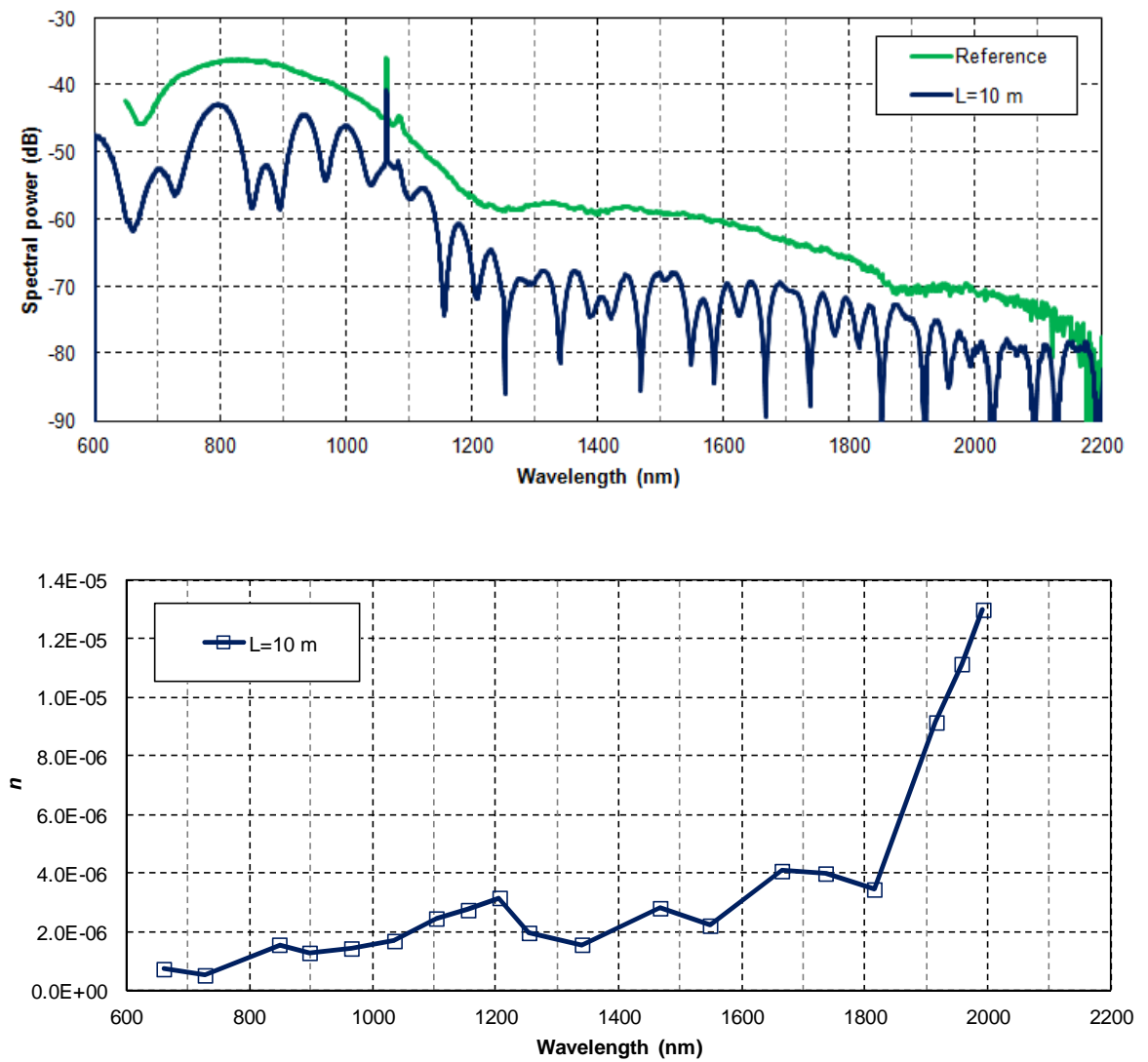


Fig.3.2.9 Full wavelength birefringence measurement. (Top) Reference spectrum and spectra of two fibre lengths with interference fringes. (Bottom) n values calculated using signal spectra in top figure

3.2.3 Polarisation relative intensity noise

A modification to the PER measurement system (Fig.3.2.1) is shown in Fig.3.2.10. To facilitate broadband RIN analysis, we used a BPF with a pass-band of 10 to 12 nm at full width at half maximum (FWHM), using 100 nm wavelength intervals between 500 nm and 1800 nm (FKB-VIS-10 and FKB-IR-10, Thorlabs). We have also studied the RIN of the two separate polarization components by looking into the spectral response. Three separate DC coupled photo receivers (PRs) were used [42]. They consisted of a UV/visible PR for measurement in 450-1000 nm, a near-IR PR for measurement in 1000-1600 nm (Si and InGaAs combined), and a long wavelength PR for measurement between 1600-2400 nm with an extended InGaAs receiver. The filtered signal is sent to a digital phosphor oscilloscope (model TDS5052B, 500 MHz, 5 GS/s, Tektronix, Oregon, USA). As the purpose of our measurement was to evaluate SC RIN performance for polarization OCT applications, we focused mainly within the spectral bands for visible wavelength OCT (650-950 nm) and long wavelength broadband OCT (1150-1600 nm).

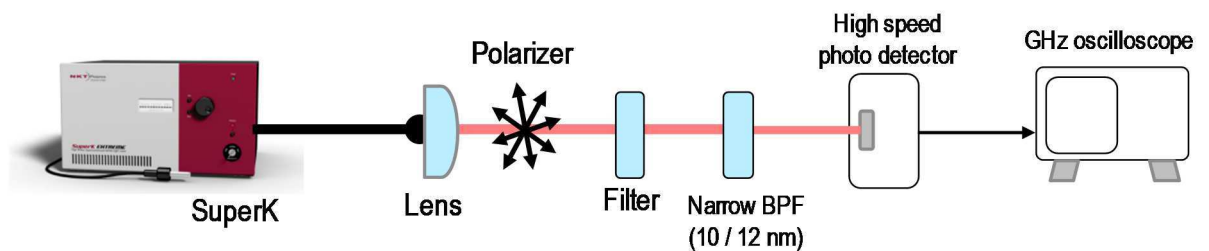


Fig.3.2.10 Experimental setup for pulse-to-pulse RIN measurement using a high-speed GHz oscilloscope, photo detectors and combination of band pass filters (BPF).

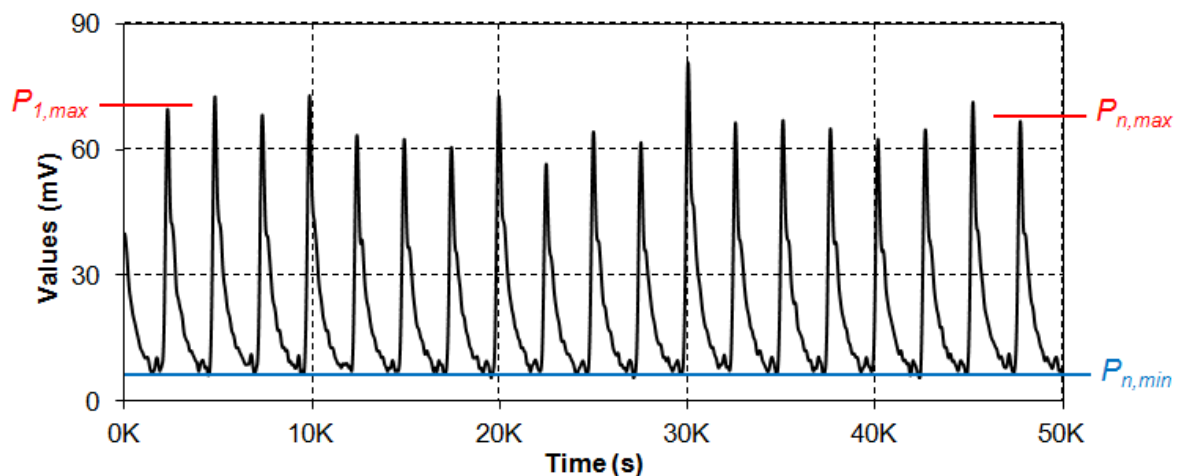


Fig.3.2.11 Pulse-to-pulse RIN amplitude measured with an oscilloscope and band pass filters.

Pulse-to-pulse signal fluctuations in Fig.3.2.11 were analyzed according to [43-45]. This was done by subdividing the oscilloscope time trace of an 80 MHz PRF source into time windows of 12.5 ns, to capture 800 individually separated pulses. We define a collection of pulses as $P_k = P_1, P_2, P_3, \dots, P_n$, where $P_1 = P_{1,max} - P_{1,min}$, $P_2 = P_{2,max} - P_{2,min}$, $P_3 = P_{3,max} - P_{3,min}$, \dots , $P_n = P_{n,max} - P_{n,min}$, up to $n=800$. $P_{n,min}$ and $P_{n,max}$ represent the minimum and maximum values, respectively, for the pulse in each window. Statistical analysis involves the calculation of sample average, \bar{p} and sample variance σ_p^2 using Eqn. 3.37 and 3.38 respectively. RIN for each case is calculated by dividing the variance to its mean, as shown in Eqn. 3.39 [46].

$$\bar{p} = \frac{1}{n} \sum_{k=1}^n p_k \quad (3.37)$$

$$\sigma_p^2 = \frac{1}{n-1} \sum_{k=1}^n (p_k - \bar{p})^2 \quad (3.38)$$

$$RIN = \frac{\sigma_p^2}{\langle p \rangle} \quad (3.39)$$

Higher order moments about the mean were calculated. The 3rd order and 4th order moments, skew (γ) in Eqn. 3.40 and kurtosis (κ) in Eqn. 3.41 [47], are used to evaluate the pulse-to-pulse noise distribution.

$$\gamma = \frac{\mu_3}{\sigma^{3/2}} = \frac{\frac{1}{n} \sum_{k=1}^n (p_k - \bar{p})^3}{\left[\frac{1}{n} \sum_{k=1}^n (p_k - \bar{p})^2 \right]^{3/2}} \quad (3.40)$$

$$\kappa = \frac{\mu_4}{\sigma^4} = \frac{\frac{1}{n} \sum_{k=1}^n (p_k - \bar{p})^4}{\left[\frac{1}{n} \sum_{k=1}^n (p_k - \bar{p})^2 \right]^2} \quad (3.41)$$

where μ_n is the expected value at n^{th} moment, σ is the standard deviation, \bar{p} is the sample average, k is the sequence of pulses (i.e. $k = 1, 2, 3, \dots, 800$), and n is 800. The data standardisation techniques used is shown in Appendix A4.

3.2.3.1 RIN

Independent to PER measurements performed in Sec.3.2.1, RIN was measured at two different polarizations when the maximum polarization was optimized to give the maximum total power after narrow band pass filtering (BPF). As we are only interested in relative intensity variation, we measured RIN on maximum and minimum transmissions by rotating the polarizer at 90° to each other, when recording the pulses from oscilloscope (Fig.3.2.10). The RIN measured here is essentially the pulse-to-pulse amplitude fluctuations. We calculated RIN at two polarizations for three cutbacks (8.5 m, 7.5 m and 4.5 m) on the same fibre used concurrently with all PER measurements. Based on RIN measurements in Fig.3.2.12 to Fig. 3.2.14, we observed similar noise evolution reported in [44]. However, our data showed that RIN is the same for two polarizations. We further verified that RIN is larger with lower pump power (30%), and that confirmed the technical understanding where low noise operation with these commercial sources is achieved when they are operating at full pump power (100%). We can assume that RIN at different power levels is largely dependent on the different stage of SC generation, dominated by Raman or nonlinear processes, which could be modelled theoretically [48] in our future work. For RIN measurements, the polarization angles used are referenced to the optimisation at total spectral power, as in the case of PER measurement.

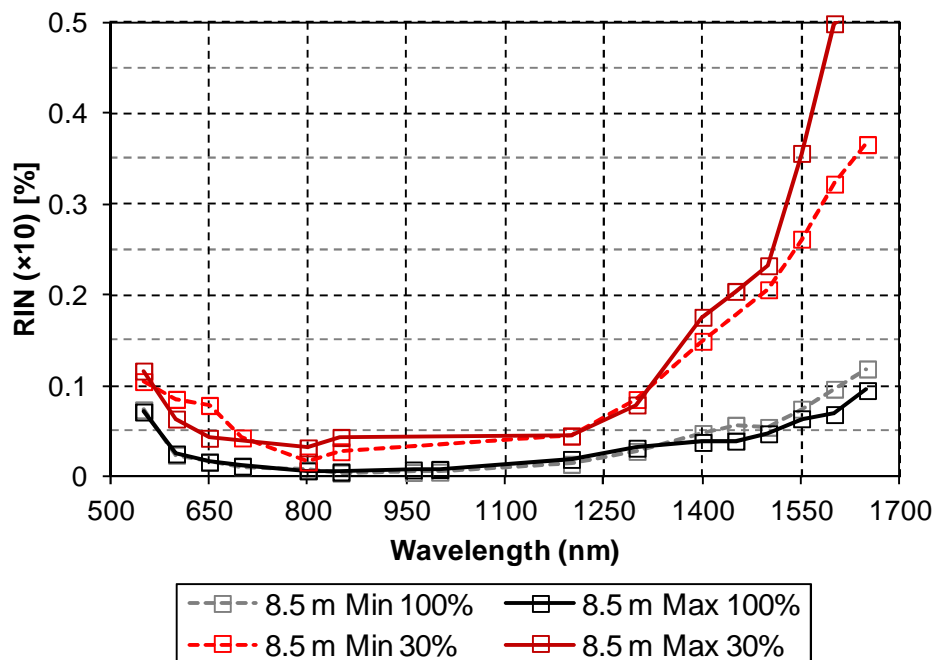


Fig.3.2.12 RIN measured at two power levels (100% and 30% for NLF length at 8.5 m.

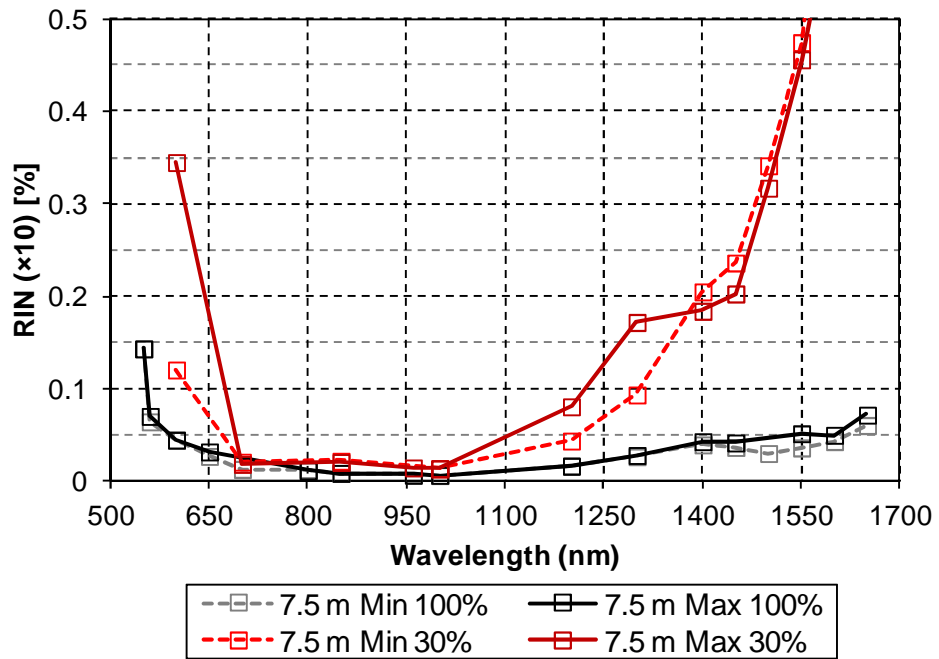


Fig.3.2.13 RIN measured at two power levels (100% and 30% for NLF length at 4.5 m).

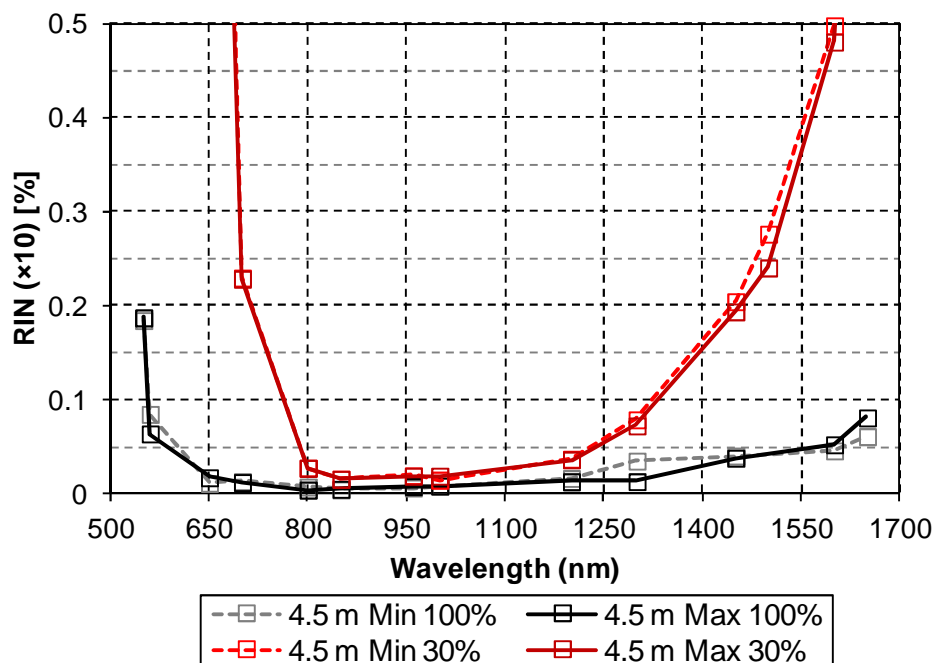


Fig.3.2.14 RIN measured at two power levels (100% and 30% for NLF length at 1.5 m).

Nevertheless, one interesting observation in Fig.3.2.12 when we operated the measurement with full length NLF, the RIN at both polarisations began to diverge at the long wavelength edge (>1500 nm). The divergence recorded is larger when we pumped with low seed power (30%) as opposed to full power (100%). No significant difference in RIN was observed for two other NLF lengths at 7.5 m and 4.5 m. This phenomenon can be explained further with the intensities histogram discussed in the following sub-section.

3.2.3.2 Pulse height histogram

The use of pulse height histogram to evaluate peak intensity statistics allow us to interpret the distribution of local maxima of noise amplitudes that emerge randomly with low probability, commonly dubbed as “rogue waves” [46,49-57]. Rogue waves are an extremely rare event, but their occurrences usually accompanied by an unexpected surge in signal amplitude that can cause destructive effect to system stability. Optical rogue wave (or rogue soliton) was initially used to describe extreme fluctuations in oceanic waves, but has now widely used to study noisy processes in optics that exhibit long-tailed probability distributions. One of those areas is the production of rare pulses of broadband light during the SC generation process when a NLF or a PCF is used. The noise in this rare process can be measured by the excess intensities or PSD at the spectrum edge. These rare events have been experimentally and analytically demonstrated to follow a long-tailed or L-shaped statistics. The SC generation process can be extremely sensitive to noise, thus the process exhibits high level of instability when pumped with a long pulse picosecond laser. For that reason, the occurrence of rogue waves indicates this instability is partly due to pulse modulation and the lack of pulse-to-pulse coherence.

To construct our histogram distribution, we needed to first determine our bin size k . To do to that, we use the Sturges’ formula (Eqn.3.42)[58], which was originally derived from a binomial distribution and unconditionally assumes that the frequency distribution to be Gaussian (symmetric). It may not be the case when rogue waves are present. The only condition for Sturges’ formula to work correctly is to have a sample size > 30 . As we have $n=800$ pulses analysed at each instance, the accuracy issue should not be a great concern.

$$k = \lceil \log_2 n \rceil + 1 \quad (3.42)$$

where n is the sample size, and the bracelet denotes the ceiling function.

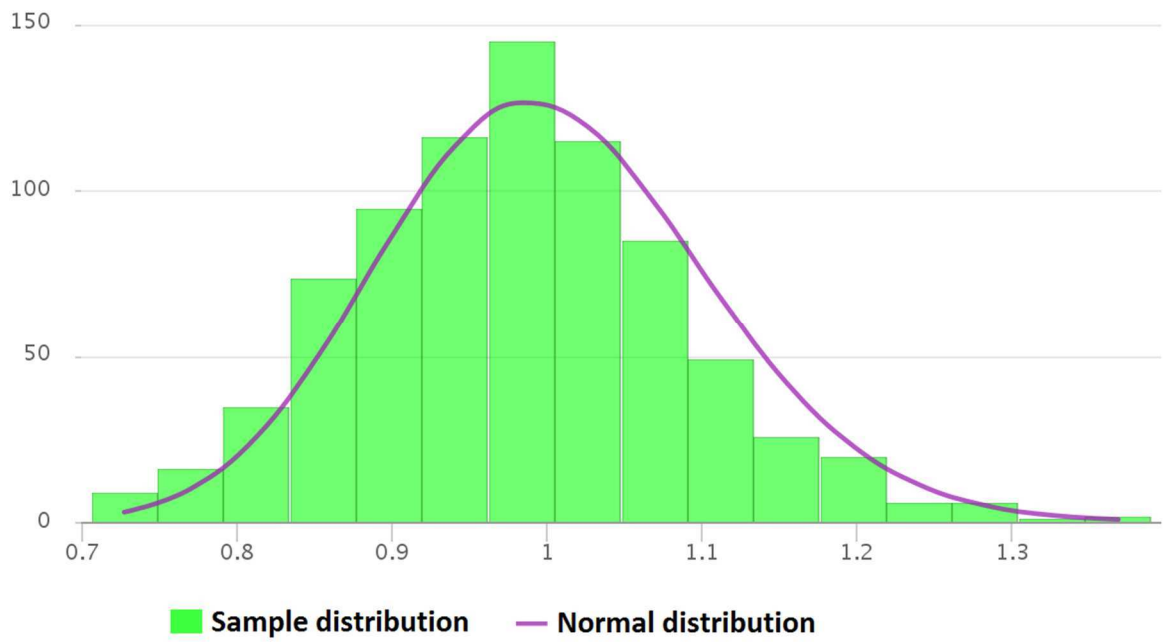


Fig.3.2.15 Near-Gaussian symmetric probability distribution for RIN measured at 1000 nm (BW 10 nm) on polarisation axis optimised to maximum total power (P_{\max}).

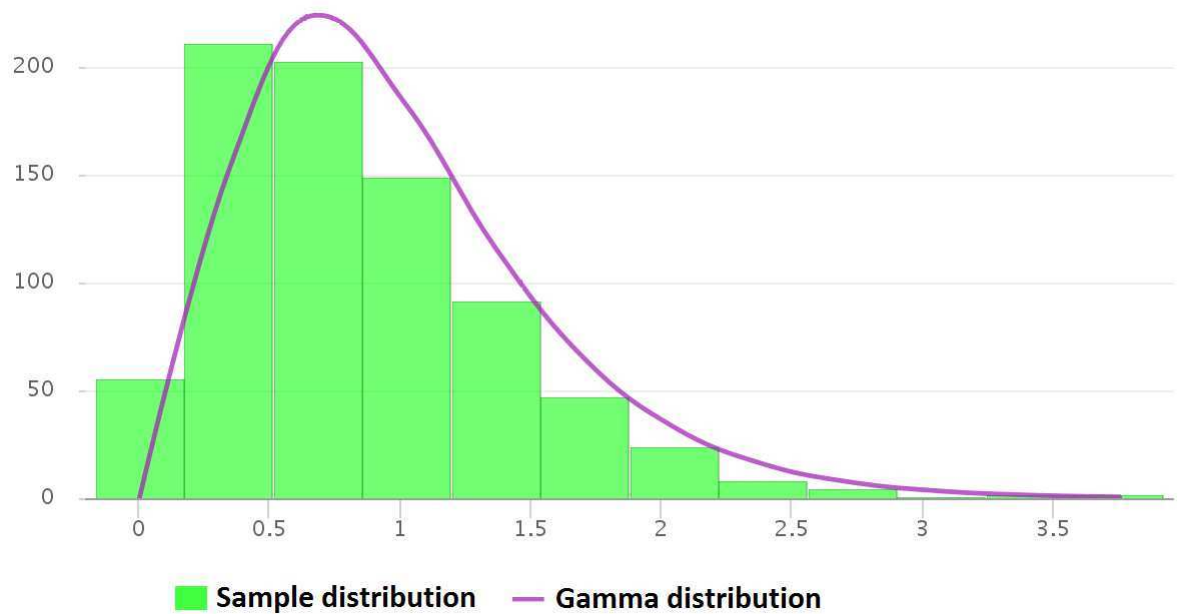


Fig.3.2.16 Long-tailed probability distribution for RIN measured at 1500 nm (BW 12 nm) on polarisation axis optimised to maximum total power (P_{\max}).

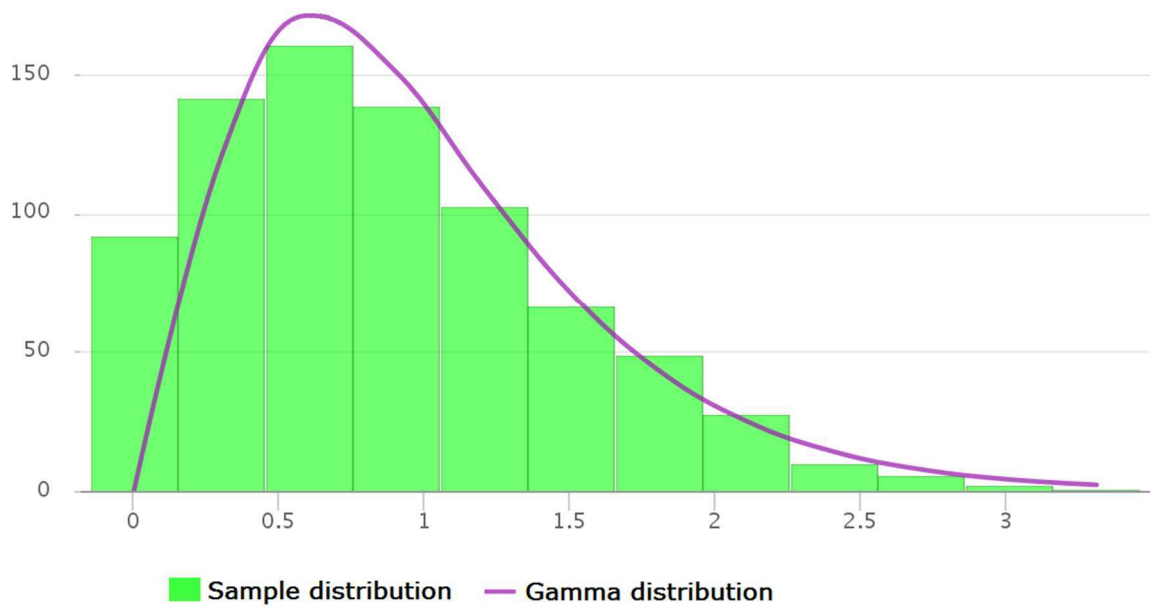


Fig.3.2.17 Long-tailed probability distribution for RIN measured at 1650 nm (BW 12 nm) on polarisation axis optimised to maximum total power (P_{\max}).

Since we were mainly interested in studying the dynamics of solitons collisions at the longer wavelengths, we plotted in Fig.3.2.15 to 3.2.17 show histograms of the pulse energy fluctuations extracted over a 12 nm bandwidth at three wavelength ranges: 1000 nm, 1550 nm and 1650 nm. The use of histograms at specific wavelengths are useful to illustrate how statistics of pulse amplitude fluctuations can vary from symmetric patterns (Gaussian distribution overlay) near the pump (1000 nm) to long-tailed right-skewed (Gamma distribution overlay) that decay exponentially near the red edge of the SC spectrum (1500 nm and 1650 nm). In the former case, we can safely assume that near the pump, the pulse break up is dominated by modulation instability (MI). In the later case, around the long wavelength edge, the pulse dynamics is dominated by Raman soliton self-frequency shift (SFSS), as validated in our PER measurements in Sec. 3.2.1.1. The pulse intensity histogram for the full SC spectrum (including visible wavelength and the blue edge) is shown in Fig. 3.2.18.

Another way to analyse the extreme events in a spontaneous MI-driven SC generation is to look at the higher-order statistical moments, such as skew and kurtosis. Sorensen et al [46] has shown that the skew-kurtosis product ($\gamma \cdot \kappa$) is a useful indicator of the presence of rogue wave like dynamic behaviour.

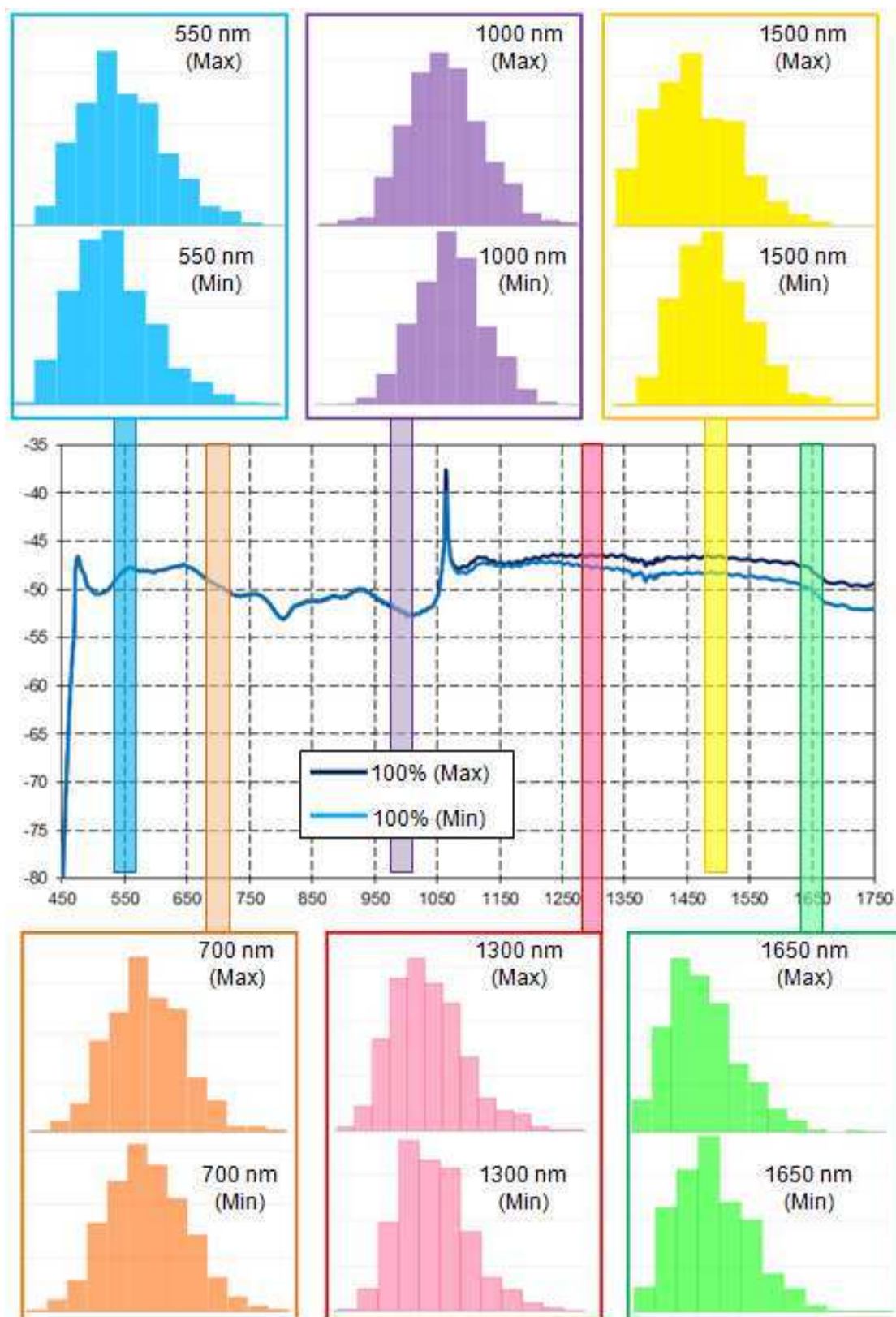


Fig.3.2.18 Pulse height histograms at selected wavelengths optimised for two polarisation components (P_{\max} and P_{\min}) on full SC power (100%).

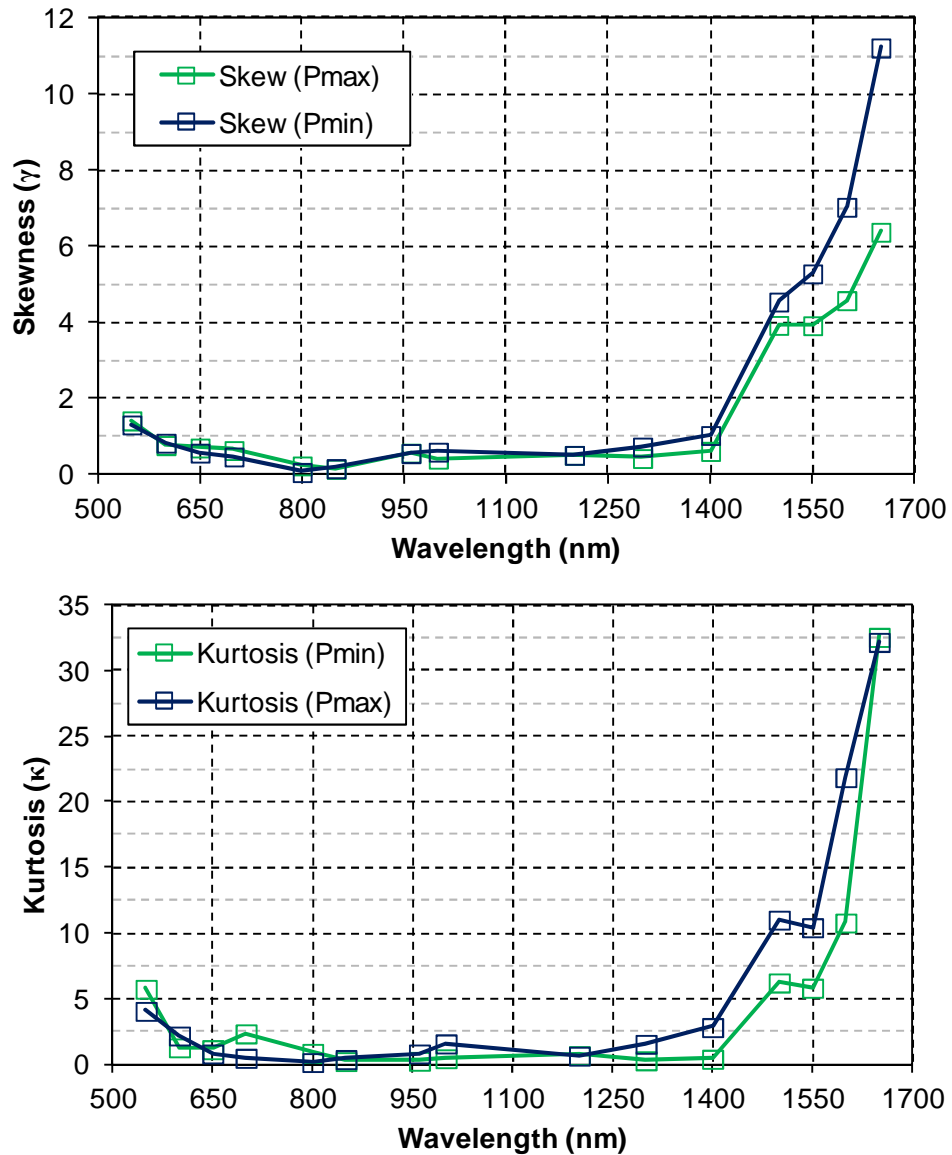


Fig.3.2.19 Skew and kurtosis calculated from intensity histogram for two polarisation directions at full SC power (100%).

Table 3.2.2 Skew and kurtosis calculated for polarisation with highest power (Pmax).

Wavelength (nm)	Skew (γ)	Kurtosis (κ)	Product ($\gamma \cdot \kappa$)
550	1.42	4.08	5.7936
850	0.16	0.41	0.0656
1000	0.42	1.61	0.6762
1300	0.43	1.56	0.6708
1500	3.93	11.03	43.3479
1650	6.38	32.19	205.3722

We have chosen six wavelengths of interest, and tabulate the values of skew and kurtosis in Fig.3.2.19 into Table 3.2.2. If the pulse intensity histogram exhibits a perfectly Gaussian distribution function, we shall obtain zero for both skew and kurtosis [46,49]. However, our results have shown that it is not the case. For wavelengths in the vicinity of the pump (between 850 nm and 1300 nm), we recorded the lowest values for both parameters. Likewise from the histogram data, we observed that the pulse intensity fluctuations are low. This is an indication that the noise characteristics in these wavelength regions are dominated by low amplitude pulses generated through spontaneous MI [46,48]. However, at the spectral red edges, the pulse intensity fluctuations became significant as evidenced from long-tailed (non-Gaussian) [59] histogram statistics, and this dynamics can be attributed to stimulated Raman scattering (SRS), where red-shifted solitons were first ejected from the pump pulse, and then underwent collisions in the Raman gain regime [46, 51-54]. Solitons collisions also caused dispersive waves to be generated in the blue edge of the SC spectrum [49,51,56], and this event can be seen by the right-skewed histograms extracted at 550 nm, while the increase in skew and kurtosis were recorded at this wavelength. On the other hand, the rogue wave event had been observed at 1500 nm and 1650 nm, when the pulse dynamics become dominated by extreme sensitivity to peak power variations, as evidenced in the excess value of skew-kurtosis product ($\gamma \cdot \kappa = 43.35$ at 1500 nm and $\gamma \cdot \kappa = 205.37$ at 1650 nm). These values are in good agreement to the simulation data performed by [46], where they had previously shown that the skew-kurtosis product > 10 yields rogue wave event during SC generation process.

Our measurement and analysis subsequently verified earlier findings on the long-tailed statistical distribution that the optical rogue waves were originated from the amplification of noise in the MI process, while the pump pulse experienced Raman induced SSFS, wave-breaking process results in spectral broadening as these solitons propagate down the long PCF, and as pulse-to-pulse fluctuations become significant, the stability SC generation is subsequently affected. Several methods to control strong pulse amplitude fluctuations and harness rogue waves have been proposed [60-63] in order to improve the noise performance of a SC source.

3.3 Polarisation noise in OCT applications

In standard narrowband lasers PER is easy to quantify and its cause is generally relatively simple to explain if one knows how the laser is constructed. However, due to the complex nature of SC generation processes and the resulting wide spectrum, polarization properties of produced SC are hard to quantify, characterize and explain. This is perhaps the reason why this field has not previously been explored in detail. In all three measurement optimizations in Sec.3.1, we observed significant PER around the pump. This is expectable 1060-1070 nm as the fibre is short and the polarized pump is not expected to be completely scrambled by the nonlinear fibre. It is however interesting that the PER at the pump is reduced at higher pump powers. There are also some polarization effects around 1100 nm which is the region where the Raman gain from the pump and the modulation (MI) gain both have peaks [29,37,64-65]. As the Raman effect is polarization sensitive it is not unexpected to see PER effects here. We would have expected to find the majority of the light generated around 1100 nm is in the same axis as the majority of the pump light as the Raman Gain is stronger to the same polarization than to the opposite polarization. However while the measurements consistently show some PER in this region there is no clear trend as to whether the majority of the light around 1100 nm is in the same axis as the pump or the opposite. Further from the pump i.e. >1200nm we see a PER which consistently increase with wavelength but decreases or is pushed to longer wavelengths with longer fibre and/or higher peak power. This region is the part of the spectrum which is generated by solitons which red-shift from the MI region through the Raman caused soliton self-frequency shift effect [35]. The reason the increasing PER with wavelength could be that the polarization sensitivity of the Raman effect gradually “cleans up” the polarization of the solitons polarization as they red-shift, however this would not explain why PER then decrease with fibre length and increasing power. Another theory could be that the highest power solitons for some reason is generated in one polarization axis of the fibre and that the birefringence of the fibre is strong enough to keep them in that axis and that the longest wavelengths which correspond to the strongest solitons are thus always birefringent [66]. It is also worth noting that although clear PER effects are visible in the long wavelength part of the spectrum there was little or no PER at wavelengths shorter than the pump which is surprising as it is well known that the solitons at the long wavelength edge of the continuum are responsible for the shifting of light to the shortest wavelengths.

Our investigation concluded that there can be clear PER on the long wavelength edge of picosecond generated SC from nominally non-birefringent silica PCF. We demonstrate that some parts of the spectrum shows stable PER of over 10 dB, when measured with reference to total spectra power. Specifically, wavelength of high PER occurred only in the immediate vicinity of the pump wavelength, and for increasingly longer wavelengths. We experimentally investigated how the spectrally resolved polarization develops with increasing power, NLF length and wavelength, through the measurement of spectra and RIN analysis. We found that there is no significant difference in the RIN of the two polarizations and that at normal operating conditions i.e. long fibre and high power. The source has negligible PER in the spectral bands typically used for OCT (650-950 nm and 1150-1550 nm). This report therefore validates the SC sources from NKT Photonics A/S for use in polarization sensitive OCT applications within with optimal low-RIN performance and some PER.

The other effect we have seen with our measurement is polarisation selection. Since we are using a commercial light source, the NLF was assumed to be PM. Depending on orientation of polarisation axis we assume the NLF to be non-birefringent. However, results in Sec.3.2 showed the NLF to be nominally birefringent ($<10^{-6}$). We also observed the change of PER reduces as fibre length decreased, and is valid for all fibre lengths we measured. This indicates it is not due to confinement loss or any polarising effect as both axes lose power [48]. It is worth noting the change in PER at the pump wavelength. With shorter fibre, there is a systematic trend that PER reduction is significant away from pump. First, we showed that the same signed PER is obtained when total power measurement is used. In this case, the pump doesn't move, regardless of pump power. It appears that some changes happen at longer wavelength. At low power, the maximum axis becomes minimum axis, as evidenced in Fig.3.2.6. This can be consists of the superposition of the supercontinua generated along each polarisation axis [66]. Second, the PER is fixed at the pump. This is because everything measured around pump is a nonlinear process. Therefore it is the principle fibre axis orientation that results in self-induced polarisation changes [67], thus higher PER. Third, PER increases with pump power at longer wavelengths. Higher power induces greater Raman self-frequency shift (SFS) on solitons, causing them to experience greater red-shift. Forth, we observed the birefringence increases with wavelength. This could be attributed to pulse walk-off that reduces the polarisation interaction length, resulting in pulses in two polarisation axes stopped interacting [66].

We do not propose to explain the clear PER effects that we have measured SC generation process are simply too complex to do so with any certainty. The general understanding of how supercontinua are generated have emerged gradually over nearly a decade of comparison of measurements and increasingly detailed simulations. However measurements have generally focused on the visible wavelength of the supercontinua and appear to have over looked these PER effect on the long wavelength edge. Meanwhile most simulations have generally assumed ideal perfectly non-birefringent fibres and often only modelled the evolution of a single evolution. It is therefore expected that considerable effort will be needed before these PER effects can be fully explained.

On the noise studies, we are unable to make new conclusion on the polarisation dependency. However, the use of higher order moments about the mean, such as skew and kurtosis, allows us to at least quantify the noise at different regions of the spectrum. Our results have preliminarily validated the earlier claims from Moller et al that RIN is low around the pump, and increase in a parabolic way for wavelengths further out to the spectral edges. Nevertheless, we can only observe a minor variation in noise from our pulse height histogram (PHH) statistics, for the two polarizations. Our long tailed probability distribution did show little difference in PD-RIN at different pump power. Without these rigorous analysis, these variations are too little to be noticed experimentally, and to our understanding, these effect will be insignificant to general SC operations or when used in imaging applications such as OCT.

Our investigation concluded that the degree of polarisation varies at edge of the spectrum in nominally non-birefringent silica PCF. We demonstrate that some parts of the spectrum shows stable PER of over 10 dB, when measured with reference to total spectra power. Specifically, wavelength of high PER occurred only in the immediate vicinity of the pump wavelength, and for increasingly longer wavelengths. Region where PER appears is dependent on power and fibre length. We experimentally verified how the spectrally resolved polarisation develops with increasing power and along the length of the NLF, through the measurement of birefringence and pulse to pulse RIN analysis. The experimental results are compared to numerical simulations of coupled polarisation states mimicking the experimental conditions. This report therefore validates the SC sources from NKT Photonics A/S for use in polarisation-sensitive OCT applications within two spectral bands (650-950 nm and 1150-1550 nm) with optimal low-RIN performance and some PER. The results we published are to be used to assist in future simulation to explain our findings.

References

1. W. V. Sorin and D. M. Baney, "A simple intensity noise reduction technique for optical low-coherence reflectometry," *IEEE Photonics Tech. Lett.*, vol. 4, no. 12, pp. 1404-1406, 1992.
2. K. Takada, "Noise in optical low-coherence reflectometry," *IEEE J. Quantum Elec.*, vol.34, pp. 1098-1108, 1998.
3. A. Rollins and J. Izatt, "Optimal interferometer designs for optical coherence tomography," *Opt. Lett.*, vol. 24, pp. 1484-1486, 1999.
4. R. C. Haskell, D. Liao, A. E. Pivonka, et al., "Role of beat noise in limiting the sensitivity of optical coherence tomography," *J. Opt. Soc. Am. A*, vol. 23, no. 11, pp. 2747-2755, 2006.
5. L. Mendel, "Interference and the Alford and Gold effect," *J. Opt. Soc. Am. A*, vol. 52, no. 12, pp. 1335-1339, 1962.
6. S. A. Dyer, *Wiley survey of instrumentation and measurement*, Wiley-IEEE Press, pp. 459-461, 2004.
7. C. C. Rosa and A. Gh. Podoleanu, "Limitation of the achievable signal-to-noise ratio in optical coherence tomography due to mismatch of the balanced receiver," *Appl. Opt.*, vol. 43, no.25, pp. 4802-4815, 2004.
8. A. Yariv, *Optical Electronics*, 4th ed., Saunders, Philadelphia, PA, pp. 520-529, 1991
9. M. Born and E. Wolf, *Principles of Optics*, 6th ed., Pergamon, Oxford, pp. 503-529, 1991.
10. R. Leitgeb, C. K. Hitzenberger, A. F. Fercher, "Performance of fourier domain vs. time domain optical coherence tomography," *Opt. Expr.*, vol. 11, no. 8, pp.889-894, 2003.
11. H. Hodara, "Statistics of thermal and laser radiation," *Proceedings of the IEEE*, pp. 696-704, 1964.
12. T. Yoshino, M. R. Ali, B. C. Sarker, "Performance analysis of low-coherence interferometry taking into consideration of beat noise," *J. Opt. Soc. Am. A.*, vol. 22, pp. 328-335, 2005.
13. E. A. Swanson, D. Huang, M. R. Hee, et al, "High-speed optical coherence domain reflectometry," *Opt. Lett.*, vol. 17, no. 2, 1992.
14. G. L. Abbas, V. W. S. Chan, T. K. Yee, "A dual-detector optical heterodyne receiver for local oscillator noise suppression," *J. Lightwave Tech.*, vol. LT-3, no. 5, pp. 1110-1122, 1985.
15. H. P. Yuen, V. W. S. Chan, "Noise in homodyne and heterodyne detection," *Opt. Lett.*, vol. 8, no. 3, pp.177-179, 1983.
16. J. Brown, S. Kim, and A. Wax, "Noise characterization of supercontinuum sources for low-coherence interferometry applications," *J. Opt. Soc. Am. A* 31, 2703-2710 (2014)
17. J. T. Woodward, A. W. Smith, C. A. Jenkins, C. Lin, S. W. Brown and K. R. Lykke, "Supercontinuum sources for metrology", *Metrologia*, 46(4) S277 (2009).
18. C. F. Kaminski, R. S. Watt, A. D. Elder, J. H. Frank, J. Hultm "Supercontinuum radiation for applications in chemical sensing and microscopy," *Appl. Phys. B* 92, 367-378 (2008).
19. S. Coen, J. D. Harvey, G. Genty, and J. M. Dudley, "Fiber Based Supercontinuum Sources for Optical Fibre Sensors," *OSA Technical Digest (CD)*, paper TuA2 (2006).
20. P. Wang et al., "White Light Trapping Using Supercontinuum Generation Spectra in a Lead-Silicate Fibre Taper," in *J. Lightwave Tech.* 32(1), 40-45 (2014).
21. W. Drexler, M. Liu, A. Kumar, T. Kamali, A. Unterhuber, R. A. Leitgeb, "Optical coherence tomography today: speed, contrast, and multimodality," *J. Biomed. Opt.* 19(7), 071412 (2014).

22. M. Yamanaka, T. Teranishi, H. Kawagoe, N. Nishizawa, "Optical coherence microscopy in 1700 nm spectral band for high-resolution label-free deep-tissue imaging," *Sci. Rep.* 6, 31715 (2016).
23. P. Bhatia, S. Choudhari, A. Rodrigues, M. Patil and R. Makkar, "High resolution imaging system using spectral domain Optical Coherence Tomography using NIR source," *IEEE Xplore (WiSPNET)*, 2212-2216 (2016).
24. You, C. Wang, Y. Lin, A. Zaytsev, P. Xue and C. Pan, "Ultrahigh-resolution optical coherence tomography at 1.3 μm central wavelength by using a supercontinuum source pumped by noise-like pulses," *Laser Phys. Lett.* 13, 025101 (2016).
25. W. J. Brown, S. Kim, A. Wax, "Noise Characterization of Supercontinuum Sources for Low Coherence Interferometry Applications," *J. Opt. Soc. Amer. A.* 31(12), 2703–2710 (2014).
26. Z. Zhu and T. G. Brown, "Polarization properties of supercontinuum spectra generated in birefringent photonic crystal fibers," *J. Opt. Soc. Am. B* 21(2), 249-257 (2004).
27. Z. Zhu and T. Brown, "Experimental studies of polarization properties of supercontinua generated in a birefringent photonic crystal fiber," *Opt. Express* 12(5), 791-796 (2004).
28. D. Solli and B. Jalali, "Direct Time-Domain Measurements of the Pulse Amplitude Statistics of a Fiber Supercontinuum Source," *CLEO Conference, OSA Technical Digest Series (CD) CMB3* (2007).
29. S. G. Murdoch, R. Leonhardt, and J. D. Harvey, "Polarization modulation instability in weakly birefringent fibers," *Opt. Lett.* 20(8), 866-868 (1995).
30. M. Tianprateep, J. Tada, and F. Kannari, "Influence of polarization and pulse shape of femtosecond initial laser pulses on spectral broadening in microstructure fibers," *Opt. Rev.* 12(3), 179-189 (2005).
31. S. Wabnitz, E. M. Wright, and G. I. Stegeman, "Polarization instabilities of dark and bright coupled solitary waves in birefringent optical fibers," *Phys. Rev. A* 41, 6415 (1990).
32. N. Hanik, Modelling of nonlinear optical wave propagation including linear mode-coupling and birefringence, *Opt. Comm.* 214(1), 207-230 (2002).
33. S. R. Domingue and R. A. Bartels, "Overcoming temporal polarization instabilities from the latent birefringence in all-normal dispersion, wavebreaking-extended nonlinear fiber supercontinuum generation," *Opt. Exp.* 21, 13305-13321, (2013).
34. H. Tu, Y. Liu, X. Liu, D. Turchinovich, J. Lgsgaard, and S. Boppart, "Nonlinear polarization dynamics in a weakly birefringent all-normal dispersion photonic crystal fiber: toward a practical coherent fiber supercontinuum laser," *Opt. Expr.* 20, 1113-1128 (2012).
35. J. M. Dudley, G. Genty, S. Coen, "Supercontinuum generation in photonic crystal fiber", *Rev. Mod. Phys.*(4). 78, 1135-1184 (2006).
36. V. L. Kalashnikov, P. Dombi, T. Fuji, W. J. Wadsworth, J. C. Knight, P. St. J. Russell, R. S. Windeler, and A. Apolonski, "Maximization of supercontinua in photonic crystal fibers by using double pulses and polarization effects," *Appl. Phys. B* 77(2-3), 319-324 (2003).
37. S. Coen, A. H. L. Chau, R. Leonhardt, J. D. Harvey, "Supercontinuum generation by stimulated Raman scattering and parametric four-wave mixing in photonic crystal fibers", *J. Opt. Soc. Am. B* 19(4) 753-764 (2002).
38. Y. Yang, W. Duan and M. Ye, "High precision measurement technology for beat length of birefringence optical fiber," *Meas. Sci. Technol.* 24, 025201 (2013)
39. P. Hlubina and D. Ciprian, "Spectral-domain measurement of phase modal birefringence in polarization-maintaining fiber," *Opt. Express* 15 (25), 17019-17024 (2007).

40. Y. Mizuno, Z. He and K. Hotate, "Polarization Beat Length Distribution Measurement in Single-Mode Optical Fibers with Brillouin Optical Correlation-Domain Reflectometry," *Appl. Phys. Express* 2 046502 (2009).
41. S. C. Rashleigh, "Measurement of fiber birefringence by wavelength scanning: effect of dispersion," *Opt. Lett.* 8, 336-338 (1983).
42. D. Derickson, ed., *Fiber Optic Test and Measurement* (Prentice Hall, 1998)
43. J. Ramsay, S. Dupont, and S. R. Keiding, "Pulse-to-pulse noise reduction in infrared supercontinuum spectroscopy: Polarization and amplitude fluctuations," *Laser Phys. Lett.* 11, 095702 (2014).
44. Y. Liu, Y. Zhao, J. Lyngsø, S. You, W. L. Wilson, H. Tu, "Suppressing short-term polarization noise and related spectral decoherence in all-normal dispersion fiber supercontinuum generation," *J. Light. Tech.* 33(9), 1814-1820 (2015).
45. U. Møller, S. T. Sørensen, C. Jakobsen, J. Johansen, P. M. Moselund, C. L. Thomsen, and O. Bang, "Power dependence of supercontinuum noise in uniform and tapered PCFs," *Opt. Express* 20, 2851-2857 (2012).
46. S.T. Sørensen, O. Bang, B. Wetzels, J.M. Dudley, "Describing supercontinuum noise and rogue wave statistics using higher-order moments," *Opt. Comm.* 285, 2451-2455 (2012).
47. H. Cramér, "Mathematical methods and statistics," Princeton Univ. Press (1999).
48. M. H. Frosz, "Validation of input-noise model for simulations of supercontinuum generation and rogue waves," *Opt. Express*, 18(14), 14778-14787 (2010).
49. Shanti Toenger, Thomas Godin, Cyril Billet, Frédéric Dias, Miro Erkintalo, Goëry Genty & John M. Dudley, "Emergent rogue wave structures and statistics in spontaneous modulation instability," *Sci. Rep.* 5, 10380 (2015).
50. C. Lafargue, J. Bolger, G. Genty, F. Dias, J. M. Dudley, and B. J. Eggleton, "Direct detection of optical rogue wave energy statistics in supercontinuum generation," *Electron. Lett.* 45, 217-219 (2009).
51. D. R. Solli, C. Ropers, P. Koonath, and B. Jalali, "Optical rogue waves," *Nature* 450, 1054-1057 (2007).
52. B. Wetzels, A. Stefani, L. Larger, P. A. Lacourt, J. M. Merolla, T. Sylvestre, A. Kudlinski, A. Mussot, G. Genty, F. Dias and J. M. Dudley, "Real-time full bandwidth measurement of spectral noise in supercontinuum generation," *Sci. Rep.* 2(882), 1-7 (2012)
53. C. Lafargue, J. Bolger, G. Genty, F. Dias, J. M. Dudley and B. J. Eggleton, "Direct detection of optical rogue wave energy statistics in supercontinuum generation," *Electron. Lett.* 45(4), 217-219 (2009).
54. A. Aalto, G. Genty, and J. Toivonen, "Extreme-value statistics in supercontinuum generation by cascaded stimulated Raman scattering," *Opt. Express* 18, 1234-1239 (2010).
55. K.L. Corwin, N.R. Newbury, J.M. Dudley, S. Coen, S.A. Diddams, B.R. Washburn, K. Weber, R.S. Windeler, "Fundamental amplitude noise limitations to supercontinuum spectra generated in a microstructured fiber," *Appl. Phys. B* 77(2-3), 269-277 (2003).
56. J. M. Dudley, F. Dias, M. Erkintalo, and G. Genty, "Instabilities, breathers, and rogue waves in optics," *Nature Photon.* 8, 755-764 (2014).
57. M. Erkintalo, G. Genty, and J. M. Dudley, "Rogue wave like characteristics in femtosecond supercontinuum generation," *Opt. Lett.* 34, 2468-2470 (2009).
58. H.O. Lancaster, "An Introduction to Medical Statistics," John Wiley & Sons (1974).
59. Y. E. Monfared and S. A. Ponomarenko, "Non-Gaussian statistics and optical rogue waves in stimulated Raman scattering," *Opt. Express* 25, 5941-5950 (2017)

60. D. R. Solli, C. Ropers, and B. Jalali, "Active Control of Rogue Waves for Stimulated Supercontinuum Generation," *Phys. Rev. Lett.* 101 (23), 233902 (2008).
61. J. M. Dudley, G. Genty, and B. J. Eggleton, "Harnessing and control of optical rogue waves in supercontinuum generation," *Opt. Express* 16, 3644-3651 (2008).
62. G. Genty and J. M. Dudley, "Route to Coherent Supercontinuum Generation in the Long Pulse Regime," *IEEE J. Quantum Electron.* 45(11), 1331-1335 (2009).
63. A. Kudlinski, B. Barviau, A. Leray, C. Spriet, L. Hélot, and A. Mussot, "Control of pulse-to-pulse fluctuations in visible supercontinuum," *Opt. Express* 18, 27445-27454 (2010).
64. S. Wabnitz, "Modulation polarization instability of light in a nonlinear birefringent dispersive medium," *Phys. Rev. A* 38, 2018-2021 (1988).
65. E. A. Golovchenko and A. N. Pilipetskii, "Unified analysis of four-photon mixing, modulational instability, and stimulated Raman scattering under various polarization conditions in fibers," *J. Opt. Soc. Am. B* 11(1), 92-101 (1994).
66. A. Proulx, J.-M. Ménard, N.Hô, J. Laniel, R. Vallée, and C. Paré, "Intensity and polarization dependences of the supercontinuum generation in birefringent and highly nonlinear microstructured fibers," *Opt. Expr.* 11(25), 3338-3345 (2003)
67. H. G. Winful, "Self-induced polarization changes in birefringent optical fiber," *Appl. Phys. Lett.* 47, 213-215 (1986).

4

Dispersion in OCT systems

High-resolution optical coherence tomography (OCT) has become increasingly common for non invasive imaging of three-dimensional (3D) microstructures and biological tissues, especially in ophthalmology [1]. The demand of commercial high-resolution imaging has increased in the last decade owing to improved capability to track sub-micron features and layered structures. The development of such systems requires the use of optical components with different glass thickness and densities. However, the presence of various glass materials of different refractive indices in an OCT configuration makes the phase velocity dependent on the wavelength of the excitation signal.

To achieve the theoretical axial resolution determined by the bandwidth $\Delta\lambda$ of the source, compensation for dispersion in the interferometer is essential. Dispersion occurs because the refractive index varies with the wavelength. Therefore, group velocity mismatch between different wavelength components in the spectrum leads to deterioration of the axial resolution, irrespective of the OCT method used: time domain, spectrometer-based (spectral domain) [2] or swept source based (Fourier domain) OCT systems [3]. Despite the widespread use of spectrometer-based and swept source-based methods. In recent times, time-domain OCT retains niche applications in microscopy, where high transversal resolution is achievable using high numerical aperture (NA) objectives [4].

For a time-domain OCT system, a typical compensation method, referred to here as the full-width at half-maximum (FWHM) method, is based on iterative adjustment of dispersion inserted into the interferometer until the FWHM of the autocorrelation function is minimised. This operation is time-consuming, as it requires repetitive procedures and easily prone to measurement errors. After each adjustment, there is no way to know in which direction to proceed, whether to add or reduce glass length to adjust the dispersion introduced by the optical components in the system. The classical procedure only aims at finding a minimum of the autocorrelation peak width.

We therefore present a better method to evaluate dispersion in time-domain interferometers. This method involves using a tuneable optical source in a broadband

range, a mirror placed in the object arm of the interferometer and measuring the relative position of the autocorrelation peak in optical path difference (OPD) versus the central wavelength of the tuneable source. The method is illustrated on a time-domain OCT systems. It is also applicable for Sp-OCT, SS-OCT and conventional FD-OCT.

Previous reports have documented the utilization of rods of SF11 glass [5] and of spectral delay lines for dispersion characterization [6–13]. Similar methods of dispersion compensation are illustrated here. In this chapter, we present a novel approach to use different BK 7 rod glasses to compensate for dispersion of a time-domain OCT system operating at 1300 nm.

4.1 Dispersion and coherence

4.1.1 Coherence

In low coherence interferometers with negligible dispersion, the theoretical limit for the axial resolution is determined by half of the source coherence length C_L . For a Gaussian spectral-shaped source spectrum, with λ the central wavelength and a FWHM bandwidth of $\Delta\lambda$, C_L is given by.

$$C_L \approx \frac{4 \ln(2)}{\pi} \frac{\lambda^2}{\Delta\lambda} \quad (4.1)$$

The inverse proportionality with $\Delta\lambda$ makes broadband light sources essential for achieving high axial resolution [1,5,6]. In recent years, broadband supercontinuum sources have been used extensively in many OCT applications. The larger the optical bandwidth, the shorter the coherence length. However, dispersion is manifest, as variation of index of refraction with wavelength becomes significant.. If dispersion is left uncompensated in the interferometer, the autocorrelation peak width of an A-scan measured using a mirror as object becomes wider, resulting in degradation of imaging resolution.

To study dispersion in optics, let us first consider a Gaussian shaped pulse, with an amplitude A_0 , angular frequency ω propagating along z -axis through a dispersive medium with a wave constant β as shown in Fig. 4.1. The general expression for this pulse can be written as in Eqn.4.2.

$$\begin{aligned}
A_0(z, t) &= \int d\omega A_0(\omega) \exp[j(\omega t - \beta z)] \\
&= \exp[j(\beta_1 \omega_0 - \beta_0)] \int d\omega A_0(\omega) \exp[j\omega(t - \beta_1 z)]
\end{aligned} \tag{4.2}$$

where β_1 is the wave constant of the pulse.

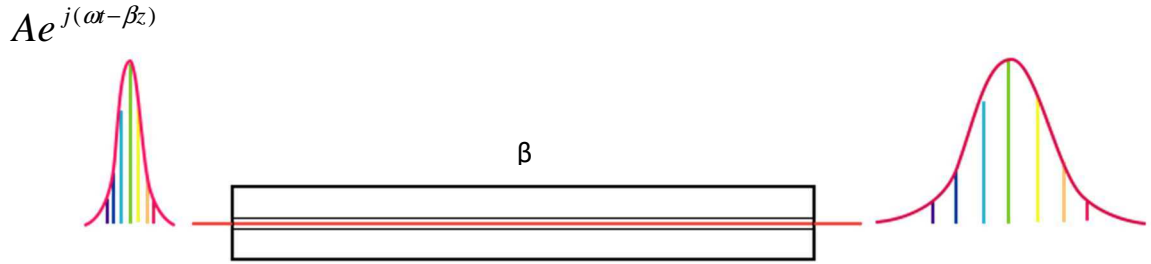


Figure 4.1: Illustration of broadening of FWHM of a pulse travelling through a dispersive medium.

4.1.2 Dispersion

Dispersion disperses a pulse in both space and time. To better understand these two effects, we can mathematically represent of angular dispersion, using as a time delay autocorrelation of the pulse. We can therefore write the expression in terms of wave number as in Eqns 4.3. Its dependence on the angular frequency is the dispersion.

$$\beta(\omega) = \beta_0 + (\omega - \omega_0)\beta_1 + \frac{1}{2}(\omega - \omega_0)^2 \beta_2 + \frac{1}{6}(\omega - \omega_0)^3 \beta_3 + \dots \tag{4.3}$$

$$\text{where } \beta_1 = \frac{d\beta}{d\omega} = \frac{1}{v_g} \tag{4.4}$$

$$\beta_2 = \frac{d^2\beta}{d\omega^2} = -\frac{\lambda^2}{2\pi c^2} \frac{d\beta_1}{d\lambda} = GDD \tag{4.5}$$

$$\beta_3 = \frac{d^3\beta}{d\omega^3} = \frac{\lambda^4}{4\pi^2 c^3} \left(3 \frac{d\beta_1}{d\lambda} + \lambda \frac{d^2\beta_2}{d\lambda^2} \right) = TOD \tag{4.6}$$

In the Eq. (4.3), the first term from the left denotes a constant phase β_0 . The second term describes time delay in the form of group velocity v_g . The third term defines group delay dispersion (GDD) as function of wavelength λ . The fourth and subsequent terms in the

Taylor series expansion denote third order dispersion (TOD) and higher order dispersions (HOD) respectively.

In our context of dispersion analysis, we calculate dispersion up to second order (GDD). The method presented here allows measurement of a parameter D ($\mu\text{m}^2/\text{nm}$) that represents the axial change in the autocorrelation peak position versus change in wavelength $\Delta\lambda$.

This can be evaluated as a slope of a fitting line over a graph of experimental data collected from the OCT system for different input wavelengths as shown in Fig. 4.2 below. The slope, D for different cases of dispersion is illustrated here.

From the definition of GDD we can write it as function of time and displacement:

$$GDD = \frac{\Delta t}{\Delta z} = \frac{\Delta z}{\Delta w} = 2\pi \frac{\Delta z}{\Delta \nu} \quad (4.7)$$

where Δt represents time, Δz displacement, Δw angular frequency and $\Delta \nu$ optical bandwidth.

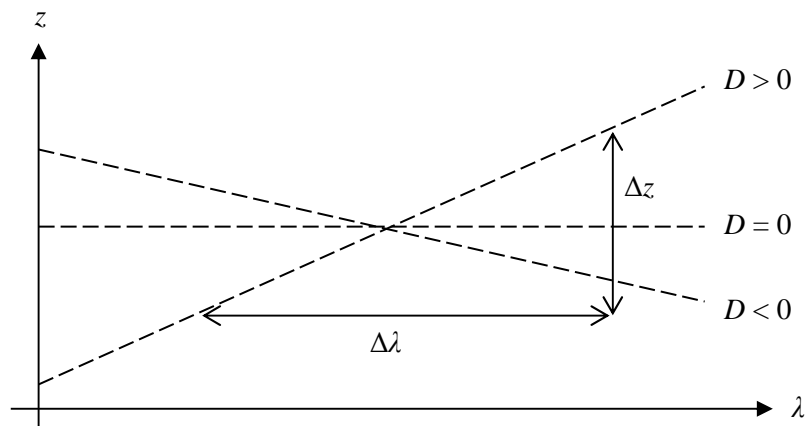


Figure 4.2: Dispersion slope as function of dispersion versus wavelength (Δz is the displacement, D is the dispersion, $\Delta\lambda$ is the optical bandwidth)

In the graph of Fig. 4.2 above, we experimentally measure two quantities Δz and $\Delta\lambda$. From the well known equation of $c = \nu\lambda$, we could relate $\Delta \nu$ to $\Delta\lambda$ by

$$\Delta \nu = \frac{c}{\lambda^2} \cdot \Delta\lambda \quad (4.8)$$

D in Fig.4.2 is connected to GDD in Eqn. 4.7 by

$$GDD = -\frac{D\lambda^2}{2\pi c^2} \quad (4.9)$$

4.1.3 Autocorrelation of a pulse

The definition of an autocorrelation function is shown in Eqn.4.10.

$$S(\xi) = \int_{-\infty}^{\infty} I(t)I(t-\xi)dt \quad (4.10)$$

where $I(t) = |E(t)|^2$ represents the temporal pulse intensity function, and $I(t - \xi)$ represents the intensity of time shifted replica of the pulse.

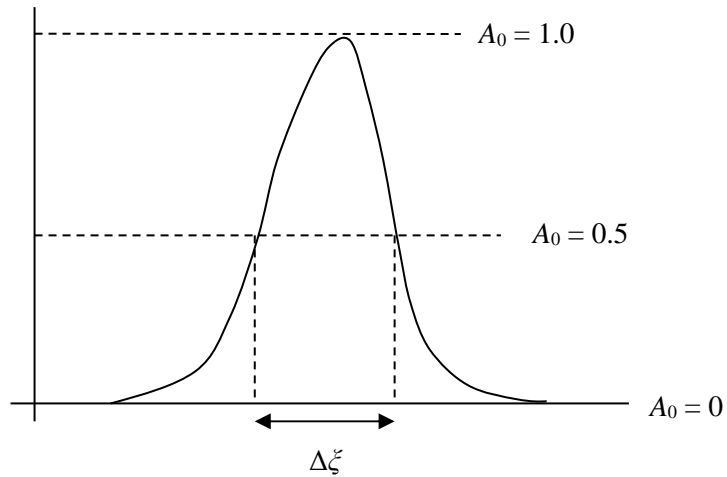


Figure 4.3: A Gaussian shaped pulse with FWHM indicated

Now, taking into account of pulse broadening effect due to dispersion, the corresponding change in FWHM of the pulse through a glass of thickness L can be assessed as function of dispersion length L_D as

$$\Delta\xi_{out} = \Delta\xi_{in} \sqrt{1 + \left(\frac{L}{L_D}\right)^2} \quad (4.11)$$

where

$$L_D = \frac{\Delta\xi_{in}^2}{4\ln(2) \cdot GVD} \quad (4.12)$$

Dispersion length is defined as the propagation distance after a pulse travels, the pulse width broadens by a factor of $\sqrt{2}$.

Therefore, the output temporal pulse autocorrelation function is:

$$\Delta\xi_{out} = \Delta\xi_{in} \sqrt{1 + \left(4\ln(2) \frac{GDD}{\Delta\xi_{in}^2} \right)^2} \quad (4.13)$$

$$\text{where} \quad GDD = L \times GVD \quad (4.14)$$

Finally, we have to relate the mathematical expression of acousto-optic tuneable filter (AOTF) method to the formulas derived for the method of measuring FWHM of autocorrelation function. To do that, we first need to evaluate n versus wavelength, and this is the dispersion problem. Let us now consider c is the speed of light, the inverse proportionality of coherence length ρ from C_L in Eq. (4.1), we define

$$\rho = \frac{\pi c}{\sqrt{2\ln(2)}} \frac{\Delta\lambda}{\lambda^2} \quad (4.15)$$

The shape of the autocorrelation function $S(\xi)$ [7,8] can be written as

$$S(\xi) = \frac{A_0^2}{\sqrt[4]{1+d^2}} \exp\left[-\frac{1}{2c^2} \frac{\rho^2 \xi^2}{1+d^2}\right] \quad (4.16)$$

where ξ is measured along the depth coordinate, and d defines the dispersion enlargement, related to the group delay dispersion (GDD) by.

$$d = \rho^2 GDD \quad (4.17)$$

The larger the GDD, the wider the A-scan peak. By expanding the terms for d we obtain

$$d = -D \frac{\Delta\lambda}{C_L} \quad (4.18)$$

To obtain the FWHM of the autocorrelation peak, we set the exponential term in Eqn.4.16 to 0.5, and solve for Eqns. 4.9, 4.16 and 4.17. The FWHM of the autocorrelation becomes

$$\Delta\xi = \frac{C_L}{2} \sqrt{1 + \left(D \frac{\Delta\lambda}{C_L} \right)^2} \quad (4.19)$$

By comparing two methods, AOTF measurement of D and FWHM of the autocorrelation peak, we can observe theoretically that as $|D|$ approaches zero from both positive and negative slope, $\Delta\xi$ becomes minimum.

In the following section, we will evaluate the benefits of AOTF method in comparison to FWHM method when it comes to minimising dispersion from both positive and negative D .

4.2 Methods to evaluate and reduce dispersion

As an optical tuneable source, a SuperK SELECT (NKT Photonics, Denmark) employing an acoustic optical tuneable filter (AOTF) is used. Light is emitted from an 80 MHz broadband supercontinuum (SC) source with a spectrum from 550 to 2400 nm, and 2 W visible power (SuperK Extreme EXR20, NKT Photonics). The SC output is then sent to the AOTF module. The AOTF acts as a narrowband optical bandpass filter, and combined with the SuperK, it emits a linewidth $\Delta\lambda$ as narrow as 5 nm at wavelength λ_m , tuned within two bands: 500–900 nm (visible) and 1150–2000 nm (NIR), as shown in Fig. 4.4. We refer to this procedure in the following as the AOTF method.

The AOTF module is a computer-controlled accessory attached to the main SC source (SuperK Extreme). The graphical user interface software (Super Kontrol 1.06b) as shown in Fig. 4.5 was used to facilitate the wavelength selection process. The software allows multiple advanced configuration of output selection, such as one to eight simultaneous filtered wavelengths output, and power level controls.

To compare the AOTF method with the classical method of FWHM measurement of the autocorrelation function, a spectral splitter (SuperK Split, NKT Photonics) is used. This allows transmission of a large optical bandwidth and measurement of the axial resolution for different conditions of dispersion adjustment. The value predicted by Eq. (4.1) is only achievable if dispersion is compensated for.

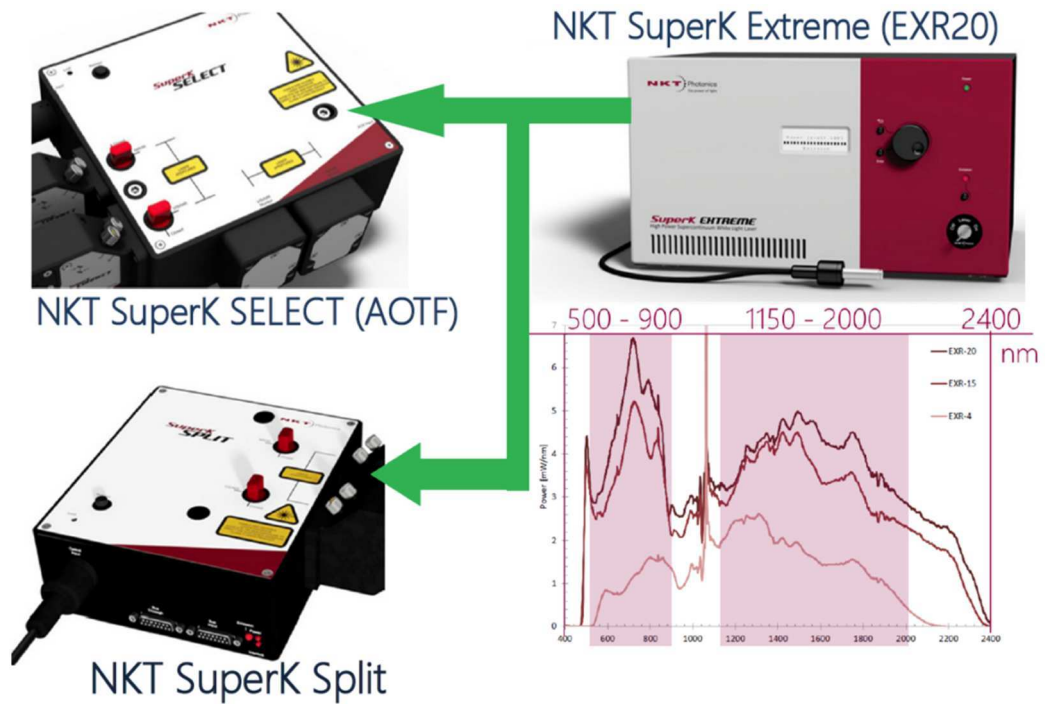


Figure 4.4: Broadband supercontinuum source (NKT SuperK Extreme) with its output fed into two spectral filtering accessories (either into the AOTF or SuperK Split). The spectra on bottom right shows the full supercontinuum output with two selected bands coloured in red (500-900 nm and 1150-1200 nm) denote possible output wavelengths for AOTF unit.

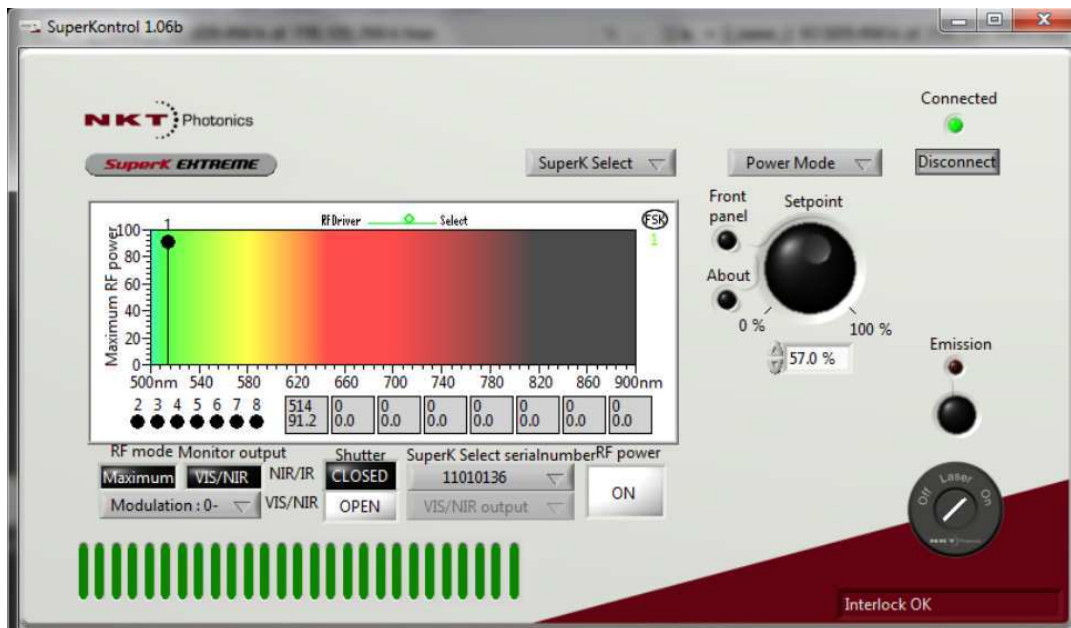


Figure 4.5: Graphical control user interface for output wavelength selection at the AOTF

The SuperK Split is a passive optical box attached to SuperK Extreme output. This splitter unit contains a dichroic mirror to transmit longer wavelengths ($\lambda > 1150$ nm) and reflect shorter wavelengths ($\lambda < 1100$ nm). The output of spectral splitter is shown in Fig. 4.6 below. The reflected part of the spectrum is used for similar purpose.

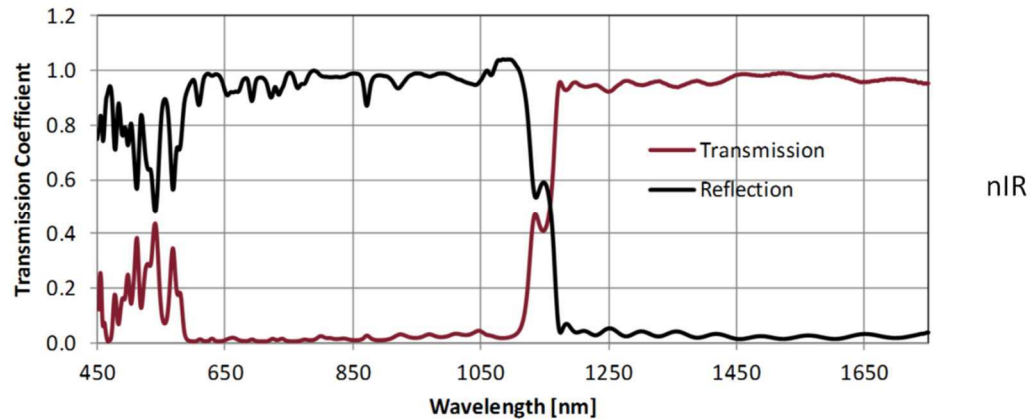


Figure 4.6: Output spectrum from SuperK Split splitter module

4.3 Dispersion experiments

4.3.1 Experimental set-up with time-domain OCT at 1300 nm

The AOTF with a wavelength range from 1200 to 1500 nm was chosen for dispersion measurement. The schematic in Fig. 4.7 shows a fibre based time-domain OCT configuration. The light from the SC (SuperK Extreme) enters either the AOTF (Sections 4.4.1 and 4.4.3) or SuperK Split (Sections 4.4.2 and 4.4.4), respectively. Light from the corresponding module enters into the first directional coupler (DC1, model FOBC-2-1310-20, AFW Technologies, Australia) with a splitting ratio of 80:20. One output delivers 80% of light intensity into the reference arm, and 20% of light into the object arm. Immediately after DC1, light enters free space in both arms and is collimated by an achromatic lens (AC-127-030-C, Thorlabs). The beam from the reference arm is reflected off a set of gold mirrors (M1, M2), then into the second directional coupler (DC2, model FOBC-2-1310-50, AFW Technologies), where it is combined with light from the object arm, to produce an interference signal at the output of two InGaAs (G10899, 500–1700 nm, Hamamatsu) balanced detectors (PD1, PD2).

In the object arm, various optical elements contribute to dispersion in the system. These include two lenses for beam collimation (CM) (FL=7.5 cm, Thorlabs) in each arm of the interferometer, four lenses for beam expansion (L1-L4, FL=7.5 cm, Thorlabs) and a scan lens (SL). The SL is a high NA microscope objective (20× 0.45, LC PlanN, Olympus, Japan). A dual-axis galvoscanner, G (Cambridge Technology, USA), is installed in the system to perform OCT imaging (not used here for this scope). One of the galvo scanners is employed here to introduce a small phase modulation via small path modulation. The galvo scanner is driven with a small sinusoidal signal at 1.5 mVpp and 460 Hz. The main purpose is to modulate the optical path [14], which translates into phase variation and determines a modulation of the photo detected signal as long as the OPD is less than the coherence length. The amplitude was kept sufficiently small, to secure an OPD variation smaller than a fraction of the coherence length; otherwise, the measurement of the axial resolution is affected. This modulation needs to exhibit a high frequency, sufficient to distance it from the low-frequency range where the $1/f$ noise dominates the signal. The strength of the AC component is used to guide the OPD adjustment toward OPD = 0, where the AC signal is maximum.

When the lengths of the two arms are matched, the frequency of the photo detected signal contains frequency components from DC up to 100 kHz.

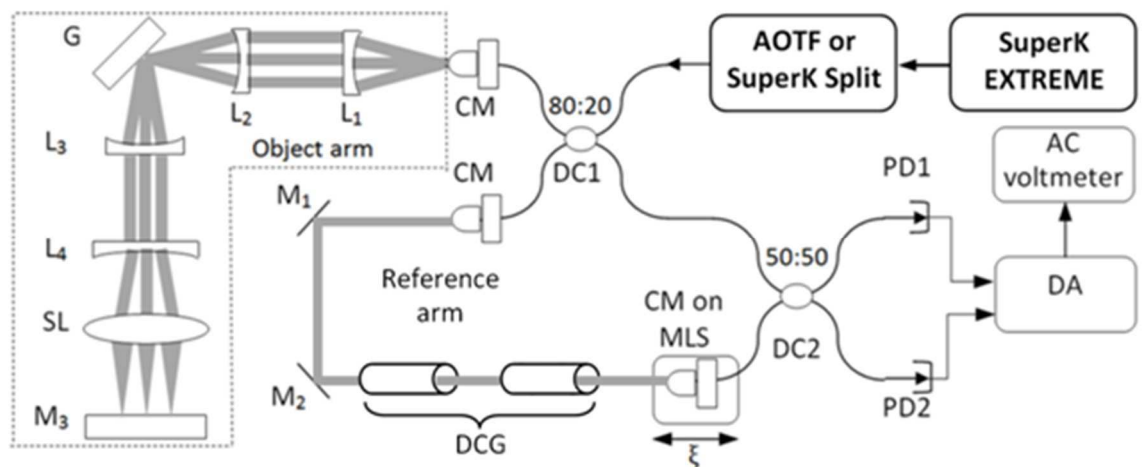


Figure 4.7: System configuration for dispersion characterisation using a time-domain OCT system at 1300 nm (G: Galvo-scanner, CM: free-space to fibre collimator lens, M1 & M2: mirrors, MLS: motorised linear stage, PD1 & PD2: photodiodes, DC1 & DC2: directional fibre-coupler, DA: digital-to-analogue converter, L1-L4: lenses, M3: object arm mirror, DCG: dispersion compensation glass)

4.4 Dispersion analysis

4.4.1 Dispersion measurement with AOTF at 1300 nm

To compensate for the dispersion caused by the optical components, dispersion compensation glass (DCG) rods made of BK7 glass are introduced in the reference arm of the system in Fig. 4.7.

We started with eight BK7 lenses, making a length of 25.5 cm, to compensate for the four lenses used in the object arm (12.25 cm in total thickness). In the next step, we added a glass rod of 10 cm more, to compensate for the SL (microscope objective) of 5 cm thickness. For the next steps, several combinations of BK7 glass rod lengths were tried.

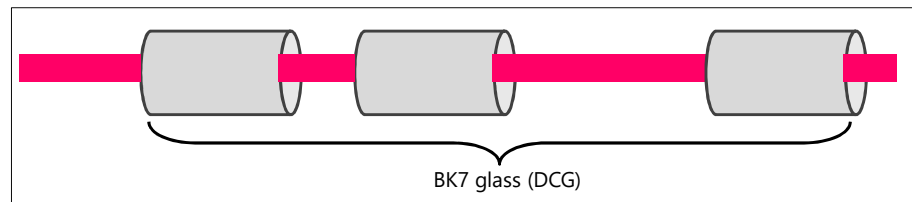


Figure 4.10: Illustration of iterative glass addition method for dispersion compensation in the 1300 nm system

Results are presented in Fig. 4.11 and Table 4.2 for $L = 55$ cm, 60 cm, and 65 cm. For each such glass length, L , the OPD position, ζ , of the A-scan peak was measured versus wavelength.

The motorized linear stage (MLS) in the reference arm is moved in steps of $1 \mu\text{m}$ to locate the peak of the time-domain interference measured via the electrical signal delivered by the balanced photo detector. The process is repeated 10 times and an average value of the autocorrelation peak position is calculated. The detector voltage is measured using the AC voltmeter, with frequency range from 10 Hz to 100 kHz. For each of the selected λ , the position, ζ , where a maximum AC voltage is obtained corresponding to the largest interference signal, is recorded. According to the specifications, the MLS has a positioning error of $0.2 \mu\text{m}$.

Let us denote ζ_0 as the OPD value of the A-scan peak at 1300 nm. Then, the difference in OPD, $\Delta\text{OPD} = \zeta - \zeta_0$ versus wavelength is graphically represented in Fig.

4.11. Each curve is fitted using a line crossing through the reference point (ξ_0 , 1300 nm). For each such line, a dispersion slope, D ($\mu\text{m}/\text{nm}$) is evaluated and its value placed in Table 4.2. The 1300 nm reference point was chosen because DC1 and DC2 have maximum transmission at 1300 nm.

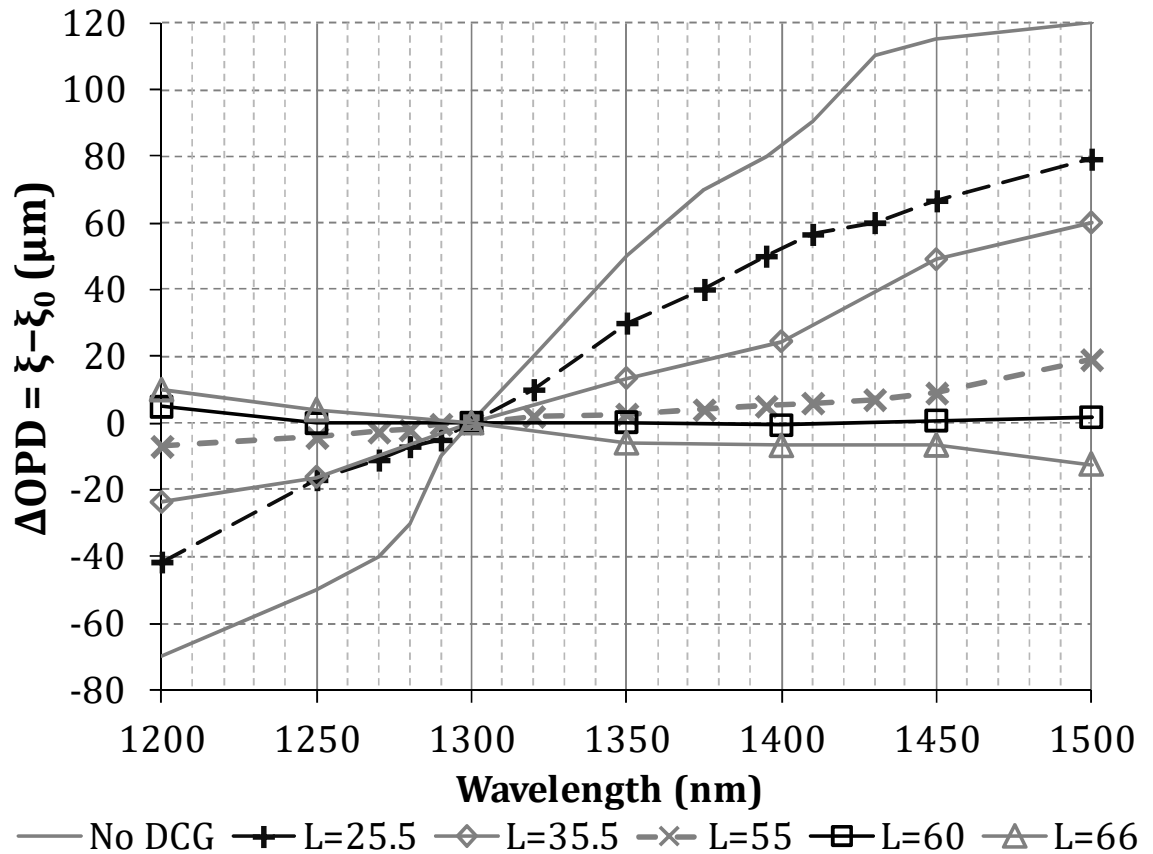


Figure 4.11: ΔOPD versus wavelength λ_m for different DCG length

The data in Fig. 4.11 shows that, in the uncompensated system, the dispersion slope, D , is greater than $200 \mu\text{m}/300 \text{ nm}$. For an added length $L = 60 \text{ cm}$, the slope is reduced to $D = 4 \mu\text{m}/300 \text{ nm}$. By increasing L slightly, to $L = 66 \text{ cm}$, the slope of the curve in Fig. 4.11 is reversed to $D = -25 \mu\text{m}/300 \text{ nm}$.

An interesting exercise is to estimate theoretically the glass length, L_{th} , of DCG rods of BK7, needed to compensate for each measured dispersion D in the system. By referring to Eq. (4.5), (4.9) and (4.12), we could rewrite $GDD = L_{\text{th}} \times GVD$, where L_{th} can be obtained after rearranging terms

$$L_{th} = \left| -\frac{D\lambda^2}{2\pi c^2} \cdot \frac{1}{GVD} \right| \quad (4.20)$$

where

$$GVD = \left. \frac{d^2\beta}{d\omega^2} \right|_{\omega_0} = \frac{d}{d\omega} \left(\frac{1}{v_g} \right) \quad (4.21)$$

Group dispersion can be expressed as function of wavelength λ and refractive index n

In non-vacuum, n increases with ω , therefore $\frac{dn}{d\omega} > 0$.

$$v_g = \frac{c/n}{1 + \frac{\omega}{n} \frac{dn}{d\omega}} = \frac{c}{n - \lambda \frac{dn}{d\lambda}} \quad (4.22)$$

$$GVD = \frac{\lambda^3}{2\pi c^2} \frac{d^2n}{d\lambda^2} \quad (4.23)$$

where $\frac{d^2n}{d\lambda^2}$ is the second-order derivative of the refractive index, n is the BK7 glass

obtained from its Sellmeier equation (Schott N-BK7, Edmund Optics) in the form of:

$$n - 1 = \frac{A_1\lambda^2}{\lambda^2 - A_0} + \frac{B_1\lambda^2}{\lambda^2 - B_0} + \frac{C_1\lambda^2}{\lambda^2 - C_0} \quad (4.24)$$

with the following coefficient values in Table 4.1.

Table 4.1: Sellmeier coefficient constants for N-BK7 glass

A_0	A_1	B_0	B_1	C_0	C_1
0.00600	1.03961	0.02002	0.23179	103.5606	1.01047

In order to calculate L_{th} , an average GVD between 1300 and 1310 nm of 1.65 fs²/mm is used. The resulting L_{th} values are listed in the seventh column of Table 4.2.

Then, using the dispersion values D for lengths of glass of 55, 60, and 65 cm and assuming a linear dependence of slope to D , we have evaluated that D can be brought to

zero using a length $L_0 = 60.78$ cm. Then we compared the variation in length of glass at each step, $L_0 - L$ and compared it with the predicted theoretical value inferred by using Eq. (4.20) and obtained the errors $\epsilon = L_0 - L - L_{th}$ in column eight. These are obviously affected by how good the estimation of the slope D was.

Figure 4.12 presents useful information provided by the AOTF method, in addition to the measurement of the slope D . For each central wavelength, λ_m , of the light from the AOTF, the amplitude of the interference signal is measured. This measurement is shown for each correction step in terms of the length of BK7 rods. The curves are represented in normalized form, as only the spectral dependence of such amplitude is relevant for this analysis. The FWHM of these profiles show the overlap of the spectra of signals from the object and reference arms that contribute to interference. The overlap of spectra is generally less than the optical bandwidth at the input of the system. These FWHM values are denoted as $\Delta\lambda_{EXP}$ and are listed in the third column of Table 4.2. The associated coherence length, $C_{L,EXP}$, corresponding to measured $\Delta\lambda_{EXP}$, are calculated using Eq. (4.1) and are listed in the fourth column in Table 4.2.

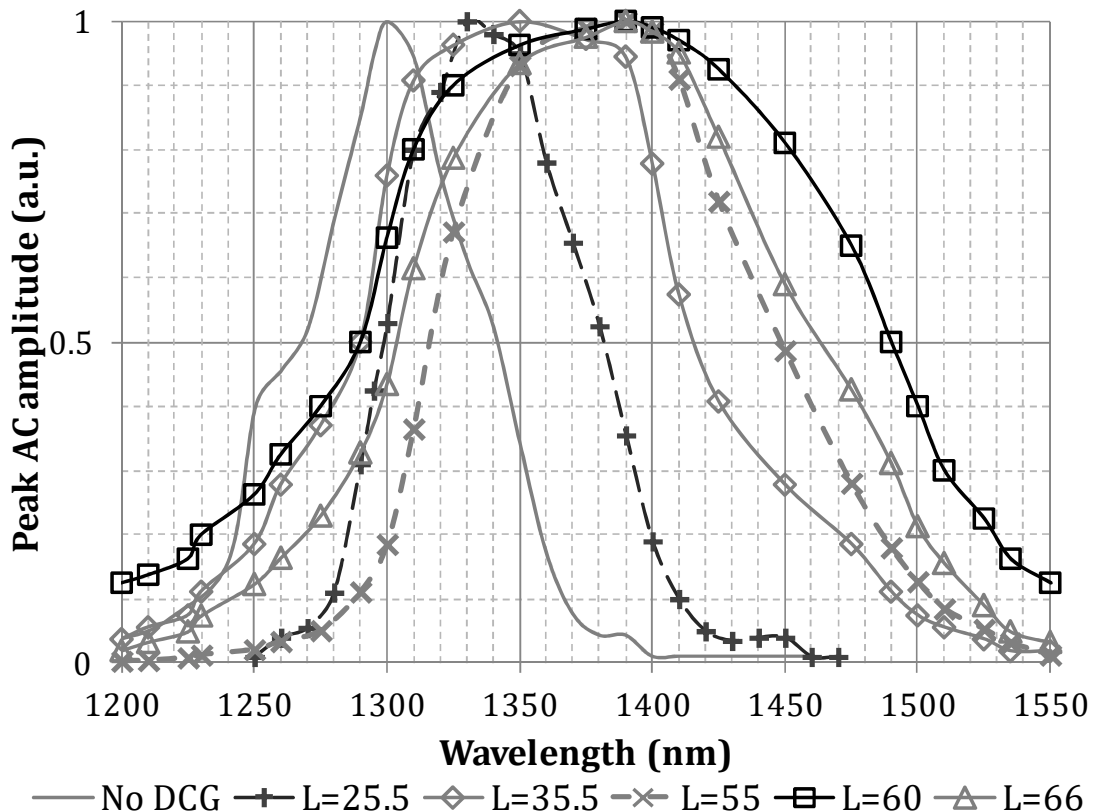


Figure 4.12: Interference strength versus wavelength λ_m selected by AOTF

4.4.2 Dispersion measurement with FWHM of autocorrelation at 1300 nm

The AOTF is replaced with a SuperK Split. This outputs a 300 nm bandwidth from 1200 to 1500 nm. The output spectrum is shown in Fig. 4.6. The theoretical axial resolution for this bandwidth would be $3.1 \mu\text{m}$, but the achievable axial resolution depends on the optical spectrum, determining the interference signal as well as on the dispersion left uncompensated. The MLS is moved around the position where the maximum amplitude is obtained, to positions ξ_+ and ξ_- where the amplitude is 50% of that at the maximum.

The experimental values of the $|\xi_+ - \xi_-|$ interval are listed in the fifth column in Table 4.2. These values represent the FWHM of the correlation function, as shown in Fig. 4.13. The autocorrelation function for $L = 60 \text{ cm}$ (squares on solid line) in Fig. 4.13 displays a minimum FWHM, giving an axial resolution of the system of $\sim 9 \mu\text{m}$. This should be compared to the most uncompensated case of no DCG (unmarked line), at $102 \mu\text{m}$. The best adjustment is between the curve for $L = 60 \text{ cm}$ (squares on solid line) and that for $L = 66 \text{ cm}$ (triangles on solid lines).

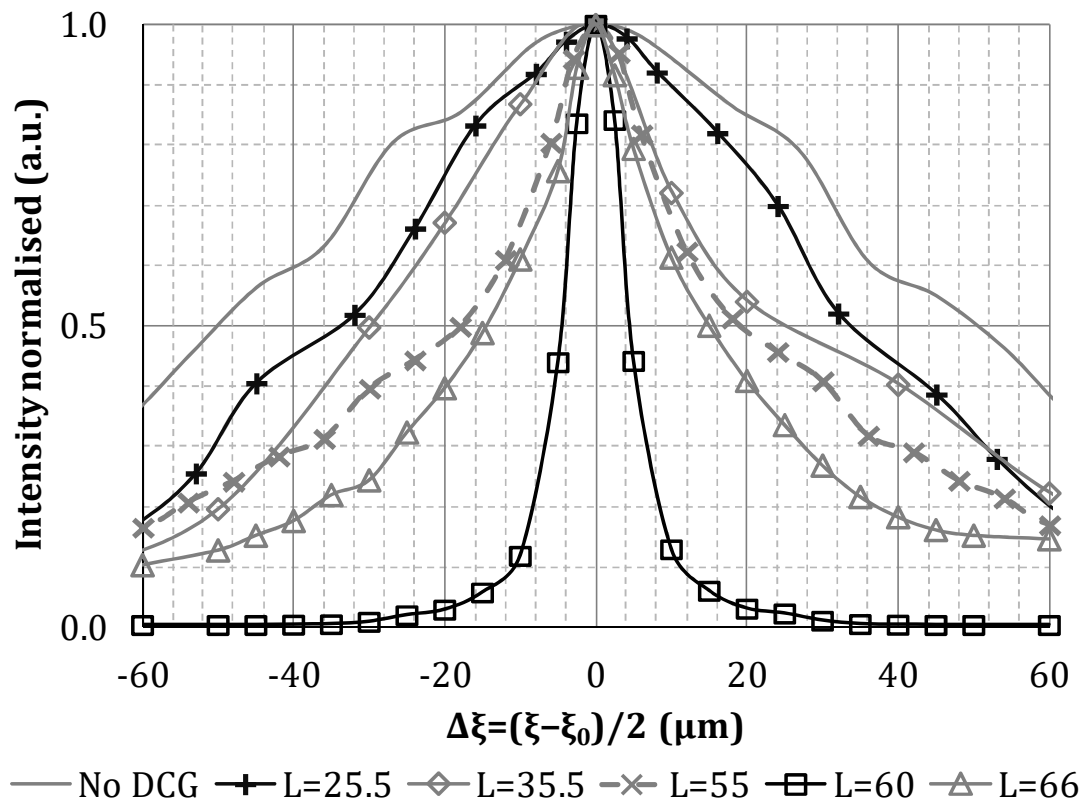


Figure 4.13: Autocorrelation function for 1300 nm system

Because ξ signifies OPD, the FWHM of the autocorrelation peak is obtained as $\Delta\xi/2$ given by Eq. (4.19). In Table 4.2, the theoretically estimated FWHM values are calculated using D measured in Fig. 4.11, by applying Eq. (4.19) and using the corrected C_L values as inferred from $\Delta\lambda_{\text{EXP}}$. These values should be compared with the theoretical $C_L = 4.96 \mu\text{m}$ given by Eq. (4.1). However, due to the limited transmission band of the coupler (DC1, DC2) and of the injection efficiency from free space to fibre, the wavelengths within the full 300 nm bandwidth of the signal applied from the source do not contribute equally to the interference.

Table 4.2: Comparison between Experimental and Calculated FWHM of Autocorrelation Function for Six Values of Dispersion for system at 1300 nm

DCG length L (cm)	D , slope ($\mu\text{m} / 300$ nm)	$\Delta\lambda_{\text{EXP}}$ (nm)	$C_{L, \text{EXP}}$ (μm)	$\Delta\xi_{\text{theory}}$ using			
				D and C_L , EXP (μm)	$\Delta\xi_{\text{FWHM}}$ M (μm)	L_{th} (cm)	$L_0 - L - L_{\text{th}}$ (cm)
No DCG	200	75	21.3	100.6	102	60.38	0.40
$L = 25.5$	120	85	17.3	60.6	70	39.85	-4.57
$L = 35.5$	85	125	12.9	43.0	55	22.06	3.22
$L = 55$	31	165	10.3	16.3	36	4.84	0.94
$L = 60$	4	200	8.5	4.7	9	0.36	0.42
$L = 66$	-25	170	10	13.5	29	-4.38	-0.84

4.5 Comparison between AOTF and FWHM autocorrelation

Two methods of dispersion compensation have been presented and utilized on two systems operating at two different wavelength bands. In a low-coherence interferometer, driven by a broadband source, the simplest, yet time-consuming procedure to compensate for the dispersion is based on the FWHM measurement of the autocorrelation peak. This is performed iteratively by adjusting the dispersion up or down until FWHM minimum is achieved. The method can reach a FWHM minimum, depending on the possibility to proceed in sufficiently small steps. Adjusting the glass length in System 1 may be difficult, depending on the availability of different lengths of glass.

The SDL used in System 2 allows continuous adjustment of the dispersion compensation, in contrast to the stepped variation of the length of BK7 glass rods. Thus, it is more likely to achieve the desired minimum dispersion compensation than using steps of glass. Irrespective of the method, however, a single measurement of FWHM does not tell which way to proceed, to increase or decrease the glass length of dispersion in the SDL, while a single slope measurement using the AOTF method provides such information. Therefore, the AOTF method appears more convenient for the task of dispersion compensation.

4.5.1 Superiority of AOTF method

The biggest advantage of the AOTF method is that the minimum slope for the graphs in Figs. 4.4 and 4.7 represent an absolute achievable condition, and this corresponds to a zero value, which is known. The value toward which we tend to direct adjustments is not known in the FWHM method. In an ideal situation, when the dispersion is fully compensated for, the FWHM of autocorrelation theoretically becomes $\Delta\delta = C_L/2$.

However, in reality, the value measured is typically larger, as the two interfering waves may not have similar spectral shapes and may not be as wide as the original optical source spectrum. Deviations of the source spectrum shape from Gaussian increase the value in Eq. (4.1). Even if the spectral shape from the source is Gaussian, the injection into the fibre may not be uniform over the spectrum, resulting in alteration of the spectral shape of the interfering field. In other words, the value toward which we push the FWHM measurement is not known.

When using the AOTF method, a change of sign in the slope immediately suggests the direction of the next step. In opposition to the AOTF method, the best adjustment when using the FWHM method is reaching a minimum value for the FWHM. Therefore, when using the FWHM method, it is necessary to apply dispersion correction until a minimum is found, and this can only be established by continuing with the process until an increase of the FWHM value is measured.

If the slope of the graph obtained with the AOTF approaches zero, this means that the dispersion is compensated and further optimization is not required. Therefore, measuring the slope with the AOTF method requires only a single iteration, because the optimal DCG length can be

- (i) calculated from the first measured slope, and
- (ii) in principle, can be obtained from dispersion data of the material. This procedure was illustrated in Section 4.4.1.

4.5.2 Minimising dispersion

On the other hand, even if a slope near zero $\mu\text{m}/\text{nm}$ is achieved using the AOTF method, this does not mean that the $\Delta\zeta_{\text{FWHM}}$ reaches the theoretical limit predicted by Eq. (4.1) for reasons mentioned above, and as shown by values in Tables 4.2 and 4.3. Some large differences between the FWHM $\Delta\zeta_{\text{FWHM}}$ measured and $\Delta\zeta_{\text{theory}}$ are observed in the two tables. These differences may be explained based on the facts that:

- (i) the spectra of the two interfering beams do not coincide, due to the spectral dependence of fibre injection;
- (ii) not all parts of the overlapping spectra contribute to interference due to polarization mismatches; and
- (iii) the theory presented above for the shape of the autocorrelation function assumed a Gaussian profile of the spectrum, which is not the case in practice.

Also, there are several different types of glass in the interferometer, with their own dispersion. Additionally, the slopes of graphs in Figs. 4.11 and 4.14 are estimated based on fitting straight lines to curves that exhibit clear nonlinear behaviour.

From a different perspective, let us consider the process of seeking minimum dispersion that can be achieved by the two methods, based on guidance using FWHM measurements and using the AOTF measurements. Using a derivative of the FWHM, $\Delta\xi$ in Eq. (4.19) in respect to D ,

$$\frac{d(\Delta\xi)}{d(D)} = \frac{D \cdot \Delta\lambda^2}{2C_L \sqrt{1 + \frac{(D \cdot \Delta\lambda)^2}{C_L^2}}} \quad (4.25)$$

gives the dependence of the FWHM method on the dispersion coefficient D . Let us consider that we are close to small values in D , in which case (4.25) becomes

$$\frac{d(\Delta\xi)}{d(D)} \approx \frac{D \cdot \Delta\lambda}{2C_L} \quad (4.26)$$

In case of a good dispersion adjustment, the delay in OPD at the extreme values of the AOTF bandwidth is δm , determining a minimum measurable dispersion coefficient:

$$D = \frac{\delta m}{\Delta\lambda} \quad (4.27)$$

Considering that the minimum in D equals the error in D evaluation, i.e., $d(D) \approx D$, using (4.26) and (4.27), the error in FWHM measurement becomes

$$d(\Delta\xi) \approx \left(\frac{\delta m}{\Delta\lambda} \right)^2 \frac{(\Delta\lambda)^2}{2C_L} = \frac{(\delta m)^2}{2C_L} \quad (4.28)$$

As long as $\delta m < 2C_L$, then $d(\Delta\zeta) < \delta m$. This means that the error in FWHM of the AOTF, as determined by $d(\Delta\zeta)$, is less than the error in positioning the peak in the A-scan δm . That is in fact the error in measuring the FWHM in the method relying on FWHM measurement. Therefore, Eq. (4.28) demonstrates superiority of the AOTF method over the FWHM measurement method in bringing the setup closer to minimum dispersion.

4.5.3 Application of AOTF in broadband OCT dispersion measurement

As shown by the measurement of the interference signal versus wavelength selected by the AOTF in the setup at 1300 nm (Fig. 4.12), the accuracy of the FWHM measurement of autocorrelation peak is limited to a bandwidth of signals contributing to interference. This may be narrower than the bandwidth of the AOTF method. In other words, the AOTF method allows measurements at a whole range of wavelengths, including and beyond the overlapped part of the interference spectrum that determines the effective bandwidth. Hence better accuracy in compensating for the dispersion is achievable with the AOTF method.

The AOTF method presented is an alternative to the methods at hand in OCT systems using spectrometers or swept sources, where spectral information can be used to compensate for the dispersion. Although the method presented employs the time-domain principle, it is equally applicable to swept source OCT configurations, where the swept source is replaced with the AOTF module, dispersion is minimized, and then the swept source is placed back into the system.

References

1. R. Yadav, K. Lee, J. Rolland, J. Zavislan, J. Aquavella, and G. Yoon, “*Micrometer axial OCT for corneal imaging*,” *Biomed. Opt. Express* 2, 3037–3046 (2011).
2. Z. Yaqoob, J. Wu, and C. Yang, “*Spectral domain optical coherence tomography: a better OCT imaging strategy*,” *BioTechniques* 39, S6–S13 (2005).
3. M. Wojtkowski, R. Leitgeb, A. Kowalczyk, T. Bajraszewski, and A. F. Fercher, “*In vivo human retinal imaging by Fourier domain optical coherence tomography*,” *J. Biomed. Opt.* 7, 457–463 (2002).
4. A. Dubois, K. Grieve, G. Moneron, R. Lecaque, L. Vabre, and C. Boccara, “*Ultra-high-resolution full-field optical coherence tomography*,” *Appl. Opt.* 43, 2874–2883 (2004).
5. B. Hofer, B. Považay, A. Unterhuber, L. Wang, B. Hermann, S. Rey, G. Matz, and W. Drexler, “*Fast dispersion encoded full range optical coherence tomography for retinal imaging at 800 nm and 1060 nm*,” *Opt. Express* 18, 4898–4919 (2010).
6. G. J. Tearney, B. E. Bouma, and J. G. Fujimoto, “*High-speed phase and group-delay scanning with a grating-based phase control delay line*,” *Opt. Lett.* 22, 1811–1813 (1997).
7. A. V. Zvyagin, E. D. J. Smith, and D. D. Sampson, “*Delay and dispersion characteristics of a frequency-domain optical delay line for scanning interferometry*,” *J. Opt. Soc. Am. A* 20, 333–341 (2003).
8. A. Meadway, S. H. H. Darbrazi, G. Dobre, R. B. Rosen, and A. Gh. Podoleanu, “*A rapid method of measuring dispersion in low coherence interferometry and optical coherence tomography systems*,” *J. Opt.* 12, 015302 (2010).
9. C. C. Rosa, J. Rogers, and A. G. Podoleanu, “*Fast scanning transmissive delay line for optical coherence tomography*,” *Opt. Lett.* 30, 3263–3265 (2005).
10. F. Toadere, A. Bradu, W. Poon, D. Schultz, and A. Podoleanu, “*Spectral delay line for display control in swept source OCT*,” *Proc. SPIE* 9258, 92581X (2014).
11. K. S. Lee, A. C. Akcay, T. Delemos, E. Clarkson, and J. P. Rolland, “*Dispersion control with a Fourier domain optical delay line in a fiber optic imaging interferometer*,” *Appl. Opt.* 44, 4009–4022 (2005).
12. H. Ye, D. Ling, Y. Xu, and X. Huang, “*Dispersion and compensation of optical coherence tomography using double path rapid scanning optical delay line*,” *Proc. SPIE* 9656, 96560K (2015).
13. K. K. M. B. D. Silva, A. V. Zvyagin, and D. D. Sampson, “*Extended range, rapid scanning optical delay line for biomedical interferometric imaging*,” *Electron. Lett.* 35, 1404–1406 (1999).
14. A. Gh. Podoleanu, G. M. Dobre, and D. A. Jackson, “*En-face coherence imaging using galvanometer scanner modulation*,” *Opt. Lett.* 23, 147–149 (1998).

5

Ultra-broadband polarisation sensitive optical coherence tomography

Polarisation sensitive optical coherence tomography (PS-OCT) is a functional extension to intensity based light imaging system by utilising additional information carried by polarized light to provide enhance contrast. In traditional imaging, when only backscattered intensity is collected and analyzed, information related to depth and layered structure are neglected. In a typical microscopy system, researchers in the field worked to improve axial resolution and penetration depth, hoping to pick up sub-micron features not currently visible with most commercial OCT systems. Most research target at expanding the broadband capabilities of such systems by using super continuum light sources. At the same time, intense research has been going on to develop new techniques to extract additional information otherwise not discoverable with intensity based imaging.

PS-OCT on the other hand measures depth-resolved phase retardation of incident optical light and the altering state of light reflected from the target sample as a formed birefringence. Birefringence is the optical property of a material having a refractive index that depends on the polarisation state and propagation direction of light. When a light enters a material of birefringence, the incident light can be decomposed into two orthogonal components with varying refractive indices, commonly known as parallel (co-) and perpendicular (cross-) optical axes, thus polarisation dependent phase velocity. Birefringence occurs in many biological materials such as biological tissue structures, polymers and organic fibres. These structures alter the polarisation state of the light and show varying degree of birefringence. Therefore a light specific contrast not observable in conventional OCT system can be seen clearly in PS-OCT images.

For that reason, many new developments in PS-OCT have been published. The technique used to implement a PS-OCT system is rather similar to the normal OCT, as previously described in Chapter 2. Broadly speaking, these techniques can be divided into two main categories: (a) time-domain, and (b) spectral or Fourier domain. Within each of these two methods, there exist a free-space (bulk) and a fibre-based implementation, all for

the reasons similar to conventional non-polarisation systems. On the typical approaches to acquire a PS-OCT image, most of the articles published used a circularly polarised incident light, particularly those implemented in a free-space (or bulk) set-up. The use of a bulk configuration has its own advantages. It is easier to manage since the polarisation of the free space beam can be easily controlled with free-space polarising components, such as a polariser or a wave plate. It is also cheaper to install as it does not required the use of polarisation-maintaining (PM) fibres and fibre-based polarisation rotator.

Fibre-based PS-OCT system was first showcased by Izatt [1] back in 2001, with a single-detector. This approach was subsequently devised with PM fibres configuration by Chen [2] in 2003. A year later, Guo et al [3] extended the working principle of depth resolved birefringence measurement without PM-fibres by revising a new mathematical algorithm to take into account of the optical axis orientation of the imaged sample. More recently in 2015, Ding et al [4] has demonstrated that sample birefringence can be extracted using the Mueller matrix, in an all single-mode (SM) fibre configuration and single input polarisation state. Speed advantage is another concern for OCT imaging.

Free-space implementations are rather the preferred method to demonstrate proof of concept for reasons describe above. Hee [5], Hitzengerger [6], and de Boer [7], have all shown the use of circular polarised incident light into the sample to eliminate the need of complex mathematical calculation such as Stokes vector or Mueller matrix. More recently, the use of single A-scan to extract sample polarisation information has been demonstrated by [8].

Since PS-OCT is a relatively recent add-on extension to functional imaging, most of the published articles now use some variant of bandwidth tuneable lasers. At the same time, the use long pulse supercontinuum (SC) light sources in OCT imaging has seen greater adoption in recent years, replacing traditional SLDs and swept sources. The SC sources therefore open up the new possibility of ultra-broadband PS-OCT. To the best of our knowledge, there has been no publication on the use of an SC source in PS-OCT. Furthermore, the results from our polarisation extinction ratio (PER) measurements in Chapter 3 have shown that the random polarisation output from SC sources can be controlled, thus allowing us to select one polarisation at one part of the spectrum for use in OCT application. Therefore, in this chapter, we will demonstrate the practical application of imaging banknotes using a dual-spectrometer setup, powered by a high power NKT SuperK system. Our spectrometer based PS-OCT combines the working principles shown in [1,4,6].

5.1 Proof of concept

5.1.1 Polarisation of light

Light as an electromagnetic wave, is composed of an electric (E-field) and a magnetic (H-field) that travel at the same velocity in the same direction. Both E- and H-fields are vector quantities, carrying information on magnitude and orientation. Maxwell's equation relates E-field to H-field: they are always 90° out of phase and mutually perpendicular to each other. The light polarisation can be defined by the orientation of its E-field. There are three polarisation states: (a) linear, (b) circular, and (c) elliptical, as shown in Fig.5.1. Their Jones vectors are in Table 5.1.

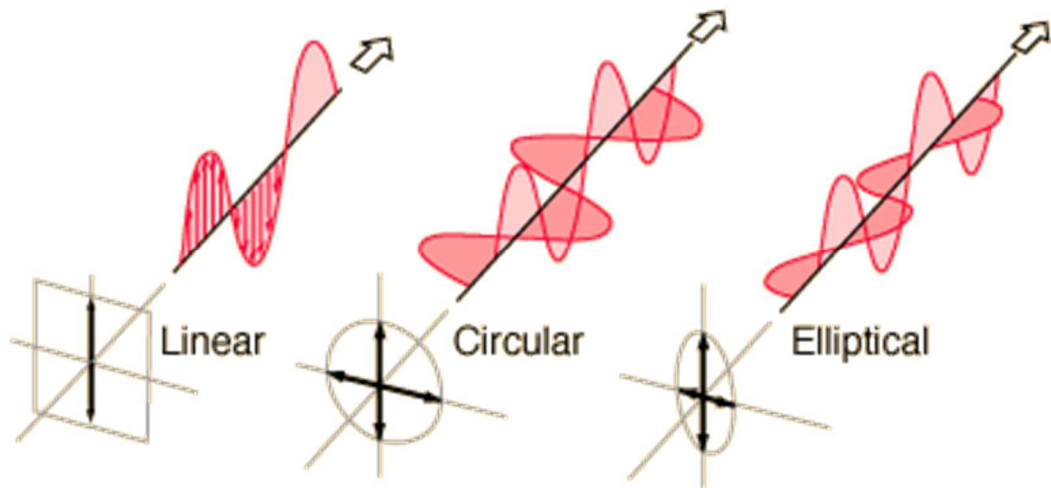


Fig.5.1 Illustration of linearly, circularly and elliptically polarised EM waves, and their Jones vector directions. [Source: <http://hyperphysics.phy-astr.gsu.edu/hbase/phyopt/polclas.html>]

To analytically describe the polarisation of light, we consider a monochromatic plan wave of frequency ν travelling in the z -direction, in free space, with speed of light c . The electric field lies in the xy -plan and can be describe as in Eqn.5.1 [9]

$$\vec{E}(z, t) = \text{Re}\{A \exp[j2\pi\nu(t - z/c)]\} \quad (5.1)$$

where t is time, $\text{Re}\{\}$ denotes the real part of the complex field, the vector \mathbf{A} represents the complex envelop of the sinusoidal function. The notation \mathbf{A} can be decomposed into A_x (horizontal) and A_y (vertical) components, as in Eqn.5.2.

$$\mathbf{A} = A_x \hat{x} + A_y \hat{y} \quad (5.2)$$

The propagation of two polarisation components can be described using the polarisation states, s- and p-. S- and p- polarisation states refer to the plane in which the electric field of a light wave is oscillating, as illustrated in Fig.5.2. S-polarisation (S-pol) is the plane of polarisation perpendicular to the page, while p-polarisation (P-pol) is the plane of polarisation parallel to the page [10].

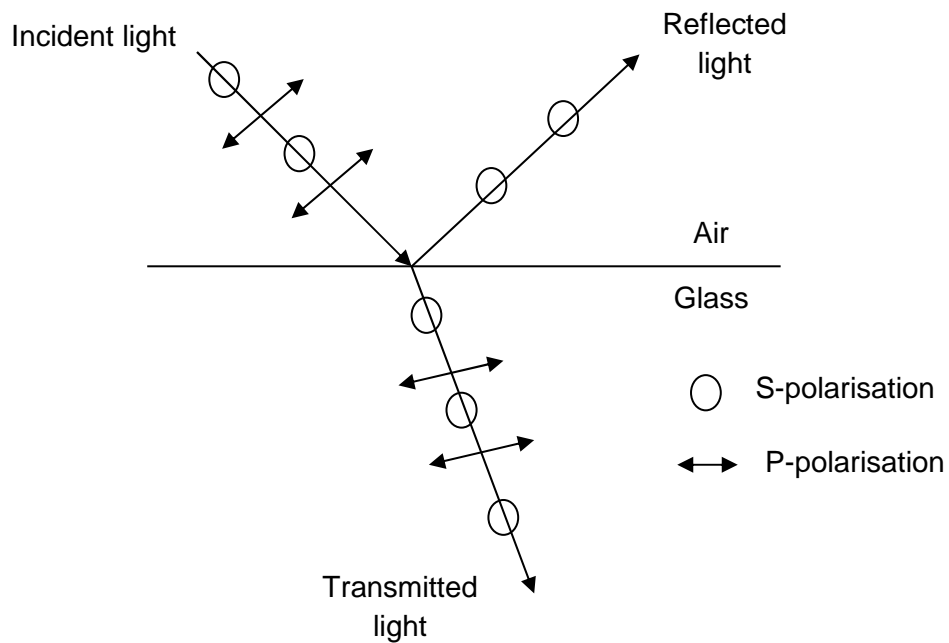


Fig.5.2 Illustration of s- and p-polarisation states for incident, transmitted and reflected lights interacting between air and glass interface.

Table 5.1 Jones vectors for different polarisations [11]

Linearly polarised			Circularly polarised	
Horizontal (x-direction)	Vertical (y-direction)	α° from x-axis	Left hand	Right hand
$\begin{pmatrix} 1 \\ 0 \end{pmatrix}$	$\begin{pmatrix} 0 \\ 1 \end{pmatrix}$	$\begin{pmatrix} \cos \alpha \\ \sin \alpha \end{pmatrix}$	$\frac{1}{\sqrt{2}} \begin{pmatrix} 1 \\ i \end{pmatrix}$	$\frac{1}{\sqrt{2}} \begin{pmatrix} 1 \\ -i \end{pmatrix}$

5.1.2 Slow and fast axes determination

Slow and fast axes in the context of optical birefringence refer to the difference in phase velocity between the two modes. In a birefringent material, such as an optical retarder, the fast axis is the axis with the lower effective index, allowing the light through faster, thus a higher phase velocity. On the other hand, the slow axis corresponds to the mode with the higher effective index, and lower phase velocity. The phase velocity, v_p of light can be determined if the effective index, n_{eff} of the medium it traverses through is known, using Eqn.5.3.

$$v_p = c / n_{eff} \quad (5.3)$$

where c is the free space velocity of light ($\sim 3 \times 10^8$ m/s).

To correctly determine the axis of a retarder, such as a half wave plate (HWP, $\lambda/2$) or quarter wave plate (QWP, $\lambda/4$), is essential. There is a simple way to find the axes of a retardation plate. This procedure requires two linear polarisers, LP₁ and LP₂. The first step involves orienting one LP₁ so the axis is horizontal. The second step requires that the other linear polarizer LP₂ is placed in front of LP₁, and orienting LP₂ so that the axis is vertical. Finally, the optical retarder is to be placed between the two crossed polarisers, and the retarder is to be rotated until maximum transmission is reached. The transmission light intensity can be probed using a broadband optical power meter. The fast and slow axes will be at $\pm 45^\circ$ from horizontal.

Table 5.2 Input and output polarisations with QWP and HWP

	Input	Output
Quarter wave plate (QWP)	Linear +45°	Right hand circular
	Linear -45°	Left hand circular
	Linear non 45°	Elliptical
	Left hand circular	Linear +45°
	Right hand circular	Linear -45°
Half wave plate (HWP)	Linear θ	Linear $-\theta$
	Left hand circular	Right hand circular
	Right hand circular	Left hand circular

5.1.2 Jones matrices

The Jones matrix calculus is a matrix formulation of polarised light. It consists of two forms: a 2×1 Jones vectors to describe only the field components, and a 2×2 Jones matrix to describe the polarising components. The use of Jones formulation is only limited to treating the completely polarised light. Therefore, unpolarised or partially polarised light cannot be represented with Jones formulation. The Jones matrices are also used when treating interference phenomena or when the electric field amplitudes are superposed. To illustrate Jones formulation, we first introduce the Jones matrices for a general retarder in Eqn.5.4, and then use it for different polarising elements, such as a retarder, a polariser, a half wave plate and a quarter wave plate are represented in Eqn.5.5 to 5.8 [11].

$$M(\delta, \theta) = \begin{pmatrix} \cos^2 \theta + (\sin^2 \theta \cdot e^{-j\delta}) & \cos \theta \sin \theta \cdot (1 - e^{-j\delta}) \\ \cos \theta \sin \theta \cdot (1 - e^{-j\delta}) & (\cos^2 \theta \cdot e^{-j\delta}) + \sin^2 \theta \end{pmatrix} \quad (5.4)$$

Where δ is the phase retardation and θ is the fast-axis orientation.

If we now consider a retarder plate with y-axis as fast-axis and x-axis the slow axis, the retarder's Jones matrix becomes

$$M_{\delta} = \frac{1}{\sqrt{2}} \begin{pmatrix} e^{j\delta} & 0 \\ 0 & e^{-j\delta} \end{pmatrix} \quad (5.5)$$

A polariser with polarising axis along x-axis can be written as

$$M_{P(x)} = \begin{pmatrix} 1 & 0 \\ 0 & 0 \end{pmatrix} \quad (5.6)$$

A QWP with the fast-axis along the x-axis is therefore

$$M_{QWP} = \frac{1}{\sqrt{2}} \begin{pmatrix} 1-j & 0 \\ 0 & 1+j \end{pmatrix} \quad (5.7)$$

A HWP with slow-axis along the y-axis becomes

$$M_{HWP} = \begin{pmatrix} 0 & j \\ -j & 0 \end{pmatrix} \quad (5.8)$$

We will use the Jones matrices discussed here to represent the polarized beam propagating through different polarising elements in a PS-OCT system. We'll describe our polarisation sensitive interferometer in Sec.5.2, and the controlling polarisation in Sec.5.2.1.

5.1.4 Bank notes

Bank notes or paper currency are secured instruments. These papers usually have security identifiers such as micro embossed threads, watermarking, diffractive holograms, and specialized inks, printed traditionally on cotton fibre or more recently on polymer substrates. Common security features include variation of paper thickness and density to create subtle variations in the light and dark areas, inks pigments that exhibit dichroic properties that alter light polarisation at angles, as well as more sophisticated liquid crystal holograms that are birefringent, as documented in [12].

Most recently, the introduction of polymer bank notes have transformed the industry. The new polymer notes are more durable, cleaner, waster resistance and difficult to counterfeit. The use of plastics in security documents extends beyond currency. More and more previously paper based documents, such as driving license, identity cards and access control credentials are now phased out in favour of the polymer version.

Since polymer substrate is made out of the synthetic composite material, its composition has widely characterised in the chemistry laboratories using well-established spectroscopy techniques, such as X-ray diffraction, FTIR, Raman and UV/visible spectroscopy. Many of these analytical techniques are use to determine the molecular structure of unknown organic compounds present in polymer. Many of these compounds are birefringent. The use of optical coherence tomography (OCT) to perform meso-scale, volumetric characterisation of polymer composites, polymer blends, biomaterials, and ceramic coatings have been done by researchers in the National Institute of Science and Technology (NIST) in USA [13-14].

5.2 PS-OCT system set-up

An OCT system configuration with dual-spectrometer detection is constructed as in Fig.5.2. A free-space in bulk concept of Michelson interferometer is used. To illustrate wideband OCT capabilities, a commercial, low-noise supercontinuum source (SuperK Extreme EXR 9, NKT Photonics, Denmark) that emits a broadband light from 480-2400 nm (visible power 900 mW), pulse repetition frequency (PRF) of 320 MHz, and pulse duration of 5 ps is used in this experiment. The SuperK output is fed into a spectrum splitter unit, SuperK Split (NKT Photonics). The SuperK Split is a passive optical accessories attached to SuperK Extreme output. This splitter unit contains a dichroic mirror to transmit longer wavelengths ($\lambda > 1150$ nm) and reflect shorter wavelengths ($\lambda < 1100$ nm). In this experiment, the visible band with usable bandwidth from 650-1100 nm is used. The theoretical axial resolution for this bandwidth would be 1.2 μm , but the achievable axial resolution depends on the polarisation of optical spectrum, determining the interference signal as well as on the dispersion left uncompensated. A broadband double Glan-Taylor Calcite polarizer (350-2300 nm, Thorlabs) is used to rotate the output beam into linear vertical polarisation. This beam is split by a non-polarizing beam splitter (BS), into the reference (reflected) and sample (transmitted) arms. Dispersion optimization was performed using advanced method described in [4].

The reference beam transmits through a dispersion compensation glass (DCG, LSM03DC, Thorlabs), and a quarter wave plate (QWP_R), oriented with its fast axis rotated to 22.5° to the horizontal polarisation, resulting in a right handed circular polarisation. The reference beam is reflected at movable reference mirror (MR). The back propagating beam, now left handed circularly polarized, passes through QWP_R , and resulted in the reference beam rotated at -45° to the linear horizontal. This beam provides reference intensity equally in two components, horizontal and vertical, which will be decomposed with polarizing beam splitter (PBS) at the interferometer output.

In the sample arm, a quarter wave plate (QWP_S) is oriented at 45° to provide a circular wave into the sample. The beam passes through a 2-axis galvanometric scanner (XY), denoted respectively as G_X (frame) and G_Y (line). Both G_X and G_Y are driven with sinusoidal signal. Since camera has a maximum line rate of 250 kHz, each of the 500 lateral pixels are acquired within 4 μs . To achieve an image of size 500×500 , that requires 2 s per B-scan. The scanned beam goes through an OCT optimized microscope objective lens (LSM02, 5x, Thorlabs) with focal length 7 mm. With a measured transversal resolution of 10 μm , the lateral image size is limited to 1.8 cm \times 1.8 cm. The maximum

scan area is triggered when 5V TTL signal is supplied to both galvo-scanners. The backscattered beam from the sample passes through QWPs, resulting in an elliptical polarisation state containing birefringence information from the sample.

The interferometric signals from reference and sample arms are combined at BS, and are sent through a PBS where two polarisation components are extracted, collimated into a fibre using a free-space to fibre coupler (SCT, SuperK Select, NKT Photonics), and delivered to separate spectrometers (SP1, SP2) for detection. The detection mechanism consists of broadband visible range spectrometers (model Cobra-S C-650-950-S2K, 650-950 nm, Wasatch Photonics), one for each polarisation component.

5.2.1 Polarisation selection and switching

At the output of SuperK Split, the light is polarised, as resulted from random nature of supercontinuum generation. A broadband polarizer selects a vertical linear polarisation, represented by its Jones vector as

$$\vec{E} = E_0 \begin{pmatrix} 0 \\ 1 \end{pmatrix} \quad (5.9)$$

Where $E_0 = A_0 \exp(j\omega t)$, \mathbf{E} denotes vector component of electric field, A_0 is the signal amplitude, Jones matrix of 0 and 1 represent horizontal and vertical polarisation states. The backscattered sample signal detected before the PBS [5] can be written as

$$\vec{E}_S = \frac{E_0}{2} \sqrt{R} \begin{pmatrix} \cos(\delta) e^{-j\delta} \\ \sin(\delta) e^{j(\pi - \delta - 2\theta)} \end{pmatrix} \quad (5.10)$$

The back propagated reference signal can equally be represented as

$$\vec{E}_R = \frac{E_0}{2} \frac{1}{\sqrt{2}} \begin{pmatrix} 1 \\ -1 \end{pmatrix} \quad (5.11)$$

Another way to experimentally verify that a circular is sent to the sample is to put the second polariser P2 at the position of sample (S). With the reference arm blocked, light from the first polariser (P1) enters the QWPs, bouncing off the galvo-scanner mirrors XY, and into P2. Polariser P2 is then rotated around 360°. If the polarisation coming out from the QWPs is circular, power reading at the P2 output remains constant for all angles of P2.

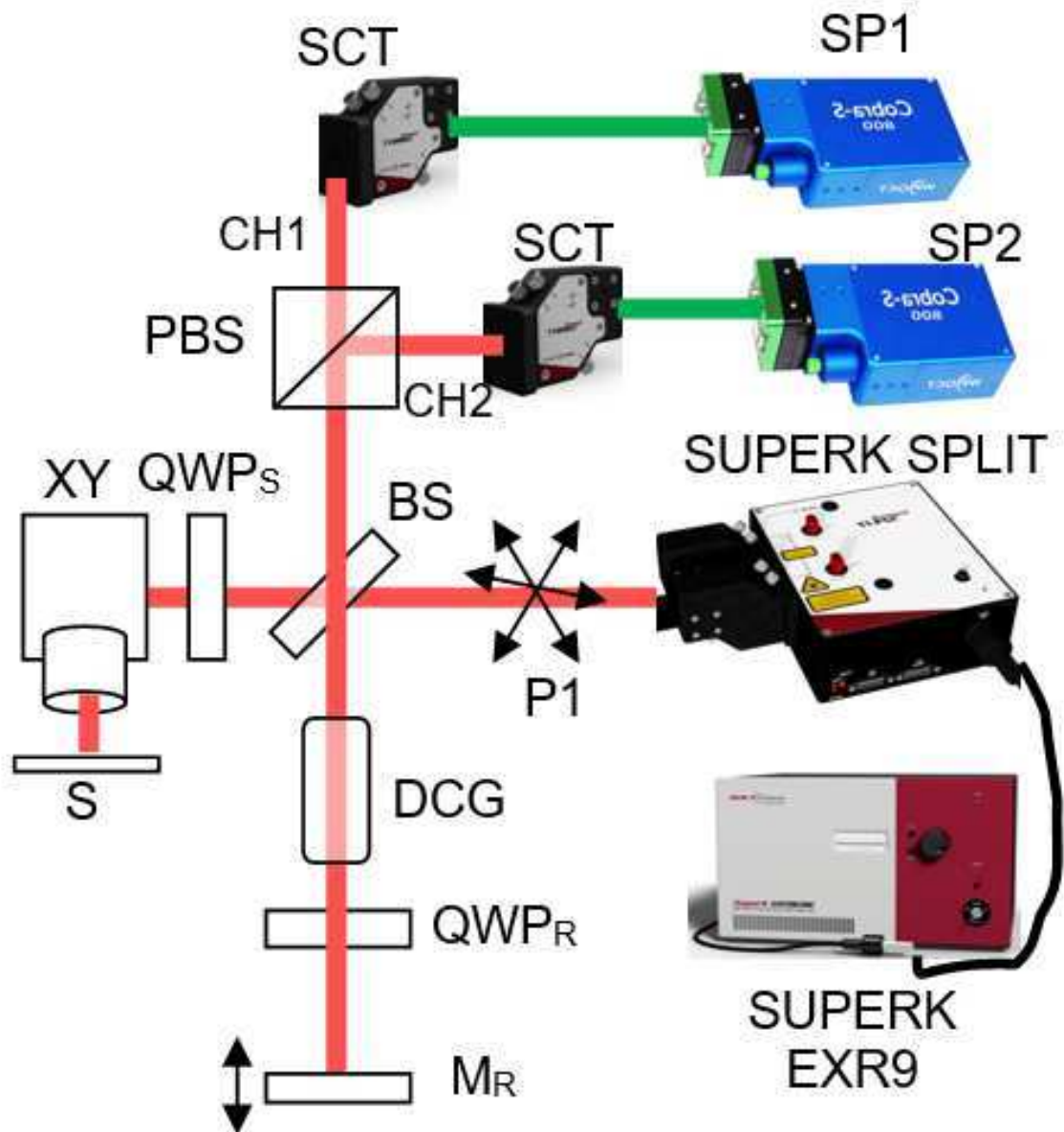


Fig.5.3 Experimental set up of a broadband dual-spectrometer PS-OCT system powered by a supercontinuum source. (BS: beam splitter, DCG: dispersion compensation glass, M_R : movable reference mirror, P_1 : broadband polarizer, PBS: polarizing beam splitter cube, QWP: quarter wave plate (subscripts 'R': reference, 'S': sample), SCT: SuperK Connect free-space to fibre coupler, SP: Wasatch spectrometers, XY: dual-axis galvo-scanner. The QWP_R is rotated to 22.5° of the fast-axis, a round-trip beam is rotated by 45° and $QWPS$ is rotated to 45° to provide circular light into the sample. CH1 & CH2 represents the horizontal and vertical polarisations.)

5.2.2 Polarisation detection

OCT interference signal recorded from the spectrometer can be written in Eqn.5.12 as the sum of amplitude modulation in both sample and reference arms

$$I_{CH}(z) = I_{R,CH} + I_{S,CH} + 2\sqrt{I_{R,CH} I_{S,CH}} \cdot \gamma(z - z_0) \cos(\Phi_{CH}) \quad (5.12)$$

where I_{CH} represents interfered signals for two channelled polarisation components, horizontal and vertical ($CH1$, $CH2$), I_R and I_S each corresponds to signal intensities recorded in reference and sample arms, z is the OPD position (where z_0 is when $OPD=0$), $\cos(\phi_{CH})$ is the phase term of the oscillating signal. The interference signal at different OPD position is fast Fourier transformed (FFT) to produce A-scans. B-scan is produced by transverse scanning the sample orthogonal to the surface, as discussed before in Sec.2.3 in Chapter 2 on spectrometer-based OCT method.

At the interferometer exit, the OCT light beam is split up into its horizontal (H) and vertical (V) component by the PBS, and are then detected by separate detection units, spectrometers SP1 and SP2. By the respective signal amplitudes (A_{CH1} , A_{CH2}) and the relative phase difference $\Delta\Phi_{CH}$, Jones vectors are detected for every image pixel. These Jones vectors enable the calculation of the sample's birefringent properties, namely of phase retardation δ as well as sample reflectivity intensity R_D [15]:

$$R_D = |A_{CH2}^2 - A_{CH1}^2| \quad (5.13)$$

$$\delta = \tan^{-1}\left(\frac{A_{CH2}}{A_{CH1}}\right) \quad (5.14)$$

Since $\delta = \Delta n \times L$ is dependent on sample birefringence, the value of δ accumulates as a function of L , the distance light travelled in a birefringent material [15]. Therefore, the measured phase retardation results are cumulative. The birefringence measured in this case is similar to the one measured in nonlinear fibre (NLF) in Section 3.2.2, where the beat length analogy in fibre is similar to the thickness of birefringent material imaged. In nominally non-birefringent samples, the phase retardation however is small and limited. In a strongly birefringent sample, the cumulative phase retardation can be huge.

5.2.3 Dispersion compensation and spectrometer calibration

To optimize for polarisation sensitive sample response, we calibrated our spectrometers using a dummy sample of known birefringence: layered transparent masking tape on top of an IR sensor card. A simple calibration consisting of transmission polarisation extinction ratios (PER), verifying the polarisation state across all points of interest along the beam paths, were measured. The subsequent step involved wavelength to pixels calibration of our spectrometer. Calibration involves a two steps process: (a) placing narrow bandpass filters (BW \sim 10 nm) of central wavelengths at every 50 nm interval between 650-950 nm, in the reference arm of the interferometer in Fig.5.2, and (b) interpolating the peak pixel number recorded at wavelengths interrogated. The resulting calibration curve for this specific model of Cobra-S spectrometer is shown in Fig.5.3. Based on our calibration data, we can assign lowest pixel number 1 to 650 nm, and highest pixel number 2048 to 950 nm, thus giving us a broadband operating range of 300 nm.

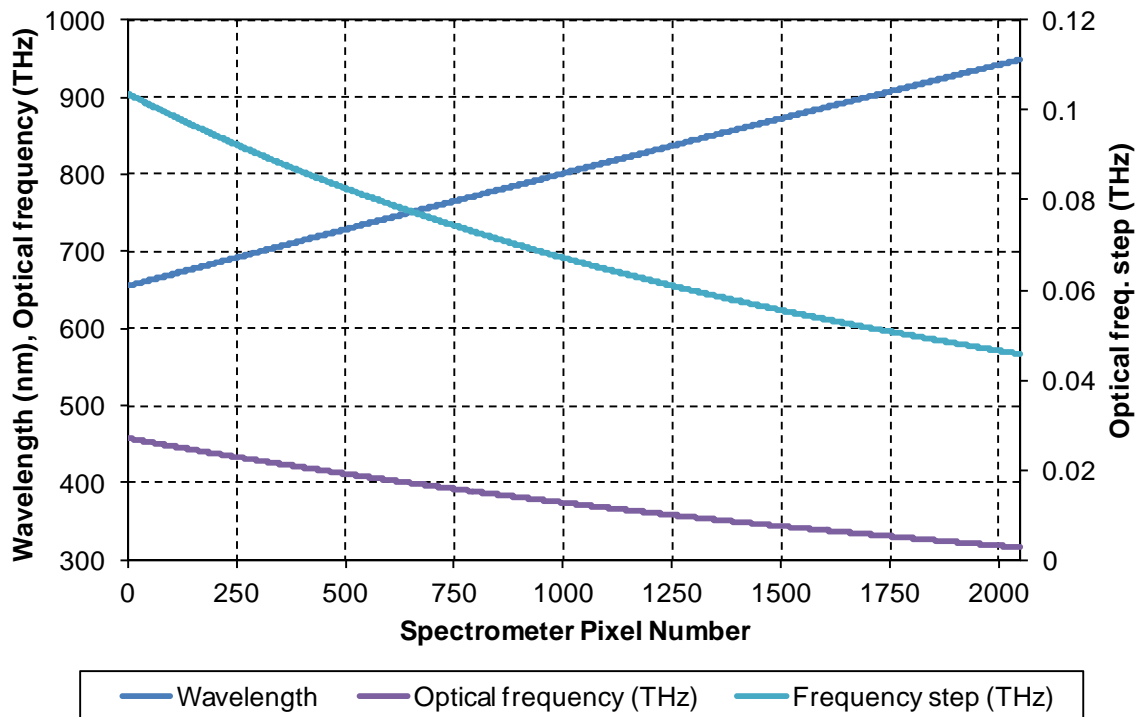


Fig.5.4 Pixel number to wavelength calibration curve for Wasatch Cobra-S model spectrometer (650-950 nm)

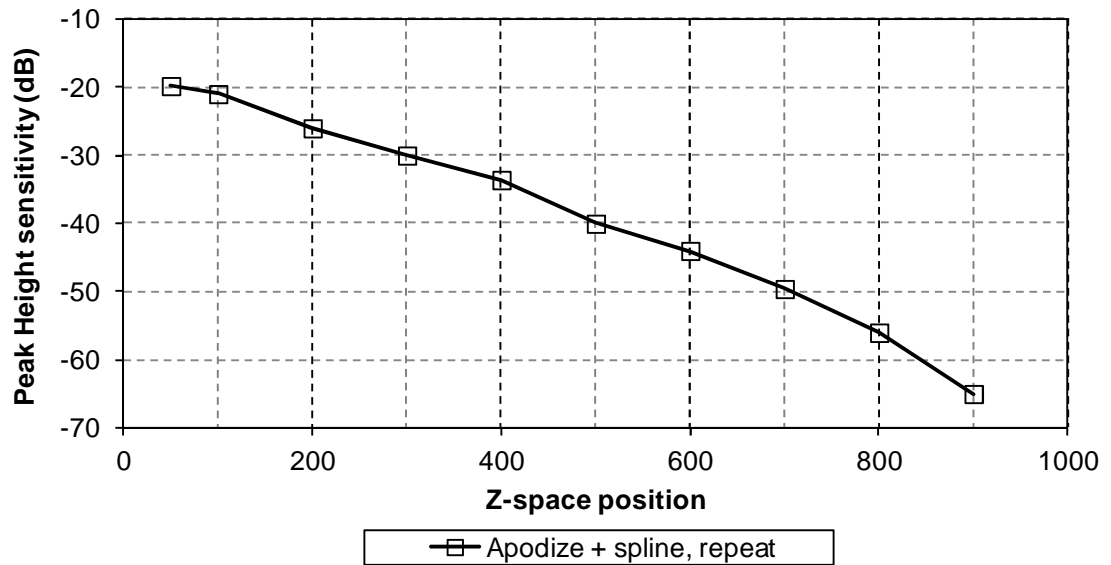


Fig.5.5 Sensitivity roll-off for Wasatch Cobra-S spectrometer

5.2.4 Technical challenges

To ensure that both channels are calibrated, we performed power and spectral reference measurements using a mirror as the sample. One challenge when using a free-space configuration is to maintain the same beam injection efficiency into the SM fibre connected to the input of the spectrometers. We released 10 mW from the SuperK Select. After the first polariser P1, total power available for the interferometer was measured at 7 mW (equivalent to 3.5 mW each into the reference and sample arm). Throughout the beam propagation path, from P1 output, to the sample (S) and reference mirror (M_R), spectral shape was checked with a short-wavelength optical spectrum analyser (OSA, model AQ6354, ANDO) to ensure the optical bandwidth was intact. By blocking the sample arm, a well calibrated recorded an equal 250 μ W at SP1 and SP2 after the SCT (taking into account of 35% free-space to fibre coupling efficiency).

We then performed the similar procedure and measured the “reference sample arm spectrum”. This is the reference (baseline) spectrum recorded for two polarisations output when a mirror is used instead. The main reason these spectra were acquired was to obtain a baseline so it can be used to normalise against the spectrum recorded with our birefringent sample, in each individual channel (SP1 and SP2), thus offsetting fibre coupling efficiency and improve SNR due to the low backscattered signal from our sample. This will give us the correct interference spectrum irrespective of beam alignment issue. The output

spectrum from the sample is shown in Fig.5.6. Note that there is some differences between the two spectra, due to the rotated polarisation state of backscattered circular wave from the mirror. By comparing the spectra in Fig.5.6 against the calibration curve in Fig.5.4, we can be certain that the full 300 nm BW was detected at the spectrometers end.

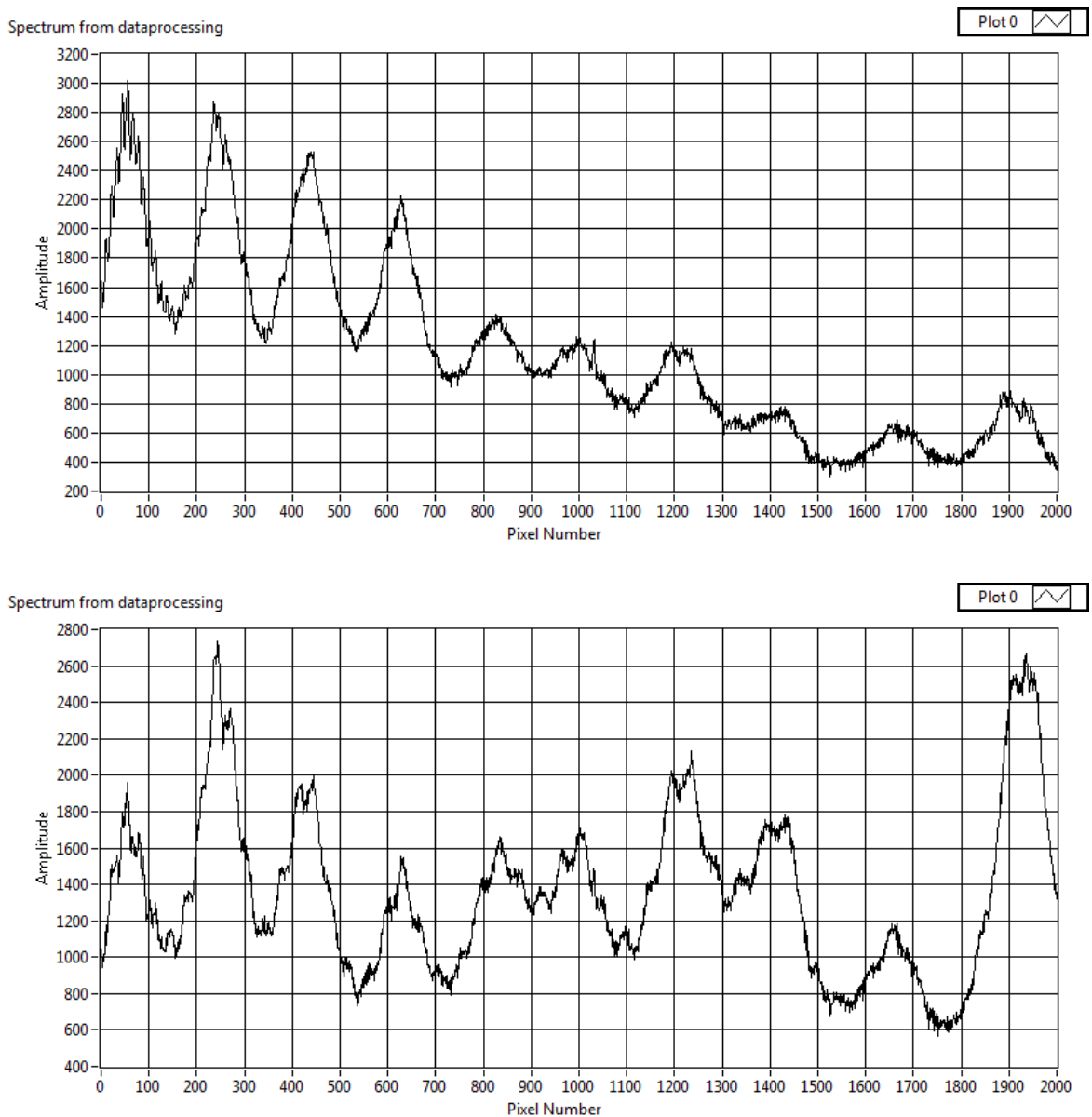


Fig.5.6 The “reference sample spectrum” recorded at the output of (top) Channel 1, using spectrometer SP1 and (bottom) Channel 2, using spectrometer SP2.

5.3 Imaging results

5.3.1 Birefringence samples

Two bank notes, specimen 1 (US \$20, cotton-fiber paper, Federal Reserve) and specimen 2 (£5, polymer, Bank of England), were imaged on their obverse side. The area imaged for both bank notes are crossed out in Fig.5.7 and 5.8 respectively. The area imaged for specimen 1 is the upper-right corner around the numeral ‘5’ imprint. For specimen 2, the image area is around eagle marking, at the bottom section.



Fig.5.7 The sample with a crossed out section showing the scan area of 8 mm × 8 mm of Specimen 1 [Source of image: <http://www.bbc.co.uk/newsround/36426215>]



Fig.5.8 The sample with a crossed out section showing the scan area of 8 mm × 8 mm of Specimen 2 [Source of image: <https://www.uscurrency.gov/security/20-security-features-2003-%E2%80%93-present>]

5.2.2 Cross-section images

To demonstrate the sophistication of our PS-OCT system, we collected cross-sectional images (B-scans) from two different banknotes with scan regions identified in Fig.5.7 and 5.8. To facilitate the collection of B-scans for both polarisations, the two channels of the PS-OCT output were used [6]. Each of the B-scans were normalised to the reference sample spectrum collected using mirror as sample to eliminate intensity discrepancy due to different fibre coupling efficiency at each channel. The data were then processed using Eqn.5.13 and 5.14 to produce the images of reflectivity and phase retardation, respectively. The direct cross-section output images for Specimen 1 are shown in Fig.5.9, while the post-processed PS-OCT images for reflectivity and phase retardation are shown in Fig.5.10. For Specimen 2, the corresponding images are shown in Fig.5.11 and 5.12, respectively.

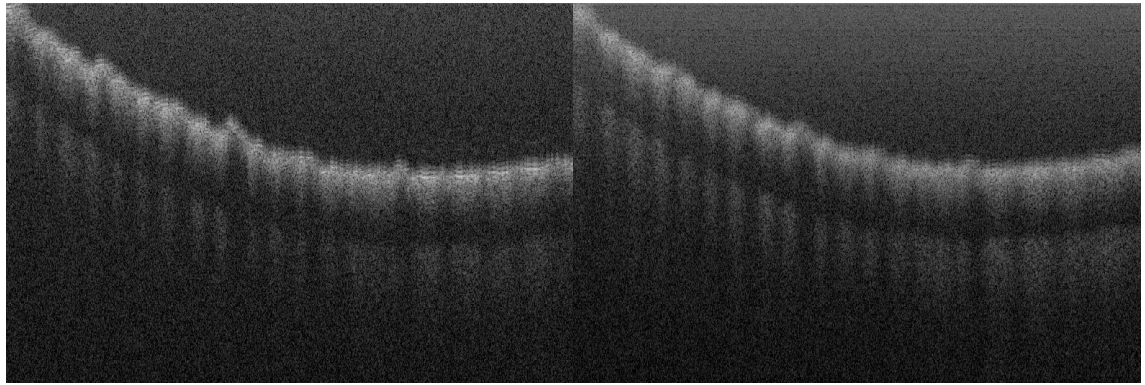


Fig.5.9 PS-OCT images output from (left) horizontal polarisation, and (right) vertical polarisation for Specimen 1.

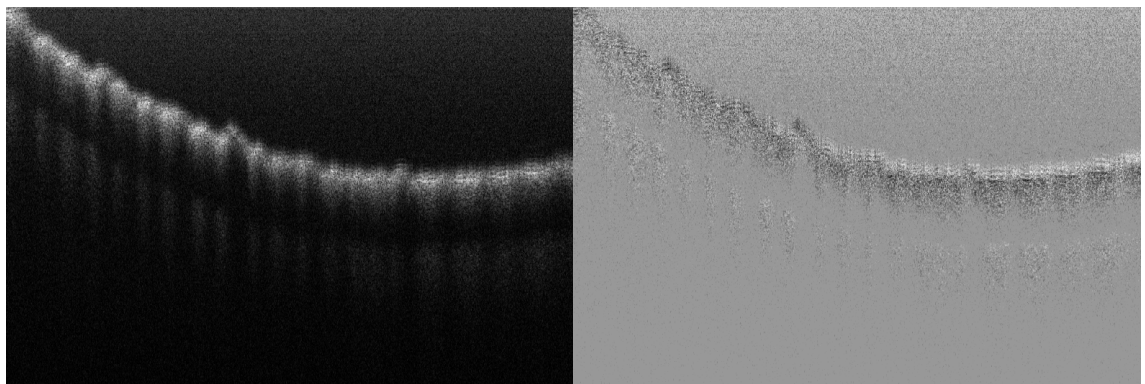


Fig.5.10 Post-processed PS-OCT images of Specimen 1 (left) intensity image showing reflectivity, (right) phase retardation.

From Fig.5.9, we observed that the reflectivity image provided us only the depth information as well as the microstructure of the imprint and the polymer layer underneath. We can deduce from Fig.5.10 (left) that the polymer substrate is basically transparent, and reflects the imprint structure as light passes through it, as the non-structure in this layer registered the same periodicity as the first imprint layer, only reduction in signal strength.

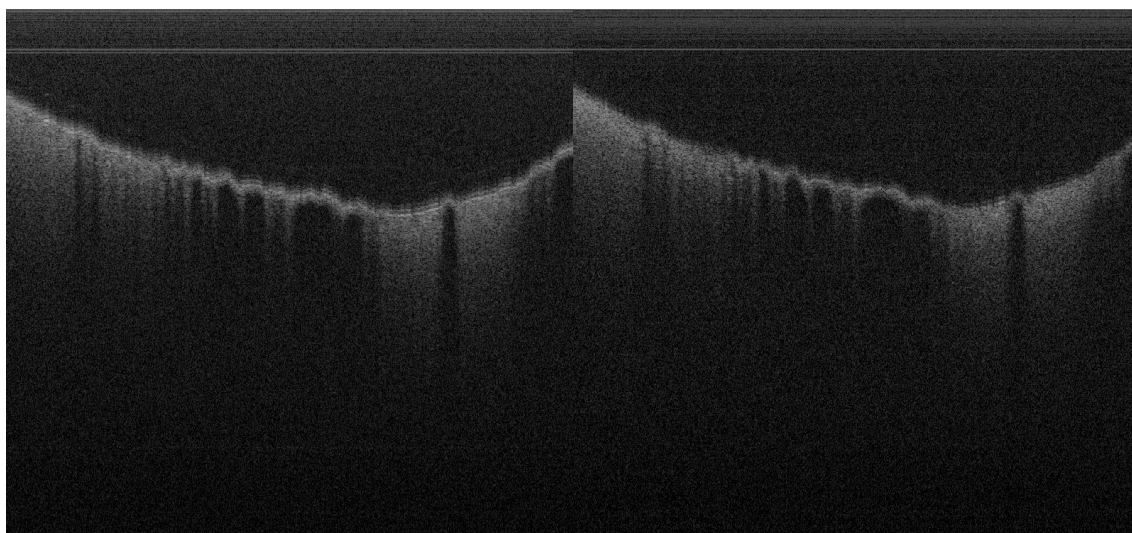


Fig.5.11 PS-OCT images output from (left) horizontal polarisation, and (right) vertical polarisation for Specimen 2.

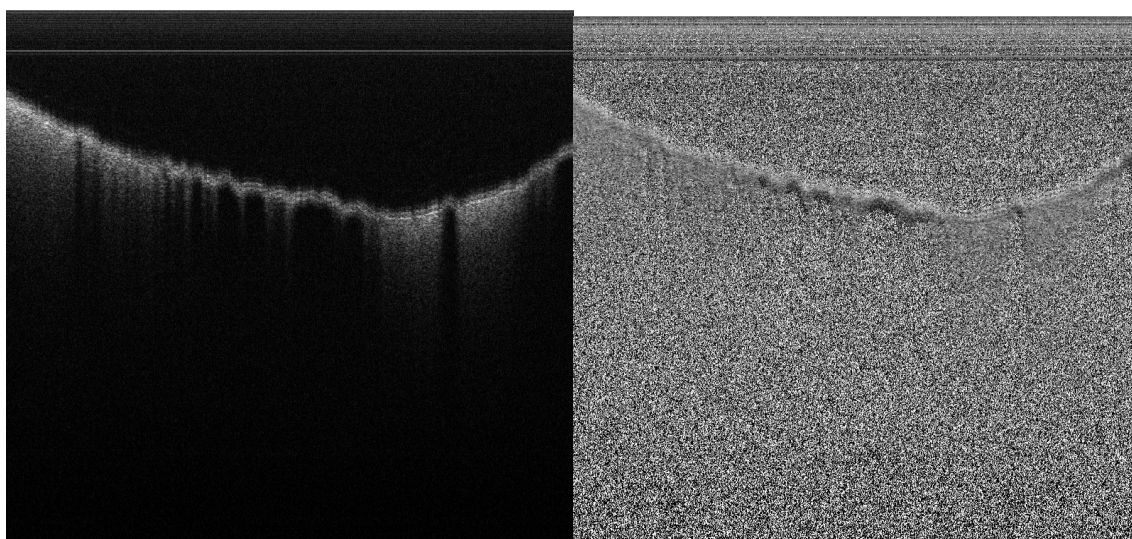


Fig.5.12 Post-processed PS-OCT images of Specimen 2 (left) intensity image showing reflectivity, (right) phase retardation

A very good example to compare the difference between polymer birefringence and fibre paper is to look at B-scan obtained in Fig.5.12 (left). In the latter case, we observed that the reflectivity image registered a structure of uneven surface of the paper.

We have therefore illustrated the proof of concept of a novel broadband PS-OCT technique with a dual-spectrometer set-up, with 300 nm optical bandwidth between 650-950 nm, powered by a supercontinuum source. This configuration allows us to achieve an axial resolution of 5 μm in air.

5.3 Future work

Our dual-spectrometer approach allows the use of single spectrometer with an automatic fibre-based switch replacing the PBS cube at the interferometer output. This recommendation will eliminate free-space to fibre coupling deficiency as only one single input to the detector is needed. The automatic polarisation switch will allow sequential recording of B-scan from each polarisation component, thus saving cost. This is the recommendation future implementation when the polarising optical parts become commercially available.

References

1. J. E. Roth, J. A. Kozak, S. Yazdanfar, A. M. Rollins, and J. A. Izatt, "Simplified method for polarization-sensitive optical coherence tomography," *Opt. Lett.* 26, 1069-1071 (2001).
2. J. Zhang, S. Guo, W. Jung, J. Stuart Nelson, and Z. Chen, "Determination of birefringence and absolute optic axis orientation using polarization-sensitive optical coherence tomography with PM fibers," *Opt. Express* 11, 3262-3270 (2003).
3. S. Guo, J. Zhang, L. Wang, J. Stuart Nelson, and Z. Chen, "Depth-resolved birefringence and differential optical axis orientation measurements with fiber-based polarization-sensitive optical coherence tomography," *Opt. Lett.* 29, 2025-2027 (2004).
4. Z. Ding, C.-P. Liang, Q. Tang, and Y. Chen, "Quantitative single-mode fiber based PS-OCT with single input polarization state using Mueller matrix," *Biomed. Opt. Express* 6, 1828-1843 (2015).
5. M. R. Hee, D. Huang, E. A. Swanson, and J. G. Fujimoto, "Polarization-sensitive low-coherence reflectometer for birefringence characterization and ranging," *J. Opt. Soc. Am. B* 9, 903-908 (1992).

6. C. K. Hitzenberger, E. Götzinger, M. Sticker, M. Pircher, and A. F. Fercher, "Measurement and imaging of birefringence and optic axis orientation by phase resolved polarization sensitive optical coherence tomography," *Opt. Express* 9, 780-790 (2001).
7. J. F. de Boer, T. E. Milner, M. J. C. van Gemert, and J. S. Nelson, "Two-dimensional birefringence imaging in biological tissue by polarization-sensitive optical coherence tomography," *Opt. Lett.* 22, 934-936 (1997).
8. E. Götzinger, M. Pircher, and C. K. Hitzenberger, "High speed spectral domain polarization sensitive optical coherence tomography of the human retina," *Opt. Express* 13, 10217-10229 (2005).
9. B. E. A. Saleh and M. C. Teich: *Fundamentals of Photonics*, 2nd Ed. Wiley (2007).
10. P. N. Butcher and D. Cotter: *The Elements of Nonlinear Optics*, Cambridge Univ. Press (1991).
11. E. Collett, *Field Guide to Polarisation*, SPIE Press, Bellingham, WA (2005).
12. M. E. Brezinski, *Optical Coherence Tomography: Principles and Applications*, Academic Press, 197-236 (2006).
13. J. P. Dunkers, F. R. Phelan, D. S. Sanders, M. J. Everett, W. H. Green, D. L. Hunston, and R. S. Parnas, "The Application of Optical Coherence Tomography in Problems in Polymer Matrix Composites", *Journal of Optics and Lasers in Engineering*.
14. J. P. Dunkers, M. J. Everett, D. P. Sanders, and D. L. Hunston, "Imaging of Composite Defects and Damage Using Optical Coherence Tomography", *Proc. of PLAST, Advancing with Composites* (2000).

6

Application of OCT in biomedical imaging

Optical imaging of skin malignancy has generated huge interest among the medical community recently thanks to more recent development of contactless and non-invasive imaging technique such as OCT. In this chapter, we teamed up with clinicians from the Maidstone and Tunbridge Wells NHS Trust Hospital, Prof. Dr John Schofield, Dr Mona Khandwala, and Miss Rongxuan Lim, to image basal cell carcinoma (BCC) using the *en-face* OCT system we developed in Applied Optics Group, at the University of Kent.

BCC is the most common form of skin cancer in Caucasians [1] and accounts for 80-90% of all eyelid malignancies [2,3]. It is estimated that there are 53,000 new BCC cases diagnosed in UK yearly [4]. The gold standard for tumour diagnosis involves surgical biopsy for histological analysis [5]. To reduce patient morbidity from surgery, non-invasive methods of diagnosis and determining tumour margins have been investigated in recent years. They include reflectance confocal microscopy (RCM) [6], high frequency ultrasound (HFUS) [7], multispectral imaging [8], multiphoton microscopy [9], fluorescent technique [10], confocal scanning laser microscopy (CSLM) [11] and optical coherence tomography (OCT) [12,13]. Although these technologies provide valuable information, they are not yet widely adopted by mainstream health care professionals to provide high level of certainty essential for accurate treatment. None of these emerging techniques have been used entirely independently, or proved to be superior to the gold standard. These new techniques are often used to bridge the gap of limitation on established technologies, demanding new imaging systems with better penetration depth and sensitivity. Nevertheless, recent literature has suggested that OCT in *en-face* imaging mode presents the potential of improved diagnostic specificity of BCC morphology compared with clinical assessment and dermoscopy alone [14-15].

For this reason, we implemented an *en-face* optical coherence tomography (OCT) system powered with our enhanced master-slave (MS) technique [16]. Compared to conventional fast Fourier transform (FFT) based OCT, the MS technique is tolerant to the

non-uniformities in the modulation frequency of the spectra acquired as well as to dispersion in the interferometer [17]. Therefore, the MS technique allows achieving the theoretical expected parameters for the sensitivity and for the axial resolution, as determined by the bandwidth of the system, and by the spectral domain principle. The MS technique leads to attainment of such values with no need for resampling of data. In conventional FFT based OCT, the axial resolution and sensitivity are as good as the resampling and data linearization methods, which generally operate well at shallow depths only. Additionally, the MS technique gives direct access to information from selected depths, allowing real time display of one or more en-face OCT images from such depths [18]. The MS method has been applied to OCT imaging of the eye fundus, and by harnessing the power of graphic cards, real time production of *en-face* images was made possible [19].

This is a pilot study aiming to correlate the histological features of periocular BCC to features seen on the OCT scan using the MS technique. To the best of our knowledge, this is the first pilot study using Master/Slave OCT technique for imaging periocular BCCs. Prior to this thesis work, three other studies to image BCC were conducted by our group in collaboration with clinicians from the Maidstone Hospital. These studies have explored the use of dual wavelengths (840 nm and 1300 nm) time domain (TD)-OCT [20], FFT based OCT [21] and dynamic focus (DF)-OCT [22]. Based on the experience we gathered from these three tests, we identified that essential in performing accurate correlations with histology data, is to acquire high resolution OCT images and correctly identify the margins of any skin lesion precisely. On the wavelength selection, we identified that light at 1300 nm suffers less scattering in tissue, thus providing better signal strength compared to 850 nm when used for imaging BCC [19-23].

Independent to our group's research, the use of 1300 nm for OCT imaging was further documented by the study of BCC that employs a combined RCM/OCT system for ex-vivo imaging [24]. The data processing of OCT signals is based on conventional FFT based technique. In contrast to MS technique, dispersion compensation and interpolation are employed. The resulting set of 512 OCT raster images using their method could be acquired in 13 s. While the RCM channel delivers en-face images, the OCT is performed in cross section. Single en-face images are inferred by software cut of volumes of A-scans and placed in comparison with the RCM images. Another study employed a commercial 20 kHz tuneable laser to produce 120 stack OCT images of size 6 mm × 6 mm in between 10-20s [25]. None of the OCT systems referenced above are capable of producing *en-face* images in real time.

As we move towards clinical diagnosis, speed is of ultimate premium when it comes to sheer volume of patients. Across the UK, most patients spent only 3-5 mins at their general practitioner (GP) office. The ability to get an *en-face* scan done within this timeframe will revolutionise the way OCT is perceived in the medical community, and open the door for rapid technology adoption across all health care sectors.

The use of high-definition OCT as an auxiliary diagnostic tool to histology has received overwhelming positive response by clinicians, as evidenced by a study that looked into the effectiveness of locating BCC with OCT. This was compared to histology analysis involving both experienced and inexperienced dermatologists [26]. We drew inspiration from these state-of-the-art research studies in developing our Master/Slave OCT system, with an aim to offer simplified, more robust image display in a shorter time.

6.1 Clinical significance of BCC

6.1.1 Classification of BCC

Basal cell carcinoma occurs when one of the skin's basal cells develops a mutation in its DNA. Most of the damages to basal cell's DNA are resulted from accumulated dosage of direct ultraviolet (UV) radiation, such as chronic sunlight exposure, persistent use of commercial tanning lamps, undergoing repetitive radiation therapy for psoriasis or other skin conditions. However, many clinical findings have shown that sun exposure alone is not necessary the only cause of skin cancers that develop on skin not ordinarily exposed to sunlight. Several risk factors in Table 6.1 could indicate potential development of BCC.

Table 6.1 Four major statistical risk factors of BCC patients

Risk factors	BCC likelihood
(a) Age	BCCs are more prevalence for over 50s since tumours take decades to develop and metastasise
(b) Sex	Men are statistically (about twice) more likely to develop BCC than women in general populace
(c) Hereditary	Persons with family history of skin cancer can expect higher probability to develop BCC some stage in their life
(d) Skin pigment	People with fair, light skins are more likely to contract BCC than those with darker skin tones

Based on the statistics gathered over decades, physicians can now better identify group of patients with higher risk of developing BCC in their life, and perform early diagnosis as part of the routine medical examination.

Classical treatment protocols for BCC involve surgical techniques carried out by a surgeon and a histologist. After the patient was taken to surgical theatre, the skin area with distribution of basaloid cells is marked off, and then excised together with a variable margin of clinically normal surrounding tissue. This approach of removing additional healthy tissue is to make sure the entire sector of basaloid cells is excised in one go, to prevent tumour tissue left behind. Depending on initial diagnosis, the variable margin can often result in too much normal skin being discarded. Therefore, one of the aims of an *en-face* OCT system is to address this problem by probing the actual tumour margin. After the surgical operation, the peripheral and deep surgical margins of the excised tissue are examined histologically using intra-operative frozen sections. A more common way is to use the postoperative vertical sections taken from formalin-fixed, paraffin-embedded tissue. This approach is used primarily for increasingly wide surgical margins for incompletely excised and recurrent lesions.

Broadly speaking, clinical classification of BCC falls into four major types: nodular, superficial, pigment and morpheaform. Other more complex forms of BCC such as infiltrating, micro-nodular, and differentiated BCCs contain one or more features of the major subtype. In Table 6.2, we grouped the dominant characteristics of BCC associated to its sub-types, with the reported occurrence of each type relative to the others.

Table 6.2 Four major BCC subtypes and their associated histomorphology features

BCC subtype	Histomorphology features	Prevalence
Nodular	translucent node with a rolled border, peripheral palisade of basaloid cells	Most common
Superficial	proliferation of basaloid cells parallel to long axis of the epidermis, slit-like retraction of the basal cells	Common
Morpheaform	sclerosing type with columns of thin basaloid cells enmeshed in a densely collagenised stroma	Least common
Pigment	subset of superficial BCC predominately on people with dark eye colour and darker skin phototypes	Very rare

The symptoms of an early stage BCC can be identified by the area of skin or lesions that appears to change in texture, colour and structure. By relating these symptoms to major BCC subtypes, we can design an OCT system to identify patients with these skin characteristics. For the most common case, a nodular BCC exhibits a translucent lesion with pearly white, skin-coloured or pink bump, allowing tiny blood vessels to be visible from the lesion surface. An OCT system operating in the 1300 nm is best suited to probe this kind of BCC. On the other hand, BCCs with a flat, scaly and reddish patch scattering around the skin can be detected by naked eye. An OCT system can be used to aid the validation of tumour, therefore eliminating false diagnosis. However, as the presence of BCC on skin lesions can be random, an OCT technology capable of automatically distinguishing one BCC subtypes from another is useful. In our application chapter, we concentrate only on eyelid (periocular) BCC using our MS-OCT system.

6.1.2 Histology tissue imaging

Three consecutive patients over the age of 18 with a biopsy proven periocular nodular BCC, without previous eyelid surgery, were enrolled into the study. The study protocol (“Ethical Approval”) was approved by the Research and Development Department of the Maidstone and Tunbridge Wells NHS Trust, and also by the Ethics Committee at the School of Physical Sciences, University of Kent. Informed consent was obtained from the participants. All procedures relating to removal, storage and transport were carried out in accordance to Human Tissue Act 2004 (UK) under the licence acquired by the NHS Trust from Human Tissue Authority (HTA).

All BCC lesions were surgically excised with predetermined 2 mm margins of normal skin. The orientation of each specimen was specified by using 6/0 silk sutures of various lengths to mark 3 of the margins of the lesion. The excised specimens were placed in 10% neutral buffered formalin and transported from Maidstone Hospital to the University of Kent within 3 hours of excision for OCT imaging. For purpose of image acquisition, the BCC tissue was placed on a transparent microscope glass slide, with its superior margin aligned to the horizontal direction of the optical beam axis at the microscope focus of the OCT machine. After OCT imaging was completed, the specimens were placed back into 10% neutral buffered formalin and transported to the Maidstone Hospital Histology Department the same day.

6.1.3 Histology correlation

The specimens were allowed to fix in 10% neutral buffered formalin for 24 hours and then "bread sliced" at 2 mm intervals at 90 degrees to the skin surface retaining orientation as denoted by marking sutures. Each slice was processed and paraffin embedded with serial sections cut at 2 μm intervals, then mounted on glass slides, stained with haematoxylin and eosin and viewed in a conventional light microscope. Photomicrographs were captured for comparison with OCT images and correlation undertaken by identification of the matching features of the OCT and histology images under supervision of Prof. Dr. John Schofield, at the Maidstone Hospital.

The procedures to correlation are described in details in Section 6.2.2. *En-face* OCT images are matched side by side to histology image at different tissue depth, beginning from slice 192 (denoted as middle point) and extend every 5 slice interval above and below the middle. Probable BCC features on *en-face* images are searched by naked eye comparison to description in Table 6.2, then correlate against confirmed BCCs in histology image. To assist with large number of *en-face* images, ImageJ software was used to facilitate image manipulation: slice stacking, transformation and 3D volume construction.

6.2 *en-face* imaging

The imaging of *en-face* BCC samples were performed using a custom built MS-OCT system as discussed in Section 6.2.1. The post-analysis and step-by-step correlation of *en-face* images to histology scans are demonstrated in Section 6.2.2. Finally, a technical comparison has been made between our current results, image qualities and OCT system performance in Section 6.2.3.

6.2.1 Master/Slave OCT machine

The schematic diagram of the MS-OCT system assembled is shown in Fig. 6.1. Light is first emitted from a tuneable swept source (SS) operating at 1310 nm central wavelength with a 100 nm sweeping range, 50 kHz sweeping speed and 15 mW max output power (model SSOCT-1310, Axsun Technology, MA, USA). An interferometer, using two directional fibre couplers, DC1 and DC2 was assembled. The light from the source enters the first directional coupler (DC1, model FOBC-2-1310-20, AFW Technology, Australia) with a splitting ratio of 80:20. One output delivers 80% of light intensity into the reference arm, and 20% of light into the object arm.

In the object arm, the interface optics includes an achromatic lens (CM) to collimate the output beam of the fibre, four lenses for beam expansion (L_1 - L_4 , $f=75$ mm, AC-127-030-C, Thorlabs) and a scan lens (SL). The SL is an OCT optimized microscope objective (LSM03, 5x, Thorlabs). For a 4 mm beam diameter incident on the SL, transversal resolution of the spot on the sample is $15 \mu\text{m}$. The transversal resolution obtained was verified by imaging a USAF 1951 resolution target. To facilitate image acquisition, a set of two galvo-scanners are installed in the object arm, denoted respectively as G_X (frame) and G_Y (line) in Fig. 6.1 below.

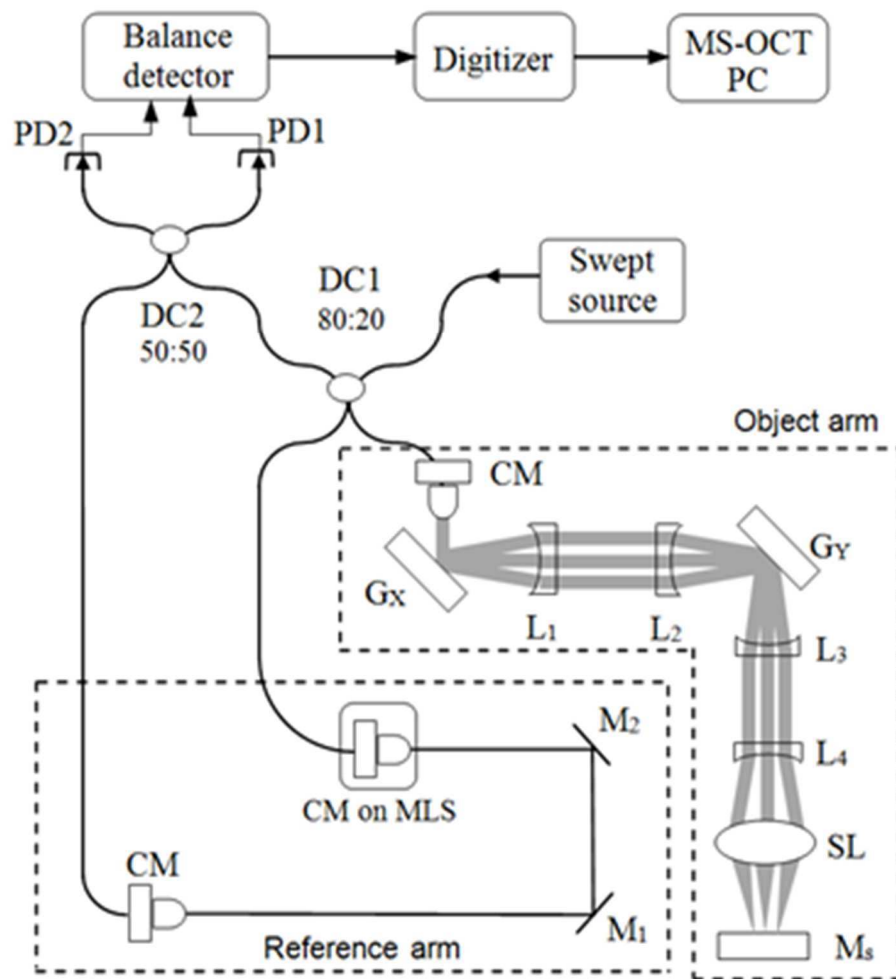


Fig. 6.1 MS-OCT system configuration (G_X , G_Y : galvo scanners, L_1 , L_2 , L_3 , L_4 : lenses, SL: scan lens, M_1 , M_2 : mirrors, CM: free-space to fibre coupler, MLS: motorized linear stage; DC: directional coupler; PD1, PD2: InGaAs photodiodes; M_s : mirror used at the Master stage, to be replaced with the BCC specimen at the Slave stage).

Both G_X and G_Y are driven with triangular ramps. Since SS has a tuning frequency of 50 kHz, each of the 200 lateral pixels are acquired within 20 μ s. G_X is driven with a triangular signal, where each ramp duration is $20 \mu\text{s}/\text{pixel} \times 200 \text{ pixels} = 4 \text{ ms}$, with every other ramp discarded, so at a frequency of 125 Hz. The frame scanner G_Y is driven with a triangular signal, which for 200 lines, requires 1.6 s. With a measured transversal resolution of 15 μ m, the lateral image size is limited to 3 mm \times 3 mm. A single ramp of the frame signal is used for data acquisition while the other ramp is used for data transfer to the GPU and data processing. As a result, the time needed to acquire each 2D en face dataset of $200 \times 200 = 40,000$ channelled spectra is 1.6 s.

The light into the reference arm is reflected off a set of mirrors (M_1 , M_2), then into the second directional coupler (DC2, model FOBC-2-1310-50, AFW Technology, Australia), where it is combined with signal from the object arm, to produce interference patterns. The outputs of the DC2 are connected to the photo detectors PD1 and PD2 of a balance photo-detector module (model BPD-200, Santec, Japan, 200 MHz). This signal is sent to a digitizer (Alazartech, Canada, model ATS9350, 500 MB/s). This is embedded into a PC with an Intel Xeon processor (model E5646, 2.4 GHz, 6 cores) and a GPU card (GeForce GTX 780 Ti), loaded with a custom 64-bit LabVIEW 2014 program to display simultaneously en-face images from 40 different depths [28-29].

The imaging process using the master-slave (MS) method is a two-step process. First, at the Master stage, a mirror (M_S) is placed in-lieu of the BCC specimen in the focal plane of SL. A set of 384 channelled spectra (masks), are collected and stored. The masks are acquired for MLS positions separated by 10 μ m steps using a motorized translation stage, MLS (model MFA-CC, repeatability 0.3 μ m, speed 2.5 mm/s, Newport) driven by a motion controller (ESP301, Newport). These masks represent the channelled spectra at the OCT interferometer output for 384 values obtained by equivalently displacing the mirror M_S by 5 μ m. Thus, with 384 masks, an axial depth range of 1.8 mm in air is achieved.

A special program was created to allow quick acquisition of masks by shifting the MLS to a new incremented position by the chosen differential interval (10 μ m) followed by time to wait for mechanical vibrations to settle and then followed by the storage of mask for that position, and then moved to the next position and so on. The whole process takes less than 5 minutes and once masks are collected the process does not need to be repeated. Collection of masks is performed with no voltage applied to the two galvo-scanners, i.e. using the optical beam on axis.

The second (Slave) stage involves imaging the BCC specimen that replaces the mirror Ms. Each BCC specimen is positioned in front of the SL. 384 *en-face* images are obtained by correlating the 384 masks with the acquired channelled spectra of the BCC tissue, but a reduced number of such images is displayed, in this case 40. Figure 6.2 shows a typical screen of the raster displayed by the MS technique. Three categories of images are simultaneously presented and they are refreshed simultaneously:

- (a) *en-face* OCT images (reference to XY plane) at 40 simultaneous depths,
- (b) two cross section images (B-scans, one at 90° orthogonal to surface YZ, another at 90° orthogonal to surface XZ), and
- (c) a compound image to help with guidance, made from the average of the 40 *en-face* images displayed.

The *en-face* OCT images and the compound image have 200×200 pixels whilst the cross section OCT images have 200 pixels lateral and 384 pixels in depth (along the vertical axis, equal to the number of masks). The differential distance between the numbers of *en-face* images displayed as well as the depth of the first *en-face* images in the left corner can be adjusted with cursors on screen (not shown, but similar to the procedure detailed in [28]). The compound display was found useful in adjusting the relative position of the specimens in front of the scan lens SL. Here this uses the 40 images displayed, however this can be modified to use any number in any order of the 398 *en-face* images generated by the end of each scanning frame.

Each category of images is produced using a special program developed in CUDA (Compute Unified Device Architecture). The simultaneous display of the three categories of images takes advantage of methods developed in previous reports [22], [29], to speed up the processing of comparison operation at the core of the MS technique to the level where it can compete with the FFT based OCT method, while maintaining the other MS advantages (tolerance to dispersion and tuning nonlinearities with implications in achieving high axial resolution and better sensitivity).

The axial resolution of the system is determined by the tuning bandwidth of the optical source. With a SS of $\Delta\lambda=100$ nm bandwidth, we can expect an axial resolution of around 7.5 μm (Eqn. 2.1). When a broadband source ($\Delta\lambda>300$ nm) is used, a sub-5 μm axial resolution can be achieved.

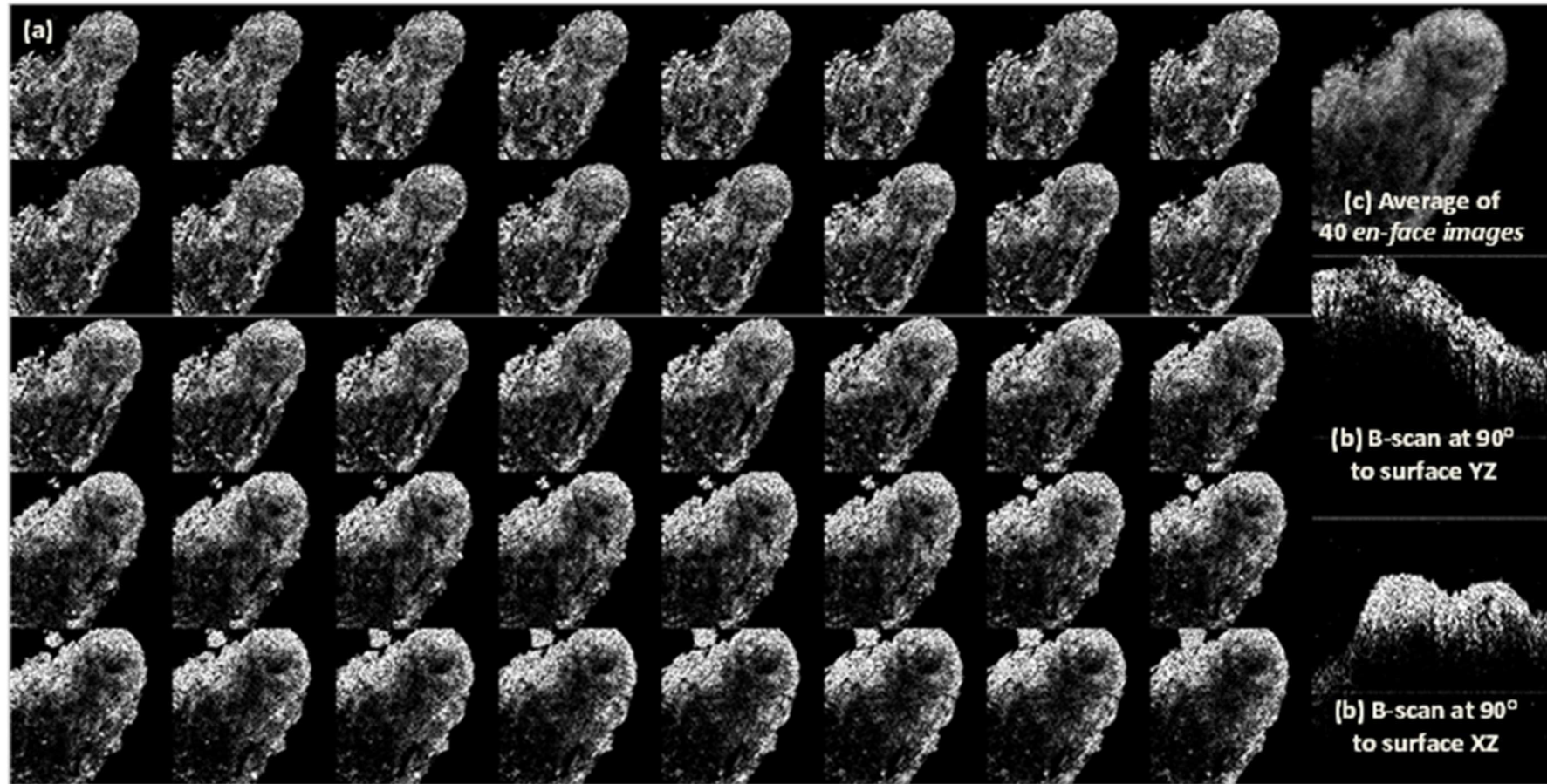


Figure 6.2: Illustration of Master/Slave raster made from 3 categories of images. (a) 40 en-face OCT images separated axially by $5 \mu\text{m}$ (measured in air), (b) two cross-section OCT images acquired from two orthogonal orientations and (c) an average of the en-face images displayed for guidance. The horizontal size of all images and the vertical size of en-face OCT images: $3 \text{ mm} \times 3 \text{ mm}$. The vertical size of the two cross section images is $3 \text{ mm} \times 1.5 \text{ mm}$ (measured in air). The en-face images have 200×200 pixels while the cross section images 200×300 pixels.

Histology data are collected in cross-section plane. Therefore, to compare and correlate suspected BCC features side by side, we need to prepare such cuts from the *en-face* images produced by the MS technique. Therefore, for subsequent analysis, the *en-face* slices acquired are stacked to form a 3D volume. A slice was cut orthogonally to the *en-face* surface to produce a cross section OCT image, as shown in Fig. 6.3.

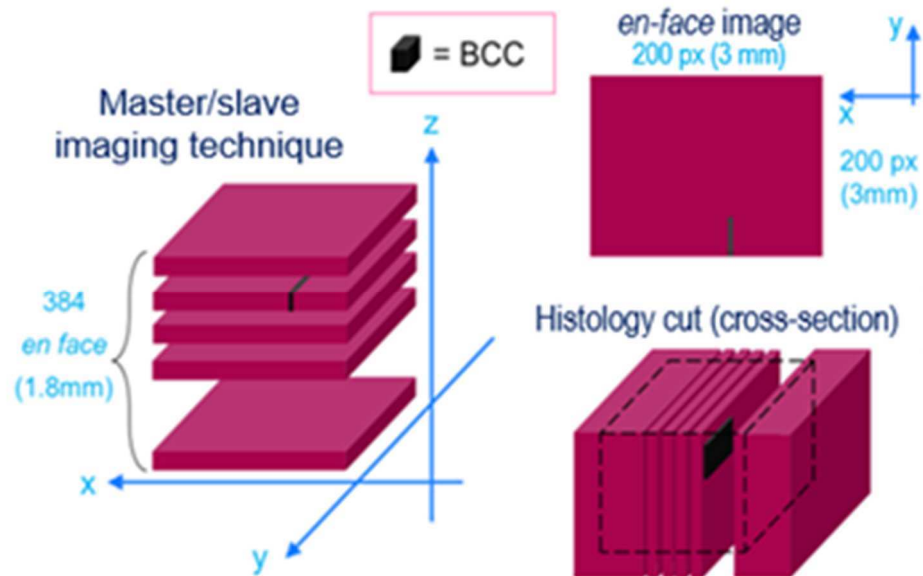


Fig. 6.3 Illustration of assembling cross-section scans from *en-face* images. *En-face* images are delivered by the MS-OCT technique

6.2.2 BCC correlation techniques and results

The three separate excised BCC specimens' biopsy tissues from the three patients were imaged using the MS-OCT system. Each sample has been marked Case 1, Case 2 and Case 3 respectively.

To allow comparison to histology data, we assembled the *en-face* images into a 3D volume. A cross section OCT image was then sliced orthogonally to the volume surface. Using this method, 200 cross section images were reconstructed at different lateral positions. We ran our algorithm through all these images from the centre of the sample to locate possible BCC features contained within each cross section images. Diagnosis of BCC via OCT correlation requires demarcation of tumour margins to determine BCC invasion, and visual interpretation of morphological features as reported in pathology-to-OCT correlation studies [30-33].

Histology images of Case 1 using an Olympus BX50 microscope are shown in Fig. 6.4. The haematoxyphilic (purple) areas equate to lobules and strands of BCC. The eosinophilic (pink) areas are supporting stroma and normal dermis. The corresponding OCT cross sections are shown in Fig. 6.5. The areas containing BCCs are compared against the marked area in the histology image. *En-face* images taken at 30 μm axial interval from each other (measured in air), showing features at depths of 450, 480 and 510 μm from the top of the sample are shown in Fig. 6.6. The corresponding BCC areas are noticeable with several dark spots surrounded by bright regions.

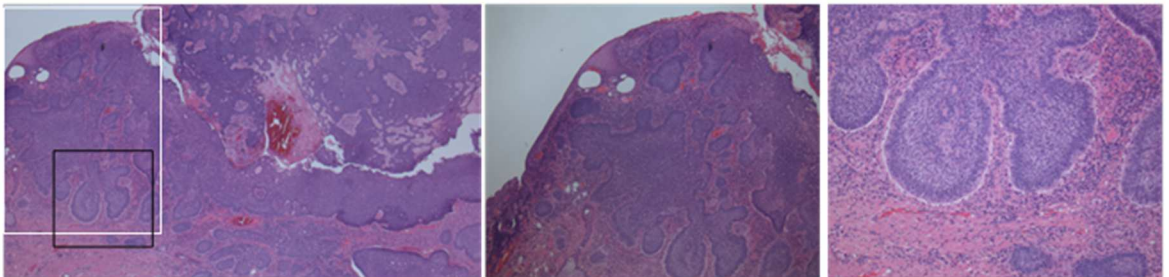


Figure 6.4: Histology images of the nodular BCC corresponding to tissue sample of Case 1. The images show tumour lobules that correspond to honeycomb structures. The lateral size \times depth size of left image is 5 mm \times 3 mm. The middle image shows an enlarged view of the white boxed region in the left image. The right image shows an enlarged view of the black box area in the left image. Magnification: left $\times 10$, middle $\times 20$, and right $\times 100$.



Figure 6.5: Results of Case 1. Cross section OCT images of eyelid BCC taken from three consecutive transverse slices at the centre of the sample. The left, middle and right slices are each separated by 15 μm . The size of image is 1.2 mm \times 0.8 mm. The arrows show the suspected areas of BCC.

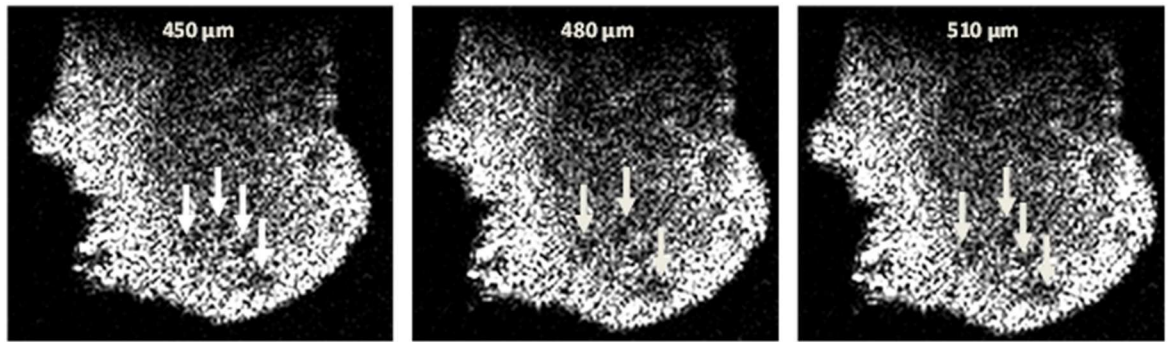


Figure 6.6: Results of Case 1. *En-face* OCT images of eyelid BCC taken at different depths. The depth was measured from the top of the sample in air. The lateral size of image is $1.5 \text{ mm} \times 1.5 \text{ mm}$. The arrows show the areas of BCC correlated with histology data.

A more extensive type of BCC was spotted from another region of Case 1 as shown in Fig. 6.7. The tumours spread around in a non-uniform pattern surrounded by healthy tissue. In the *en-face* image, noticeable pattern of uneven dark stretches indicate the presence of tumour. One definite indicator of BCC in OCT images is the reduction of signal intensity. The presence of BCC in the *en-face* images in Figs. 6.6-6.7 are manifested in clusters of signal-free dark spots, rather than in continuous bounded areas, primarily due to the position of BCC tumour spreads across multiple axial layers of *en-face* images.

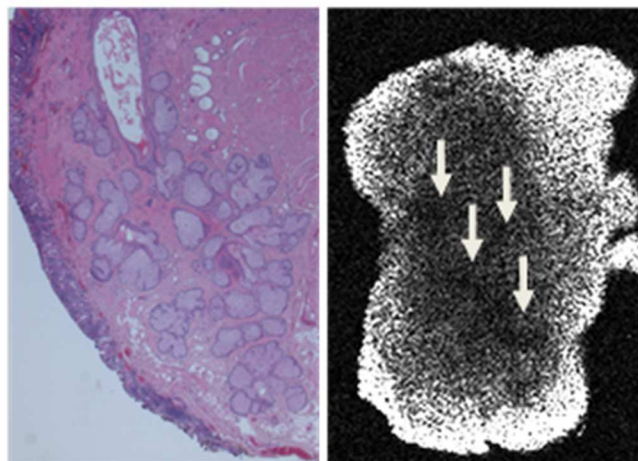


Figure 6.7: Results for another region of Case 1. (left): histology image showing blocks of BCC tumours. (right): *En-face* OCT image of corresponding region taken at a depth of $780 \mu\text{m}$ from top of sample (measured in air).

The second experiment was carried out using samples of Case 2. Clinical microscopy images are shown in Fig. 6.8. The purple areas are identified as BCC by the histologist. Cross section and *en-face* images taken from this case with features associated of BCC are shown in Figs. 6.9 and 6.10. Various features are detected in the cross section OCT images in Fig. 6.9:

- (1) sweat ducts identified by a consistent shallow shaft,
- (2) cross section blood capillary showed up as a highly reflective circle, and
- (3) suspected BCC tumours with irregular reflectivity contrasts.

Other features suspected to be BCC in OCT images (detected by an early report using time domain OCT with dynamic focus [22]) can also be seen in images generated using the MS-OCT.

These features are noticeable in Fig. 6.10 with scattered high-reflectivity areas that exhibit size enlargement as we move deeper into depth. BCC tissues are usually highly reflective at 1300 nm, leading to dark scattered margins surrounded by low-reflectivity tissue. The tissue areas that are lacking these random dark patches are identified as healthy tissue.

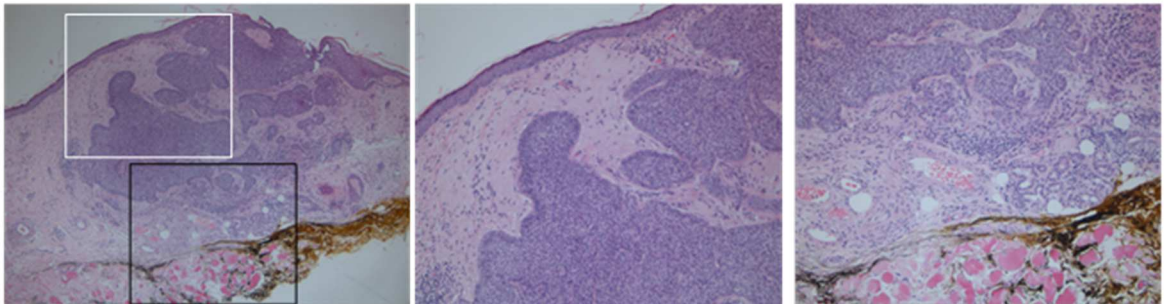


Figure 6.8: Histology images of superficial BCC from tissue sample of Case 2. The image on the left shows a tumour exhibiting nested and budding patterns. The lateral size \times depth size of the left image is 4 mm \times 3 mm. The middle image is an enlarged view of the white boxed region in the left image. The right image is an enlarged view of the black box area in the left image. Magnification: left \times 20, middle \times 50, and right \times 50

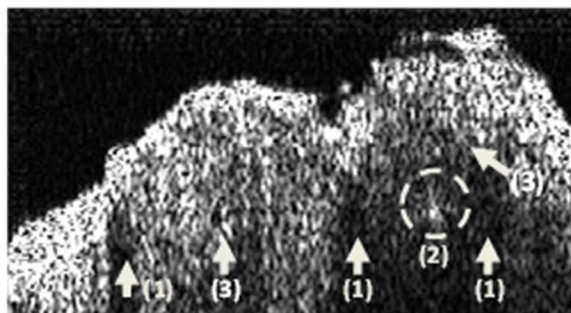


Figure 6.9: Results of Case 2. Cross section OCT images of eyelid BCC taken from the centre of tumour. (1) sweat ducts. (2) blood capillary under the dermis layer. (3) suspected areas of BCC. The lateral size \times depth size of image is 1.5 mm \times 0.6 mm

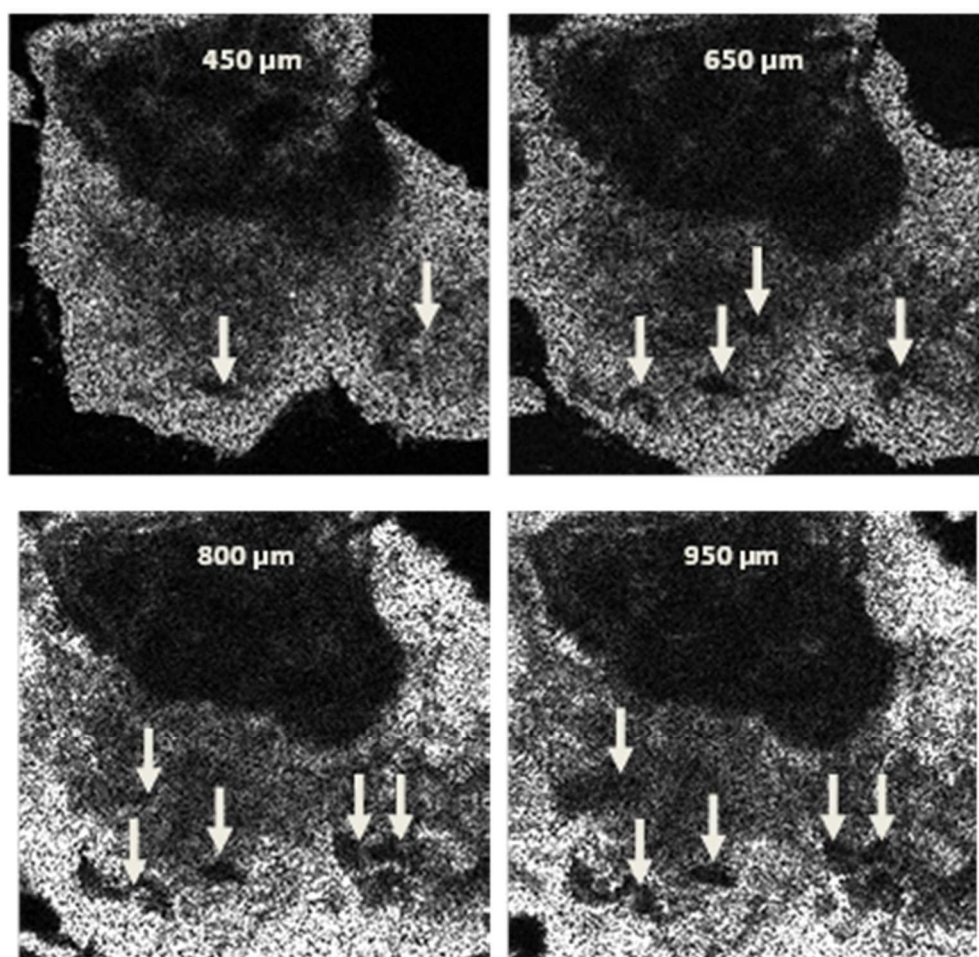


Figure 6.10: Results of Case 2. *En-face* OCT images of eyelid BCC taken at different depths between 450 to 950 μ m. The depth was measured from the top of sample in air. The arrows show the areas of BCC correlated with histology data in Fig. 6.8. The size of each image is 1.5 mm \times 1.5 mm

An immediate practical advantage of *en-face* imaging is showing the direction in which tumours metastasize. With each *en-face* image displaying the area of BCC in transverse plane in constant intensity, less complicated analysis is required to identify the tumours, compared to measuring reduction of signal strengths in the cross section OCT images. This feature is particularly important to determine the lateral borders of a BCC tumour adjacent to healthy tissue.

The MS-OCT ability to detect pigmented type BCC is further evidenced in Case 3. Histology images in Fig. 11 show tumour lobules concentrated in pigment surrounded by healthy tissue. Due to high reflectivity of BCC, higher concentration of tumour cells blocked light transmission in tissue, producing a signal-free dark spot in the middle of the cross section OCT image as evidenced by arrows in Fig. 12.

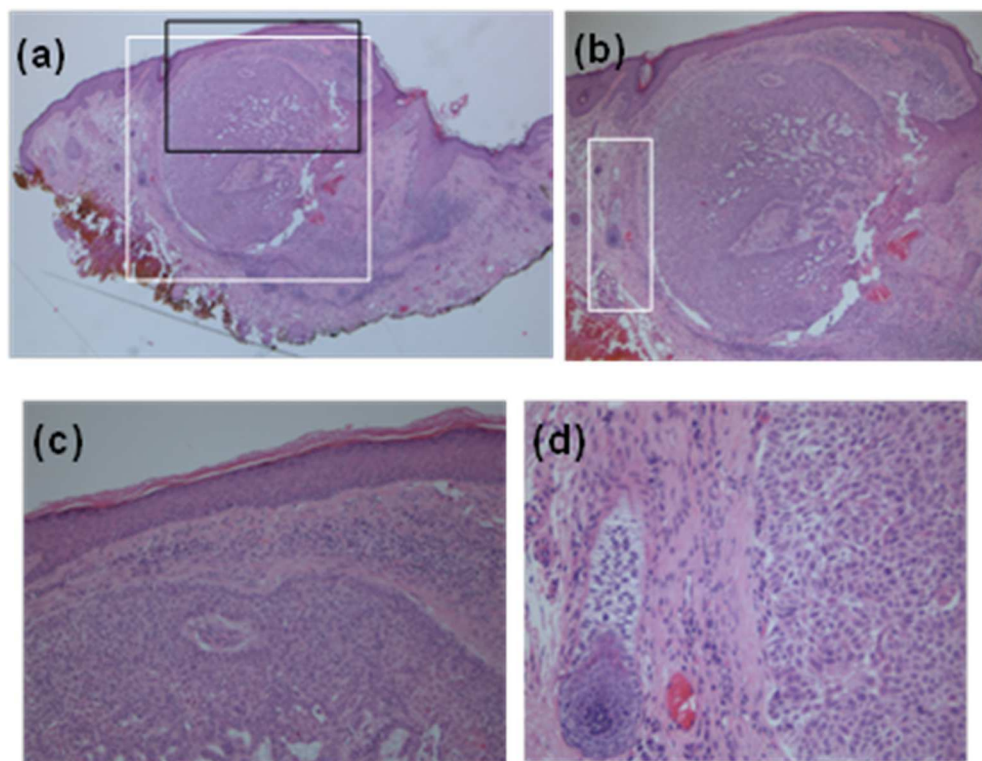


Figure 6.11: Histology images of Case 3. Image in (b) shows an enlarged view of the white boxed region in image (a). Image (c) shows an enlarged view of the black box area of image (a). The image (d) shows an enlarged region of image (b) indicating presence of nodular pigmented type BCC tumour lobules beneath the epidermis. Magnification: (a) $\times 20$, (b) $\times 50$, (c) $\times 100$, (d) $\times 200$

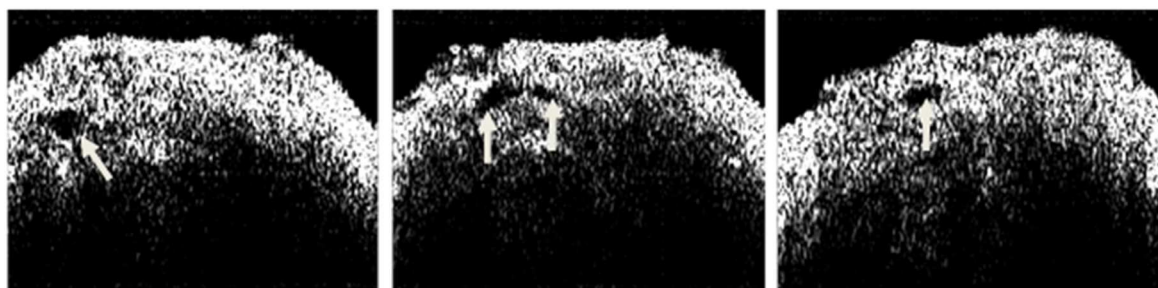


Figure 6.12: Results of Case 3. Cross section OCT images of suspected BCC taken at three lateral positions from the centre of sample. The arrows show the areas with pigment correlated with histology images. The lateral size \times depth size of each image is $1.5 \text{ mm} \times 0.6 \text{ mm}$

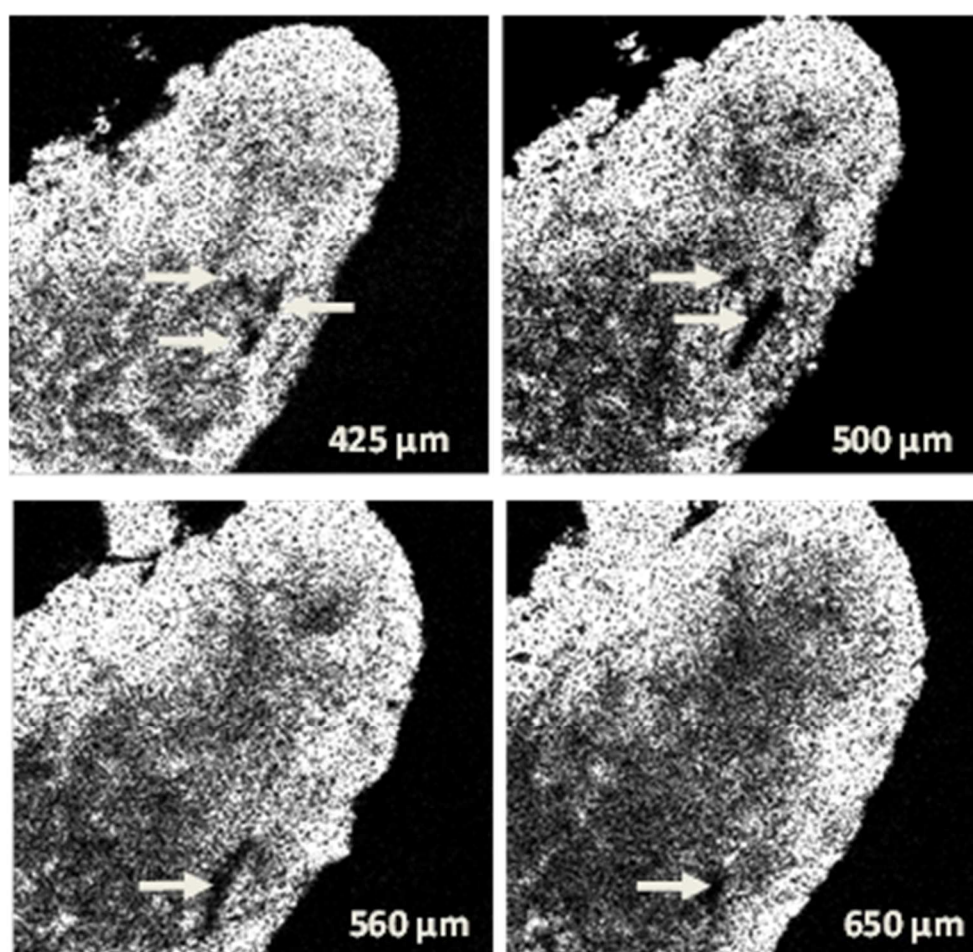


Figure 6.13: Results of Case 3. *En-face* OCT images of eyelid BCC taken at different depths in the range $425\text{-}650 \mu\text{m}$. The depth was measured from the top of the sample in air. The arrows show the areas of BCC. The size of each image is $1.5 \text{ mm} \times 1.5 \text{ mm}$

This region can be further verified by scanning through different layers of the *en-face* images in Fig. 6.13. As we move further in depth, more common features pointing to potential BCC start to unfold. OCT images are placed side by side with histology images where correlation of tumour features was performed. In Fig. 6.11, depth data from *en-face* images are in agreement with histology data that show structures of BCC at approximately 0.5 mm underneath the dermis. *En-face* images in Figs. 6.6, 6.10 and 6.13 are in their original form, free from any quality adjustment. In the slightly pixelated cross section OCT images of Figs. 6.5, 6.9 and 6.12, predominant tumour like features remain easily recognizable. Studies have shown that image post-processing methods such as spatial compounding and de-convolution algorithms can be used to reduce speckle and enhance signal to noise ratio in the acquired multilayer images [34,35].

6.2.3 Comments on technology

Based on previous experiments to characterise BCC employing OCT systems at two different wavelengths, 830 nm and 1300 nm, we have concluded that 1300 nm was better suited for imaging eyelid skin tissue [20]. MS-OCT is an improvement on the technique used in two previous set-ups, using SS-OCT [21] and DF-OCT [22].

In Section 6.2.1 and 6.2.2, we have demonstrated that MS-OCT technique is proven to be successful in detecting complex morphological features of skin in all three specimens imaged. Several skin features that were observed using DF-OCT technique [35], are also present in the MS-OCT *en-face* images. These are:

- (1) nodular structure of abnormal tissue,
- (2) superficial structure of scattered tumour margins, and
- (3) cross section of blood vessels, sweat ducts and sweat glands in the upper dermis.

En-face images are extremely easy to manipulate, especially for clinical analysis post-processing. Since our *en-face* images are stored in TIFF (Tagged Image file format) extension, we can export these images to external software packages like MATLAB and ImageJ. A volumetric scan can be obtained by stacking all of 384 slices *en-face* images on top of each other. Subsequently, a B-scan (cross-section) image is generated when the

volume is sliced at 90° orthogonal to the *en-face* surface. BCCs in cross section OCT images can be identified by three main phenomena:

- (a) abnormal reflectivity profile as we go in depth
- (b) obscure regions with clear margins and
- (c) repetitive inhomogeneous features different from the surrounding cells.

Similar morphological features are also used to identify potential BCC candidates in the *en-face* images. A side-by-side comparison with histology images for all three cases further validates the use of these criteria in OCT images with high certainty to locate and detect various types of BCC.

In the first two BCC structures, nodal and superficial, the presence of BCC tissue in *en-face* image can be determined from the absence of back reflected signal in a bounded area with clear edges. The presence of some random, low-reflectivity black spots indicate distribution of pigmented BCC structures. The lack of signal from BCC structures can be explained by higher absorption due to their denser structure compared to normal tissue [20, 21]. This feature is predominately visible on OCT systems operating at 1300 nm than on systems using shorter wavelengths.

Conventionally, averaging multiple *en-face* images usually improves the signal to noise, allowing better location of BCCs otherwise unnoticeable in a cross section OCT image, but this is done on the expense of axial resolution. Therefore, our approach to better SNR is to improve the axial resolution by using a broadband optical source that can deliver bandwidth of 300 nm or wider. Despite this chapter demonstrating MS-OCT with a swept source, the Master/Slave method can equally be applied to an ultra broadband source, by using a supercontinuum source and a spectrometer, in order to achieve better axial resolution [37]. The fundamental work recorded in this thesis builds the foundation to future exploration of such an option.

In this pilot study, *en-face* images of BCC samples taken from three patients were produced using the novel Master/Slave method. In all cases, the suspected BCC regions showed significant reduction in the signal strengths compared to uniform signal reflectivity in neighbouring tissues. In some cases, the presence of potential BCC can be identified by irregular scattering of high reflectivity dark spots (Fig. 6.6) and inconsistent light distribution pattern (Fig. 6.7) in skin tomograms.

All features associated with BCC demonstrated in our three previous studies [20-22] are also seen with *en-face* images obtained using MS-OCT. Three common types of BCC were identified and fitted well with histology criteria. In particular, nodular BCC are noted with their low reflectivity of light at 1310 nm, closely corresponding to BCC on correlation by the histologist following standard laboratory processing. Other subtypes of BCC may also be picked up by their irregular reflectivity profile in *en-face* images. High accuracy in distinguishing uncertain tumour lesions from healthy skins was established [15].

A further study has been planned once a portable handheld probe incorporating Master/Slave technique is manufactured. This will ease the transport of technology for clinical trials at hospitals, allowing imaging to be carried out in real time, in three possible scenarios, involving both *in-vitro* and *in-vivo* experiments:

- (1) pre-surgery diagnosis,
- (2) intra-operative assessment of precise tumour margins,
- (3) post-surgical side by side histology assessment.

In-vivo OCT imaging would be preferred for its enhanced clinical value to dermatologist and pathologist [37-39], as the water content and skin optical properties are preserved. We acknowledge possible signal distortions due to *in-vitro* imaging. For this reason, further work in axial resolution improvement and the development of polarisation-sensitive capabilities will be required.

The use of MS-OCT technique has allowed *en-face* images to display noticeable BCC features in real time. With no further image processing required, rapid assessment of BCC extent and surgical margins in excised skin specimens can be carried out, allowing for enhanced management of patients in the clinical setting. In addition to that, a quick patient turnover also save time and eliminate diagnosis errors.

This is a preliminary study to assess the values of the *en-face* display in diagnosing BCC. The MS technique is ideally suited to deliver such display as the image is assembled directly while laterally scanning with no need to wait for a whole assembly of A-scans to be subsequently cut.

6.3 Imaging of mammalian embryos

In recent years, ability to perform live tissue imaging has gained traction in the area of fertility treatments. As demonstrated in previous section on the benefits of *en-face* OCT imaging for BCC, we teamed up with researchers from Dr Gary Robinson's group at the School of Biosciences, at the University of Kent, and carried out the pilot project to image pig embryos using the our MS-OCT system.

Several new researches in this area were done to improve the field of reproductive biology and medicine, the efficiency of in vitro fertilisation (IVF) to above 40% for women [40]. Currently, the lack of non-invasive treatments procedures was cited as the main cause for low fertilization efficiencies [41]. Without the use of high resolution, functional *in vivo* tomography imaging, there is no way to accurately assess the quality and development potential of embryos, prior to the IVF transfers. More recently, several groups have started to employ OCT imaging to achieve this goal [41-44].

Our aim in this project was not to primarily evaluate the oocyte development process, but rather to test our *en-face* OCT capability to achieve the axial and transversal resolutions needed to discriminate the features of sub-cellular structures of the embryos. To do that, we replaced the microscope objective (tele-centric lens) in Fig.6.1 of Sec.6.2 to a high NA version from Olympus. The new MO allows us to image with a transversal resolution of $\sim 5 \mu\text{m}$, as opposed to the previous $\sim 12.5 \mu\text{m}$ used for BCC imaging. The axial resolution remained as it was, since we used the same Axsun swept-source with a 100 nm optical bandwidth (model SS1300-OCT). The imaged pig embryos are shown in orthogonal views (XY, YZ and XZ) Fig.6.14, all 40 simultaneous *en-face* OCT raster scans in Fig.6.15 and 3D volume displays in Fig.6.16.

We have demonstrated how live embryonic imagings with *en-face* OCT can be used to assess structural and functional birth defects, during the early stage development of fertilisation process. Therefore, we have shown that our master/slave OCT technology can be used for various biomedical applications, not limited to only BCC diagnosis.

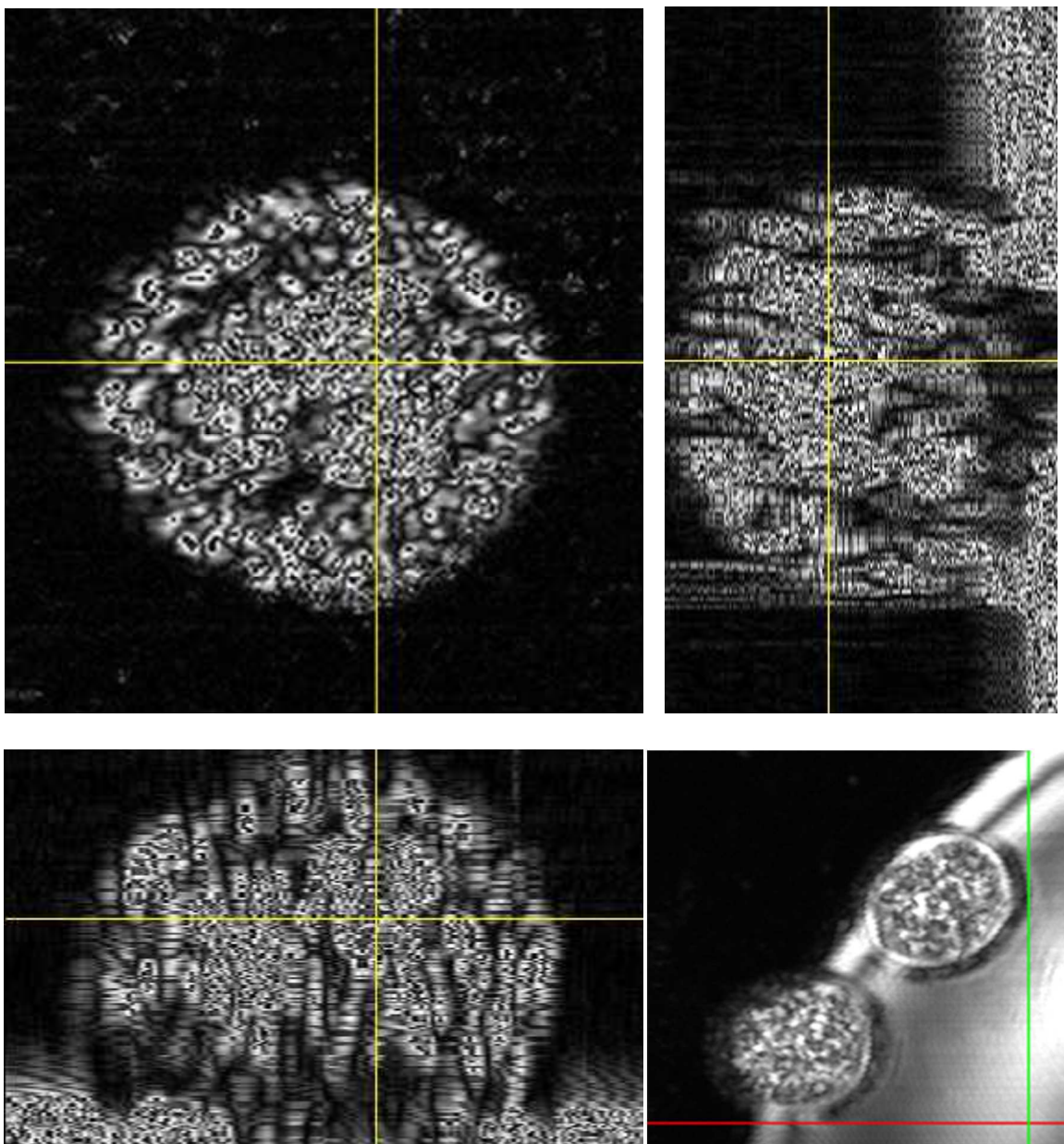


Figure 6.14: Orthogonal views of a pig embryo with cross-section diameter between 80-100 μm in ImageJ (top left: *en-face* slice XY, top right: YZ, bottom left: XZ). The cross-section yellow line indicates the centre of the image. (Bottom right: C-scan averaged taken on two adjacent pig embryos)

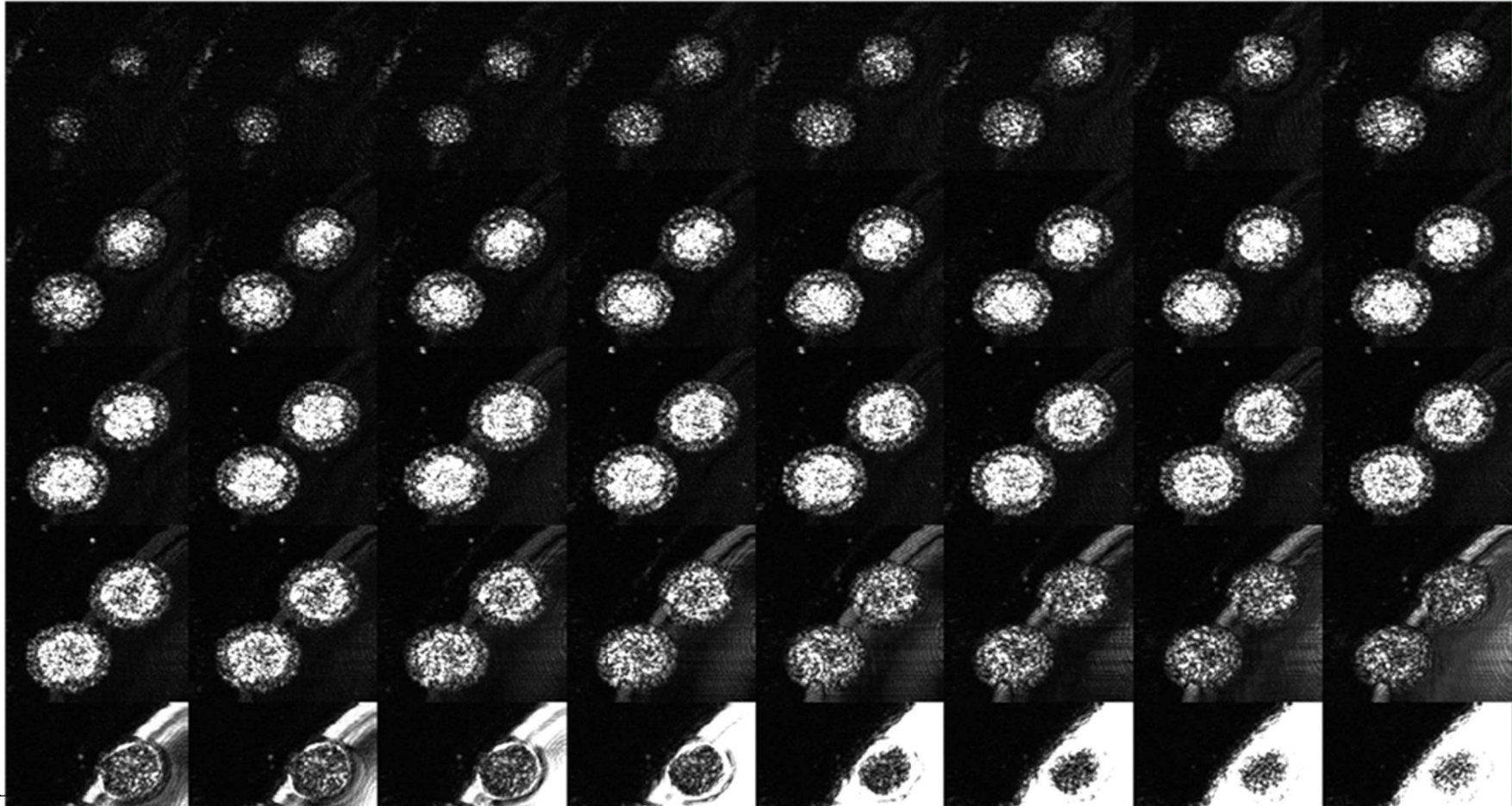


Figure 6.15: Illustration of Master/Slave raster scan for pig embryo made from 3 categories of images a) 40 *en-face* OCT images separated axially by $5\ \mu\text{m}$ (measured in air), (b) two cross-section OCT images acquired from two orthogonal orientations and (c) an average of the *en-face* images displayed for guidance

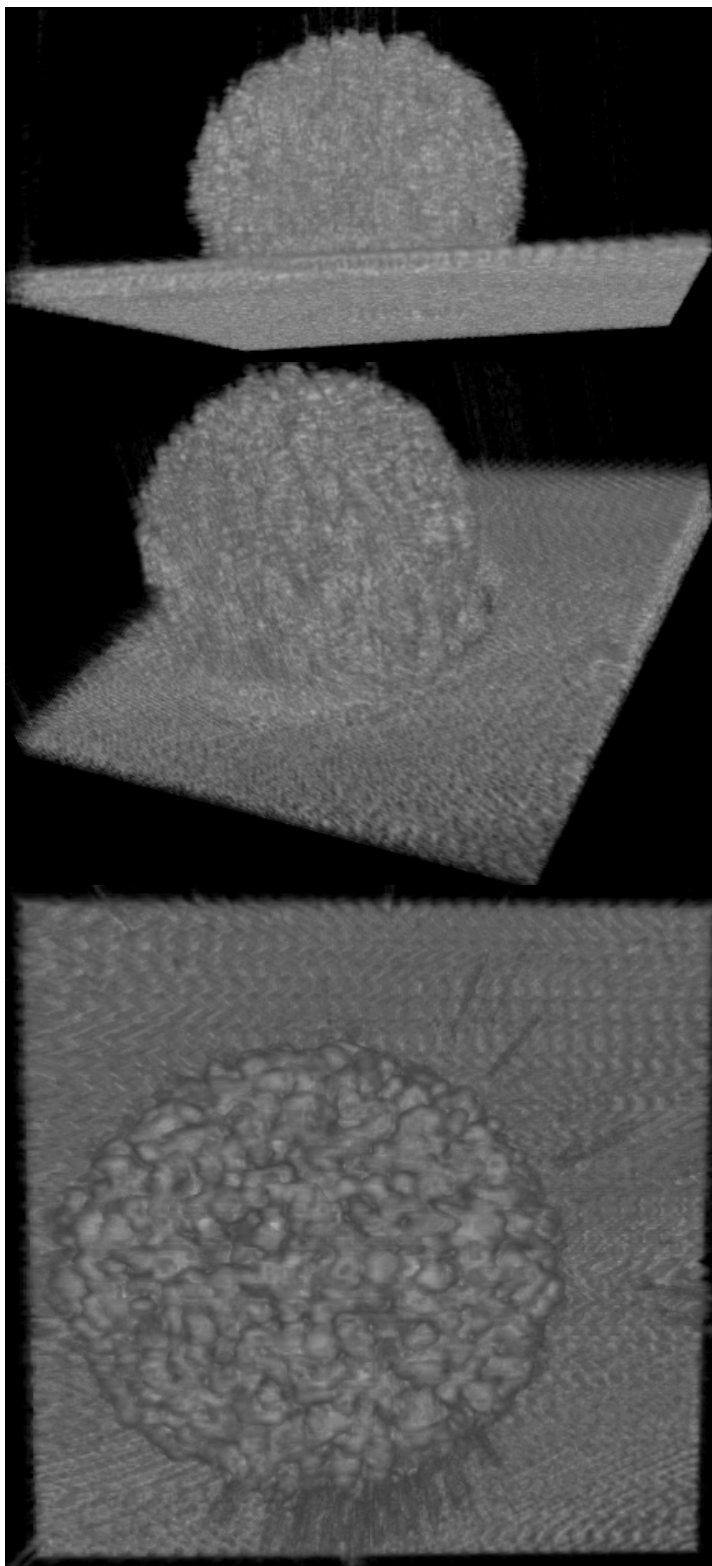


Figure 6.16: Volumetric 3D views of a pig embryo with cross-section diameter of $100\ \mu\text{m}$ in ImageJ

References

1. A. Lomas, J. Leonardi-Bee, F. Bath-Hextall, "A systematic review of worldwide incidence of nonmelanoma skin cancer," *Br. J. Dermatol.* 166 (5), 1069-80 (May 2012).
2. C. E. Margo, K. Waltz, "Basal cell carcinoma of the eyelid and periocular skin," *Surv. Ophthalmol.*, 38(2), 169-92 (1993).
3. G. W. Jung, A. I. Metelitsa, D. C. Dover, and T. G. Salopek, "Trends in incidence of nonmelanoma skin cancers in Alberta, Canada, 1988–2007," *Br. J. Dermatol.* 163, 146–154 (2010).
4. F. Bath-Hextall, J. Leonardi-Bee, C. Smith, A. Meal, R. Hubbard, "Trends in incidence of skin basal cell carcinoma. Additional evidence from a UK primary care database study," *Int. J. Cancer*, 121(9), 2105-8 (1993).
5. Improving outcomes for people with skin tumours including melanoma (update): the management of low-risk basal cell carcinomas in the community. NICE Guidance on Cancer Services. May (2010).
6. M. Venturini, G. Gualdi, A. Zanca, L. Lorenzi, G. Pellacani, P. G. Calzavara-Pinton, "A new approach for presurgical margin assessment by reflectance confocal microscopy of basal cell carcinoma," *Br. J. Dermatol.*, 174(2), 380-385 (Feb 2016).
7. M. Nassiri-Kashani, B. Sadr, F. Fanian, K. Kamyab, P. Noormohammadpour, M. M. Shahshahani, H. Zartab, M. M. Naghizadeh, M. Sarraf-Yazdy, A. Firooz, "Pre-operative assessment of basal cell carcinoma dimensions using high frequency ultrasonography and its correlation with histopathology," *Skin Res. Technol.*, 19(1), 132-138 (2013).
8. I. Kopriva, A. Persin, N. Puizina-Ivic, L. Miric, "Robust demarcation of basal cell carcinoma by dependent component analysis-based segmentation of multi-spectra fluorescence images," *J. Photochem. Photobio. B.* 100 (1), 10-18 (2010).
9. M. Balu, C. B. Zachary, R. M. Harris, T. B. Krasieva, K. Konig, B. J. Tromberg, K. M. Kelly, "In vivo multiphoton microscopy of basal cell carcinoma," *JAMA Dermatol.* 151 (10), 1068-1074 (2015).
10. R. Patalay, C. Talbot, Y. Alexandrov, M. O. Lenz, S. Kumar, S. Warren, I. Munro, M. A. A. Neil, K. Konig, P. M. W. French, A. Chu, G. W. H. Stamp, C. Dunsby, "Multiphoton multispectral fluorescence lifetime tomography for the evaluation of basal cell carcinomas," *PLoS One* 7 (9), e43460 (2012).
11. K. Busam, C. Charles, C. Lohmann, A. Marghoob, M. Goldgeier, A. Halpern, "Detection of intraepidermal microscopy," *Melanoma Res.* 12, 349-355 (2002).
12. M. A. Boone, M. Suppa, G. Pellacani, A. Marneffe, M. Miyamoto, I. Alarcon, C. Ruini, R. Hofmann-Wellenhof, J. Malvehy, G. B. Jemec, V. Del Marmol, "High-definition optical coherence tomography algorithm for discrimination of basal cell carcinoma from clinical BCC imitators and differentiation between common subtypes," *J. Eur. Acad. Dermatol. Venereol.* 29(9), 1771-80 (2015).

13. M. A. L. M. Boone, S. Norrenberg, G. B. E. Jemec, V. Del Marmol, "Imaging of basal cell carcinoma by high-definition optical coherence tomography: histomorphological correlation. A pilot study," *B. J. Dermatol.*, 167, 856-864 (2012).
14. T. Maier, M. Braun-Falco, T. Hinz, M. H. Schmid-Wendtner, T. Ruzicka, C. Berking, "Morphology of basal cell carcinoma in high definition optical coherence tomography: en-face and slice imaging mode, and comparison with histology," *J. Eur. Acad Dermatol Venereol*, 27 (1), 97-104 (2013).
15. M. Ulrich, T. von Braunmuehl, H. Kurzen, T. Dirschka, C. Kellner, E. Sattler, C. Berking, J. Welzel, U. Reinhold, "The sensitivity and specificity of optical coherence tomography for the assisted diagnosis of nonpigmented basal cell carcinoma: an observational study," *B. J. Dermatol*, 172(2), 428-435 (2015).
16. A. Gh. Podoleanu, A. Bradu, "Master-slave interferometry for parallel spectral domain interferometry sensing and versatile 3D optical coherence tomography," *Opt. Exp.* 21(16), 19324-19338 (2013).
17. A. Bradu, M. Maria, A. Gh. Podoleanu, "Demonstration of tolerance to dispersion of master/slave interferometry," *Opt Exp.* 5(11), 14148-14161 (2015).
18. J. Wang, A. Bradu, G. Dobre, A. Podoleanu, "Full-field swept source master-slave optical coherence tomography," *IEEE Photonics J.* 7(4) (2015)
19. A. Bradu, A. Gh. Podoleanu, "Imaging the eye fundus with real-time en-face spectral domain optical coherence tomography," *Biomed Opt Exp.* 5(4), 1233-1249 (2014).
20. B. R. Penmetsa, M. Khandwala, A. Bradu, M. Hughes, C. A. Jones, J. Schofield, A. G. Podoleanu, "Imaging of basal cell carcinoma tissue using en-face OCT," *Proc. SPIE* 7139, 71390J (2008).
21. M. Khandwala, B. R. Penmetsa, S. Dey, J. B. Schofield, C. A. Jones, A. Podoleanu, "Imaging of periocular basal cell carcinoma using en face optical coherence tomography: a pilot study," *Brit. J. Ophthal.* 1136, 1-5 (2010).
22. M. R. N. Avanaki, A. Hojjatoleslami, M. Sira, J. Schofield, C. Jones, A. Gh. Podoleanu, "Investigation of basal cell carcinoma using dynamic focus optical coherence tomography," *Appl. Opt.* 52(10), 2116-2124 (2013).
23. J. K. Patel, S. Konda, O. A. Perez, S. Amini, G. Elgart, B. Berman, "Newer technologies/techniques and tools in the diagnosis of melanoma," *E. J. Dermatol.* 18, 617-631 (2008).
24. N. Iftimia, G. Peterson, E. W. Chang, G. Maguluri, W. Fox, M. Rajadhyaksha, "Combined reflectance confocal microscopy-optical coherence tomography for delineation of basal cell carcinoma margins: an ex vivo study," *J. Bio. Opt.* 21(1), 016006 (2016).
25. M. Ulrich, L. Themstrup, N. Carvalho, M. Manfredi, C. Grana, S. Ciardo, R. Kastle, J. Holmes, R. Whitehead, G. B. E. Jemec, G. Pellacani, J. Welzel, "Dynamic optical coherence tomography in dermatology," *J. Dermatol.* 232, 298-311 (2016).

26. G. Li, J. K. Tietze, X. Tao, D. Kulichova, T. Ruzicka, C. Berking, T. Maier, "High-definition optical coherence tomography in the diagnosis of basal cell carcinoma evaluated by an experienced versus in experienced investigator," *J. Clin. Exp. Dermatol. Res.* 5(4), 1000227 (2014).
27. A. Hojjatoleslami, M. R. N. Avanaki, "OCT skin imaging enhancement through attenuation compensation," *Appl. Opt.* 51, 4927-4935 (2012).
28. A. Bradu, K. Kapinchev, F. Barnes, A. Podoleanu, "Master slave en-face OCT/SLO," *Biomed. Opt. Exp.* 6(9), 3655-3669 (2015).
29. A. Bradu, K. Kapinchev, F. Barnes, A. Podoleanu, "On the possibility of producing true real-time retinal cross-sectional images using a graphics processing unit enhanced master-slave optical coherence tomography system," *J. Biomed. Opt.* 20(7) (2015).
30. M. A. Boone, M. Suppa, G. Pellacani, A. Marneffe, M. Miyamoo, I. Alarcon, C. Ruini, R. Hofmann-Wellenhof, J. Malvehy, G.B. Jemec, V. Del Marmol, "High-definition optical coherence tomography algorithm for discrimination of basal cell carcinoma from clinical BCC imitators and differentiation between common subtypes," *J. Eur. Acad. Dermatol. Venereol.* 29, 1771-1780 (2015).
31. T. Gambichler, I. Plura, P. Kampilafkos, K. Valavanis, M Sand, F. G. Bechara, M. Stucker, "Histopathological correlates of basal cell carcinoma in the slice and en face imaging modes of high-definition optical coherence tomography," *Br. J. Dermatol.* 170, 1358-1361 (2014).
32. A. J. Coleman, T. J. Richardson, G. Orchard, et al., "Histological correlates of optical coherence tomography in non-melanoma skin cancer," *Skin Res. Technol.* 19, 10-19 (2013).
33. M. A. Boone, S. Norrenberg, G. B. Jemec, V. Del Marmol, "Imaging of basal cell carcinoma by high-definition optical coherence tomography: histomorphological correlation. A pilot study," *Br. J. Dermatol.* 167, 856-864 (2012).
34. S. A. Hojjatoleslami, M. R. N. Avanaki, A. Gh. Podoleanu, "Image quality improvement in optical coherence tomography using Lucy-Richardson deconvolution algorithm," *Appl. Opt.* 54, 5663-5670 (2013).
35. M. R. N. Avanaki, R. Cernat, P. J. Tadrous, T. Tatla, A. Gh. Podoleanu, S. A. Hojjatoleslami, "Spatial compounding algorithm for speckle reduction of dynamic focus OCT images," *IEEE Photon. Tech. Lett.* 25, 1439-1442 (2013).
36. M. Mogensen, T. Joergensen, L. Thrane, B. M. Nurnberg, G. B. E. Jemec, "Improved quality of optical coherence tomography imaging of basal cell carcinomas using speckle reduction," *Exp. Dermatol.*, 19(8), 293-295 (2009).
37. M. Maria, M. J. M. Marques, C. Costa, A. Bradu, T. Feuchter, L Leick, A. G. H. Podoleanu, "Broadband master-slave interferometry using a super-continuum source," *Proc. SPIE*, 9697, 96972R (2016).
38. M. Mogensen, T. M. Joergensen, B. M. Nurnberg, H. A. Morsy, J. B. Thomsen, L. Thrane, G. B. Jemec, "Assessment of optical coherence tomography imaging in the diagnosis of non-

- melanoma skin cancer and benign lesions versus normal skin: observer-blinded evaluation by dermatologists and pathologists,” *Dermatol. Surg.*,35,965-972 (2009).
39. J. M. Olmedo, K. E. Warschaw, J. M. Schmitt, D. L. Swanson, “Optical coherence tomography for the characterization of basal cell carcinoma in vivo: a pilot study,” *J. Am. Acad. Dermatol.*,55,408-412 (2006).
 40. A. Ajduk, M. Zernicka-Goetz, “Quality control of embryo development,” *Molecular Aspects of Medicine*, 34(5), 903-918 (2013).
 41. K. Karnowski, A. Ajduk, B. Wieloch, S. Tamborski, K. Krawiec, M. Wojtkowski & M. Szkulmowski, "Optical coherence microscopy as a novel, non-invasive method for the 4D live imaging of early mammalian embryos," *Sci. Rep.* 7(4165) (2017).
 42. L. Zarnescu, M.C. Leung, M. Abeyta, H. Sudkamp, T. Baer, B. Behr, A.K. Ellerbee, “Label-free characterization of vitrification-induced morphology changes in single-cell embryos with full-field optical coherence tomography,” *J. Biomed. Opt.* 20(9), 096004 (2015).
 43. J. Y. Xiao, B. Wang, G. Y. Lu, Z. Q. Zhu and Y. J. Huang, “Imaging of oocyte development using ultrahigh-resolution full-field optical coherence tomography,” *Appl. Opt.* 51, 3650–3654 (2012).
 44. J. Zheng, D. Lu, T. Chen, C. Wang, N. Tian, F. Zhao, T. Huo, N. Zhang, D. Chen, W. Ma, J. Sun, P. Xue, “Label-free subcellular 3D live imaging of preimplantation mouse embryos with full-field optical coherence tomography” *J. Biomed. Opt.* 17 (2012).

7

Application of supercontinuum light sources in vision science

Application of a broadband supercontinuum source goes beyond OCT imaging. Today's supercontinuum sources have ventured into the regime of complex light manipulation and they have also taken advantage of full range power controls. This niche opens up exciting new field of possibilities in medical imaging and also vision science research. To demonstrate such capabilities, we collaborated with Dr Gurprit Lall of The Medway School of Pharmacy in Kent, and used a supercontinuum white light (SCWL) source from NKT Photonics A/S, to study the pupil light reflex in mammals upon multi-colour light stimuli.

In this chapter, we assessed the spectral sensitivity of the pupillary light reflex in wild type mice using a high power SCWL source in a dual wavelength configuration. This novel approach was compared to data collected from a more traditional setup using a Xenon arc (Xe Arc) lamp fitted with monochromatic interference filters. Irradiance response curves (IRCs) were constructed using both systems, with the added benefit of a two-wavelength, equivocal power, and output using the SCWL. The variables applied to the light source were intensity, wavelength and stimulus duration through which the physiological output measured was the minimum pupil size attained under such conditions. We showed that by implementing the SCWL as our novel stimulus, we were able to dramatically increase the physiological usefulness of our pupillometry system.

Our experiment focuses mainly on the papillary light response in the mammalian eye that closely resembles that of humans. The mammalian eye is an essential component of the central nervous systems' (CNS) sensory complement. It is primarily, responsible for generating a visual representation of our environment. This is possible through the decoding of light by a structure termed the retina, which contains complex neuronal structures capable of detecting the spectral composition of a light source and converting this into an electrical impulse. The retina, itself, coats the back of the inner eyeball and forms optic nerves that feed the brain; ultimately terminating at the occipital lobe. It's

composition consist of a number of relay networks which contain specialised cells capable of converting light, photos, into electrical signals. These cells are termed photoreceptors.

The mammalian visual system consists of three types of photoreceptors defined by their spectral sensitivity to light. Rods and cones are typically referred to as the ‘classic’ photoreceptors and are responsible for creating a visual image of our environment. A third class of photoreceptors has been identified in the retinal ganglion cell (RGC) layer of the retina, with the sole role of encoding ambient light for non-image forming (NIF) visual responses e.g. pupillary light reflex, circadian entrainment - impacting behavioural and/or physiological responses. However, establishing the individual contribution of each photoreceptor class to NIF events remains problematic due to the overlap in spectral sensitivity across these cell types, shown in Fig. 7.1. There is a clear distinction in sensitivity profiles of each receptor, however there is also great overlap. In an intact retina, it is extremely difficult to tease out the contribution of each photoreceptor to a physiological or behavioural response. Traditionally, studies have used murine transgenic models, which either ablate or disable function of a particular photoreceptor class. However, a limitation of such an approach is the likely probability of alterations in physiological function and structural reorganisation of the retina.

The pupillary light reflex (PLR) is an autonomic response to bright light. It is well established that the degree of iris constriction is relative to the intensity of the source light being presented to the eye. Foremost, this reflex acts to protect the retina from damage by bright light. However, we can also use this reflex to understand how light is decoded by the retina and used to determine a physiological output. Through manipulation of the light source, for both intensity and wavelength, it is possible to assess/allude to the contribution of each receptor class to the PLR. Clinically, the PLR has shown promise in the assessment of brainstem function and in the management of pain, through the impact of pupil sensitivity to opioids [1].

Traditionally, the PLR set-up has utilised a powerful Xe Arc light source with wavelength and intensity all regulated by chromatic or neutral density (ND) filters. This set-up is ideal for looking for the change in pupil constriction to single intensities at particular wavelengths, be it monochromatic or band pass (BP) in nature; however lacks the ability to look at responses to dynamically changing light stimuli.

In this study, we propose the use of a broadband SCWL source to generate a dual light stimulus of equivocal power. We will use this design to show the ability of a two-channel setup in demonstrating the retinal sensitivity to light. There is great potential in

this novel use of a SCWL in both providing better understanding of photoreceptor contribution to physiological outputs as well as increasing the resolution of this technique to assist in clinical diagnosis and healthcare.

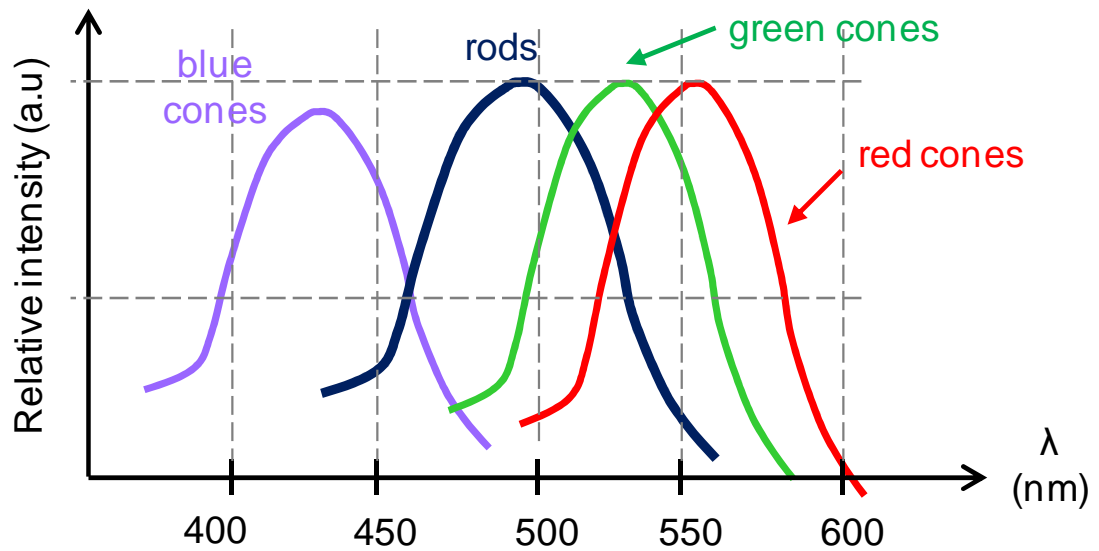


Fig. 7.1 Spectral sensitivity profiles of the classic retinal photoreceptors.

7.1 Pupillometry

7.1.1 Pupil light reflexes in mammals

Pupillometry was conducted as previously described (Lucas et al., 2003) [1] on anaesthetised adult mice. Animals were stably entrained to a 12 hr: 12 hr light dark (LD) cycle (white LED source, 1000 lux) and recordings were restricted to between 4 and 7 hr after lights on. All experiments were preceded by 1 hr of dark adaptation (Fig. 7.2). Pupillary responses were elicited through a Ganzfeld integrating sphere applied to one eye, previously dilated with 0.1% atropine, allowing consensual pupil constriction from the other eye to be recorded with a digital charged-coupled device (CCD) camera. Light sources consisted of either a Xe Arc source, filtered with neutral density and monochromatic interference filters, half bandwidth (FWHM ≤ 10 nm) or a dual laser configuration with a broadband SCWL source, and two computer controlled wavelength selection modules. Stimulus protocols were programmed and run via the associated NKT controller computer software, generating a multi-wavelength output.

7.1.2 Animals and ethics

Experimental procedures were carried out under licence by the Home Office (UK) in accordance with the Animals (Scientific Procedures) Act (1986) and following ethical approval from the University of Kent ethics board.

Adult C57BL/6J mice (50-80 days old, $n = 20$) were maintained under a 12:12 light – dark (LD) cycle, room temperature 22 ± 2 °C. All efforts were made to minimise the number of animals used and their suffering. Animals are kept in secure facilities at the Charles River laboratory in Ramsgate, Kent. Experiments on light stimuli with supercontinuum light sources were conducted at similar facility.

7.1.3 Image capture and analysis

Pupil recordings lasted for 63 seconds in all experiments. Images were captured at a frequency of six per second. The first three seconds were used to record fully dilated dark-adapted pupils. For the experiments using the Xe Arc, images were captured for 60 seconds with the stimulus set to a 480nm light. However, under the SCWL, images were taken for 15 second under a 560nm light and then the addition of a 480 nm light for 45 seconds ensued. Fig. 7.2 shows the stimulus protocols for both configurations. Fig. 7.3 and 7.4 show the entire experiment cycle with wild type mice, and the recorded pupil size throughout the process.

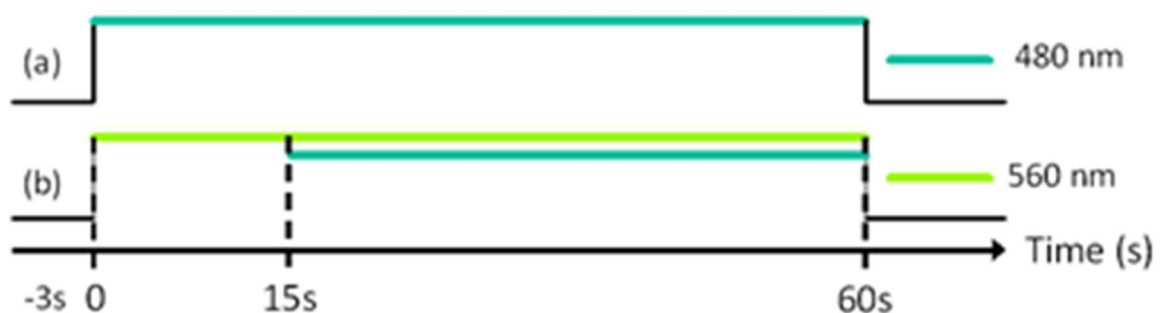


Fig. 7.2 Stimulus protocols for a Xenon arc consisting of: (a) a single 480 nm light pulse for 60s, and through the SCWL and (b) a dual stimulus generated at 560 nm for 60 s and at 480nm signal for the last 45s.

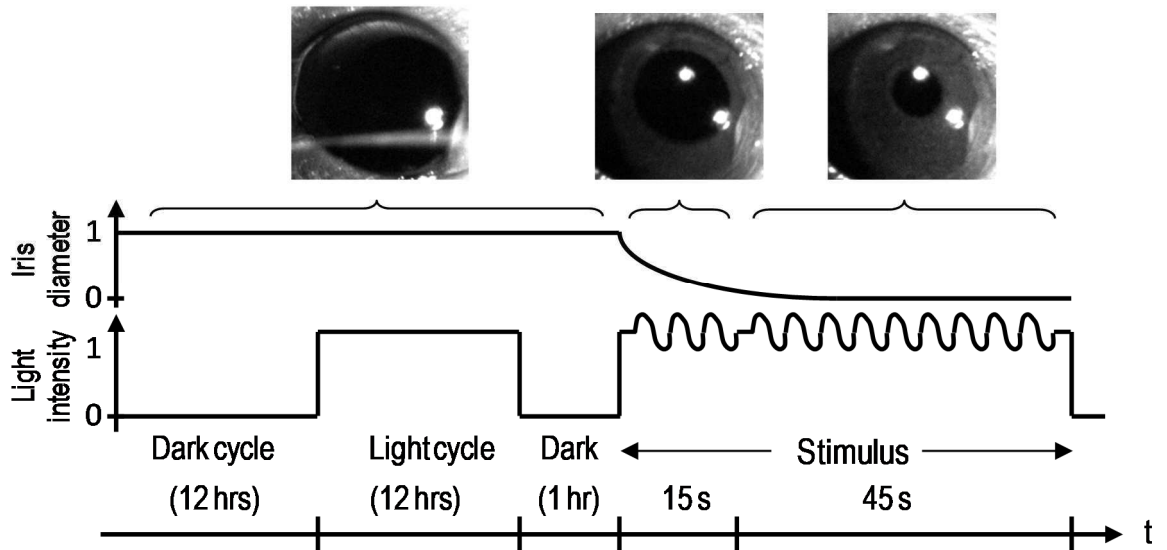


Fig. 7.3 Stimulus protocols for supercontinuum consisting of a dual stimulus generated at 560 nm for full 60 s and at 480nm signal for the last 45s (from $t=15$ s onwards).

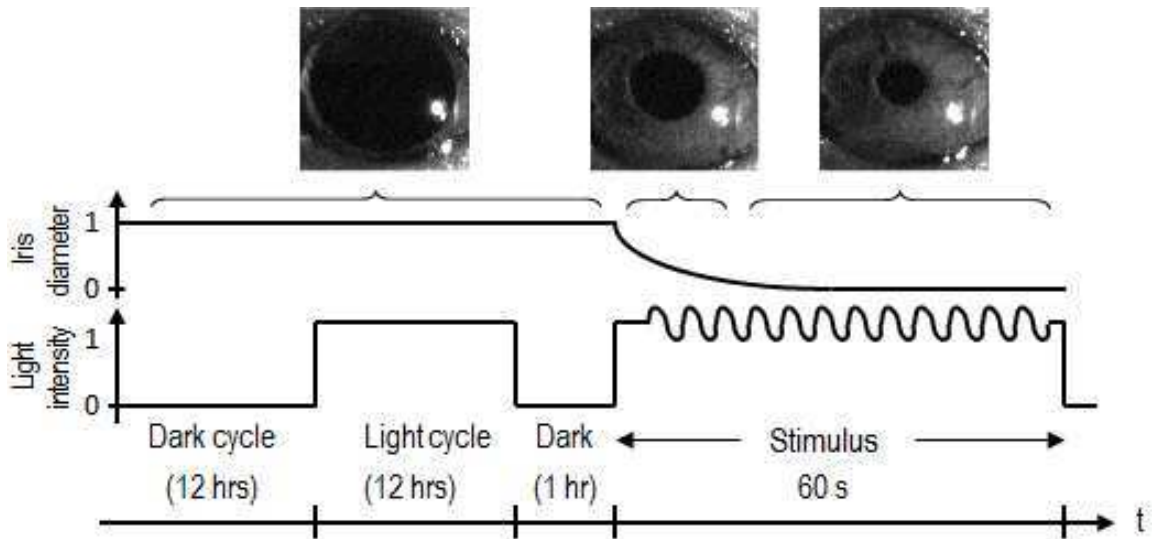


Fig. 7.4 Stimulus protocols for a supercontinuum consisting of: a single 480 nm light pulse for 60s.

Minimum pupil sizes were calculated by obtaining the smallest pupil size attained under any given light stimulus and presented relative to the dark-adapted pupil areas of individual animals. In detail, the normalised minimum pupil area (A_{Npupil}) is calculated by dividing the smallest pupil area achieved through the stimulus duration (N_{min}) by the largest dark-adapted pupil (N_{ref}) pre-stimulus (Eqn. 7.1).

$$A_{Npupil} = \frac{N_{min}}{N_{ref}} \quad (7.1)$$

Statistical analysis: Nonlinear regression (curve fit) analysis was performed by measuring the irradiance response curve (IRC) from the differing light stimuli and sources. Significance was assigned using the extra sum-of-squares F test set to $p < 0.05$. All analysis was undertaken using Graphpad Prism (Ver.6 for Macintosh, Graphpad Software, La Jolla CA, USA).

Pupil areas were measured using ImageJ software (v1.50, NIH, open source). Collected images were imported into ImageJ as TIFF files (8-bit). The ellipse tool was used to highlight the circumference of the pupil and the area (pixels²) computed as shown in Fig. 7.5.

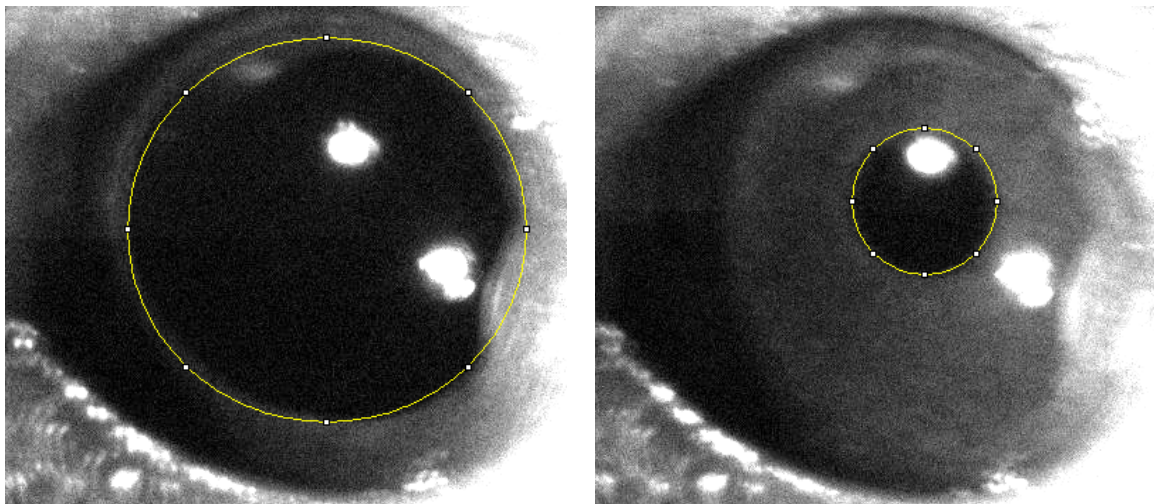


Fig. 7.5 Pupil area was measured by drawing ellipses around the circumference of the pupil in dark adapted, dilated (left) and constricted (right) eyes.

7.1.4 Dual laser and multi-wavelength setup

Two separate laser systems were used for this experiment, Xenon Arc and supercontinuum from NKT Photonics A/S.

7.1.4.1 Xenon Arc

The traditional, single light source, pupillometry apparatus typically consists of a full spectrum xenon arc lamp fitted with a filter holder and shutter. A light pipe was used to feed the integrating sphere, where the light stimulus was presented to the mydriatic containing eye. The system schematic is shown as in Fig. 7.6. In this configuration, the Xe Arc light is sent into a light tube (LT), which is then sent into an integrating sphere (INTS).

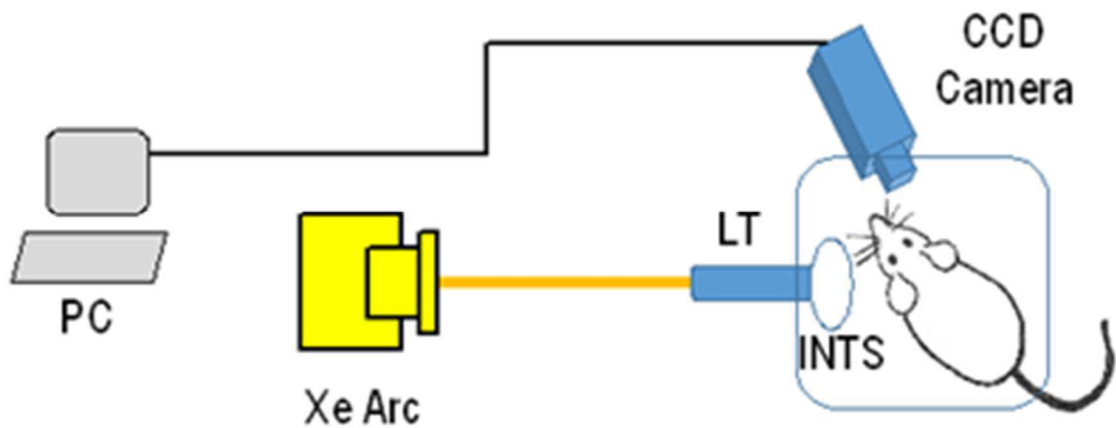


Fig. 7.6 Schematic of a single Xe Arc light source used to provide a stimulus. (LT: light tube, INTS: integrating sphere, CCD: charge-coupled device camera)

7.1.4.2 NKT supercontinuum white light source

A broadband SCWL source (SuperK Extreme EXR20, 500-2400 nm, NKT Photonics, Denmark) was used to provide a dual light configuration capable of generating high power light at two different wavelengths. As shown in Fig. 7.7, the output of the SCWL was fed into two wavelength tuning units, a visible/NIR multi-line selector (SuperK VARIA, 500-840 nm, NKT Photonics) to generate $560 \text{ nm} \pm 10 \text{ nm}$ light, and a UV extension module (EXTEND-UV, 350-480 nm, NKT Photonics) to produce light at a bandwidth of $480 \text{ nm} \pm 10 \text{ nm}$. The SuperK Varia has spectral line output as shown in Fig. 7.8. Wavelength selection was made possible through a single interface user software developed by NKT on a PC running Microsoft Windows.

The 560 nm light from SuperK VARIA was reflected off a gold mirror (M) and combined with 480 nm light from Extend-UV using a long pass dichroic mirror (DM, DMLP505, Thorlabs). The combined beams were then coupled into one end of a silica light tube (LT), while the other end was connected to the providing port for the integrating sphere, INTS (IS200-4, Thorlabs). The effective light power was measured using a digital handheld optical power meter (PM100D, Thorlabs), equipped with a Silicon diode sensor (S120C, Thorlabs). The illuminating beam spot at the presenting port of INTS has an area of 0.5 cm² (Table 7.1). Each beam of the two wavelengths had a 1 mW initial power measured at the stimuli port of the INTS.

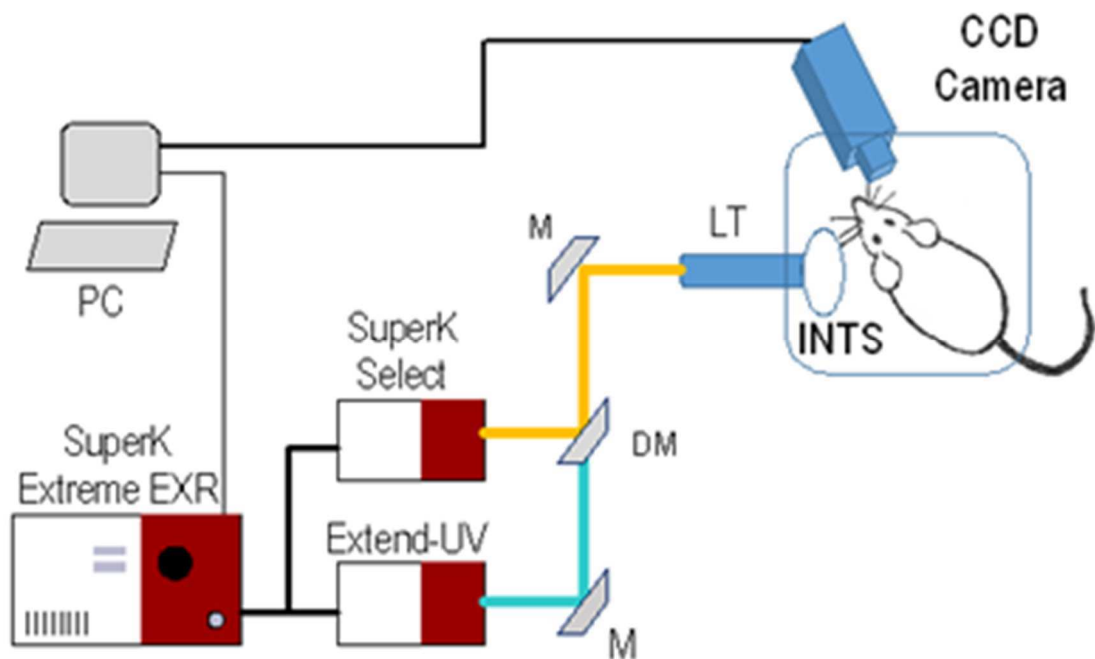


Fig. 7.7 Schematic of the dual stimulus SCWL light source. (M: mirrors, DC: dichroic mirror, LT: silica light tube, INTS: integrating sphere)

Absorptive neutral density filters (part numbers NE10A to NE40A, Thorlabs) were used to attenuate power by a factor of 10. The effective quantum flux densities (in \log_{10} eff photons/cm²/s) of each stimulus was estimated by integrating the spectral power density of illuminating wavelengths (470-480 nm and 555-565 nm) using Eqn. 7.2. The corresponding power values are shown in Table 7.1.

$$N_p = \frac{E_c}{E_p} = \frac{E \cdot \lambda \cdot 10^{-9}}{h \cdot c} = E \cdot \lambda \cdot 5.03 \times 10^{15} \quad (7.2)$$

where $E=P/d_s$ is the illuminating energy per unit area, P is the power metered intensity in mW and d_s is the illuminating beam spot in cm^2 . E_c is the total illuminating energy per pulse emitted from the SCWL source, and E_p is a constant value obtained from the product of Planck's constant h (6.636×10^{-34} J.s) and the speed of light, c (3×10^8 m/s).

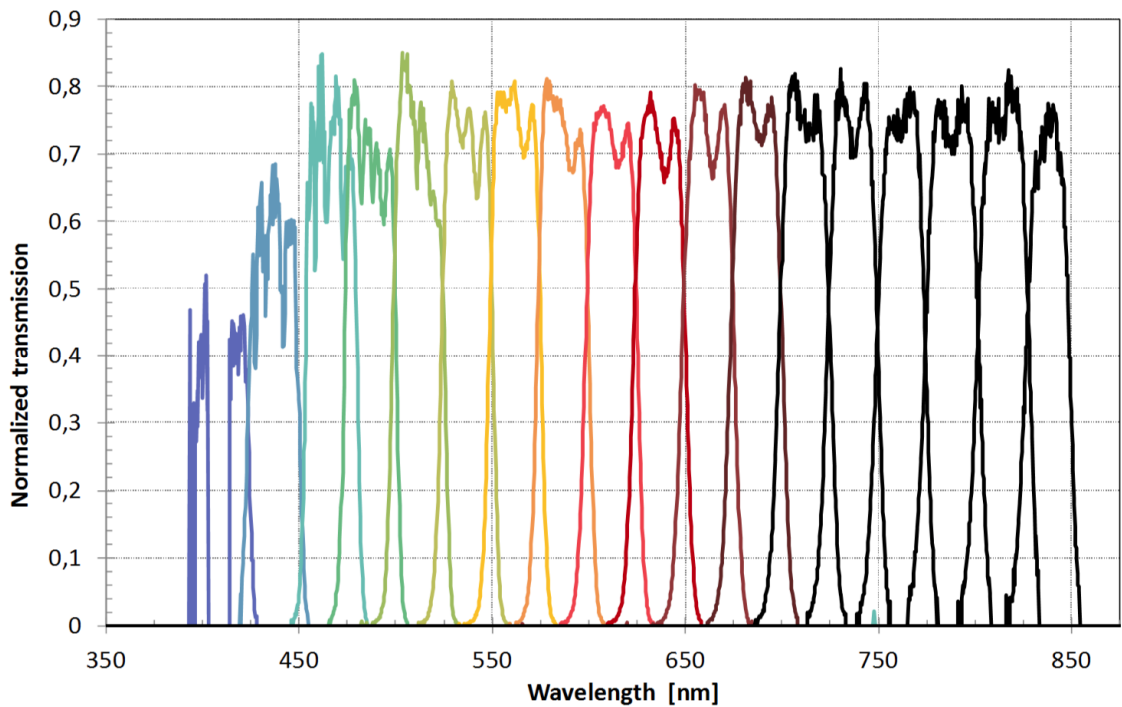


Fig. 7.8 Spectral line output of SuperK VARIA (NKT Photonics A/S, Denmark).

7.2 Pupil stimulus and results

7.2.1 Light stimulus

The initial set of experiments was performed using the traditional Xenon arc light source. Minimal pupil sizes were measured following exposure to a single intensity of 480 nm light. An irradiance response curve (IRC) was constructed showing the relationship between minimal normalised pupil size and intensity (Fig. 7.9). Irradiance response curve shows maximum pupil constriction to the brightest light, with a decline in response as

intensity reduces. At the highest light intensity used we attained a normalised minimum pupil size of 0.09 ± 0.001 (mean \pm SEM, $n=5$), approximate $>90\%$ constriction. The amount of constriction declined as a function of light intensity, with the dimmest light invoking the least response.

The use of the SCWL source allowed us to generate two optical beams, power equivocal, of different wavelengths of light, 560 nm and 480 nm. Following dark adaptation, a 560 nm stimulus was presented for 15 seconds. This allowed the pupil to reach a steady state at the high intensities of light used at this wavelength. Under these conditions, we were able to generate an approximate 60% constriction at the brightest intensity; however, this soon tapered off, as the stimulus intensity was reduced (Fig. 7.10).

Following the 15 seconds of exposure to the 560 nm light, we presented a second pulse consisting of 480 nm. The combination of the 560 nm and the 480 nm stimulus was able to generate a full constriction in a similar manner to that achieved with the Xenon arc. The captured pupil diameter at different time instances, at different illumination intensities, are shown in sequence in Fig. 7.11. On further analysis, the overall decrease in sensitivity is statistically significant, with a reduced sensitivity observed with the 560 nm light stimulus ($p < 0.001$, $F(3, 58) = 58.48$). This decrease in constriction, relative to 480 nm, can be attributed to alterations in mouse retinal photoreceptor responsiveness. Finally, both IRCs produced using the Xeon arc and SCWL in dual light were statistically identical ($p > 0.05$, $F(1, 58) = 0.23$, Fig. 7.12), thus, affirming the use of the SCWL as a viable alternative to the traditional Xenon arc light source in driving the PLR.

Table 7.1. Effective quantal flux density calculated at different wavelengths and illuminating power levels.

Power per wavelength (μW)	Quantum flux density (\log_{10} effective photons/ cm^2/s)			
	Dual-wavelength SCWL			Xe Arc
	560 nm	480 nm	480+560 nm	480 nm
1000	15.75	15.68	16.02	-
100	14.75	14.68	15.02	14.51
10	13.75	13.68	14.02	13.51
1	12.75	12.68	13.02	12.51
0.1	11.75	11.68	12.02	11.51
0.01	10.75	10.68	11.02	10.51

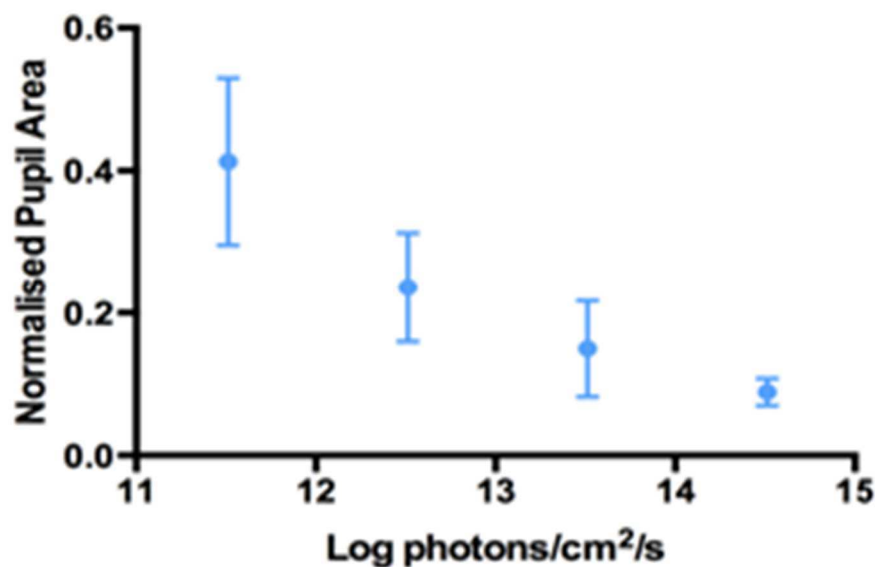


Fig. 7.9 The pupillary light reflex of dark-adapted mice using a 480 nm light generated by a Xe arc source.

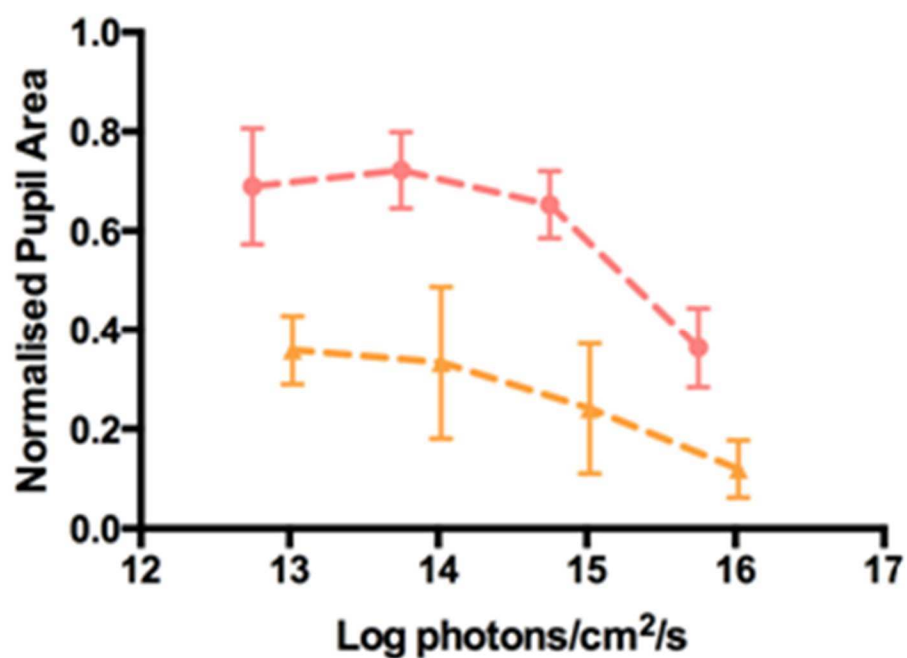


Fig. 7.10 Irradiance responses using a 560 nm light (orange curve) and irradiance responses using a 560 nm+480 nm (light red curve) stimulus.

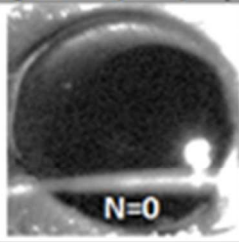
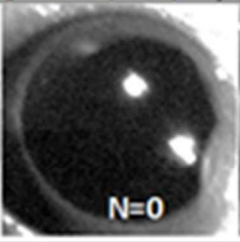
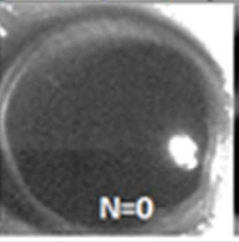
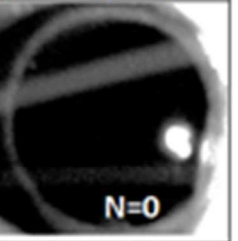
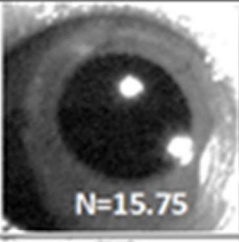
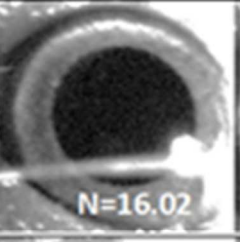
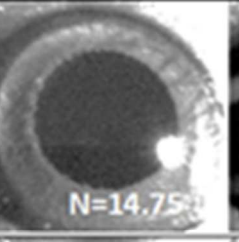
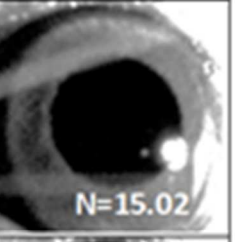
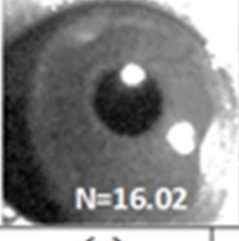
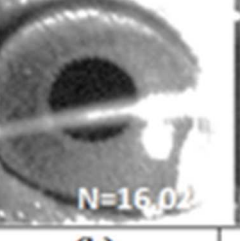
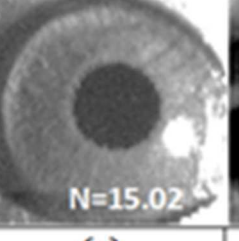
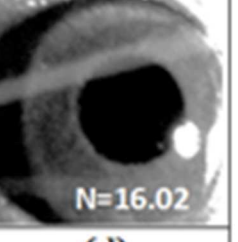
	Dual-wavelength with SCWL			
480+560 nm intensity	16 log photons/cm ² /s	15 log photons/cm ² /s	14 log photons/cm ² /s	13 log photons/cm ² /s
t = -3 s No light	 N=0	 N=0	 N=0	 N=0
t = 10 s 560nm	 N=15.75	 N=16.02	 N=14.75	 N=15.02
t = 20 s 560nm+ 480nm	 N=16.02	 N=16.02	 N=15.02	 N=16.02
	(a)	(b)	(c)	(d)

Fig. 7.11 (a)-(d) pupil images from dark adapted (t=-3s) through to 560 nm light (t=10s) and finally 480 nm+560nm (t=20s).

The mammalian retina exhibits varying spectral sensitivity to both environmental and full spectrum white light. It is most sensitive to 'daylight' blue, something that had developed through evolution. With the use of the SCWL we were able to show this shift in spectral sensitivity remarkably easily. The mouse retina was less sensitive to the 560 nm light; however, we were able to recover the full response by the presentation of a 480 nm stimulus. This difference can be attributed to the responsiveness of the photoreceptors to photonic wavelengths.

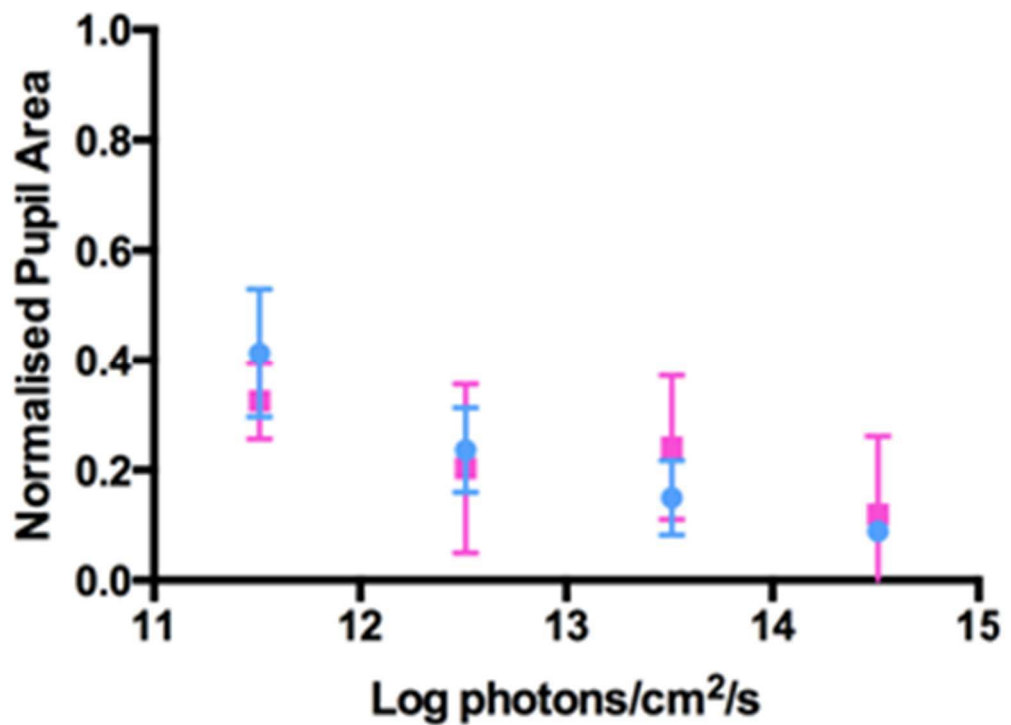


Fig. 7.12 The dark adapted pupillary response from a 480 nm Xe arc versus a dual 480 nm+560 nm pulse, with same irradiance response profile ($p > 0.05$).

7.2.2 Advantage and significance

The use of a SCWL is a significant leap forward from the Xe Arc light traditionally used in recording pupillary light responses. The SCWL gives the experimenter much more control over the light stimulus, through wavelength, intensity and, most importantly, a dual light configuration. Together, this will allow more complex lighting protocols to be developed that can further assist in unravelling the complex coding of light that gives rise to the pupil light reflex and other photic driven physiological responses.

The SCWL has a great advantage over other bespoke systems. A typical dual-wavelength stimulus, using a Xe Arc, would require a complicated configuration of optical band pass filters, shutters and light/ power generators. This presents with some significant limitations; for instance, a two-wavelength optical configuration would require two optical pathways, thus increasing the complexity and footprint of the apparatus. Our approach minimizes space usage and eliminates the need for sequential light illumination (Fig.7.13).

One of the major issues faced with any experimental protocol using filtered light from a full spectrum light source is the consistency of power output at varying wavelengths. The use of a SCWL laser enables us to select the output power at a specific wavelength. This is possible because the power density is proportional to the laser repetition rate and the optical bandwidth; the SuperK VARIA is able to maintain these parameters constantly across the entire visible spectrum for every wavelength (450-850 nm, Fig. 7.8 and Fig.7.14), thus allowing the user to select the desired power output. In addition, the output intensity can be manipulated by varying, the picoseconds pulse duration and optical bandwidth in steps of nanometres, thus maximizing the available spectrum peak power.

The timing of a stimulus is also critical. We were able to use a delayed onset in light stimulus in order to highlight the spectral sensitivity of the retina to different wavelengths. Our protocol required the two wavelengths to be presented 15 seconds apart. However, our SCWL has a variable repetition rate ranging from 2 MHz to 80 MHz, which can generate triggering rates between 15 ns to 0.5 μ s; thus allowing rapid cycling of stimuli with varying intensities and wavelengths.

There is great potential in using the SCWL in both basic biological sciences and within the clinical setting. We have just touched the surface here by demonstrating the usefulness of a dual wavelength light source in dissecting out physiological spectral sensitivity in a mouse model. In addition, there is a range of clinical uses for such a system spanning from neurosurgery, psychiatry, ophthalmology through to sleep medicine. There is a wide spectrum application for the SCWL and we believe this to be of great benefit to the advancement of science and healthcare.

7.2.3 Potential breakthrough in vision science

In recent years, age-related macular degeneration (AMD) has become one of the main causes of blindness. Vision degradation can be attributed to photoreceptor loss. Earlier studies [13] had concluded that in mid-to late-stage AMD patients, retinal pigment epithelium becomes dysfunctional, resulting in rods die in older eyes and cones began to degenerate. The relative numbers of rods to cones become imbalance. Our approach to testing receptor sensitivity can be used to diagnose patients with early-stage AMD, by probing the individual photoreceptor response. It is an efficient technique made possible by the dual/ multi-wavelength selection on the supercontinuum source.

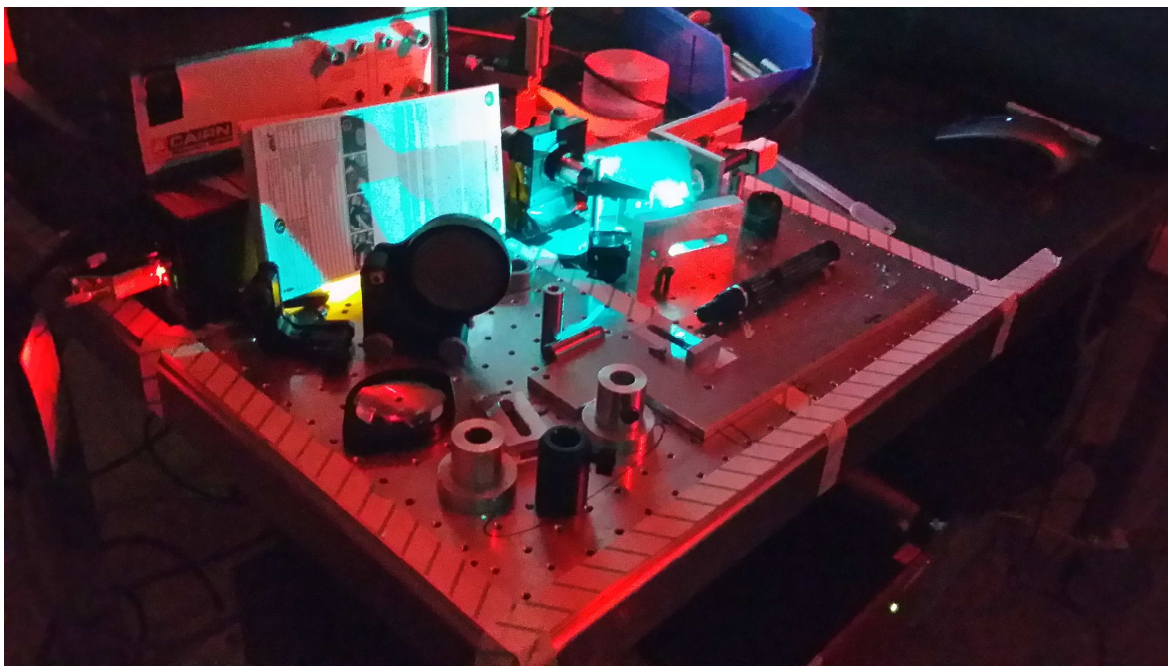


Fig. 7.13 Experimental set-up at Charles River laboratory.



Fig. 7.14 Multi-wavelength output of the NKT SuperK Varia module.

References

1. R. J. Lucas, G. S. Lall, A. E. Allen, and T. M. Brown, "How rod, cone, and melanopsin photoreceptors come together to enlighten the mammalian circadian clock," *Progress in brain research* 199, 1-18 (2012).

2. D. G. McMahon, P. M. Iuvone, and G. Tosini, "Circadian organization of the mammalian retina: from gene regulation to physiology and diseases," *Progress in retinal and eye research* 39, 58-76 (2014).
3. C. M. Altimus, A. D. Guler, N. M. Alam, A. C. Arman, G. T. Prusky, A. P. Sampath, and S. Hattar, "Rod photoreceptors drive circadian photoentrainment across a wide range of light intensities," *Nature neuroscience* 13, 1107-1112 (2010).
4. G. S. Lall, V. L. Revell, H. Momiji, J. Al Enezi, C. M. Altimus, A. D. Guler, C. Aguilar, M. A. Cameron, S. Allender, M. W. Hankins, and R. J. Lucas, "Distinct contributions of rod, cone, and melanopsin photoreceptors to encoding irradiance," *Neuron* 66, 417-428 (2010).
5. R. J. Lucas, R. H. Douglas, and R. G. Foster, "Characterization of an ocular photopigment capable of driving pupillary constriction in mice," *Nature neuroscience* 4, 621-626 (2001).
6. R. J. Lucas and R. G. Foster, "Neither functional rod photoreceptors nor rod or cone outer segments are required for the photic inhibition of pineal melatonin," *Endocrinology* 140, 1520-1524 (1999).
7. D. Lupi, H. M. Cooper, A. Froehlich, L. Standford, M. A. McCall, and R. G. Foster, "Transgenic ablation of rod photoreceptors alters the circadian phenotype of mice," *Neuroscience* 89, 363-374 (1999).
8. R. J. Lucas, S. Hattar, M. Takao, D. M. Berson, R. G. Foster, and K. W. Yau, "Diminished pupillary light reflex at high irradiances in melanopsin-knockout mice," *Science* 299, 245-247 (2003).
9. A. E. Neice, M. Behrends, M. P. Bokoch, K. M. Seligman, N. M. Conrad, and M. D. Larson, "Prediction of Opioid Analgesic Efficacy by Measurement of Pupillary Unrest," *Anesthesia and analgesia* (2016).
10. A. C. Lukaszewicz, D. Dereu, E. Gayat, and D. Payen, "The relevance of pupillometry for evaluation of analgesia before noxious procedures in the intensive care unit," *Anesthesia and analgesia* 120, 1297-1300 (2015).
11. T. M. Brown, "Using light to tell the time of day: sensory coding in the mammalian circadian visual network," *The Journal of experimental biology* 219, 1779-1792 (2016).
12. B. Feigl and A. J. Zele, "Melanopsin-expressing intrinsically photosensitive retinal ganglion cells in retinal disease," *Optometry and vision science: official publication of the American Academy of Optometry* 91, 894-903 (2014).
13. C. A. Curcio, N. E. Medeiros, C. L. Millican, "Photoreceptor loss in age-related macular degeneration," *Invest Ophthalmol Vis Sci.* 37(7):1236-49 (1996).

8

Conclusion

The works in this thesis have shown that high-resolution OCT is now one of the preferred methods for non-invasive imaging by ophthalmologists and dermatologists. The application of ultra-broadband OCT has seen significant demands from health industries with promising results. Several commercial prototypes of portable and handheld OCT devices have been manufactured in the last three years while this thesis was in progress. It is now established that OCT is a mature technology, and can be independently deployed in hospitals and surgical theatres. The general adoption of broadband OCT technology will take time. However, there is still more catching up to do to enable real-time, reliable, *in vivo* biomedical diagnosis with broadband OCT. It is therefore essential that further development in this area is more commercial oriented, so that extension of OCT capabilities can be used to attract industry interests.

Most parts of this thesis have focused on technological problems that hindered the use of OCT in clinical environments. In Chapter 2, we reviewed scientific research and technological development of OCT since its early inception in 1990. We showed how this field had overcome technical hurdles in the earlier implementation, and progressed into the robust imaging technology we know today. Chapters 3 and 4 went further into addressing numbers of specialised limitations: noise, dispersion and polarisation. We viewed these limitations as a two-sided challenge: manufacturing artefacts in the commercial light sources as well as due to the imperfect construction of the interferometer systems. Not all limitations are detrimental to our research. Some of these limitations, noise and dispersion, for example, can have adverse effects on the imaging quality if they are left unresolved, while polarisation can play a vital role in detecting additional image features, if they are used to our advantage. The technical solutions to these limitations resulted in a simple, broadband polarisation sensitive (PS-) OCT with master/slave interferometer (MSI) technology. We have discussed in detail this implementation in Chapter 5.

A large portion of this research was dedicated to characterising limitations, as we researched and resolved them step-by-step. The first technical limitation addressed was noise. In Chapter 3, we discussed extensively on methods used to quantify and minimise

noise coming out from the light source, and likewise for noise added by the OCT setup. This thesis emphasises on the use of supercontinuum sources to enhance imaging capabilities: better signal to noise ratio, minimum dispersion and ultra-high imaging resolution. We have incorporated light sources with increasing bandwidth in our noise studies: from a dual diode SLD, to swept sources, and finally supercontinuum sources. Based on the bandwidth argument, we have consistently stressed on the potential of supercontinuum to be used to power OCT systems, while we dismissed the earlier misconception of supercontinuum as being noisy as a thing of the past. We have evaluated key parameters in supercontinuum generation, and performed optimisation on several of these: pulse repetition frequency, energy emission per pulse, fibre birefringence and polarisation. These studies aimed to make supercontinuum source the preferred light source for ultra-broadband OCT imaging.

The second limitation we have overcome was dispersion. For an OCT system to resolve image features of 5 μm or less axially, it is essential that we properly compensate for dispersion. We proposed the state of the art acousto-optic tuneable filter (AOTF) method. In Chapter 4, we have shown the principle of operation with an AOTF, used together with a supercontinuum light source. This method allows us to select a narrow band light from a broadband spectrum. The AOTF module from NKT Photonics came in handy. It operates in two widely used spectral ranges for commercial imaging systems: visible from 500 to 900 nm, and near infrared from 1150 to 2000 nm. A custom built hardware-based dispersion compensation procedure was quantified using the AOTF, employing addition of dispersive glass elements. BK7 glass rods were added in the reference arm of the interferometer. Since the line width of the AOTF module can be as narrow as 5 nm, it was useful to scan across the broadband spectrum for dispersion irregularities. The AOTF method had one clear advantage: it allows us to speed up the process to obtain the variation of autocorrelation peak position in OPD versus wavelength, all in a single measurement. The slope obtained quickly determines the direction of compensation needed. This is in contrast to the time-consuming full-width at half maximum (FWHM) measurement of the autocorrelation function method, widely used in the industry. The established method requires multiple FWHM measurements, and does not provide direction of compensation needed. Our approach has established that, by estimating errors in measuring the FWHM of the A-scan peak, the AOTF method is more superior in reaching the minimum dispersion. It is also applicable for all OCT systems. Simple dispersion compensation can make commercial ultra-broadband OCT implementation easier and more attractive.

The third limitation we encountered and now resolved is polarisation. In Chapters 3 and 5, we have shown that polarisation effect is a two-way sword: it can work against us as well as in our favour. Conventional OCT imaging has been intensity based since the early days. Many commercial systems had adopted similar approach and have remained so till this day. However, we have demonstrated in Chapters 5 and 6 that there are increasing number of applications where polarisation sensitive imaging can be an advantage. This is particularly true in areas related to bio-security (explosive, narcotics), arts of historical value (paintings, archaeological artefacts) and complex histology structures (skin cancers, tooth decays, retina diseases), where these specimens have important multi-layer birefringent features. The work in second half of Chapter 3 has experimentally and theoretically verified that polarisation controlling elements can be added and manipulated in the optical sources, particularly at different stages of the supercontinuum generation process. Armed with the knowledge in polarisation selection, we can now enhance our imaging capabilities further.

The fourth limitation deals with application practicality. In an academia-only research, we focused on build to order (BTO) imaging equipment. The popularity of customisable system has become a mainstream niche in medical equipment industries. From the very simpler original equipment manufacturing (OEM) devices, to more sophisticated designs and production for application-specific equipment, the obstacles to incorporate latest research into existing commercial products need to be overcome. These hurdles involve technology integration and compatibility. UBAPHODESA researchers with academia and industrial experience can now offer feasible solutions to bridge these challenges.

Chapter 5 is a good example of how research meets market. Equipped with the knowledge and know-how from Chapters 2, 3 and 4, a bespoke PS-OCT system was assembled. We aimed to devise a high-speed and low-cost commercial solution, by developing a single, switchable spectrometer-based OCT system powered by a supercontinuum source. All optical components are readily available, and such a system can be constructed to be portable. In the past, PS-OCT was deemed too much of a challenge, due to time required to design and to manufacture a two-channel polarisation sensitive detection system, and the relatively high costs associated to acquire polarisation sensitive optical parts. We have successfully demonstrate the ability of our broadband PS-OCT system to pick up birefringent information from banknotes, and this opens up the possibility of applying polarisation imaging in counterfeit detection of other security sensitive documents.

Chapters 6 and 7 focused on the application side of low noise supercontinuum and OCT for biomedical specialists. To illustrate the practical aspect of a dispersion tolerant OCT system, we teamed up with clinicians from Maidstone and Tunbridge Wells NHS Trust Hospital to do a pilot study. In Chapter 6, we characterised different types of eyelid basal cell carcinoma (BCC), using our sophisticated master/slave (MS-) OCT system. The use of MS-OCT technique has allowed *en-face* images to detect noticeable BCC features in real time. With no further image processing required, rapid assessment of BCC surgical margins in excised skin specimens can be carried out, allowing for improved management of patients in clinics. This preliminary study to assess the values of the *en-face* display has evidenced that MSI technique is ideally suited to deliver such display, as the image is assembled directly, while laterally scanning is performed. There is no need to wait for a whole 3D volume assembly to obtain B-scans. We have illustrated the importance of collaboration between an academia (University of Kent), an industry (NKT Photonics) and a national health service (Maidstone Hospital), to explore innovative treatment options. Industrial feedback from our collaborators in Chapter 6 was positive. They have expressed interests for a clinical trial of *en-face* OCT. By combining our research in Chapter 5, we had further strengthened the case for OCT in hospitals.

Further demonstration of supercontinuum capabilities in Chapter 7 has expanded our research horizons to include a non-conventional imaging system to study vision response. In this chapter, we assessed the spectral sensitivity of the pupillary light reflex in mice using a high power super continuum source in a dual-wavelength configuration. This novel approach was compared to data collected from a more traditional, clinical setup using a Xenon arc lamp fitted with monochromatic bandpass filters. Irradiance response curves were constructed using both systems, with the added benefit of a dual-wavelength, equivocal power, and customisable output using the supercontinuum. The variables applied to the light source were intensity, wavelength and stimulus duration through which the physiological output measured was the minimum pupil size attained under such conditions. We show that by implementing the supercontinuum source as our novel stimulus, these variables can be tuned automatically and pre-programmed. Results from our tests showed that we were able to dramatically increase the physiological usefulness of our pupillometry system. We also demonstrate the efficiency and effectiveness of the supercontinuum approach, allowing for multi-wavelength, multi-speed and multi-intensity adaptation, while reducing mechanical complexity. Further works involving automation in data capture and analysis have been proposed and revised.

Most of the work described in this thesis is aimed at future applications. There is always room for technological innovation. We have seen OCT system evolves for the last 25 years, and we believe challenges remain. OCT technology is now venturing into applications in health care and pharmaceutical sectors, with great commercialisation potential. That is why we believe in constant improvement in OCT technology in areas related to signal processing, user friendliness, and equipment portability. Our approach to polarisation sensitive OCT using MSI and supercontinuum source is the first step to achieving this goal. To the best of our knowledge, there is currently no publication in this hybrid area of research.

Research and innovation are all about improving quality of life. From biomedical imaging to accelerating health care diagnosis, the results in this thesis have laid the foundation for research of the future.

8.1 Future works

The author proposes the extension of the study involving BCC in an actual clinical setting. It should be equipped with smaller optical source, and more sophisticated OCT system, which is polarisation sensitive, broadband and dispersion tolerant (enabled by MSI technique), it will become more convenient to transport such an imaging system into a local hospital for clinical trials.

Apart from the commercial and medical side, the author also noticed a huge potential in polarisation sensitive OCT applications. This thesis has demonstrated the use of high-resolution PS-OCT in detecting highly birefringent features in banknotes. The author proposes further investigation in detecting counterfeiting in valuable and secured documents by incorporating the MSI technique, in future projects.

More work is also required in the area relating to polarisation noise study. Since the author presented only the results from commercial supercontinuum sources, the author anticipates it would be interesting to also theoretically optimise the different noise parameters within the supercontinuum generation process, through simulation and modelling. The author has collaborated in part with Prof. Ole Bang's team at Danish Technical University (DTU) in Denmark, to realise this project. Further research on supercontinuum noise in general and polarisation noise in particular, will be continued by

researchers at Prof. Bang's laboratory, and further work will be carried out for the benefits of the supercontinuum community.

In the final section of PS-OCT chapter, we mentioned the need to improve sequential recording of B-scan from each polarisation component, with an automatic polarisation switch at the output of the interferometer. This is our recommendation to improve acquisition speed, reduce cost of having one instead of two identical spectrometers, as well as eliminate beam injection issues. Such an implementation is only possible when the polarising optical parts are commercially available in the future.

On the project to study light response on photo receptors, the author proposes a multi-wavelength light stimulus on transgenic mice – mice with one or more photoreceptors or melanopsin cells knocked out (or deactivated) genetically. This research regime will unleash the full potential of supercontinuum light sources, and make use of the advanced light control mechanics developed by engineers at NKT Photonics.

References

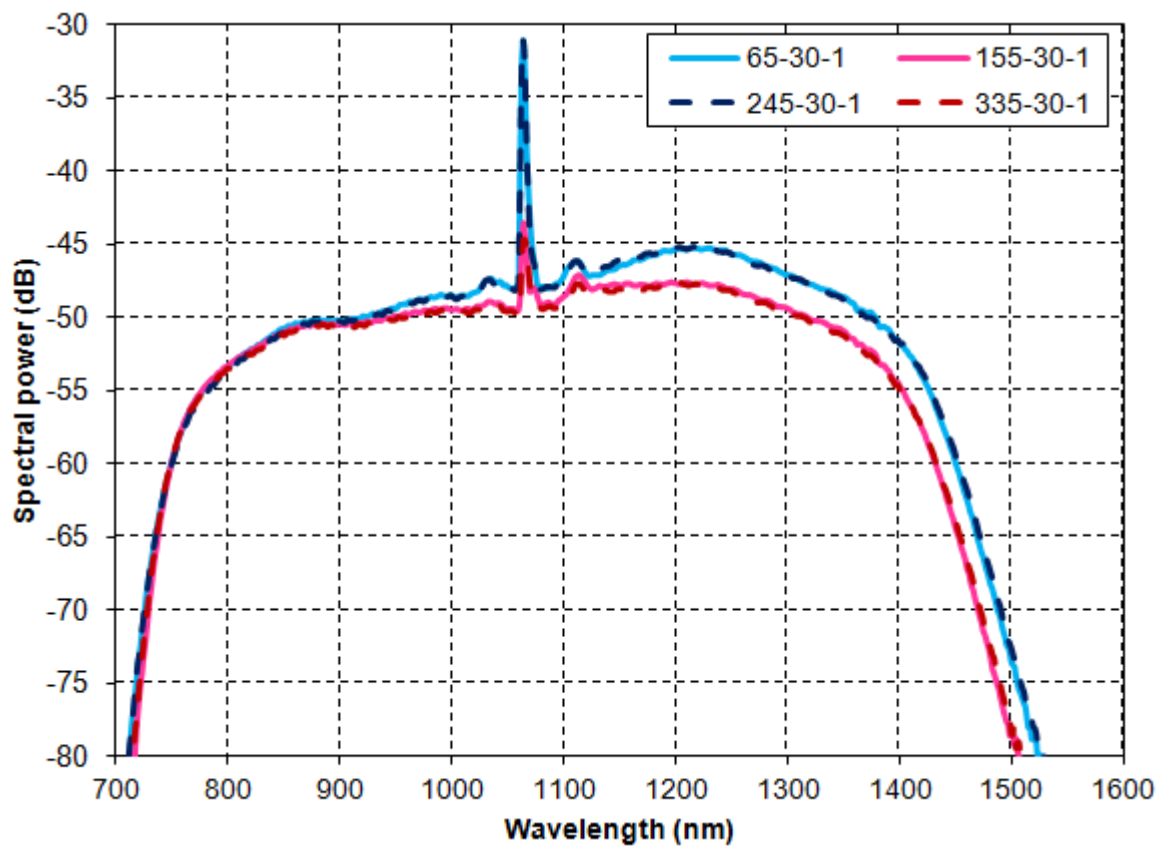
1. J. K. Lyngsø, C. Jakobsen, H. R. Simonsen, and J. Broeng, "Single-mode 7-cell core hollow core photonic crystal fiber with increased bandwidth," Proc. of SPIE 7753, 77533Q (2011).
2. S. Petersen, M. Chen, A. Shirakawa, C. Olausson, T. Alkeskjold, and J. Lægsgaard, "Large-mode-area hybrid photonic crystal fiber amplifier at 1178 nm," Opt. Lett. 40, 1741-1744 (2015).
3. S. R. Petersen, T. T. Alkeskjold, F. Poli, E. Coscelli, M. M. Jørgensen, M. Laurila, J. Broeng, "Hybrid Ytterbium-doped large-mode-area photonic crystal fiber amplifier for long wavelengths," Optics Express, 20(6), 6010-6020 (2012).
4. B. Sun et al., "Broadband Thermo-Optic Switching Effect Based on Liquid Crystal Infiltrated Photonic Crystal Fibers," in IEEE Photonics Journal, vol. 7, no. 4, pp. 1-7, Aug. 2015
5. J. Lee, B. Zhen, S. Chua, O. Shapira, and M. Soljačić, "Fabricating centimeter-scale high quality factor two-dimensional periodic photonic crystal slabs," Opt. Express 22, 3724-3731 (2014).
6. N. H. Wan, F. Meng, T. Schröder, R. J. Shiue, E. H. Chen & D. Englund, "High-resolution optical spectroscopy using multimode interference in a compact tapered fibre," Nature Comm. 7762 (2015).

Appendix A1

Polarisation extinction ratio (PER) stability test

PER test at 1.5 m fibre length at 30% pump power

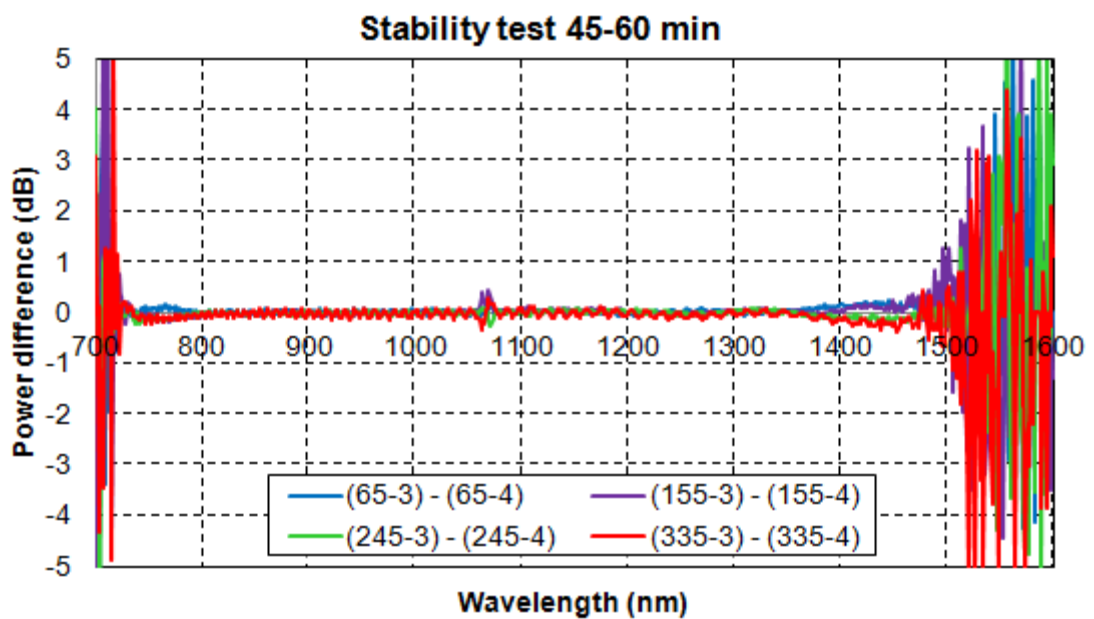
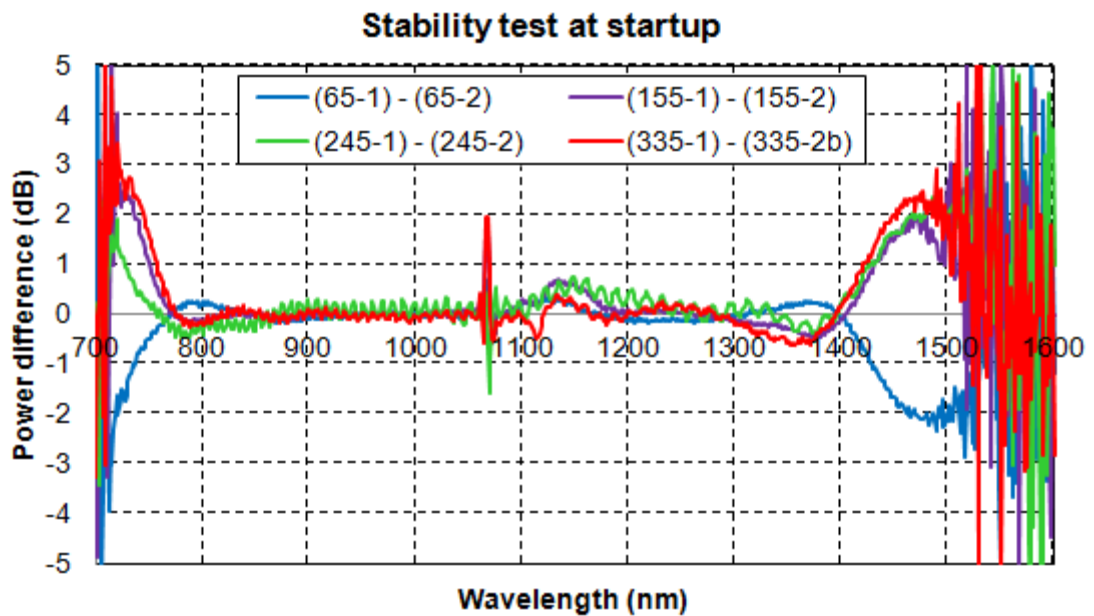
- Aim: Test for time dependent variation
- Methods: Measurement referenced to peak wavelength at 1064 nm
- Data: 4 angles (65 & 245 max, 155 & 335 min)



A1: PER test at 1.5 m fibre length at 30% pump power**Supercontinuum pump laser start-up stability test**

Four sets of measurement

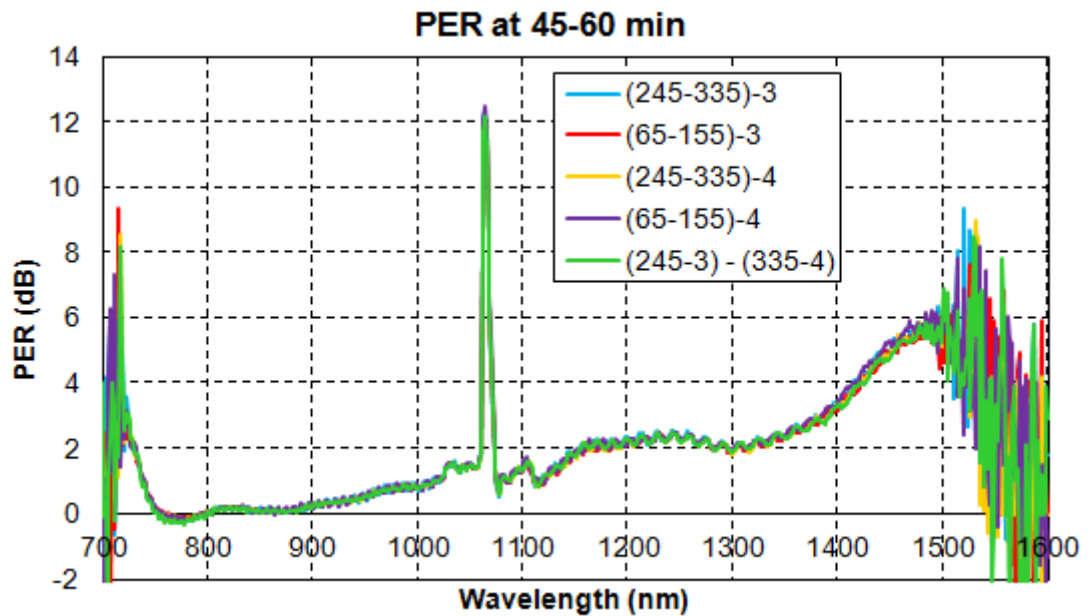
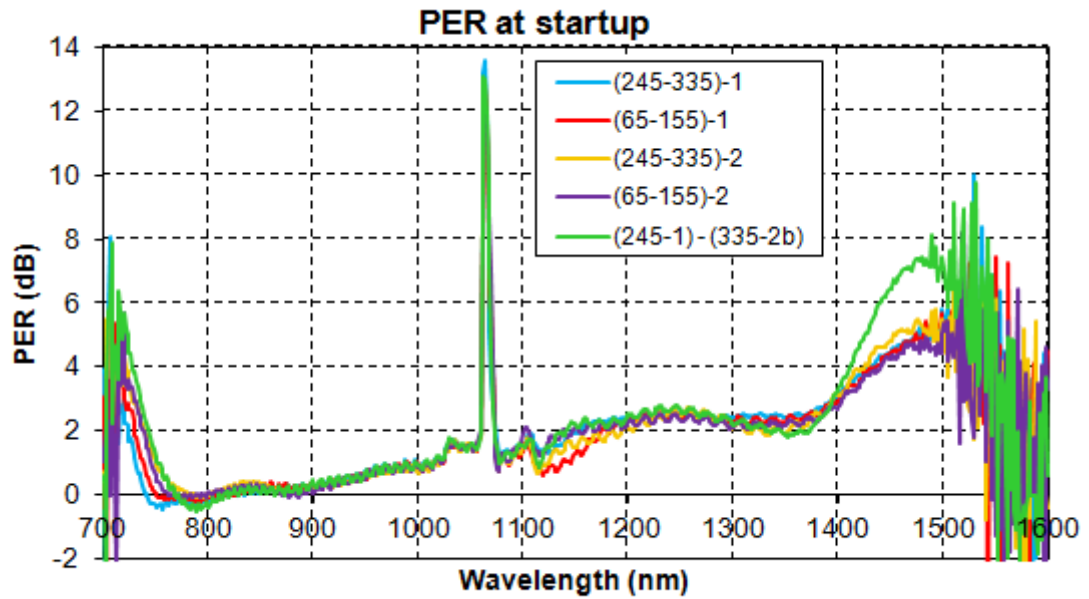
- 2 series (1,2 and 3,4)
- 1,2 began immediately after pump started emission at 30%
- 3,4 began after 45 minutes had elapsed



A1: PER test at 1.5 m fibre length at 30% pump power**Time dependent PER test**

Four sets of measurement

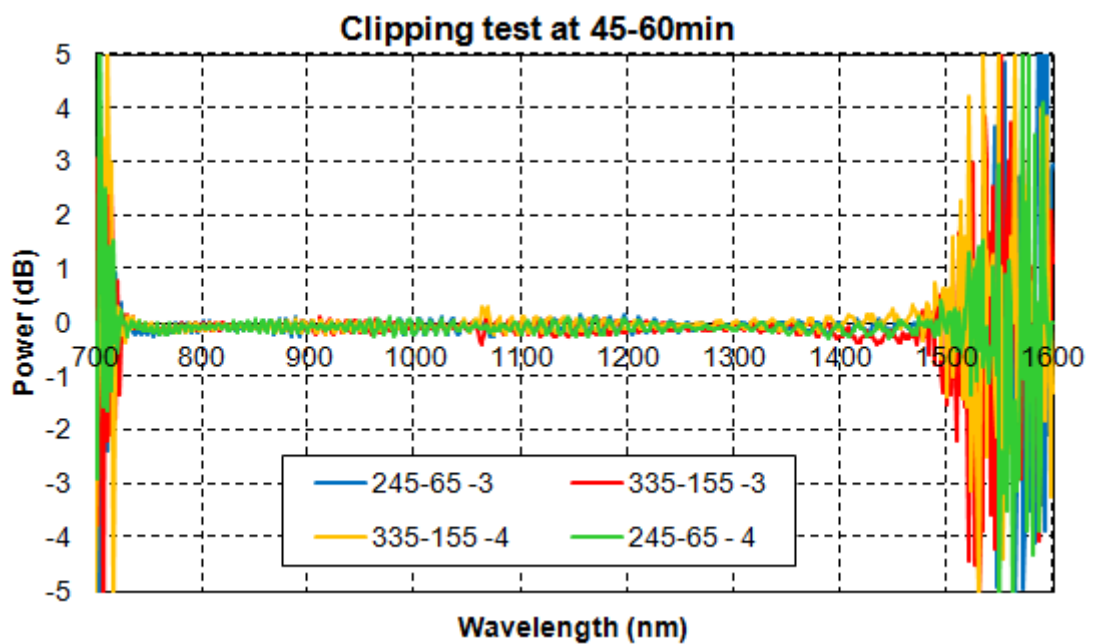
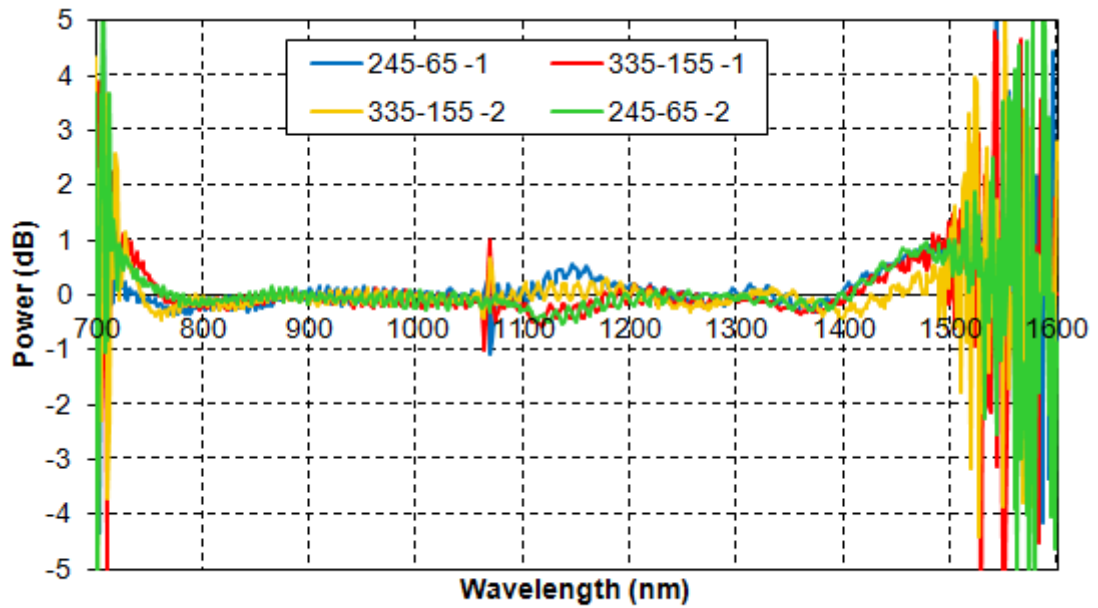
- 2 series (1,2 and 3,4)
- 1,2 began immediately after pump started emission at 30%
- 3,4 began after 45 minutes had elapsed



A1: PER test at 1.5 m fibre length at 30% pump power**Beam clipping test**

Four sets of measurement

- 2 series (1,2 and 3,4)
- 1,2 began immediately after pump started emission at 30%
- 3,4 began after 45 minutes had elapsed



Appendix A2

Birefringence and beat lengths

Analytical derivations of birefringence, beat lengths and polarisation axes

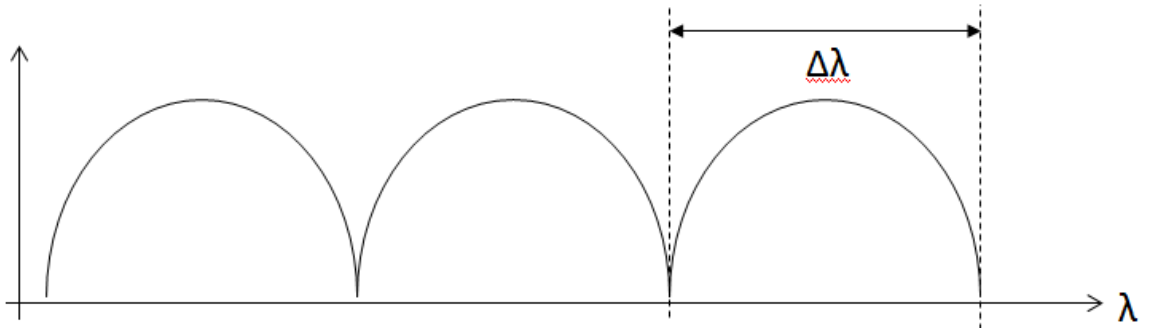
First we fixed fibre length L , we inject linearly polarized broadband light (from SuperK EXR) and to record the optical spectrum after transmission through the fibre, by rotating another polarizer to obtain max interference intensity. The interference spectrum of oscillations with a period $\Delta\lambda$, is used to calculate L_{beat} . L is cut back to obtain different L_{beat}

$$\begin{aligned} & A \exp(j\beta_1(\lambda)L) + A \exp(j\beta_2(\lambda)L) \\ &= 2A \exp\left(j \frac{\beta_1(\lambda) + \beta_2(\lambda)}{2} L\right) \times \frac{A \exp(j\beta_1 L) + \exp(j\beta_2 L)}{2} \\ &= 2A \exp\left(j \frac{\beta_1(\lambda) + \beta_2(\lambda)}{2} L\right) \times \cos(\Delta\beta(\lambda)L) \\ &= 2A \exp\left(j \frac{\beta_1(\lambda) + \beta_2(\lambda)}{2} L\right) \times \cos\left(\frac{\Delta\beta(\lambda)}{2} L\right) \end{aligned}$$

Where $\Delta\varphi = \Delta\beta L$ with $\Delta\beta \propto \frac{\Delta\lambda}{\lambda}$

Phase constant is therefore $\Delta\beta = \frac{4\pi n}{L}$

Polarisation beat length becomes $L_{beat} = \frac{2\pi}{\Delta\beta} = \frac{\lambda}{\Delta n_{eff}} = \frac{\Delta\lambda}{\lambda} L$



Appendix A3

Dual channel heterodyne detector

Analytical derivations of detector currents at the balance output

At the two outputs of DC2 before balance detection we could write the optical power that varies for each detector as intermediate frequency (IF) signal with a slightly smaller current magnitude, and a local oscillator (LO) signal with a slightly larger current magnitude. Let us assume IF has an average power of S^2 and LO has an average power of L^2 , we could now express this power relation as electric field multiplies by a matrix of coupling coefficients γ_{bal} and $(1 - \gamma_{bal})$.

$$\begin{bmatrix} \rho \\ E_1(t) \\ E_2(t) \end{bmatrix} = \exp(j\varphi_r) \begin{bmatrix} \sqrt{1 - \gamma_{bal}} & \sqrt{\gamma_{bal}} \exp(j\varphi_2) \\ \sqrt{\gamma_{bal}} \exp(j\varphi_1) & \sqrt{1 - \gamma_{bal}} \end{bmatrix} \begin{bmatrix} \rho \\ S(t) \\ L(t) \end{bmatrix} \quad (A1)$$

By proportional relationship of electric field to photocurrents, $|E(t)| \propto \sqrt{I(t)}$, we could now write the two photocurrents I_1 and I_2 of two photodetectors each with quantum efficiencies of α_1 and α_2 respectively, in the form of

$$\begin{aligned} \rho \\ I_1 &= \frac{|E_1(t)|^2}{2} \frac{\alpha_1 q_e}{h\omega} \\ &= \frac{\alpha_1 q_e}{h\omega} \left\{ (1 - \gamma_{bal}) S^2(t) + \gamma_{bal} L^2(t) + 2S(t)L(t)\sqrt{\gamma_{bal}(1 - \gamma_{bal})} \times \cos[(\omega_1 - \omega_2)t + \varphi_1 - \varphi_2] \right\} \end{aligned} \quad (A2)$$

$$\begin{aligned} \rho \\ I_2 &= \frac{|E_2(t)|^2}{2} \frac{\alpha_2 q_e}{h\omega} \\ &= \frac{\alpha_2 q_e}{h\omega} \left\{ (1 - \gamma_{bal}) L^2(t) + \gamma_{bal} S^2(t) + 2S(t)L(t)\sqrt{\gamma_{bal}(1 - \gamma_{bal})} \times \cos[(\omega_1 - \omega_2)t + \varphi_1 - \varphi_2] \right\} \end{aligned} \quad (A3)$$

Now, taking average of the photocurrents give us a DC component, and an IF component of differential frequency $(\omega_1(t) - \omega_2(t))$ of our mixed signal. When balance detection is working, we have both $\gamma_{bal} = 0.5$ and $(1 - \gamma_{bal}) = 0.5$, therefore differential current is subtracted, and IF signal term $S(t)$ can be neglected. By substituting Eqn.2-4 of main text into the simplified formulae of A2 and A3, we obtained noise components of photocurrents with one-sided power spectral density, in the form of

$$\Delta I^2(\nu) = 2q_e I(\nu) + 2q_e \gamma_{bal}(\nu) I^2(\nu) \quad (A4)$$

Thus, we can rewrite A2 and A3 in reduced form matching A4 to form noise power intensity.

$$\langle \Delta I_1^2(\nu) \rangle = 2q_e I_{1,DC}(\nu) + 2q_e \gamma_{bal}(\nu) I_{1,DC}^2(\nu) \quad (A5)$$

$$\langle \Delta I_2^2(\nu) \rangle = 2q_e I_{2,DC}(\nu) + 2q_e \gamma_{bal}(\nu) I_{2,DC}^2(\nu) \quad (A6)$$

Appendix A4

Data standardisation techniques

Statistical representation of expected value, variance and standard deviation

Data standardisation is essential for statistics. Several earlier articles have mentioned the process. These include:

1. Gaver (1985)
2. Johnson and Wichern (1992)
3. Everit (1993)
4. Van Tongeren (1995)
5. Milligan and Cooper (1988)

Techniques	Mean	Variance	Std dev
(1) 0-1 Scaling (end points scaling) $\frac{V - V_{\min}}{V_{\max} - V_{\min}}$	Different	Different	Different
(2) Dividing each value by range $\frac{V}{V_{\max} - V_{\min}}$	Different	Different	Different
(3) Z-score scaling $\frac{V - \bar{V}}{\sigma}$	0	1	1
(4) Dividing each value by standard deviation $\frac{V}{\sigma}$	Different	1	1

Appendix A5

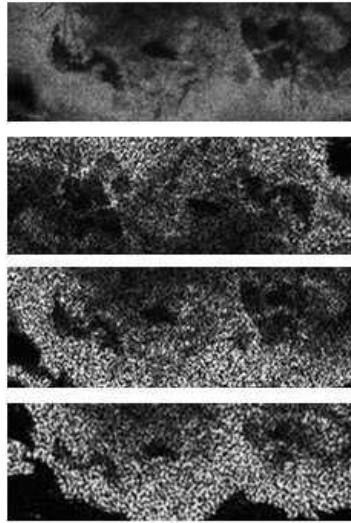
Presentation on BCC

Results (Eyelid BCC imaging)

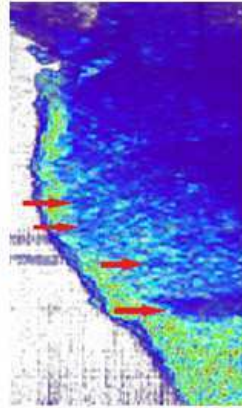
WP3-1

- Our associated partner: Maidstone & Tunbridge Wells NHS Trust Hospital (John Schofield, Mona Khandwala, Rongxuan Lim)
- Equipment: *en-face* master-slave OCT (MSI) developed in-house
- Sample imaged: biopsy proven eyelid basal cell carcinoma (BCC)
- **Resolution achieved: Axial 15 μm , transversal 10 μm**

BCC *en-face* (C-scan)



B-scan (XZ) constructed from 384 C-scans



Histology cross-section



Results from Case 2

Ethical approval for this study was obtained from both ethics committee of Univ. of Kent, and Maidstone and Tunbridge Wells NHS Trust Hospital. Research adhered to the standards of government regulations and the Declaration of Helsinki.



Mid-term Review Meeting – UBAPHODESA
Catherine Chin
Proprietary and Confidential

